LBL-15973
UC-37
CONF-830224

PROCEEDINGS
OF THE
1983 DPF WORKSHOP
ON

Collider Detectors: Present Capabilities And Future Possibilities

February 28 - March 4, 1983

Lawrence Berkeley Laboratory
University of California
Berkeley, California 94720

Prepared for the U.S. Department of Energy under Contract DE-AC03-76SF00098 and for the High Energy Physics Section of the National Science Foundation.

Printed in the United States of America
Available from
National Technical Information Service
U.S. Department of Commerce
5285 Port Royal Road
Springfield, VA 22161
Price Code: A10

LBL-15973
April 1983

PROCEEDINGS
OF THE
1983 DPF WORKSHOP
ON

Collider Detectors: Present Capabilities And Future Possibilities

February 28 - March 4, 1983

Lawrence Berkeley Laboratory
University of California
Berkeley, California 94720

Edited By
Stewart C. Loken and Peter Nemethy

Prepared for the U.S. Department of Energy under Contract DE-AC03-76SF00098 and for the High Energy Physics Section of the National Science Foundation.

FOREWORD

The "Workshop on Collider Detectors: Present Capabilities and Future Possibilities" was sponsored by the Division of Particles and Fields of the APS and hosted by Lawrence Berkeley Laboratory. It was held at LBL from February 28th to March 4th, 1983.

The organizing committee consisted of A.K. Mann (Chairman), C. Baltay, R. Diebold, H. Gordon, D. Hartill, P. Nemethy, D. Ritson and R. Schwitters. The local organizing committee was R. Cahn, S. Loken and P. Nemethy.

The workshop focused on the problems posed by high luminosities at hadron colliders, considering luminosities on a continuous range from 10^{29} to 10^{34} cm^{-2} sec^{-1}, picking two specific center-of-mass energies, 1 TeV and 20 TeV. The participants divided into the five working groups tabulated below.

These proceedings contain three sections. Section I consists of input to the workshop, the introductory comments of the organizing committee chairman (A.K. Mann); two out of our three invited talks (W.J. Willis, M. Banner, C. Rubbia) on collider experience; finally two documents, which were invaluable in getting the workshop started, theoretical estimates of relevant cross sections (R. Cahn) and of high $P_\perp$ jet behavior (F. Paige).

Section II contains the working group summary reports from the five working groups; this is the meat of the workshop. Section III is a rich mix of contributed papers relevant to the workshop.

I want to thank Jeanne Miller, our workshop secretary, and Peggy Little, the LBL Conference Coordinator, for all their help; Donna Vercelli, Judy Davenport and Loretta Lizama for their work on the proceedings. I also thank our working group leaders and scientific secretaries for their dedication and all the participants for a lively and spirited workshop. Support for this workshop was provided by the Department of Energy and the National Science Foundation.

Peter Nemethy
Workshop Organizer

WORKING GROUP	GROUP LEADER	SCIENTIFIC SECRETARY
Tracking Detectors	Don Hartill	David Herrup
Calorimetry	Bernie Pope	Melissa Franklin
Triggers	Mel Shochet	Mike Ronan
Particle Identification	Dave Nygren	Rem Van Tyen
Detector Systems	Barry Barish	Mark Nelson

TABLE OF CONTENTS

Foreword..... iii

List of Participants..... ix

SECTION I. WORKSHOP INPUT

Introductory Comments..... 3
A.K. Mann

Experience of the Axial Field Spectrometer at the CERN ISR..... 5
W.J. Willis

Search for Hadron Jets and Large Transverse Momentum Electrons at the SPS $p\bar{p}$ Collider... 21
M. Banner

Cross Section Estimates for Multi-TeV Physics..... 28
R.N. Cahn

Monte Carlo Simulation of High $P_\perp$ Jets..... 30
F.E. Paige, S.D. Protopopescu, and D.P. Weygand

SECTION II. WORKING GROUP SUMMARY REPORTS

Tracking Detectors..... 43
D. Hartill

Calorimetry..... 49
B. Pope

Triggers..... 58
M. Shochet

Particle Identification..... 62
D.R. Nygren

Detector Systems..... 64
B.C. Barish

SECTION III. CONTRIBUTED PAPERS

Track Chambers for High Luminosity..... 75
T. Ludlam and E.D. Platner

The Performance of A 16000 Wire Mini-Drift MWPC System..... 81
P. Chauvant, R. Cousins, K. Hayes, A.M. Smith, R. Bonino, J.G. Zweizig, J. Alitti, B. Bloch-Devaux, A. Borg, J.B. Cheze, A. Diamant-Berger, I. Giomataris, B. Pichard, F. Rollinger, M. Tararine, J. Zsembery

Breakdown Processes in Wire Chambers, Prevention and Rate Capability..... 88
M. Atac

The Concept of a Solid State Drift Chamber..... 97
E. Gatti and P. Rehak

Large Area Non-Crystalline Semiconductor Detectors..... 99
V. Perez-Mendez, T. Mulera, S.N. Kaplan, P. Wiedenbeck

The Design and Expected Performance of a Fast Scintillator Hadron Calorimeter..... 101
R.B. Palmer and A.K. Ghosh

Scintillation Chamber Operation of Calorimeters for Colliding Beam Detectors..... 106
L.W. Jones

High Energy Electromagnetic Shower Position Measurement by a Fine Grained Scintillation Hodoscope..... 108
B. Cox, G. Hale, P.O. Mazur, R.L. Wagner, D.E. Wagoner, H. Areti, S. Conetti, P. Lebrun, T. Ryan, R.A. Gearhart

Scintillators and Waveshifters for Fast Scintillator-WSB Calorimetry..... 111
G.E. Theodosiou

Scintillator Calorimetry with Vacuum Photodiode Readout..... 113
W. Selove and G.E. Theodosiou

A Measurement of the Response of an SCG1-C Scintillation Glass Shower Detector to 2-17.5 GeV Positrons..... 115
B. Cox, G. Hale, P.O. Mazur, R.L. Wagner, D.E. Wagoner, H. Areti, S. Conetti, P. Lebrun, T. Ryan, J.E. Brau, R.A. Gearhart

Calorimetry at $L = 10^{33}$..... 119
W. Selove and G.E. Theodosiou

Triggering at High Luminosity: Fake Triggers from Pile-Up..... 122
R. Johnson

Fast Asynchronous Level 1 Pre-Trigger for Electrons at $L = 10^{33}$ cm^{-2} sec^{-1} 125
M.J. Tannenbaum

Prospects for Cerenkov Ring Imaging at Hadron Colliders 127
M. Goldberg and D. Leith

Use of Synchrotron Radiation for Electron Identification at High Luminosity 132
S. Aronson

TOF for Heavy Stable Particle Identification 134
C.Y. Chang

Operation of a High-P_T Spectrometer Arm at 10^{33} cm^{-2} sec^{-1} with Particle Identification 137
S. Aronson, M. Goldberg, M. Holder, E. Loh

Muons and Electrons in General 140
L. Nodulman and J. Bensinger

Large Solid Angles Solenoid Spectrometer with Particle Identification by dE/dx 142
D.R. Nygren

Detecting Heavy Quark Jets 143
G. Benenson, L.L. Chau, T. Ludlam, F.E. Paige, E.D. Platner, S.D. Protopopescu, P. Rehak

Angular Coverage of Detectors 157
R. Diebold

A Detector with a 3 T Solenoid for a 10 TeV Collider 159
R. Kephart, A. Tollestrup, M. Mestayer

State of the Art 161
L.M. Lederman

Experience with High Luminosity Running at the CERN ISR 163
J.T. Linnemann

Operation of the AFS at $L = 1.4 \times 10^{32}$ cm^{-2} sec^{-1}: A First Look at Data at High Luminosity from the CERN ISR 169
The Axial Field Spectrometer Collaboration

Rates and Time Structure Expected from $\sqrt{s}$ = 40 TeV Colliders 172
R. Diebold

Advantages of Spatial and Temporal Segmentation for Detectors at High Luminosity CW Colliders..... 174
M.J. Tannenbaum

Monte Carlo Simulation of the Effect of Pileup..... 175
H.A. Gordon, R.A. Johnson, S.A. Kahn, M.J. Murtagh, D.P. Weygand

Calorimeteric Physics in the Presence of Multiple Events..... 179
J. Yoh

Virtus: A Multi-Processor Event Selector Using Fastbus..... 185
J. Ellett

LIST OF PARTICIPANTS

Jeffrey Appel
Fermilab

Samuel Aronson
Brookhaven National Laboratory

Muzaffer Atac
Fermilab

Charles Baltay
Columbia University

Marcel Banner
CEN Saclay

Barry Barish
California Institute of Technology

Wulfrin Bartel
DESY

Eugene Beier
University of Pennsylvania

Jim Bensinger
Brandeis University

Harry Bingham
University of California Berkeley

James Branson
MIT

Martin Breidenbach
SLAC

Alan Bross
Lawrence Berkeley Laboratory

Robert Cahn
Lawrence Berkeley Laboratory

Leslie Camilleri
CERN

William Carithers
Lawrence Berkeley Laboratory

Terry Carroll
SLAC

Chung Y. Chang
University of Maryland

William Chinowsky
University of California Berkeley

James Christenson
New York University

Bradley Cox
Fermilab

Robert Diebold
Argonne National Laboratory

Mark Eaton
Harvard University

Guido Finocchiaro
State University of New York

Melissa Franklin
Lawrence Berkeley Laboratory

Emilio Gatti
Istituto di Fisica Politecnico di Milano

M. Gilchriese
Cornell University

Marvin Goldberg
Syracuse University

Howard Gordon
Brookhaven National Laboratory

Douglas Greiner
Lawrence Berkeley Laboratory

Richard Gustafson
University of Michigan

Donald Hartill
Cornell University

David Herrup
Lawrence Berkeley Laboratory

Werner Hofmann
Lawrence Berkeley Laboratory

Martin Holder
University of Siegen

Walter Hoogland
NIKHEF

Frederick Russell Huson
Fermilab

Randy Johnson
Brookhaven National Laboratory

Lawrence Jones
University of Michigan

John Kadyk
Lawrence Berkeley Laboratory

Richard Kass
University of Rochester

Robert Kephart
Fermilab

Richard Kofler
University of Massachusetts

Leon Lederman
Fermilab

David Leith
SLAC

David Levinthal
Fermilab

James Linnemann
Rockefeller University

Eugene Loh
University of Utah

Stewart Loken
Lawrence Berkeley Laboratory

Thomas Ludlam
Brookhaven National Laboratory

Richard Majka
Yale University

Al Mann
University of Pennsylvania

Jay Marx
LBL/DOE

Mac Mestayer
Vanderbilt University

Peter Nemethy
Lawrence Berkeley Laboratory

Mark Nelson
Lawrence Berkeley Laboratory

Laurence Nodulman
Argonne National Laboratory

David Nygren
Lawrence Berkeley Laboratory

Renee Ong
SLAC

Frank E. Paige, Jr.
Brookhaven National Laboratory

Robert Palmer
Brookhaven National Laboratory

Sherwood Parker
University of Hawaii

Edward Platner
Brookhaven National Laboratory

Bernard Pope
Michigan State University

Veljko Radeka
Brookhaven National Laboratory

Pavel Rehak
Brookhaven National Laboratory

David Ritson
SLAC

Michael Ronan
Lawrence Berkeley Laboratory

Jerome Rosen
Northwestern University

Carlo Rubbia
CERN

Bernard Sadoulet
CERN

Fabio Sauli
CERN

Rafe Schindler
California Institute of Technology

Peter Schlein
UCLA

Roy Schwitters
Harvard University

Walter Selove
University of Pennsylvania

Kirk Shinsky
Lawrence Berkeley Laboratory

Mel Shochet
University of Chicago

Eric Siskind
NYCB Real-Time Computing, Inc.

A.J. Stewart Smith
Princeton University

Stephen R. Smith
Fermilab

Lee J. Spencer
Brandeis University

Herbert Stelzer
GSI

Harry Sticker
Rockefeller University

Michael Tannenbaum
Brookhaven National Laboratory

George Theodosiou
University of Pennsylvania

Dennis Theriot
Fermilab

Alvin Tollestrup
Fermilab

Rem Van Tyen
Lawrence Berkeley Laboratory

Hugh Williams
University of Pennsylvania

Bill Willis
CERN

Gunter Wolf
DESY

John Yoh
Fermilab

John Zweizig
UCLA

SECTION I: WORKSHOP INPUT

INTRODUCTORY COMMENTS

THE DPF WORKSHOP ON COLLIDER DETECTORS:

PRESENT CAPABILITIES AND FUTURE POSSIBILITIES

A. K. Mann
Department of Physics
University of Pennsylvania
Philadelphia, PA 19104

It is useful before beginning our work here to restate briefly the purpose of this workshop in the light of the present circumstances of elementary particle physics in the U.S.

The goal of our field is easily stated in a general way: it is to reach higher center of mass energies and higher luminosities while employing more sensitive and more versatile event detectors, all in order to probe more deeply into the physics of elementary particles. The obstacles to achieving this goal are equally apparent. Escalating costs of construction and operation of our facilities limit alternatives and force us to make hard choices among those alternatives. The necessity to be highly selective in the choice of facilities, in conjunction with the need for increased manpower concentrations to build accelerators and mount experiments, leads to complex social problems within the science. As the frontier is removed ever further, serious technical difficulties and limitations arise. Finally, competition, much of which is usually healthy, now manifests itself with greater intensity on a regional basis within our country and also on an international scale.

In the far ($\gtrsim$ 20 yr) future, collaboration on physics facilities by two or more of the major economic entities of the world will possibly be forthcoming. In the near future, we are left to bypass or overcome these obstacles on a regional scale as best we can.

The choices we face are in part indicated in the list of planned and contemplated accelerators shown in Table I. The facilities indicated with an asterisk pose immediate questions: (1) Do we need them all and what should be their precise properties? (2) How are the ones we choose to be realized? (3) What is the nature of the detectors to exploit those facilities? (4) How do we respond to the challenge of higher luminosity as well as higher energy in those colliders?

The decision-making process in this country and elsewhere depends on the answers to these technical questions. Those relating to the accelerators have been and continue to be addressed in many workshops and studies. For example, a workshop organized by M. Tigner will begin to study the means of achieving a very high energy (10 TeV x 10 TeV) hadron collider; this is scheduled at the end of March at Cornell University. If it seems desirable, continuity in the form of subsequent workshops on technical questions relating to accelerator facilities might be provided by the Division of Particles and Fields (DPF) of the American Physical Society, as it is doing here for collider detectors.

The workshop we are about to begin is intended to address questions (3) and (4) above. It is an attempt to look at those questions from a broad point of view by assembling a wide spectrum of experts from universities and national and international laboratories. It is planned to make the proceedings of the workshop available to the 1983 Woods Hole Sub-Panel of HEPAP which is charged with the responsibility for recommendations concerning the choices that face the U.S. program. This is the main reason that we are meeting at the present time.

In this connection, it is worth emphasizing that the DPF is an organization of roughly 3000 physicists from universities and national laboratories. It is an independent organization not affiliated with any laboratory or government agency. Most important, it is not a decision-making body or a lobbying group. Its aim is to provide neutral arenas for scholarly discussion of the salient issues of our area of science, e.g., the DPF Summer Study on Particle Physics and Facilities in Snowmass, Colorado, in the summer of 1982. For this reason it concentrates on technical questions such as those of this Workshop.

Lastly, let me comment on the structure of the Workshop.

First, note that according to the registration rolls there are 89 American physicists here, divided about equally between universities and national laboratories, and 15 physicists from Europe, a sign of of the beneficial international cooperation that is present in our field. In addition, there are two representatives from industry.

All of us are indebted to the three (and only three) invited speakers, W. Willis, C. Rubbia and M. Banner, who have brought us the results of their extensive experience in the subject before us. We owe thanks also to D. Shirley and D. Jackson for the hospitality of Lawrence Berkeley Laboratory; and to the local organizing committee for the Workshop: P. Nemethy, Chairman, S. Loken and R. Cahn, who have labored mightily in our behalf.

Table I. Planned and Contemplated New Facilities for High Energy Physics.

Country	Laboratory	Facility	Properties		
Switzerland	CERN	SPS Collider[1]	$\bar{p}p$:	270 GeV x 270 GeV;	10^{29} cm^{-2} sec^{-1}
		LEP	e^+e^-:	50 x 50;	10^{31}
		* ?	pp or $\bar{p}p$:	$\geq$ 5 TeV x $\geq$ 5 TeV;	?
West Germany	DESY	HERA	e^-p:	30 x 800;	0.5 x 10^{32}
Japan	KEK	Tristan	e^+e:	30 x 30;	10^{31}
U.S.A.	SLAC	SLC	e^+e^-:	50 x 50 ;	6 x 10^{30}
	FNAL	TeV I	$\bar{p}p$:	1 TeV x 1 TeV ;	10^{30}
		TeV II	fixed tgt p:	1 TeV;	> 2 x 10^{13}/60 sec
	BNL	* CBA	pp:	400 x 400 ;	10^{33}
	?	* ?	pp or $\bar{p}p$:	$\geq$ 5 TeV x $\geq$ 5 TeV;	?
U.S.S.R.	Serpukhov	---	fixed tgt p:	3 TeV;	---

[1] In operation and yielding data

EXPERIENCE OF THE AXIAL FIELD SPECTROMETER AT THE CERN ISR

William J. Willis

1. Introduction

The Axial Field Spectrometer is a facility designed with an emphasis on flexibility and measurements of energy by calorimeters of very good energy and angle resolution for both electromagnetic and hadronic particles. It was proposed by BNL-CERN-Copenhagen-Lund-Rutherford collaboration and started operating in 1979. It was designed for moderate luminosities, 10^{31-32} cm^{-2} s^{-1} or interaction rates from 0.4 - 4MHz, and charged particle multiplicities up to 50. It would certainly not operate satisfactorily at a luminosity of 10^{33}, but the rates are high enough to bring out the important differences from the operation of low rate experiments, such as the e^+e^- or $\bar{p}p$ colliders. In fact, in the survey presented to this Workshop by Lederman, the highest instantaneous rates in a full solid angle, "open" spectrometer leading to a published paper are from the ISR experiment R110, with a conventional magnet low $-\beta$ insertion, and a luminosity of $\simeq 6.5 \times 10^{31}$ cm^{-2} s^{-1}. A luminosity of 1.4×10^{32} an^{-2} s^{-1} was obtained last December in a short test of the superconducting low $-\beta$ insertion installed for the Axial Field Spectrometer. Some first results on an energy flow high P_T jet analysis will be described in these proceedings by Howard Gordon. (On the last day of this Workshop, we started a successful 60 hour run under these conditions which will yield publishable results.) The history of the record luminosity attained in the ISR over its history is shown in Figure 1. The arrow shows the design luminosity. I hope the newer colliders will have the same fortunate history. Some important consequences of the relatively high rates are:

i) The mutability of the experiment.

ii) The dominance of trigger considerations.

iii) A related technical matter: the overlapping of the data acquisition with trigger processing, in time.

2. Permutations, Combinations

The high rate allows several different experiments to share the solid angle and the core detectors, with parallel triggers which are sufficiently selective to keep the livetime high. These experiments can be completed in a reasonable time, to be succeeded by others, a steady change of configuration which I have called the "mutability" of the set-up. The rate of these individual experiments would of course be higher if they covered the full solid angle, but in a world of finite resources it is often very difficult to provide for that, unless it can be built into a universal detector of sufficiently high performance or into a device we still have not seen, even on paper.

Below we describe eight mutations of the Axial Field Spectrometer, with brief descriptions of the physics aims of each, and the list of collaborating institutions involved. Note that the original collaboration did not undertake all these efforts, nor would that have been possible. Some institutions joined the core collaboration after undertaking a specialized experiment, others participated only in a specific topic.

A. AFS Central Tracking Detector and Uranium Calorimeter - BNL-CERN-Copenhagen-Lund-Rutherford-Pennsylvania-Tel Avis

The apparatus is shown in Figure 2, with some later additions. The physics aims were the study of high E_T events, high p_T jet production, high p_T electrons and pairs. There was a great emphasis on good measurement of energy flow, with 800 independent towers over two units of rapidity, with electromagnetic and hadronic readout, and position interpolation in the towers. The single hadron energy resolution in $0.37E^{\frac{1}{2}}$ (GeV). Figure 3 gives an idea of the construction, and shows two of the four walls covering the whole ezimuth. Tracking is provided by a JADE-type drift chamber (Figure 4) with 42 layers which identifies electrons and slow hadrons by ionization (σ = 11%), as shown in Figures 5 and 6.

Typical physics results from this apparatus are the single inclusive jet cross sections shown in Figure 7, or the comparison of high $-p_T$ single particle productions by pp and $\bar{p}p$ collisions in Figure 8.

B. Identified High p_T Charged Particles - Copenhagen-Lund-Rutherford

This experiment was described in the original proposal, with a spectrometer including three Cerenkov counters and PWC's provided by the above institutions. The set up is shown in Figure 9. The physics aim is jet fragmentation and particularly quantum number dependences, and preliminary results were presented at the Paris Conference.

C. Direct Single Photon Production

This process (which had not been forseen) turned up in the data of ISR experiment R806 during the construction of the AFS, and the liquid argon photon detectors were installed to run in conjunction with the AFS from the beginning of its operation (Figure 10). This proved extremely interesting since it allowed the statistics on the photon production to be greatly increased as well as providing a complete measurement of the associated event. The photon cross section as a function of p_T is shown in Figure 11, with a slope characteristic of an elementary QCD process, compared with the pi-zero cross section measured from two photon events in the same apparatus. The ability to measure the whole event was essential to demonstrate that the photons come from the elementary QCD "Compton" process, rather than something like quark bremstrahlung. Evidence for this comes from several measurements, but most clearly from the distribution of charged particles associated with single photons and with pi-zeros (Figure 12). The pi-zero is accompanied by other particles resulting from the fragmentation of a high p_T parton, but there is absolutely no sign of other particles associated with the photon, showing it is the photon in this process. Other measurements agree with this picture, so that this process can be used as a direct measurement of the gluon distribution function. Further information comes from comparison of $\bar{p}p$ and pp interactions.

D. Forward Direct Single Photon Production - BNL-Pisa-Pittsburgh

Measurements near 90° do not provide enough information to determine distribution functions accurately. A small group of physicists built a photon detector of very fine granularity to measure direct photons at angles of 11° to 17°. The detector consists of 10mm wide scintillation and 1.7mm thick uranium plates, and provides a spatial resolution of 2mm, separating single photons from pi-zeros for energies up to ≈ 25 GeV, at only 1.8m from the source, Figure 13. The inclusive photon spectrum is shown in Figure 14, with two theoretical predictions and the analysis of the associated charged particles in underway.

E. Forward Hadron Calorimeters - Johns Hopkins-Pennsylvania

These were installed to carry out an initial double-Pomeron trigger, and added to for studies with α-α and α-p interactions, as shown in Figure 15. They allowed many measurements on the correlations of proton and α fragmentation with central rapidity region multiplicity, etc. Typical distributions are shown in Figure 16. Note that these calorimeters are very close to the outgoing beams and will be mentioned when the question of radiation damage arises later in this talk.

F. Double Diffractive Proton Trigger - Cambridge-Queen Mary College-Rutherford

This experiment is a search for gluonium, presumably enhanced in two gluon exchange, and thus in the double diffractive region. The protons are tagged by a system of small drift chambers just outside the beam pipes 5-6m from the interaction point, Figure 17. If elastic scatterings are eliminated, and events with forward particles vetoed, the coincidence rate is small enough to allow this to function as a parallel trigger.

G. Single and Double Direct Photon Detector with NaI and Vacuum Photodiodes - Athens-Moscow Engineering University-Lebedev Institute, Novosibirsk-Pisa-Pittsburg

This experiment is an improvement over the R806 photon detector in the following respects:

i) better resolution, especially at low photon energies;

ii) tower readout instead of strips;

iii) larger solid angle;

iv) (more important!) compatible with the full-coverage

It uses two arrays of $(35\ mm)^2$ NaI crystals in projective geometry, 5 radiation lengths thick and readout in a magnetic field with a vacuum photodiode, giving a noise level of about 1 MeV, as shown in Figure 18 and 19.

H. High p_T Muon Detector

The PWC's from the Cerenkov arm have been re-used to create a muon trigger covering about a tenth of the solid angle, using the calorimeter and 80cm of iron as an absorber, a total of more than eight absorbtion lengths. The energy threshold and rejection are enough to allow the trigger to run in parallel with a minimum of other conditions.

This shared mode of operation requires.

i) a sufficiently high interaction rate,

ii) a powerful trigger system to pick the particular processes of interest in a selective, efficient manner so that a number of parallel triggers can be used with a high live-time fraction,

iii) enough live-time per year to make acceptable the overheads due to more complex situation,

iv) a certain amount of good will among the experimental teams, each of whose projects will rm a bit slower than if they had sole use of the facility.

I believe that the degree of parallelism described above is not usually or ever achieved in fixed target spectrometers, due (I suppose) to a combination o$^{\circ}$ all the above factors. For example, on point i), we should recall that the continuous duty cycle of ISR gives a factor of four or so more livetime. The character of storage rings is such that if any runs, everyone runs. This has tended to provide more hours per year than fixed target programs. The fact that the arrangements were made with a minimum of intervention of a program committee has probably avoided excerbating the problem iv). Of course the question does not come up in e^+e^- machines where the ideal trigger selects all real events. All these points considered, the provision of a suitable trigger system is still the most important.

3. Triggering

The trigger system involves a number of levels, schematically indicated in Table I. A much simplified schematic of the first two levels is shown in Figure 20, showing only the part having to do with the uranium calorimeter. The system is one dimensional, in that sums are performed for fixed azimuthal angle ϕ, with weights as a function of polar angle and ϕ (to take out the center of mass motion due to finite crossing angle at the ISR) so that the sums represent p_T (ϕ). These 48 electromagnetic and 48 hadronic sums are transmitted on fast cables to the counting room together with a number of other fast signals used in the trigger, while the data aquisition signals travel on longer slow cable, giving a delay of 250ns which allows the first level of trigger processing to be nearly deadtimeless. The first level consists of a number of digitally controlled thresholds on global sums and other simple functions.

The second level is also carried out by analog computation, and can consequently be quite fast. In fact, a moderate increase in the data acquisition delay would have allowed it to be overlapped with the signal transmission, effectively eliminating its deadtime, but this did not seem to be necessary at our luminosities. There are about 700 computer controlled discriminators, whose outputs are encoded onto about 50 parallel lines, on a fast ring bus, which drives up to 48 logic modules which use those lines to form decisions, consulting fast memories loaded by computer, and "prescalers" if desired. Up to this level, the system is completely parallel, rather than organized serially, so that this addition of additional triggers has no effect on timing, or any other function of another trigger. A complete monitoring and checking system is provided.

The timing of the next level was partly dictated by electronic processing or in the PWC single particle trigger, and partly by intrinsic detector delays, as in the case of the drift chamber or NaI detector.

The next level uses the ESOP microprogrammed computer developed at CERN and used in a number of experiments. A typical use is a sagitta calculation on a track in the drift chamber, given a pointer from a shower detector at level 2, which takes 80-200 μs, depending on the number of tracks in the road, the first number being mainly the data transfer time.

This system is used with 10-20 parallel triggers, with about 6Hz of events written to tape (8000 tapes per year for 10^7s!). Each trigger then must average 0.3 H_z, or about $\sim 10^{-7}$ of the total interaction rate. High p_T thresholds can of course give as small a rate as one likes; the trick is to select the desired reactions without very high thresholds - consequently the need for sensitive, multi-level triggers.

4. Processing

Going to higher luminosities while maintaining the same sensitivity to rare, but moderately low p_T processes, seems to require the maintenance or extension of the concepts of parallelism, analog processing and overlapping seen in the first two levels of our trigger. It is difficult to envision a time when summing and weighting can be done as fast with a digital system as with an analog one. True, it doesn't matter if the trigger processing takes a bit longer as long as it is overlapped with the data acquisition through some sort of delay. This delay becomes very formidable though, as the number of channels in the detector increases; the dynamic range required increases (for example because the relative precision of our calorimetric detector is increasing as $E^{-\frac{1}{2}}$) and the time resolution of the detector is being improved to cope with the higher luminosity.

The equivalent of the first two or three levels of our system need to become more powerful to provide increased selectivity, unless one is content to accept much higher rates (of much larger events!). It will be important to keep the processing in a fully parallel mode, while dealing with more detector elements. This will require wider buses - perhaps several hundred lines for example, preferably operating faster. New ideas on connectors and mechanical design are needed. (Our ring bus represents an uneasy compromise between compactness and mechanical solidity.)

I stress this subject because it is extraordinarily elusive in the context of a workshop. It clearly doesn't correspond to a definite physical limit as some detector issues do. It is hard to identify the problem unless the detector and its use are specified in some detail. It sounds like it is just a matter of expense, but one should keep an eye on it.

5. Detector Issues Associated with High Rates

First, I should note that the detector we have used at the ISR have all been optimized for resolution, in energy or angle, with attention to high rate capability as a secondary consideration. Indeed, the experience in our field has shown that resolution is so important that I would not give up as much as a factor of two in resolution to get only a factor of two in response time, for example. Of course price and delivery time have often played a role. For example, the optical components in our scintillator calorimeter could now be replaced with faster ones with no sacrifice in performance. Figure 21 shows a small increase in hadron resolution in our calorimeter when the gate is as short as 50ns, with the electron resolution unaffected. This is presumably due to a combination of time of flight of slow hadrons, particularly neutrons, which will be dependent on absorber material, and of slow components in the scintillator induced by heavily, ionizing particles which will depend on scintillator type. In optimizing the system, one will effect the linearity of the hadron calorimeter, and its resolution, particularly for jets. This is shown, in the form of the ratio of response of e's and π's of equal available energy, in Figure 22.

6. Pileup

Working with detectors with non-negligible response times for the rates we deal with, we have had to devote a lot of attention to detection of accidentals, and pile-up. Our initiation to this problem was with our LA calorimeters, which had a bi-polar response 1200ns in overall length. We started using this system with interaction rates of about 50kH_z, and expected to have to fight a serious pile-up problem as the ISR luminosity rose by an order of magnitude. Accordingly, we equipped ourselves with sophisticated pile-up detectors built by V. Radeka. In fact, we never encountered any problem even at the highest rates, because all the physics programs with that detector turned out to involve at least one relatively high p_T particle which could be used in the trigger through the analysis might involve CMS energies as 50 MeV. The energy of the high p_T particle in the trigger was required to be localized in a solid angle of about 0.0075 steradians, which leads to a low sensitivity to accidentals. The solid angle quoted was with a detector with strip type readout. One with tower type readout, as in the case of our present NaI detector, has a cell solid angle an order of magnitude smaller, and our double direct photon experiment would function at very high luminosities, even with the slow NaI.

The solid angle occupied by a jet is larger, and we have prepared three systems for use in our planned experiment to measure jet production near the kinematic limit with $L \simeq 2 \times 10^{32}$ cm^{-2} s^{-1}.

i) Time measurement on a set of scintillators forming a central barrel, and read out at each end. The error is a few ns.

ii) A set of simple fast scintillator counters towers filling 30° cones forward and backward. The resolution is 0.7ns.

iii) The accidentals can be adequately rejected at high luminosity with the previous two systems, but we want to accept most events with "harmless" accidentals and make a small pileup corrections. For this purpose, we have installed a set of 50 fast flash ADC's looking at the p (ϕ) and other sums, with 10ns bins. With these we can usually establish whether an event has been appreciably affected by accidentals.

In order to apply this technique to E_T triggers at our luminosity, we might have to digitize the shape of the signal from our 800 towers, which would not be unreasonable, but since the ISR has only one more year, we have no plans to do that.

7. Radiation Damage and Lifetime

This can be a problem at ISR. The forward calorimeters near the beam, which were shown in Figure 14 received significant radiation damage after six months, at which point they were removed. They used acrylic scintillator, while current practice would use polystyrene based scintillator which has a longer lifetime by a factor of about five. Note that the dose delivered to a calorimeter goes up with the energy of the beam as well as the luminosity. For example, 10MHz of a 6 TeV forward jet is 10 watts, an intense radiation field, since most of it is deposited near the beam pipe in a limited angular region. Since there are many constraints which limit the length of the drift space, this will be a limited area as well. It maybe tempting to dismiss the forward energy flow as irrelevant to high p_T phenomena, but this would eliminate a very important tool for many experiments one will want to do. Even if you did not wish to know $p_{longitudinal}$ of the beam jets there is a substantial transverse energy flow in this area, compared to the potential errors on this quantity from other sources, and this consideration alone should require this measurement. The measurement of $p_{longitudinal}$ and thus the total energy, is a powerful handle on the pile-up problem, among other things, and will be extremely useful if it can be measured with extremely good time resolution. I believe that it can be, at high energy, because the very size of the energy deposit broadens the range of techniques available to measure it. The use of plastic scintillator seems ruled out in the high radiation zone. Liquid scintillator might be used if a means of reading it out can be devised.

We have been faced with exactly this problem in designing a fixed target experiment recently. We decided to look again at liquid ion chambers, but with a fast response, unlike the usual liquid argon calorimeter. The increased noise level can be tolerated because the amount of energy is large, 200-400 GeV in our case. We have designed a calorimeter with readout in $(15mm)^2$ towers, with a bipolar response full length of 100ns, using LA-CO or LA-CH_4 mixtures. It should be proof against radiation damage. Further reductions in response time should be possible, if neutron lifetime effects permit, particularly at higher energies. At 20 TeV, 100MHz rates might be possible -- this will required forced cooling of the forward detector!

The lifetime of drift chambers at high rates is not very well understood. Sometime ago, gas mixtures were found which seem to eliminate the problem of cathode deposits. Most present chambers fail due to deposits of silicon on the anodes. The source of the silicon is clearly in the environment, and since it tends to be ubiquitous in the forms of pump oil, dust and fiberglass, most practical chambers have not been well enough controlled to analyze quantitatively. We can say that the hottest wires in the Axial Field Spectrometer chambers have accumulated almost 10^4 μamp-hours/meter of wire without signs of trouble. D. Cockerill, E. Rorro and H. Hilke made careful studies of small chambers which seem to show that this problem does not occur in sufficiently clean chambers, which seems logical. The CHARM collaboration uses a controlled addition of H_2O vapor to suppress the phenomenon. My conclusion is that drift chambers running at low gas gains ($\lesssim 10^4$) will be limited by accidentals rather than destruction, if suitably constructure and operated.

8. Outlook

As luminosity is increased above 1-2 x 10^{32} cm^{-2} s^{-1}, we might forsee the following trends:

i) calorimeters can be speeded up - beyond a certain point some price will be paid in resolution as the neutron response is clipped, but this may be acceptable in the forward direction where fast response is really needed.

ii) drift chambers with small drift distances can be pushed to higher rates. They will be mechanically more complex as support for the wires is probably required, and a "clean" construction to avoid lifetime problems.

iii) the very fast response of low pressure parallel plate gas chambers would be attractive if there were a way to get signals. Examples are the BaF_2 counters of Anderson and Charpak.

iv) don't forget, lots of R & D on system problems!

v) none of this is free.

Table I. TRIGGER COMPONENTS BY LEVEL

LEVEL	DEAD TIME	COMPONENT
1	30 ns	Uranium Calorimeter NA I Ω HEX CAL 'Minimum Bias' Counters SPT Matrix (Counters + PWC) Muon 'Double Pomeron Trigger'
2	200 ns	Above Combined With: $\Delta\phi$ CAL. E_T M_1 M_2 M_3 M_4 360° 1 Hadron N_1 N_2 N_3 N_4 15° 1 Em. " " " " 7.5° Wall " " " " 90° Jet " " " " 45°
3	800 ns	NA I Localization PWC Matrix Look - up DC Sector • SPT Pointer 'e' DC Sector • EM Pointer 'e' DC Sector • NA I Pointer
4	100 μs	'ESOP' (Fast Digital Proc.) Routines: - Sagitta$_{1,2}$ k - u-CAL Localization
5		168 E Filter

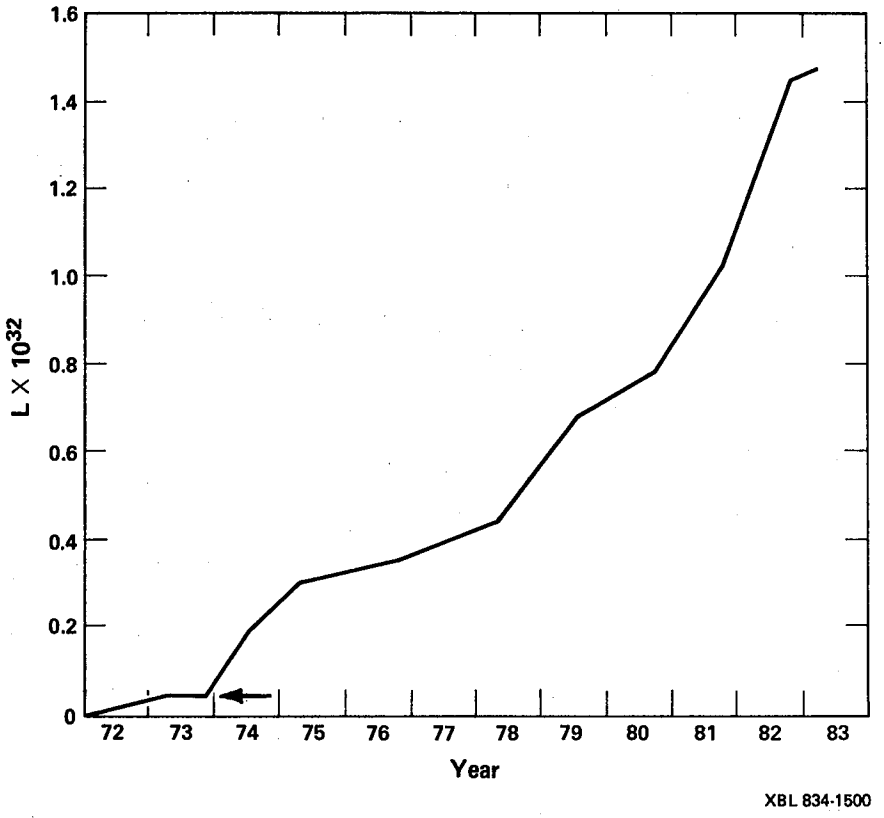

Fig. 1. History of the ISR record luminosity

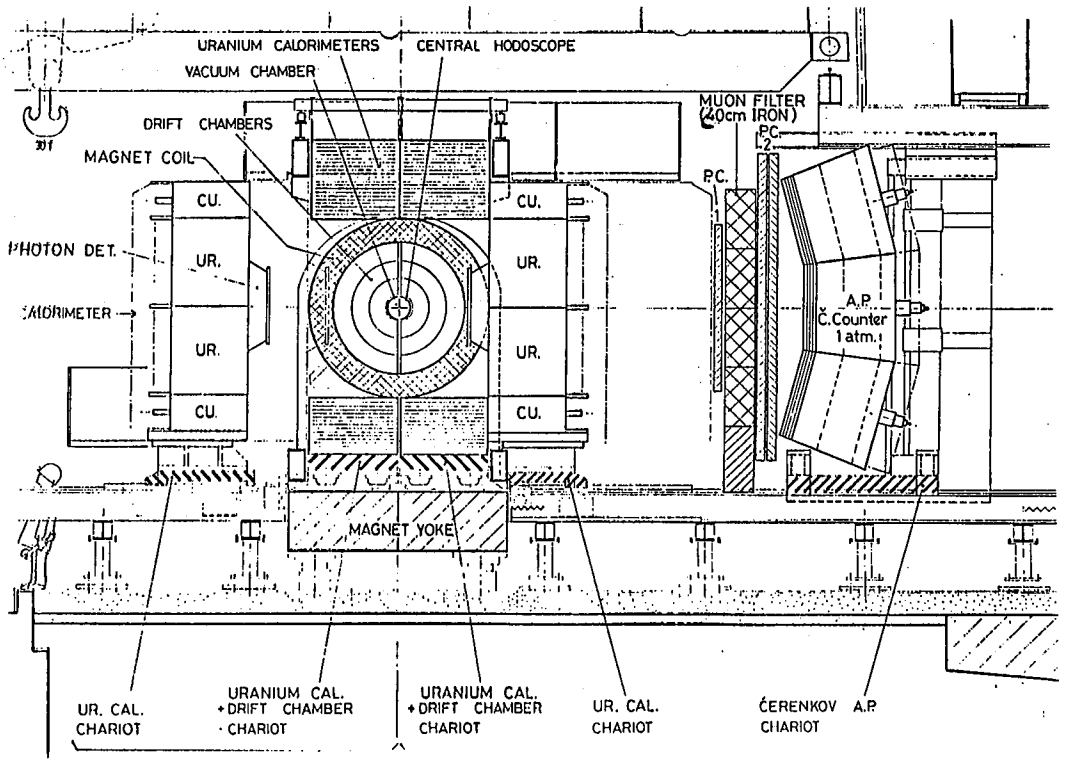

Fig. 2. AFS Central Tracking Detector and Uranium Calorimeter

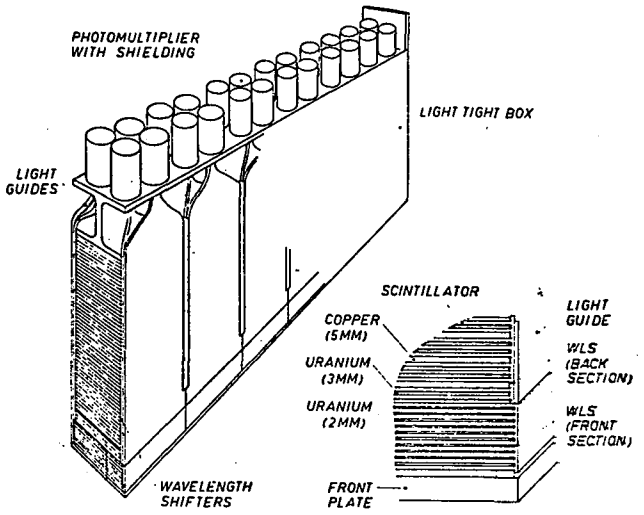

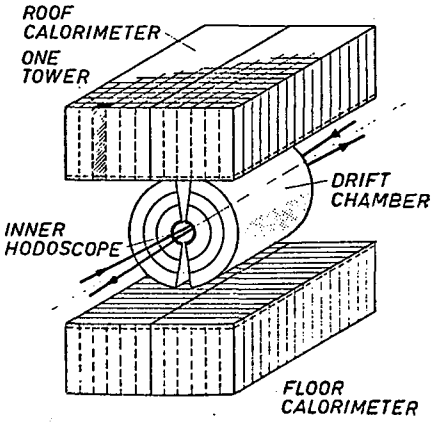

Fig. 3. Calorimeter Construction

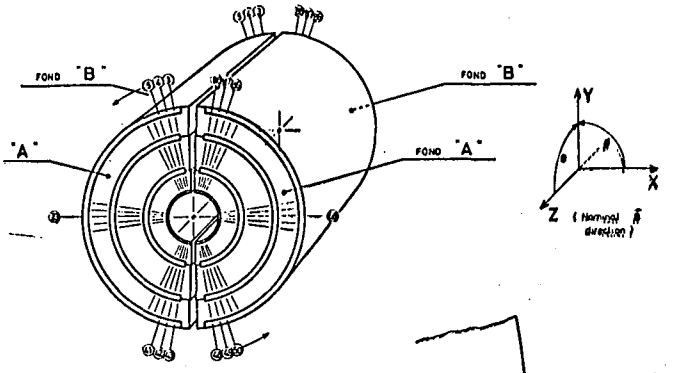

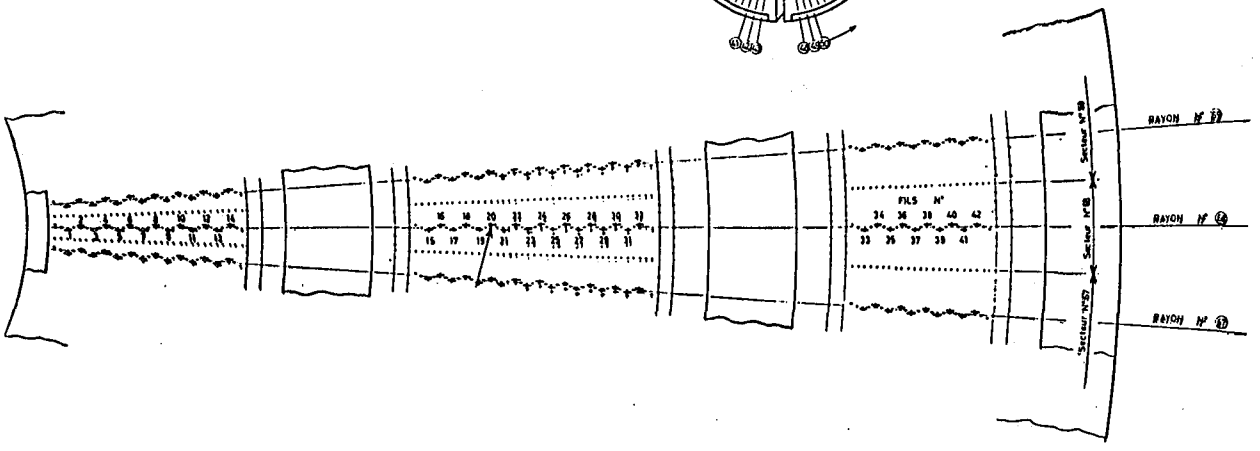

Fig. 4. Tracking Chambers

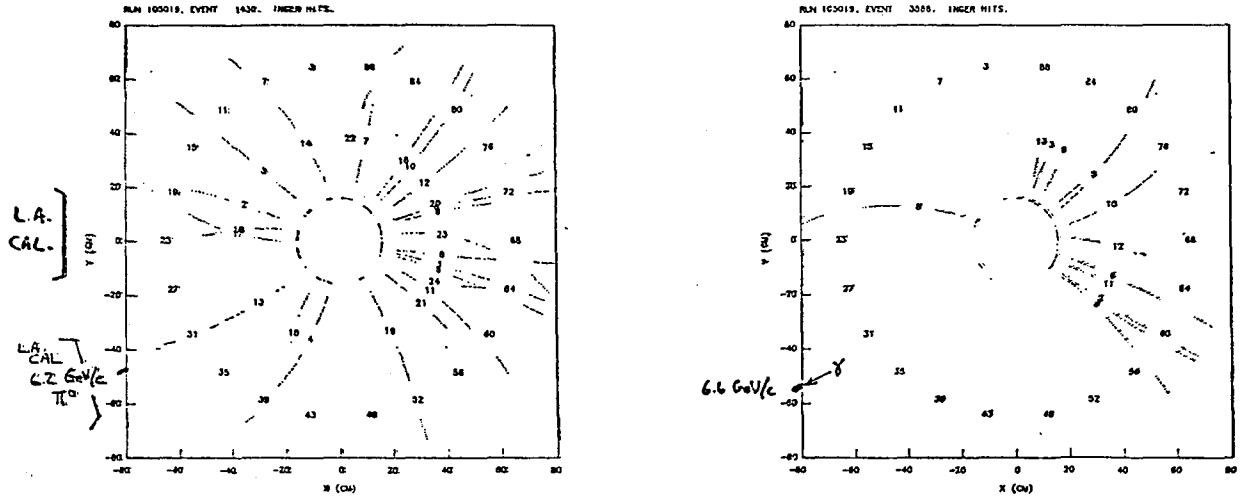

Fig. 5. Typical events reconstructed by computer

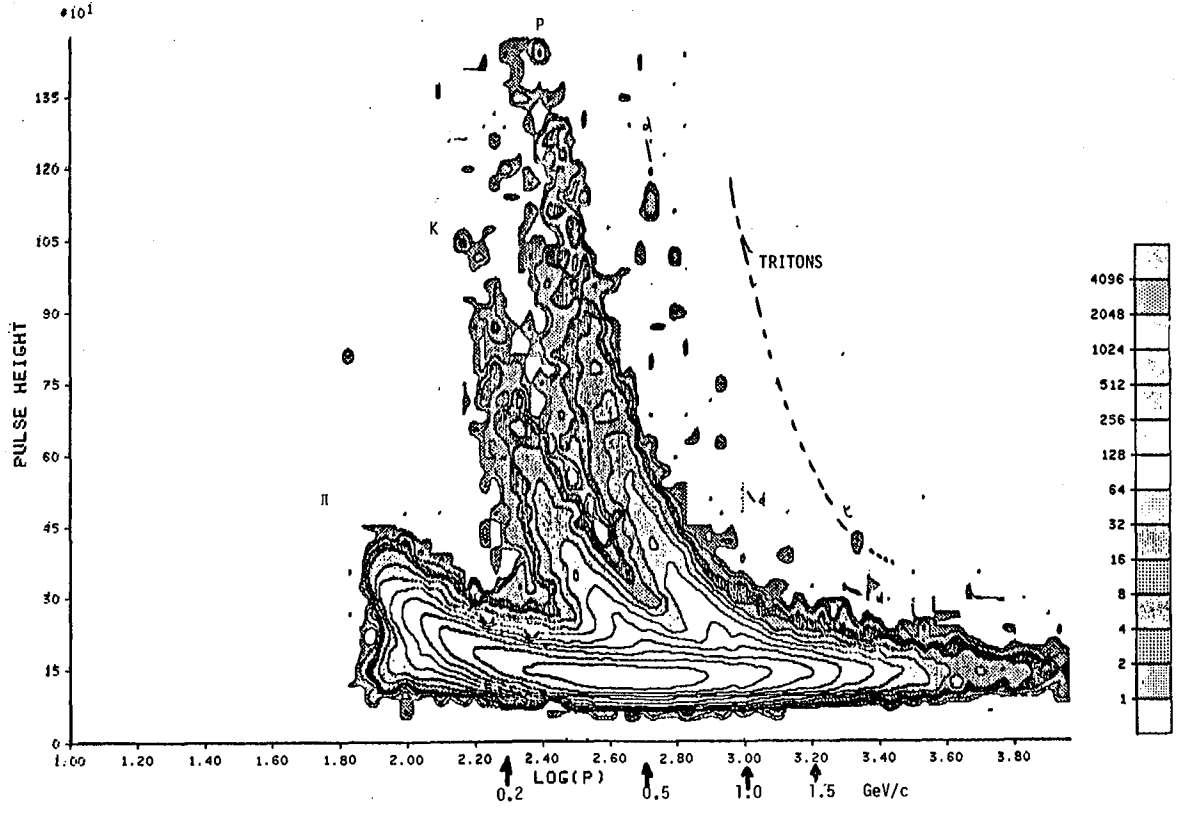

Fig. 6. Pulse height vs momentum

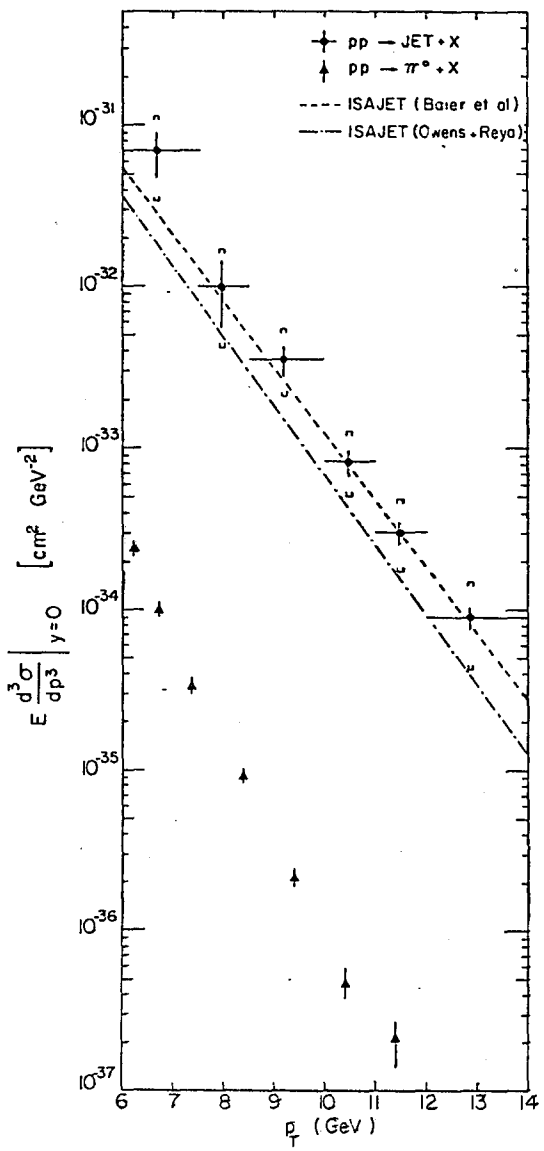

Fig. 7. Single Inclusive Jet Cross Sections

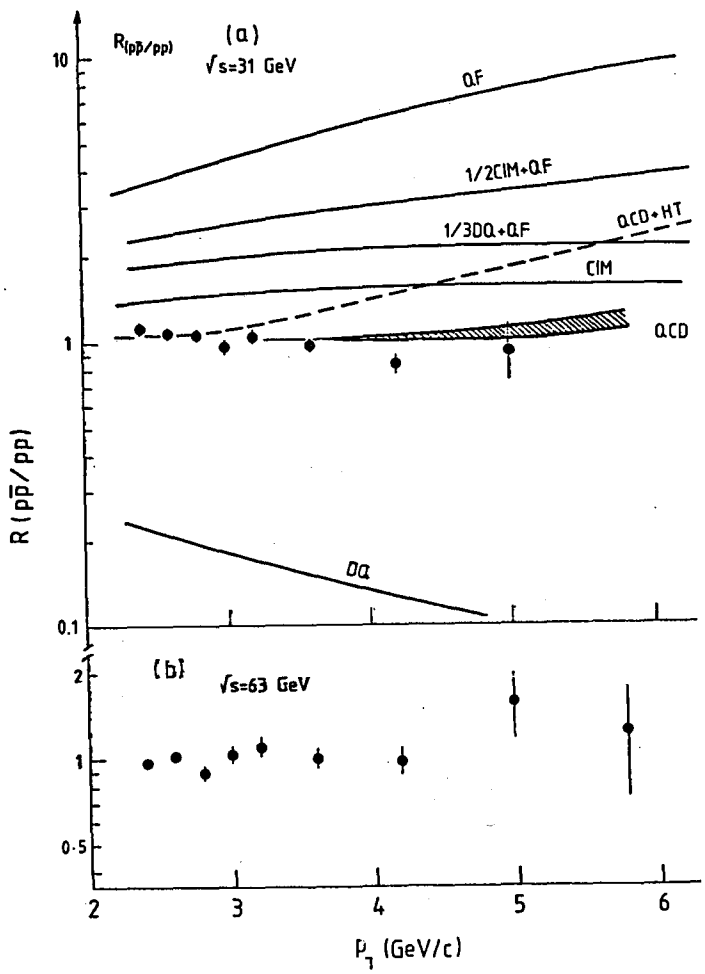

Fig. 8. Comparison of high P_T single particle production by pp and $p\bar{p}$ collisions

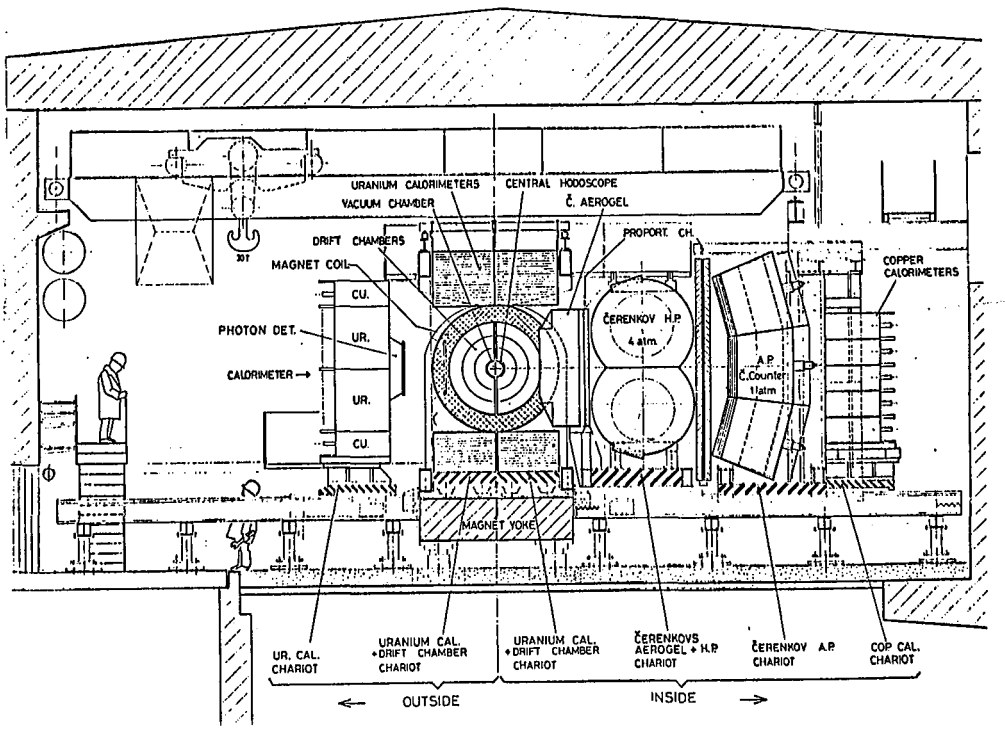

Fig. 9. Detector for High P_T Charged Particle Experiment

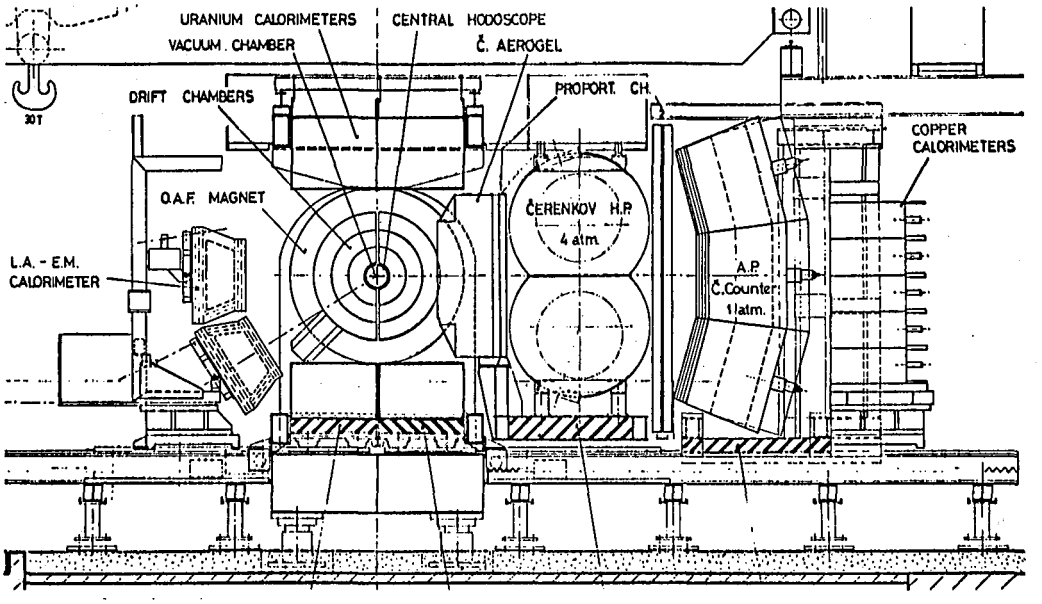

Fig. 10. Direct Single Photon Production Experiment

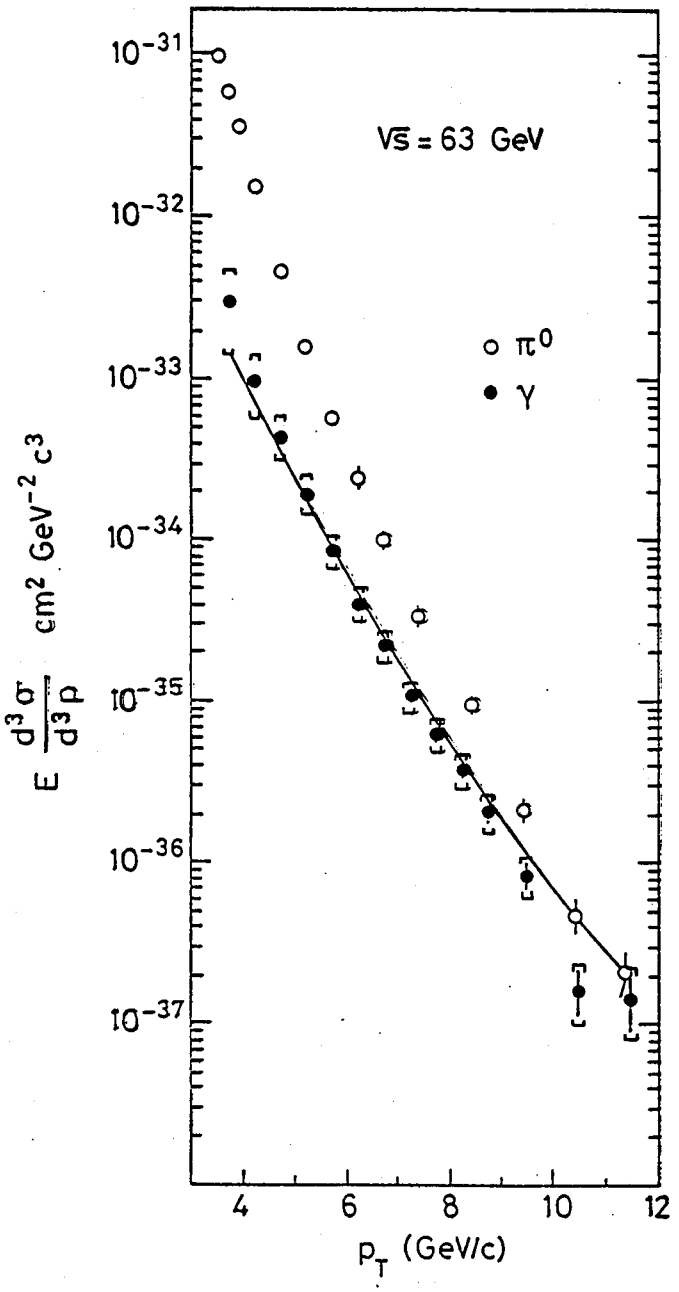

Fig. 11. Photon cross section as a function of P_T

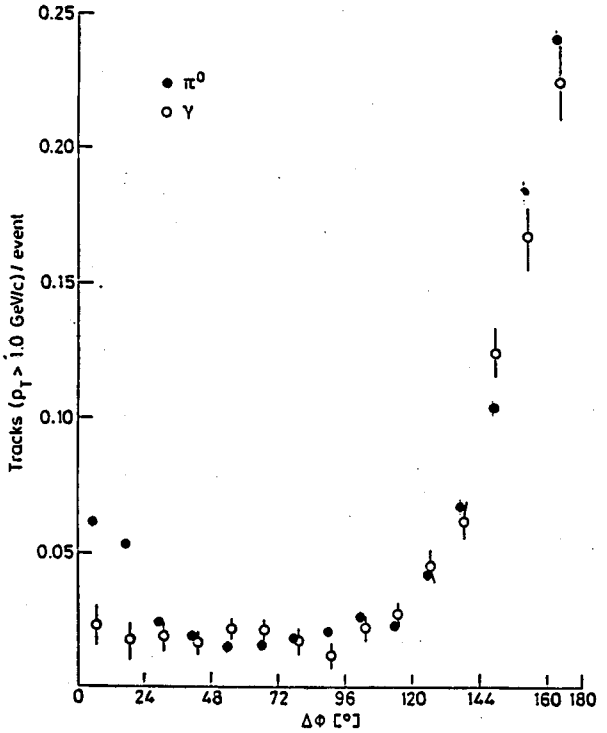

Fig. 12. Distribution of charged particles associated with single photons and with pi-zero's

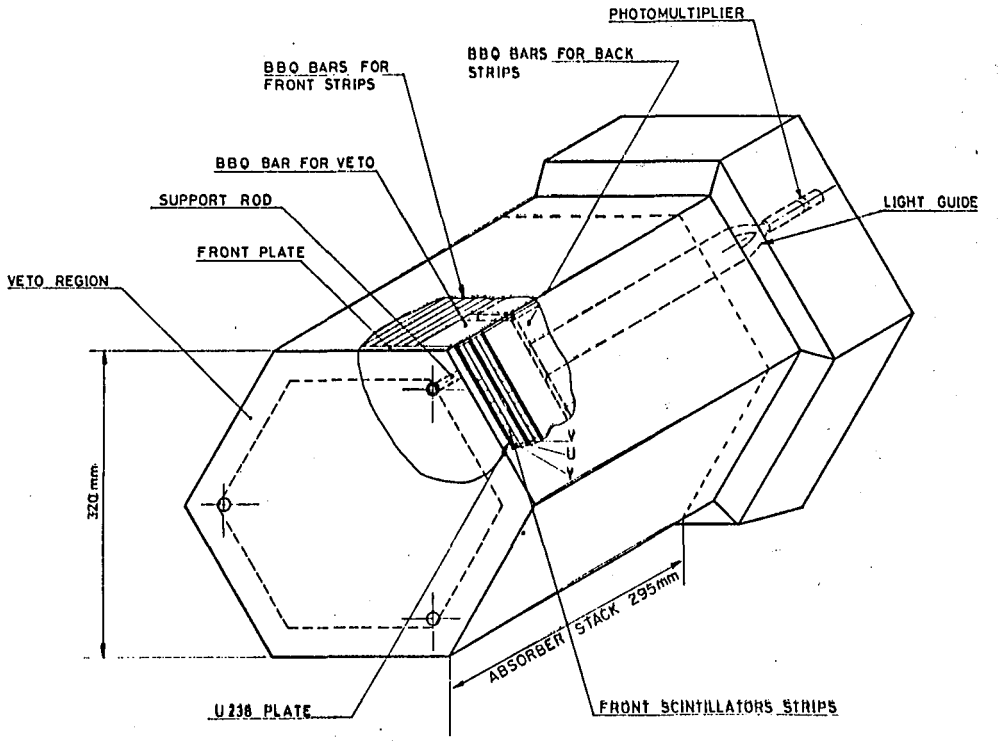

Fig. 13. Detector for forward direct single photon production

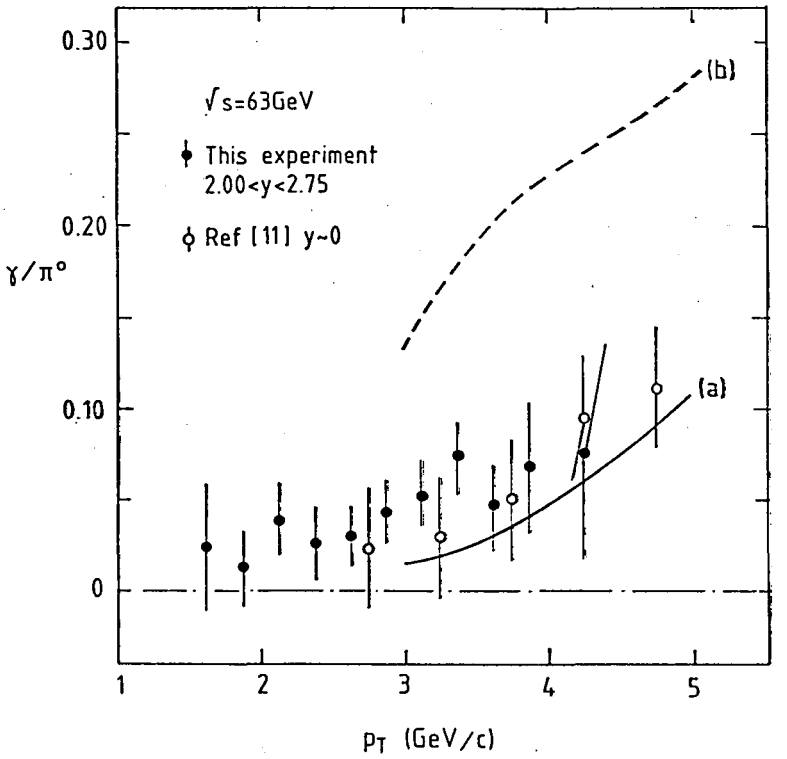

Fig. 14. Inclusive photon spectrum

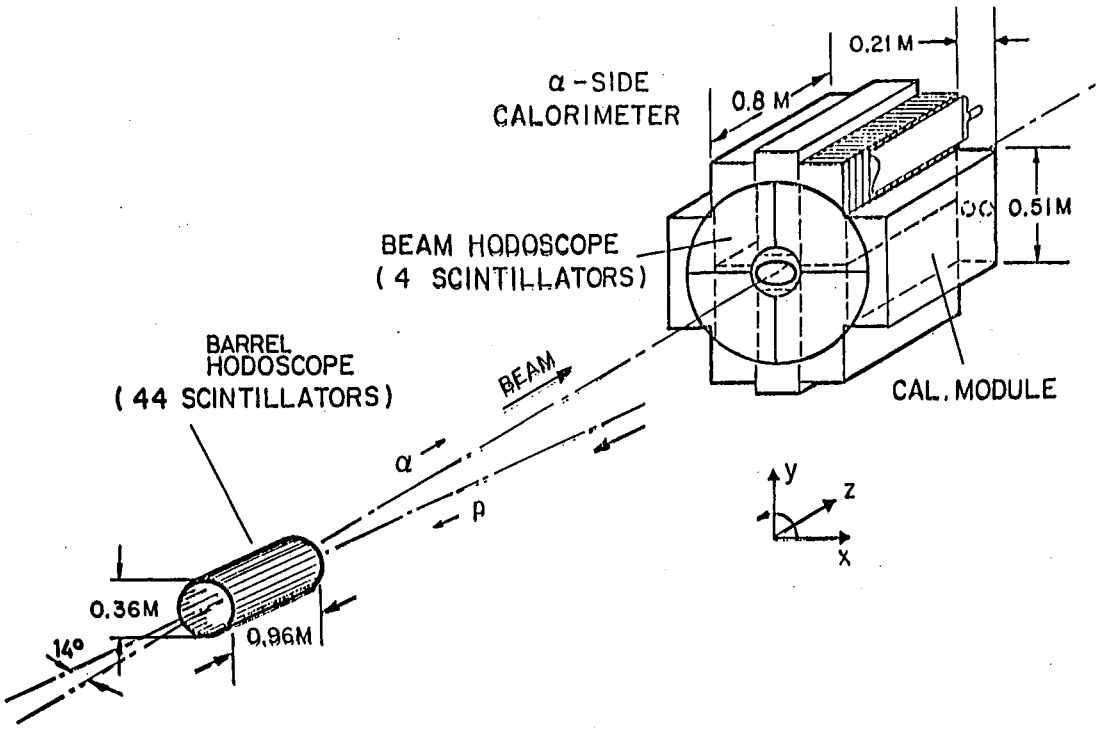

Fig. 15. Forward Hadron Calorimeters

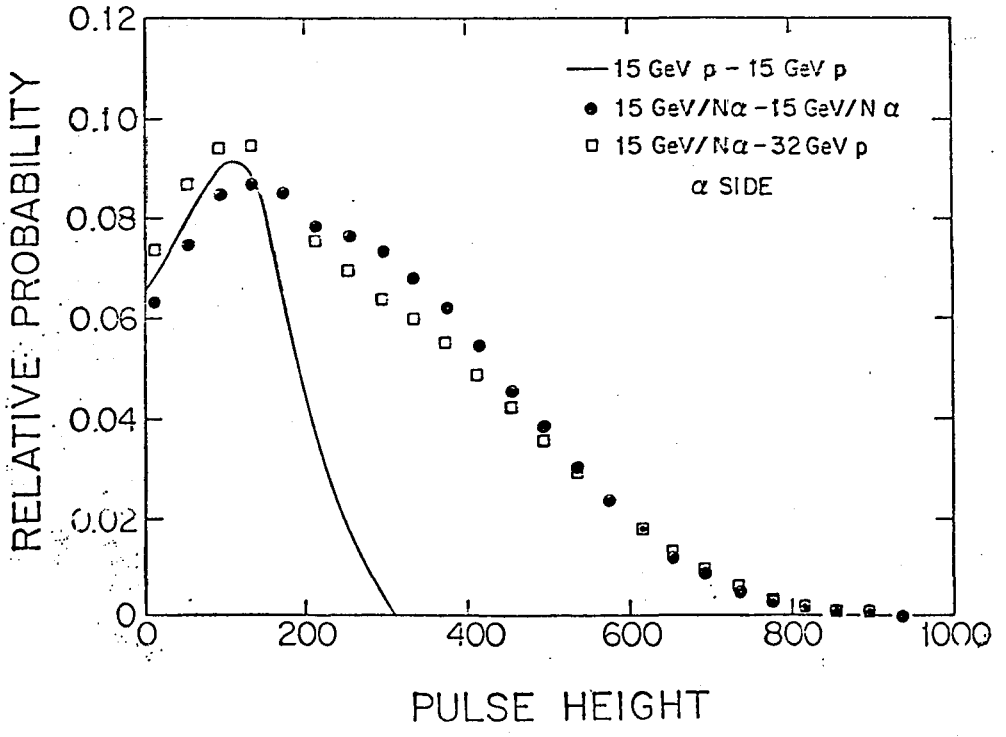

Fig. 16 Pulse height distributions

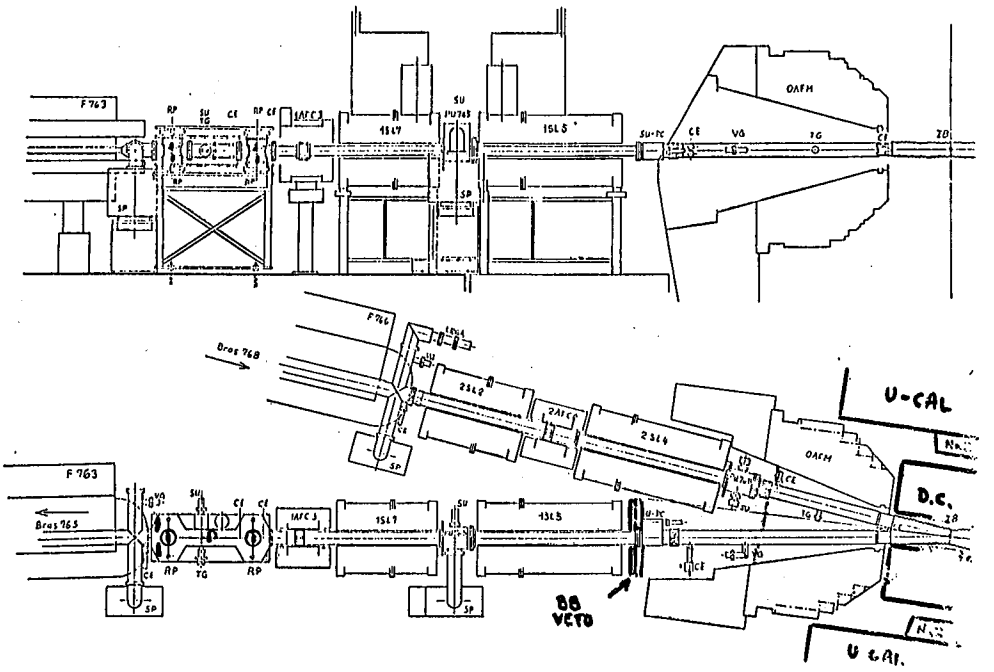

Fig. 17. Double Diffractive Photon Experiment

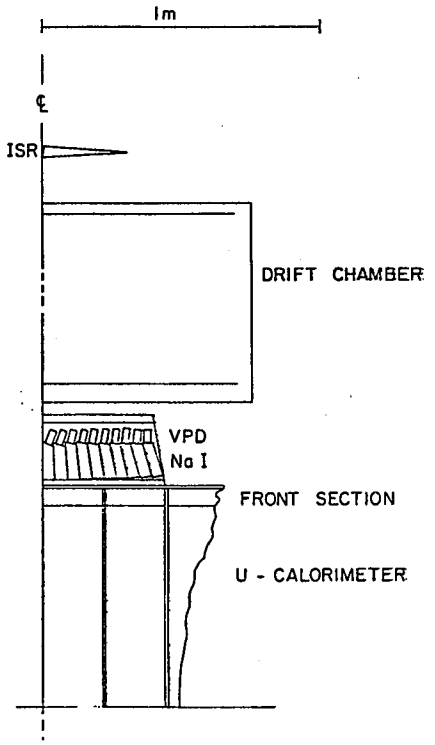

Fig. 18. Sodium Iodide Detector Array

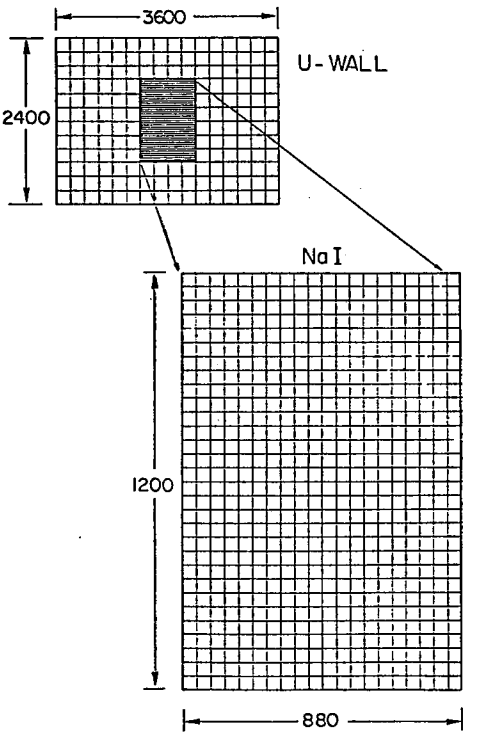

Fig. 19. Detail of Sodium Iodide Array

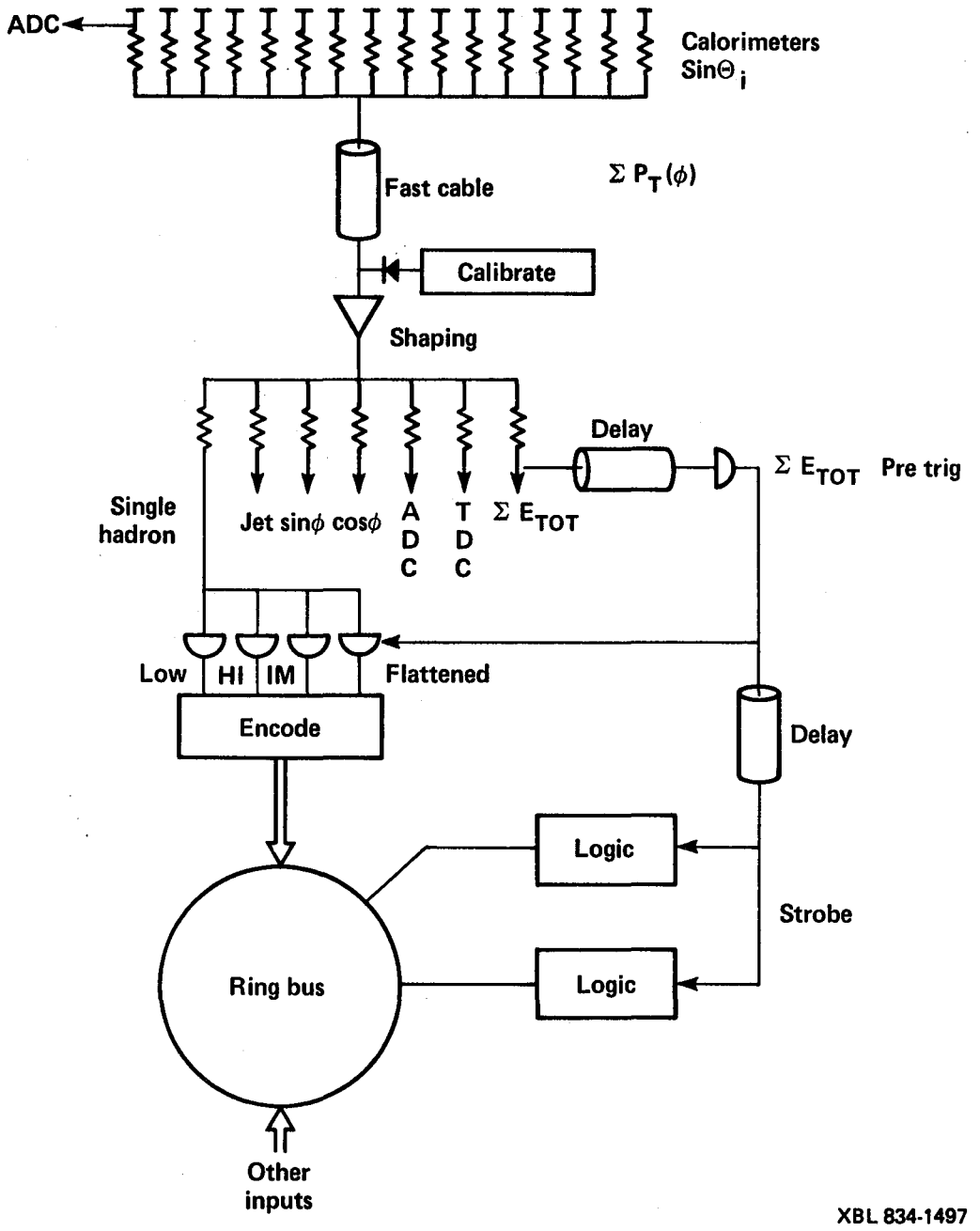

Fig. 20. Schematic of first and second level trigger for Uranium Calorimeter

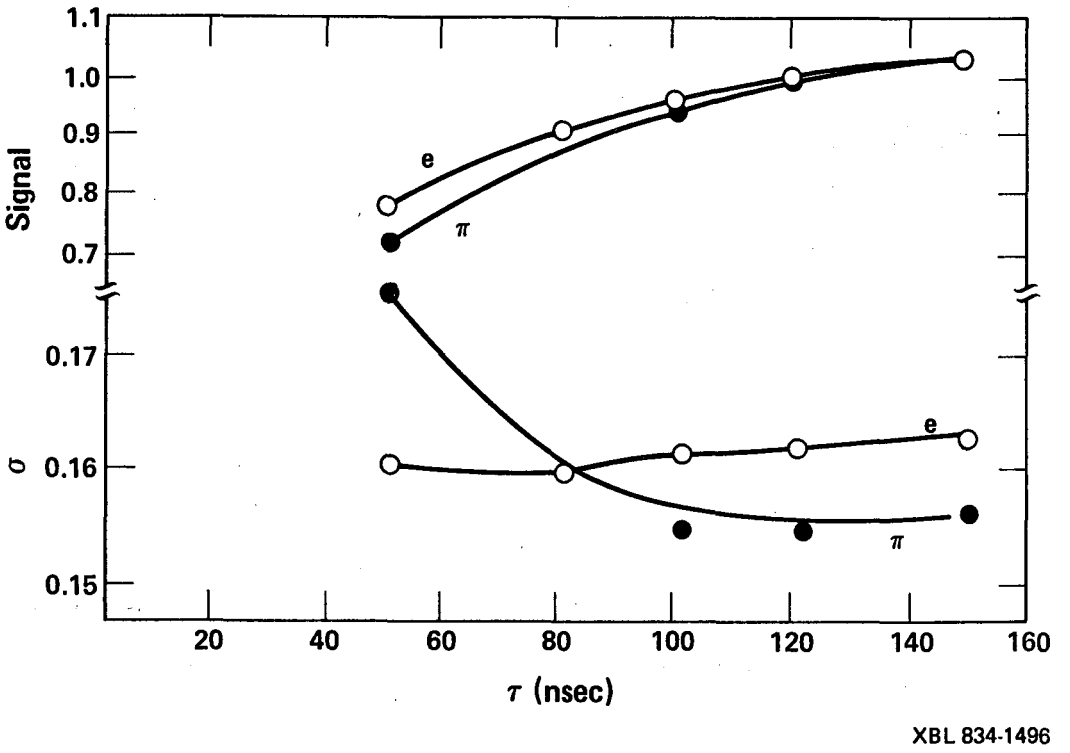

Fig. 21. Calorimeter response and resolution as a function of gate width

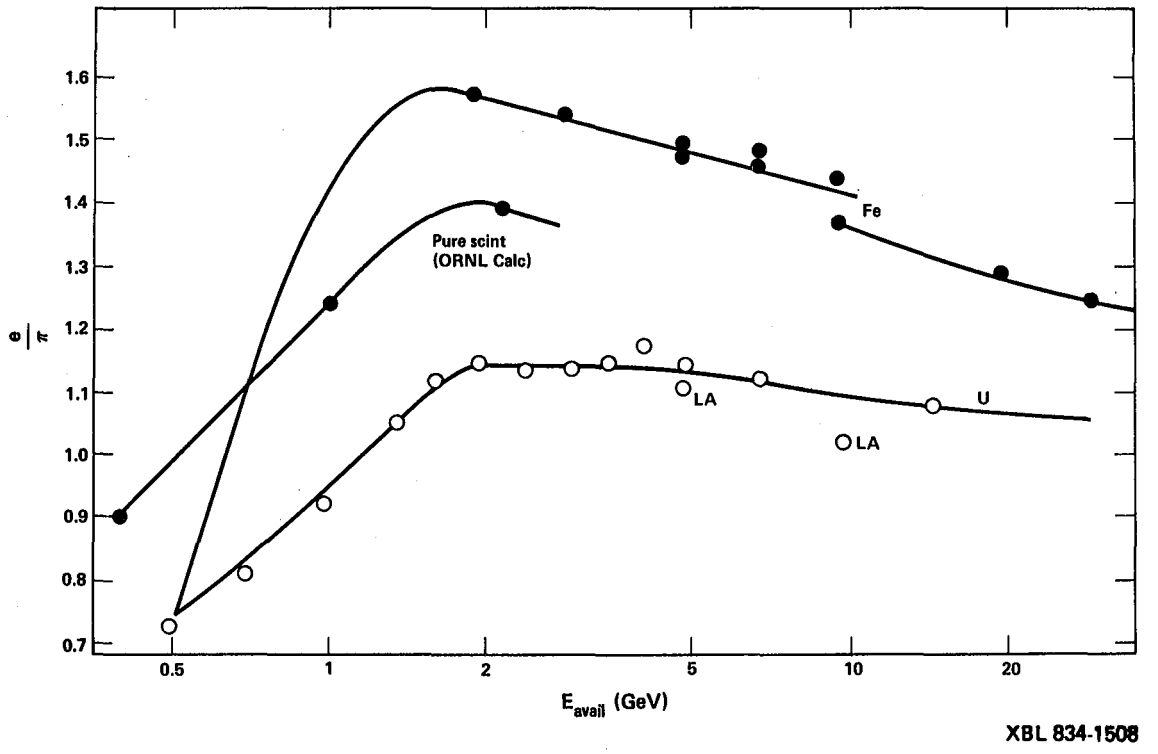

Fig. 22. Ratio of response of e's and π's of equal available energy

SEARCH FOR HADRON JETS AND LARGE TRANSVERSE MOMENTUM ELECTRONS AT THE SPS $\bar{p}p$ COLLIDER

Marcel Banner

1. Introduction

The search of high transverse momentum electrons needs the use of all the different elements of the UA2 detector; therefore the description of this search is a good way to understand the features of the apparatus, and its performance in a collider environment.

We present a preliminary analysis of the UA2 data collected during the last Collider run (20 nb^{-1} integrated luminosity) with particular emphasis on large transverse momentum hadron jets and on electrons having the configuration expected from the decay of electroweak bosons.

2. Detector and Data Taking: General Description

2.1 - Detector

The UA2 detector 1,2, shown in Figure 1, was designed mainly with the aims to observe electroweak boson decays and to study final states containing large transverse momentum hadron jets: such phenomena are expected to result from the collisions at very short distance accessible to the SPS $\bar{p}p$ Collider, the only existing facility providing a sufficient centre of mass energy, $\sqrt{s}$ = 540 GeV. The expectation that the collision products relevant to the study of such processes populate mostly the central rapidity region led us to restrict the detector coverage to ~3.5 rapidity units, within which, for example, ~2/3 of Z° decays are expected to occur. The cones corresponding to scattering angles $\theta < 20°$, $\theta > 160°$ are not covered by UA2 but are left open to house the detectors of experiment UA4 designed to measure the elastic and total $\bar{p}p$ cross sections.[3]

Despite their small branching fractions the leptonic decay modes of the electroweak bosons

$$W^{\pm} \to \ell^{\pm}\nu \qquad (BR \simeq 8\% \text{ per lepton type})$$

and

$$Z^{\circ} \to \ell^{+}\ell^{-} \qquad (BR \simeq 3\% \text{ per lepton type})$$

are supposed to be the least difficult to detect because of the very small expected background contamination. For this reason UA2 was designed to detect and identify electrons over its whole acceptance; electrons were preferred over muons because excellent energy resolutions can be achieved in compact calorimeters.

Hadron detection is also implemented over the whole UA2 acceptance but different approaches have been adopted in the central ($40° < \theta < 140°$) and forward ($20° < \theta < 40°$, $140° < \theta < 160°$) regions. The central region is instrumented with a highly segmented hadron calorimeter having a cell configuration well suited to the observation of hadron jets independently of their mode of fragmentation. The forward regions, where important $W \to e\nu$ charge asymmetries are expected to occur, are equipped with two magnetic spectrometers, each consisting of a toroidal field magnet followed by nine drift chamber planes.

A set of cylindrical wire chambers densely packed around the beam in the collision region provides measurements of the position of the event vertex and of the directions of the charged particles produced in the collision. It is made of four proportional chambers with helical cathode strips and of two drift chambers of 24 azimuthal cells each, with six drift wires per cell.

and of two drift chambers of 24 azimuthal cells each, with six drift wires per cell.

The measurement of a track pointing to an energy deposition localised in one of the electron calorimeter cells provides a powerful means of selecting electron candidates but it leaves a significant contamination of narrow π°- charged hadron pairs (overlap background). This is strongly reduced by using preshower counters in front of the electron calorimeters to provide improved space resolution. The central preshower counter is a cylindrical proportional chamber with helic
preshower counters are proportional tube planes. Each is preceded by a ~1.5 radiation length thick converter. This chamber is called C_5 in the text.

2.2 - Data Taking

The data discussed in this report were recorded using triggers sensitive to events with large transverse energy in the central and forward calorimeters. They were of three types:

-- The ΣE_T trigger required a total transverse energy (ΣE_T) measured in the central calorimeter (electron and hadron cells linearly added) in excess of ~35 GeV,
-- The W trigger required the presence of at least one quartet (2 x 2) of electron calorimeter cells (central or forward) in which the measured transverse energy exceeded 8 GeV,
-- The Z° trigger required the presence of two such quartets, each having a transverse energy in excess of 3.5 GeV, and aximuthally separated by $\Delta\phi > 60°$.

In addition the ΣE_T and W triggers (but not the Z° trigger) required a coincidence with two signals obtained from scintillator arrays coverning an angular range $0.47 < \theta < 2.84°$ on both sides of the collision region. This additional condition is satisfied by nearly all non-diffractive collisions Early signals measured in these scintillator arrays were used to tag background events induced by beam halo particles interacting in the detector.

3. Large Transverse Energy Hadrons

3.1 - The Central Calorimeter

In the present Section we restrict the analysis to events which satisfy the ΣE_T trigger. The central calorimeter is the part of the UA2 detector which is most relevant to the present study. It is segmented into 200 cells, each covering 15° in ϕ and 10° in ϕ, and built in a tower structure pointing towards the centre of the interaction region. The cells (Figure 2)

are segmented longitudinally into a 17 radiation length thick electromagnetic compartment (lead-scintillator) followed by two hadronic compartments (iron-scintillator) of two absorption lengths each. The light from each compartment is collected by two BBQ-doped light guide plates on opposite sides of the cell.

The energy resolution for electrons is measured to be $\sigma_E/E = 0.14 / E$ (E in GeV). In the case of hadrons, σ_E/E varies from 32% at 1 GeV to 11% at 70 GeV, approximately like $E^{-1/4}$. The resolution for multi-hadron systems of more than 20 GeV is similar to that of single hadrons. Calibration of the energy response was done with PS and SPS beams, then tracked carefully. The systematic uncertainty in the energy calibration for the data discussed here is less than 2% for the electromagnetic calorimeter and less than 3% for the hadronic one.

Simplifications in the very preliminary data analysis add further errors of ±10%.

3.2 - Two-Jet Dominance

Figure 3 shows the distribution of the observed events as a function of their total transverse energy, $\Sigma E_T > 100$ GeV. The increased statistical accuracy is now sufficient to give evidence of a departure from exponential when ΣE_T exceeds 60 GeV. This departure corresponds to the emergence of two-jet dominance at large values of ΣE_T. Immediate evidence for two-jet dominance is obtained from a simple inspection of energy distribution in the θ-ϕ plane: examples are shown in Figures 4a to d.

Figures 5,6,7 show details of the jet distributions.

4. Search for $W \to e\,\nu$ Decays

The decay into $e^{\pm}\nu$ of $W^{\pm}$ produced at rest in $\bar{p}p$ collision would generate a monochromatic electron with energy $E(e) = \frac{1}{2} M_W$, M_W being the rest mass of the W boson. In practice W's are expected to be produced with important longitudinal momenta. This does not affect the transverse momentum distribution of the decay electron which peaks near its end point at $E_T(e) = 1/2\ M_W$ (Jacobian peak).

W's are also expected to be produced with important transverse momenta, similar to that of a two-jet system of a same mass (see Figure 7; however part of the measured transverse momentum is of instrumental origin). This results mainly in a smearing of the Jacobian peak but does not induce significant correlations between the transverse momentum of the decay electron and that of the W (or of its associated recoil particles). We shall therefore search for large transverse momentum electrons which are not accompanied by other particles at small angles to the electron momentum. This simplified approach will strongly reduce a possible two-jet background and should not affect seriously the $W \to e\,\nu$ signal. However it precludes any search for large transverse momentum electrons among jet fragments.

We shall deal separately with the central and forward regions in which different experimental methods are used. In both cases the initial event sample is that of W-triggers.

4.1 - Search for $W \to e\,\nu$ in the Central Region

The full data sample recorded using the W trigger corresponds to a total integrated luminosity of 19.0 nb^{-1}. A first event selection is made by searching for clusters of energy with the configuration expected from isolated electrons. For each cluster satisfying some initial cuts a transverse energy E_T' is calculated using the position of the cluster centroid and assuming that the event vertex was in the center of the apparatus. The events with $E_T' > 15$ GeV (363 events) are fully reconstructed and the exact location of the event vertex (as measured in the vertex detector) is used to obtain the correct value of the transverse energy E_T. The E_T distribution for these events is shown in Figure 8a. The falloff for $E_T < 17$ GeV results from the selection requirement $E_T' > 15$ GeV applied without knowledge of the exact event vertex. For $E_T' > 17$ GeV the distribution of Figure 8a has no threshold bias. There are 7 events with $E_T > 30$ GeV, the highest E_T value being 40.3 GeV.

This sample is further reduced by requiring that one, and only one charged particle track reconstructed in the vertex detector points to the energy cluster. Such a cut, with the E_T distribution shown in Figure 8b.

We then require that the track produce a shower in the tungsten converter, with an associated charge cluster in chamber C_5, as expected in the case of electrons. This condition applied to our sample reduces the number of events from 96 to 35. The E_T-distribution for these events is shown in Figure 8c.

In order to further ensure that the electron candidate is isolated, we require that no other charge clusters are present in C_5 in a cone of 10° half-aperture around the track. Such clusters could result from the conversion of high-energy photons accompanying the charged particle in the tungsten. We estimate that the loss of events due to radiative corrections is less than 6%.

Ten events satisfy this requirement. The E_T distributions for these events are shown in Figure 8d.

As a final selection criterion we use the high segmentation of the central calorimeter to check if the shape of the energy cluster is consistent with that expected from an isolated electron impinging along the direction of the observed track. The E_T distribution for these events, which represent our final sample of electron candidates, is shown in Figure 8e.

As a check of this analysis all of the initial sample of 363 events was carefully scanned by physicists using a high resolution graphics terminal. The same three events were found.

There are three main sources of background contamination:

a) Single, isolated high-p_T π^0-or η-mesons undergoing Dalitz decay, or high-p_T photons (both single and from $\pi^0(\eta) \to \gamma\gamma$ decay) converting in the vacuum chamber wall. The expected number of background events from this source is < 0.04 for $E_T > 25$ GeV.

b) Single high-p_T charged hadrons interacting in the tungsten converter and depositing a large fraction of their energy (> 90%) in the electromagnetic calorimeter. We estimate that the expected number of background events from this source is < 0.04 events for $E_T > 25$ GeV.

c) "Overlap" events, consisting of either at least one high-p_T photon accompanied by a charged particle or of several high-p_T photons of which one converts. We estimate this background to be approximately

0.1 event for $E_T > 25$ GeV.

In conclusion, the total background contribution to the three electron candidates amounts to less than 0.2 events for $E_T > 25$ GeV. Furthermore, background sources would have an E_T-distribution similar to that of Figure 8a, whereas the distribution of the three electron candidates is inconsistent with it. This is an independent indication that the background contribution is indeed small.

4.2 Search for $W \to e\,\nu$ in the Forward Regions

The search for $W \to e\,\nu$ decays in the forward regions follows the same general guidelines as in the central region.

Each of the two forward detectors covers a range of scattering angles $20° < \theta < 37.5°$ and is instrumented in 12 azimuthal sectors with magnetic spectrometers (Figure 9). The magnetic fields are generated from two "lamp-shade" magnets of 12 coils each. The field integral is 0.38 T m on the average and the loss of azimuthal coverage caused by the magnet coils is 18%.

Depending on the sign of their charge, particles are bent towards or away from the beam and are measured in three triplets of drift chambers, having sense wires at -7°, 0° and +7° to the magnetic field direction. In the present preliminary analysis the resolution achieved in momentum measurement is $\Delta(\frac{1}{p}) \simeq 2\%\ \text{GeV}^{-1}$. Each magnetic spectrometer sector is followed by a preshower counter and an electromagnetic calorimeter. The preshower counter consists of a 1.4 radiation length thick lead converter preceding two proportional tube chambers. Each electromagnetic calorimeter sector is subdivided in 10 cells, each covering a rapidity × azimuth domain $\Delta y \times \Delta\phi \simeq 0.17 \times 15°$ similar to that covered by the central calorimeter cells. Each cell is segmented in two compartments, one 24 radiation length thick in which most of electromagnetic showers are contained, the other 6 radiation length thick serving as a veto against hadronic showers. The response and performance of the preshower counters and calorimeters have been extensively studied in a 10 GeV electron beam. A comparison of the two phototube signals receiving light from the wave-shifting light guides on each side of a cell allows the localization of the impact point to within ±2 cm.

The following are the main selection criteria applied to the sample of W triggers to select possible electron candidates:

- a forward track with more than 10 GeV associated transverse energy.
- leakage in the calorimeter veto compartment must be less than 2%.
- the quality of matching between track, preshower counters and energy in the calorimeter must be good.
- the momentum p measured in the magnetic spectrometer must be consistent with the energy E measured in the calorimeter.
- the electron candidate must be isolated: the energy measured in adjacent calorimeter cells (including the contribution of track momenta) must not exceed 3 GeV, no other track must point to the same cell as the electron candidate and no other signal facing this cell must be measured in the preshower counter.

Ten events are found to survive these straightforward selection criteria for an integrated luminosity of 16 nb^{-1}. The corresponding E_T distribution is shown in Figure 10.

Backgrounds in this sample are expected to originate from the same sources as described in Section 2. Above $E_T = 15$ GeV, 3 events survive (see Figure 10) and we estimate that less than 0.2 events could be a background event.

4.3 Missing Transverse Momentum, for $E_T > 15$ GeV

We now verify another feature of reaction $W \to e\,\nu$ namely, the presence of an undetected neutrino with transverse momentum similar in magnitude to that of the electron but opposite in azimuth.

In order to estimate the missing transverse momentum carried away by the neutrino we reconstruct the total momentum vector from the available calorimetric and spectrometric measurements. To each calorimeter cell, including those in the lead glass wall, we assign a vector $\vec{p}_i$ with magnitude equal to the energy deposited in the cell and direction along the line joining the event vertex to the cell centre. The total momentum vector $\vec{p}$ is then projected onto the direction of the electron transverse momentum vector p_{eT} to define the missing transverse momentum p_T^{miss}.

The ratio p_T^{miss}/E_T (where $E_T = |\vec{p}_{eT}|$ is shown in Figure 11a for the electron candidates found both in the central calorimeter and in the forward detectors. The events with $p_T^{miss}/E_T \simeq 1$ are consistent with reaction $W \to e\,\nu$.

The E_T distribution of the four events with $p_T^{miss}/E_T > 0.8$ is shown in Figure 11b. These electron candidates are those having the highest E_T values.

In order to verify that the large missing transverse momentum of the four electron candidates is not dominated by the limited coverage of the detectors, we have studied a sample of background events obtained with the original W trigger. This control sample is dominated by events containing a high-E_T jet, which are not expected to show a large missing transverse momentum. We find that the fraction of such events which satisfies the condition $p_T^{miss}/E_T > 0.8$ is only 20% for both the central calorimeter and the forward detectors.

Figure 11c shows the cell energy distribution in θ and ϕ for the highest E_T event. The only significant energy flow within the detector acceptance is carried by the electron candidate. The other three events have the same spectacular configuration.

5. Conclusions

The application of the various selection criteria used in the analysis to identify single, isolated electrons has reduced the original event sample to four events with $E_T > 15$ GeV and large missing transverse momentum. Both the configuration of the events and their number are consistent with $W \to e\,\nu$. Detailed analysis of all the information obtained from a carefully designed detector allows the observation of a very small signal in a very large sample of interactions.

References

1. M. Banner et al., Phys. Lett. 118B (1982) 203.

2. M. Banner et al., Phys. Lett. 115B (1982) 59.
   M. Banner et al., Phys. Lett. 121B (1983) 187.
   M. Banner et al., Inclusive charged particle production at the CERN $\bar{p}p$ Collider, to be published in Phys. Lett.

3. R. Battiston et al., Phys. Lett. 117B (1982) 126.

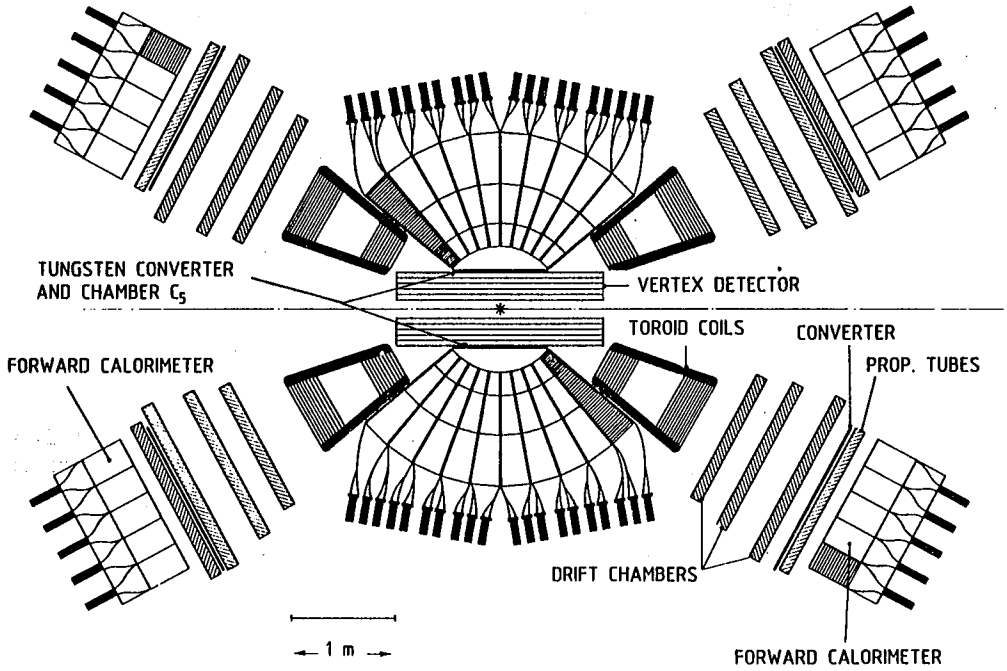

Fig. 1. UA2 Detector

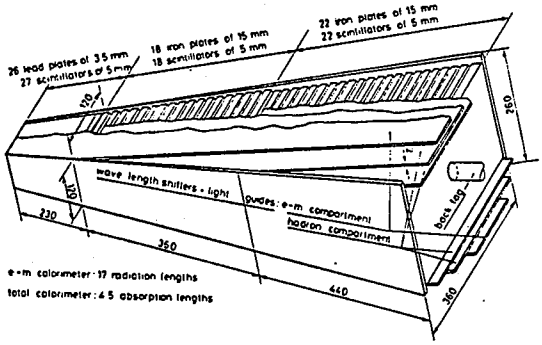

Fig. 2. Central calorimeter cells

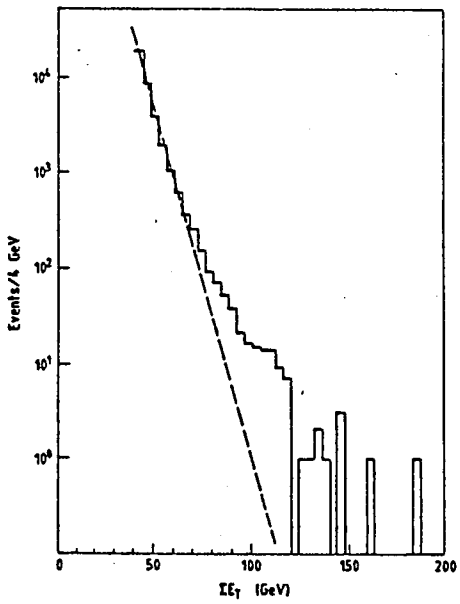

Fig. 3. Observed (uncorrected) ΣE_T distribution in the central calorimeter.

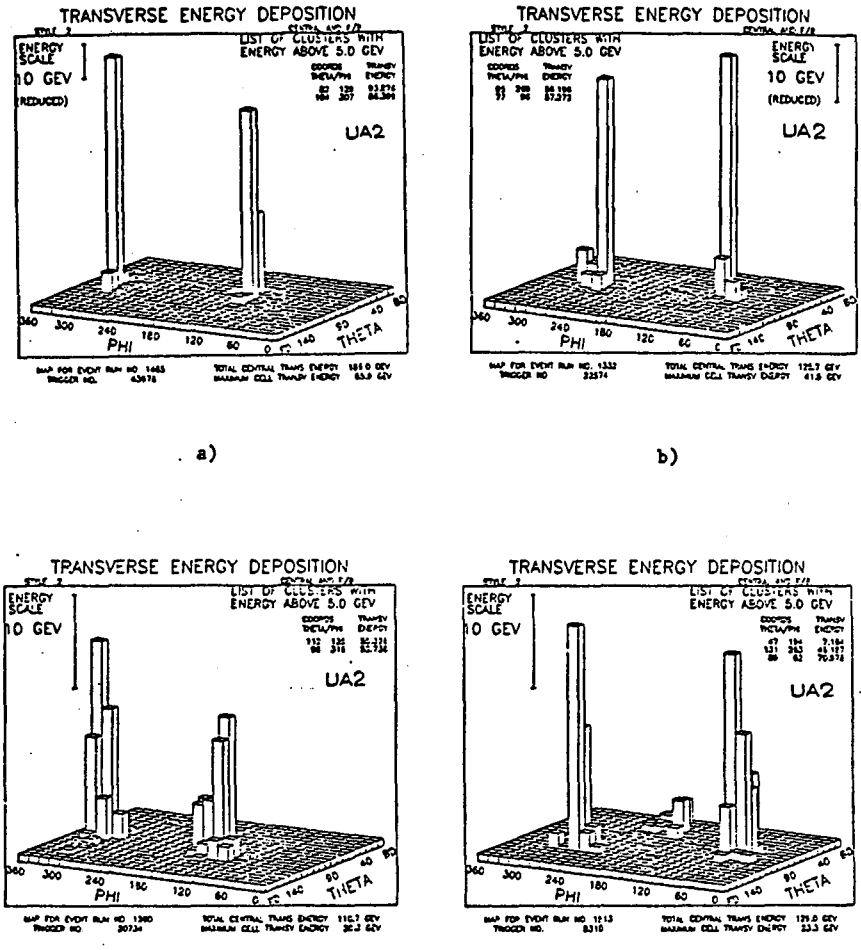

Fig. 4. Typical θ-ϕ distributions of the transverse energy in large ΣE_T events.

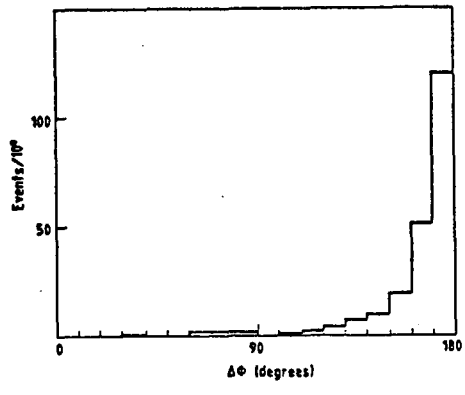

Fig. 5. Azimuthal separation $\Delta\phi$ between two jets, each having E_T > 15 GeV, in events with $\Sigma\ E_T$ > 30 GeV.

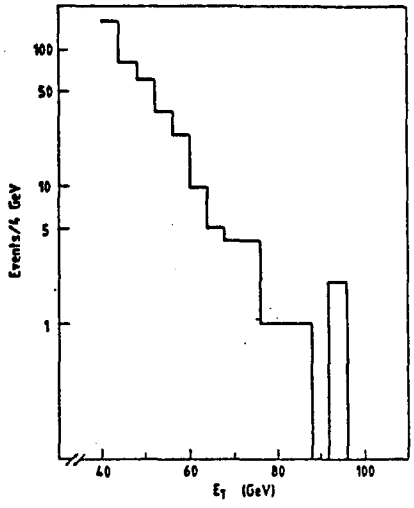

Fig. 6. Observed (uncorrected) transverse energy distribution of jets having $E_T > 40$ GeV.

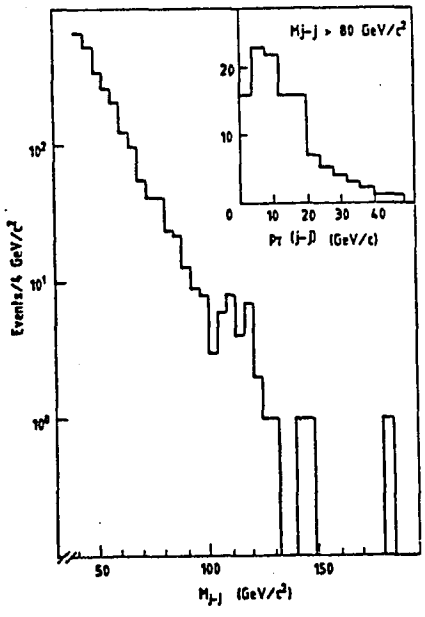

Fig. 7. Two-jet invariant mass (M_{j-j}) distribution (uncorrected). The observed (uncorrected) transverse momentum distribution of two-jet systems having $M_{j-j} > 80$ GeV/c^2 is shown in the insert.

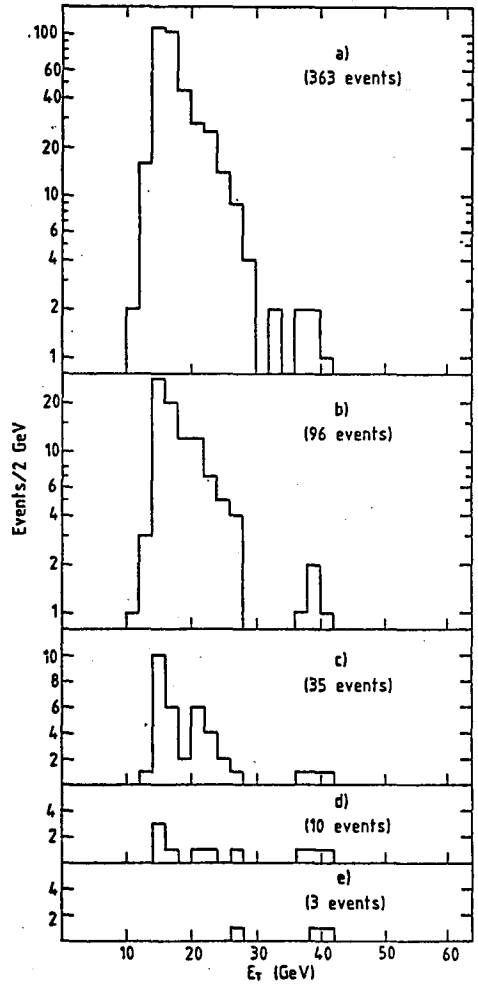

Fig. 8. Transverse energy distribution of the event samples in the central calorimeter:
a) After requirements on energy cluster;
b) After association with a track;
c) After association of the track with a shower in the tungsten converter;
d) After requiring only one such shower;
e) After further cuts on the quality of the track-energy cluster matching. This is the final electron sample.

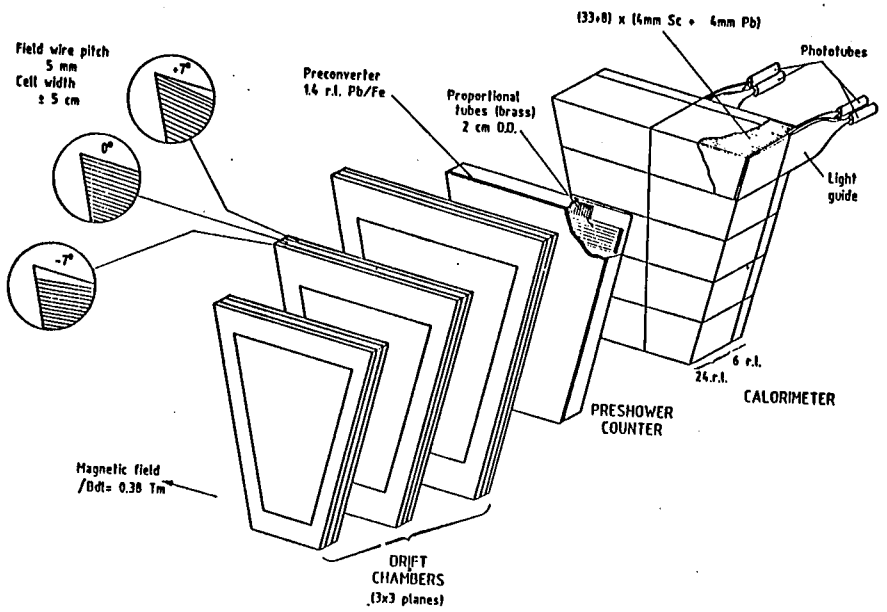

Fig. 9. Forward detector sector.

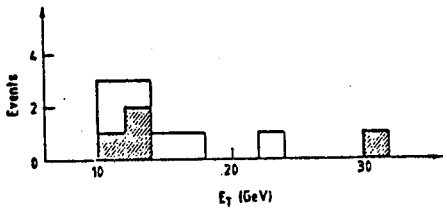

Fig. 10. Transverse energy distribution of the 10 electron candidates in the forward detectors.

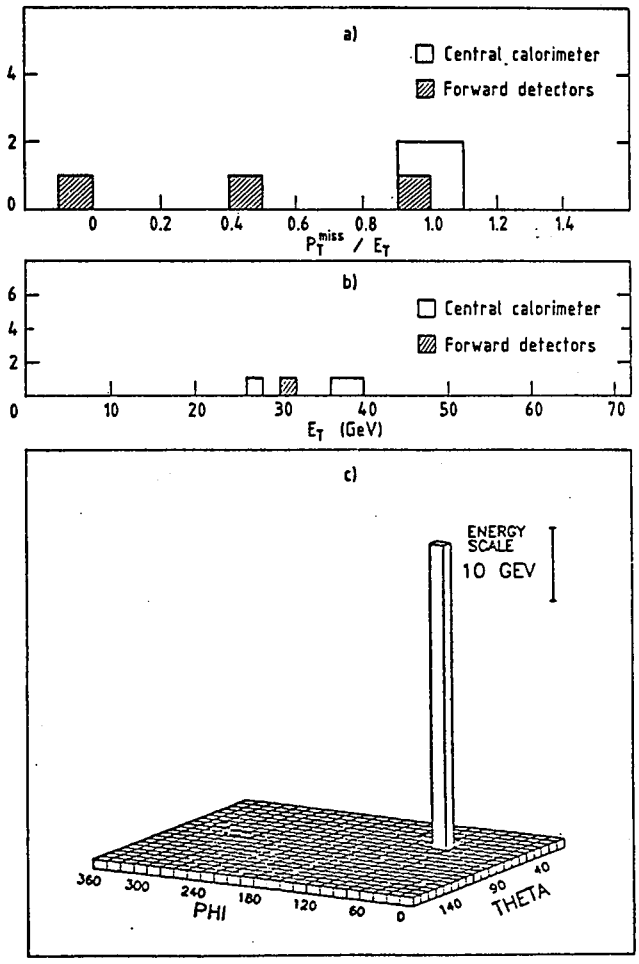

Fig. 11. a) P_T^{miss} distribution for electron candidates.
b) E_T distribution for events with $P_T^{miss}/E_T > 8$.
c) Theta-Phi distribution for highest E_T event.

CROSS SECTION ESTIMATES FOR MULTI-TEV PHYSICS

Robert N. Cahn
Lawrence Berkeley Laboratory
University of California, Berkeley, CA 94720

Summary

This note provides rough estimates for cross sections of interest in the multi-TeV regime.

Introduction

In designing detectors for the multi-TeV region, it is worthwhile to consider what cross sections might be anticipated on the basis of present experience and theoretical prejudice. Such projections must be treated with a good deal of skepticism since they require very large extrapolations from the ISR-FNAL energy range or slightly lesser extrapolations from the fragmentary SPS Collider data. Even worse, some predictions are founded nearly entirely on theoretical pictures which have not been extensively tested. Nevertheless, this is the best we can do. Depending on the process, the uncertainties may be as little as a factor of two, or as much as an order of magnitude or two.

It should be emphasized that the projections given here are not only very approximate, but furthermore do not represent what is most likely to be interesting at these very high energies. After all, we want to look for new phenomena, not just the standard catalogue of jets, dileptons, and the like. Nevertheless, these mundane items do furnish us with benchmarks, standards for the cross sections which are potentially interesting and perhaps examples of signatures which could help identify truly new physics.

These estimates are based on my SLAC Summer School Lectures of 1982 to which the reader is directed for more complete discussion and references.[1]

Total Cross Section

Ever since the rise the in pp cross section was first discovered at the ISR, it has been popular to interpret the data as saturating the Froissart bound form, $\ln^2 s$. Such a fit is indeed possible and is not inconsistent with the measurement at the SPS Collider of about 65 mb.[2] Still, it is possible to produce a fit with all the required analyticity which while giving a $\ln^2 s$ behavior at present energies, eventually becomes constant.[3] These two kinds of fits give very different predictions at $\sqrt{s} = 20-40$ TeV. Calling the pure $\ln^2 s$ fit #1 and the one which becomes constant asymptotically #2, we have

$\sqrt{s}$	Fit #1	Fit #2
0.54 TeV	71 mb	66 mb
2 TeV	100 mb	82 mb
20 TeV	173 mb	107 mb
40 TeV	200 mb	114 mb

It is worth noting that even for the total cross section where we have excellent low energy data and the theoretical constraints of analyticity, when we extrapolate to the 40 TeV region, there are uncertainties of 100%. Similar extrapolations [4] for the slope parameter of elastic scattering, B, suggest that its value which is about 13 GeV^{-2} at the ISR will be about twice that at $\sqrt{s} = 20$ TeV.

Lepton Pair Production

Lepton pair production has been a tremendously important process because it has led to the discovery of the J/ψ and the Υ and because the continuum production is an especially important process theoretically. Using a crude model for the quark distributions, it is possible to obtain a simple estimate[1] for the cross section to produce a dilepton pair with an invariant mass $m_{\mu\bar{\mu}} = \sqrt{\tau s}$:

$$\sigma(m_{\mu\bar{\mu}} > \sqrt{\tau_0 s}) \approx 10^{-37}\text{cm}^2\left(\frac{540\text{GeV}}{m_{\mu\bar{\mu}}}\right)^2 2^{-20\sqrt{\tau_0}}.$$

We see that the last factor is nearly unity at 20 TeV for reasonable cross sections, so the behavior is nearly as $m_{\mu\bar{\mu}}^{-2}$. The cross section to produce a pair with mass greater than 180 GeV is about 10^{-36}cm^2.

W and Z Production

If past history is a guide, W and Z production will be an important background for something interesting. Their masses are small enough compared to the available energy at multi-TeV machines that there is little energy dependence in their production cross sections. Using quark distributions appropriate to the SPS Collider without modifications for possible non-scaling effects, we find that the cross sections should be roughly $5 \cdot 10^{-33}\text{cm}^2$ for each species in either pp or $p\bar{p}$ machines.

High Transverse Momentum Jets

The early data from the SPS Collider indicate that high transverse momentum jets do become prominent, well-defined features at such energies in contradistinction to the situation at ISR energies where jets are often obscured by fluctuations in the non-jet events. QCD predicts cross sections for these processes but with great uncertainties. The uncertainties arise from two sources: the quark distributions and radiative QCD corrections to the basic partonic cross sections. To get a crude idea of the cross sections, we finesse these problems by ignoring them: we use scaling distributions for the quarks and lowest order calculations for the cross sections.

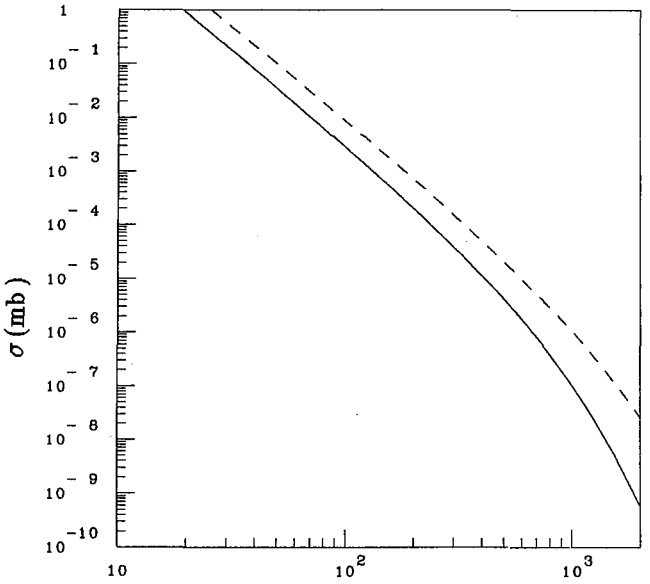

Typical results are shown in the Figure. The curves show the cross section to produce a jet with transverse momentum greater than a given amount, considering only the subprocess gluon + gluon → gluon + gluon. The solid curve is for $\sqrt{s} = 20$TeV and the dashed curve is for $\sqrt{s} = 40$ TeV.

Heavy Flavor Production

Heavy flavor production has been considered by Combridge in a QCD model.[5] If we restrict ourselves to the two mechanisms gluon+gluon → $Q\,\bar{Q}$ and $q\bar{q} \rightarrow Q\bar{Q}$, it is clear on dimensional grounds that the production cross section must go as α_s^2/M^2 where M is the heavy quark mass. There may in addition be a factor representing the suppression for making the quarks at finite s. At the multi-Tev machines, this suppression is not important for $M < \sqrt{s}/100$, so we expect a cross section nearly equal to the naive estimate above. At more detailed analysis suggests that the numerical factor which multiplies the dimensional quantity is about 5. For $M = 40$ GeV, this gives a cross section of about $5 \cdot 10^{-32}\text{cm}^2$.

References

1. R. N. Cahn, *Expectations for Old and New Physics at High Energy Colliders,* LBL-15469 and forthcoming Proceedings of the 1982 SLAC Summer Institute.
2. M. Haguenauer, UA-4 Collaboration, *Journal de Physique, 43, 21st International Conference on High Energy Physics, Paris, 1983,* p.579
3. M. M. Block and R. N. Cahn, *Phys. Letters* **120B**, 224(1983).
4. M. M. Block and R. N. Cahn, *Phys. Letters* **120B**, 229(1983).
5. B. L. Combridge, *Nucl. Phys.* **B151**, 429(1979).

MONTE CARLO SIMULATION OF HIGH p_T JETS

Frank E. Paige, Serban D. Protopopescu, and Dennis P. Weygand
Brookhaven National Laboratory, Upton, New York 11973

We discuss the properties of high p_T jets expected at high energy hadron colliders.

Perturbative QCD predicts that high p_T hadronic reactions should contain jets of hadrons from the fragmentation of quarks and gluons. Evidence for jets with about the predicted cross section as been found at the ISR[1], although the jets are not clearly separated from the background of low-p_T particles. At the SPS Collider, the jets stand out dramatically[2], and some clear multi-jet events are seen. Since jets are expected both from QCD hard scattering and from the decay of heavy particles, we will surely want to study them at any future hadron collider.

It is easy to guess the qualitative properties of jets at very high energies. The mean k_T of particles with respect to the jet axis must be determined by the jet p_T, the only scale in the problem:

$$\langle k_T^2 \rangle \sim \alpha_s(p_T^2)\, p_T^2 \quad .$$

Hence the mean opening angle is

$$\langle \theta \rangle \sim [\alpha_s(p_T^2)]^{1/2} \sim [\ell n\, p_T^2]^{-1/2} \quad .$$

This opening angle is of course a consequence of the radiation of extra gluons and quark-antiquark pairs. As p_T increases, more and more of these extra partons will have energies large compared to 1 GeV and so will be observable above the background of soft particles. Therefore the number of visible jets will increase while the opening angles between jets decrease very slowly.

To make these remarks more quantitative, we have produced samples of high p_T jet events using ISAJET[3], a Monte Carlo event generator for hadronic reactions. The program uses an approximation to perturbative QCD introduced by Fox and Wolfram[4]. In lowest order, QCD predicts just two jets. In higher orders, extra gluons and quark-antiquark pairs can be produced, giving multiple jets. The multi-jet cross sections are suppressed by extra powers of $\alpha_s(p_T^2)$ except when the partons are collinear. The collinear regions give contributions of order $\alpha_s(p_T^2)\ell n p_T^2$ producing the leading-log scaling violations of the jet fragmentation functions[5]. The Fox-Wolfram approximation keeps only the parts of the matrix elements which dominate in the collinear regions but uses exact, non-collinear kinematics. Since the parts retained involve no interference terms (in the right gauge), they can be recast as classical probabilities for a quark or gluon to split into two. Thus this approximation is very suitable for a Monte Carlo approach.

Retaining the dominant terms in the collinear region gives the correct leading-log scaling violations in the jet fragmentation and qualitatively the right cross section for multiple jets at large angles. It also leads to a very rapid increase in multiplicity[6]:

$$\langle n \rangle \sim \exp\{[12/\pi b\, \ell n\, p_T^2]^{1/2}\} \quad ,$$

$$b = (33 - 2n_f)/12\pi \quad .$$

A more correct calculation[7] summing all powers of $\alpha_s(p_T^2)\ell n^2\, p_T^2$ gives a similar form but with the coefficient of $[\ell n\, p_T^2]^{1/2}$ decreased by a factor of $\sqrt{2}$. The physical reason[8] is that the leading-log approximation treats all gluon emissions as independent, while a gluon of momentum q can only be radiated when its parent parton is separated from the others by a distance of order 1/q. Hopefully, a more correct treatment of soft partons will be included in a future version of ISAJET.

We have generated three samples of high p_T jet events at energies for which the cross sections are large:

$\sqrt{s}$ (GeV)	p_T (GeV)	$\sigma(cm^2)$
800	100- 110	5.8×10^{-34}
2000	200- 220	3.0×10^{-34}
10000	1000-1100	1.1×10^{-35}

To avoid generating too many particles, the π^0's and η's have not been decayed at the highest energy.

Fig. 1 shows the z distribution for all particles, charged and neutral, in a jet. At small z,

$$z\,\frac{dN}{dz} = \frac{dN}{dy} \sim 10 \quad ,$$

implying a significantly higher density of particles along a jet than in a low p_T beam jet. While the

program is tuned to give the right multiplicity at PETRA, the cascade of soft partons will produce an overestimate of the density of low-z particles at higher energies.

Fig. 2 shows the energy-weighted opening angle distribution with respect to the direction of the original parton. Fig. 3 shows the multiplicity as a function of this angle. These plots are based on the jets as defined by ISAJET, not on jets reconstructed by some algorithm.

Fig. 4 shows the charged particle multiplicity distribution in a jet. The multiplicity obviously grows very rapidly with p_T. While this growth is overestimated, nevertheless high multiplicities are expected.

Figs. 5 and 6 show the distributions in opening angles between pairs of particles in a jet and between pairs each having $p_T > 3$ GeV. Figs. 7 and 8 show similar distsributions on a finer scale for the charged particles. These plots indicate the segmentation needed to track individual particles in a jet. While such tracking is not very important for the gross features, it is essential if one wants, for example, to look for prompt leptons indicating the presence of heavy quarks.

At very high energies, jet events contain many sub-jets, so quantities like the mean opening angle are not very meaningful. In Fig. 9 we show the first ten events generated at $\sqrt{s}$ = 10 TeV with p_T = 1000-1100 GeV and $|y| < 1$. The particles from these events have been put into a simulation program for a calorimeter segmented into towers with $\Delta y = .1$ and $\Delta\phi = 5°$. The energy in each tower is indicated by a solid line, and the energy of each parton is shown by a dotted line. In these ten events there is one with seven distinct jets! For a typical event the program generates about 50 partons, so the visible jets are not coming from partons close to the infrared cutoff. Of course when extrapolating to such high energies we can not expect to predict correctly such details as the rate for seven jet events, even if we had a good algorithm for defining jets. Nevertheless, it seems likely that events in this p_T range will show a rich and complicated structure.

Acknowledgment

The submitted manuscript has been authored under contract DE-AC02-76CH00016 with the U.S. Department of Energy.

References

1. Axial Field Spectrometer Collaboration, Phys. Letters 118B, 185, 193 (1983).
2. UA1 Collaboration, CERN-EP/82-134 (1982); UA2 Collaboration, Physics Letters 115B, 59 (1982).
3. F.E. Paige and S.D. Protopopescu, BNL 31987, to be published in the Proceedings of the DPF Workshop on High Energy Physics and Future Facilities (Snowmass, 1982).
4. G.C. Fox and S. Wolfram, Nucl. Phys. B168, 285 (1980).
5. J. . Owens, Phys. Letters 76B, 85 (1978); T.A. DeGrand, Nucl. Phys. B151, 485 (1979).
6. D. Amati, A. Bassetto, M. Ciafaloni, G. Marchesini, and G. Veneziano, Nucl. Phys. B173, 253 (1979).
7. A.H. Mueller, Phys. Letters 104B, 161 (1981).
8. Yu. L. Dokshitser, V.S. Fadin and V.A. Khoze, Leningrad-82-789 (1982).

Fig. 1: **z(dN/dz) vs z.** (a) p_T = 100 GeV. (b) p_T = 200 GeV. (c) p_T = 1000 GeV.

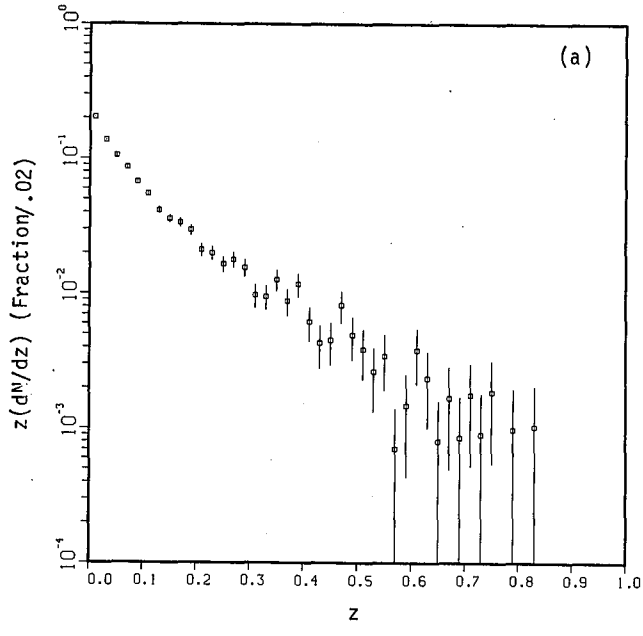

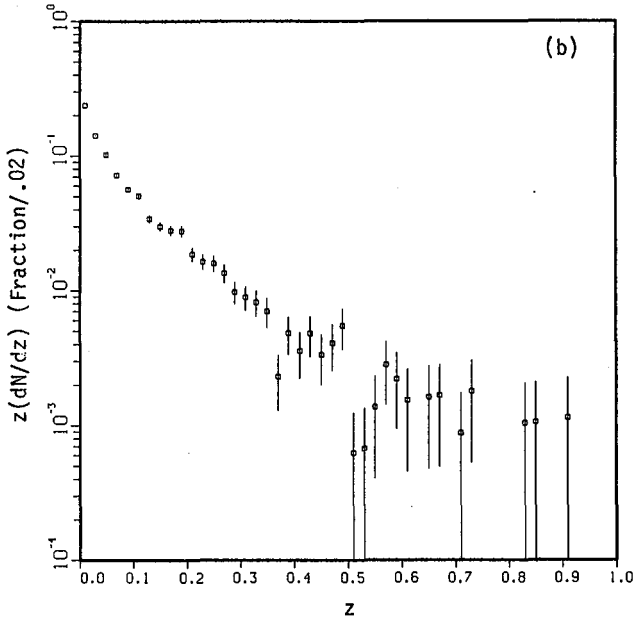

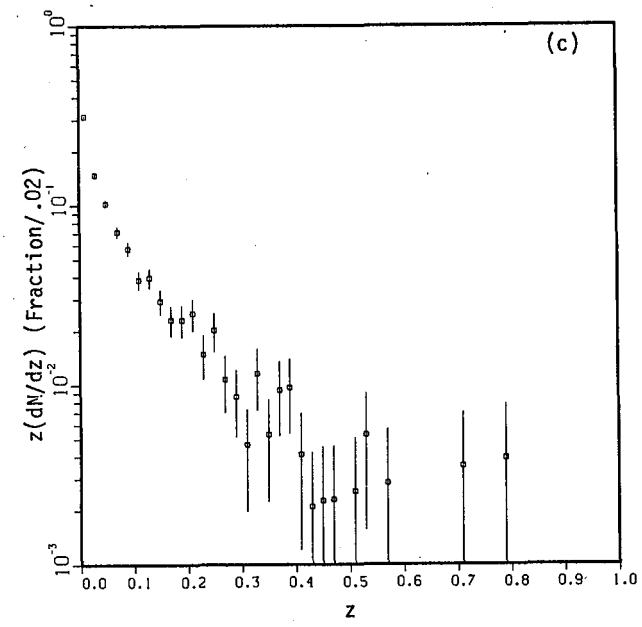

Fig. 2: z(dN/dθ) vs θ.

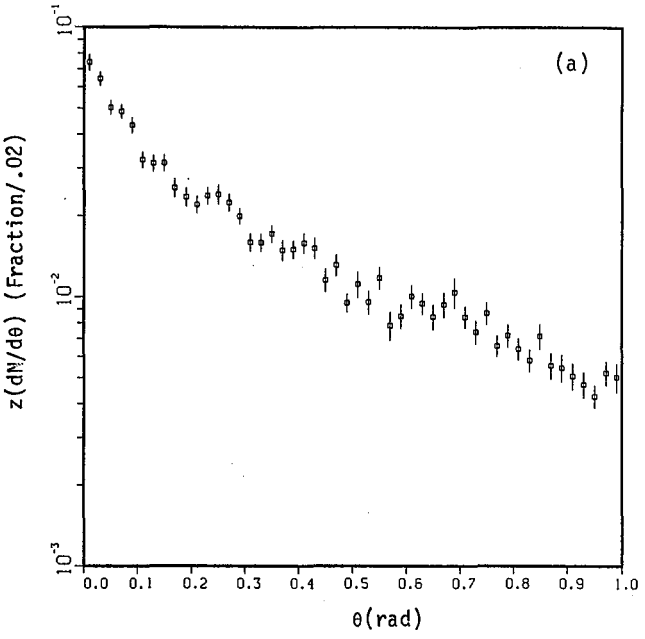

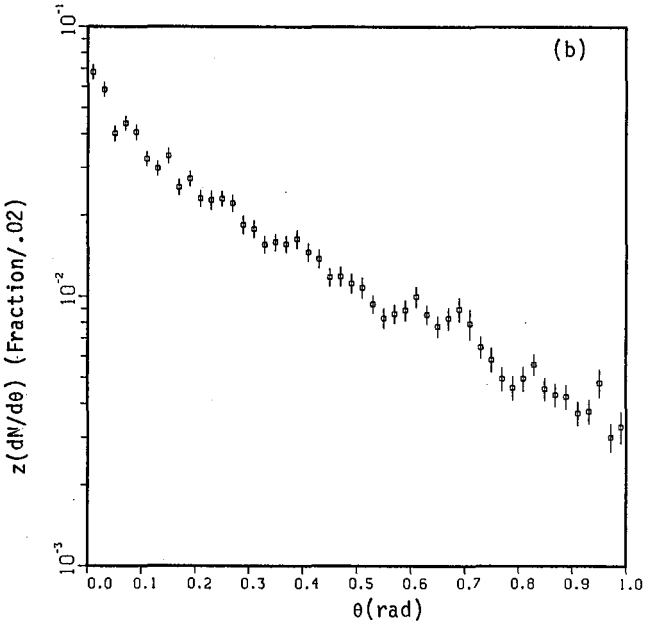

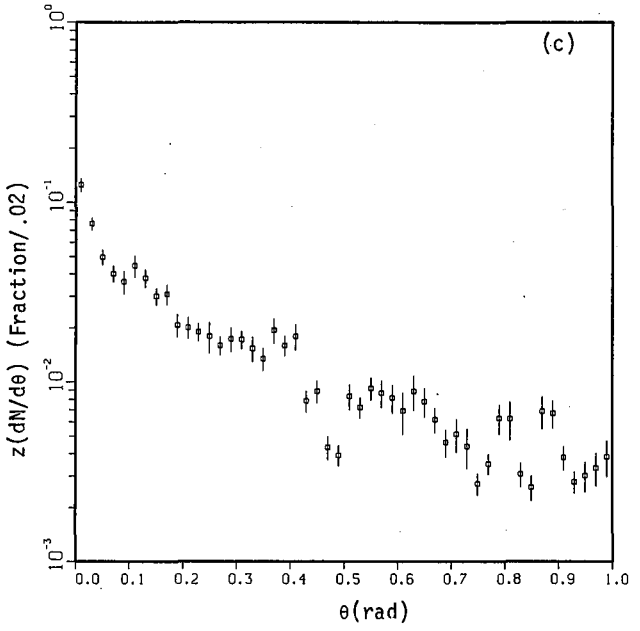

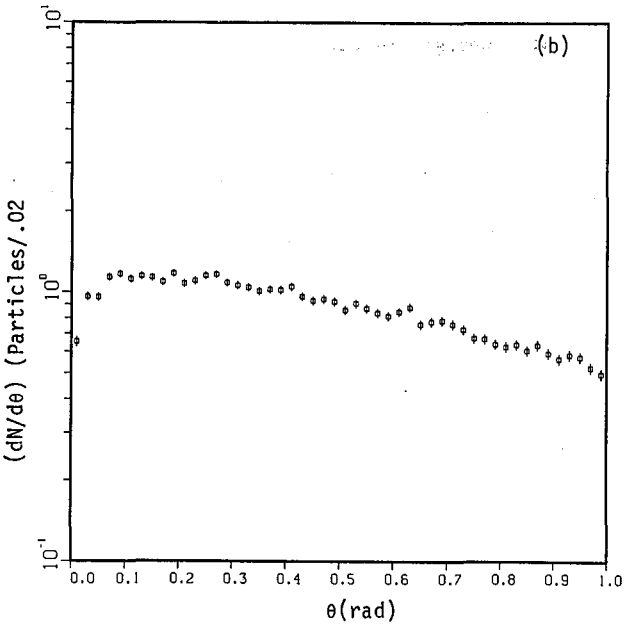

Fig. 3: dN/dθ vs θ.

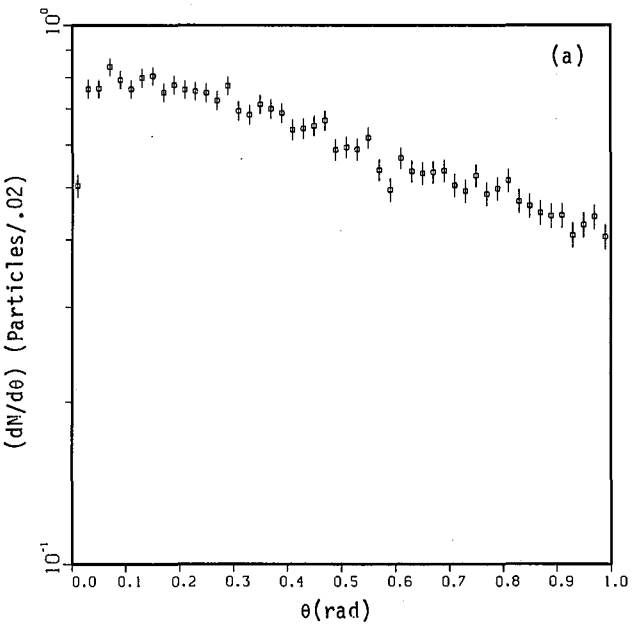

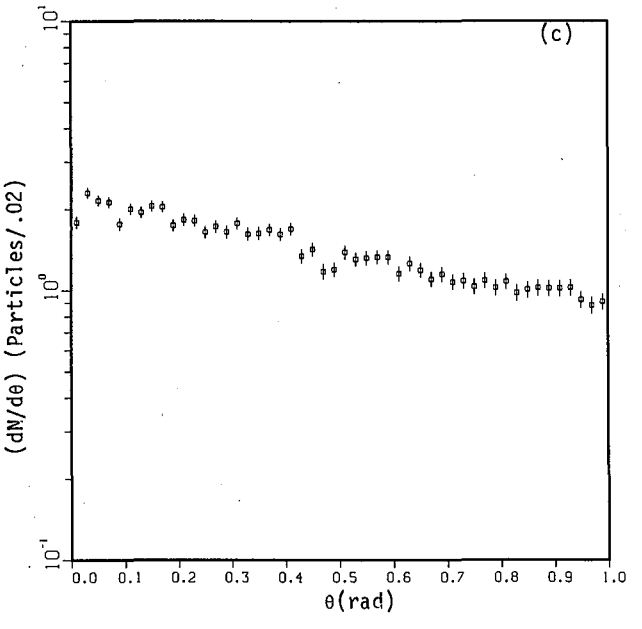

Fig. 4: Charged multiplicity.

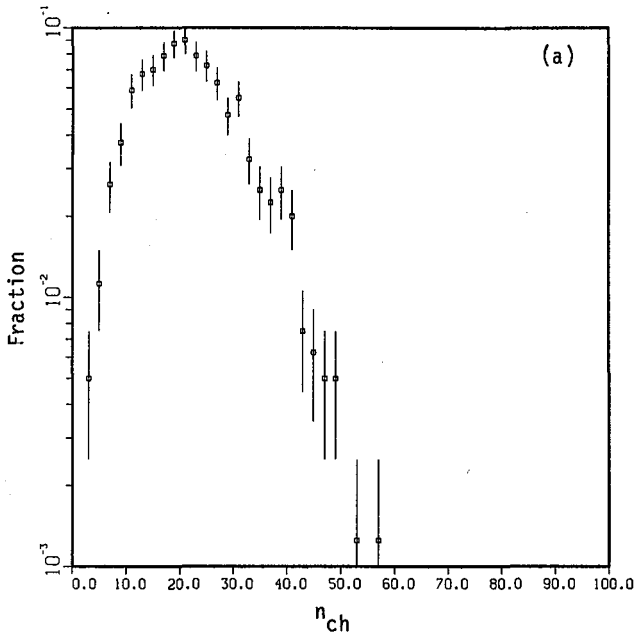

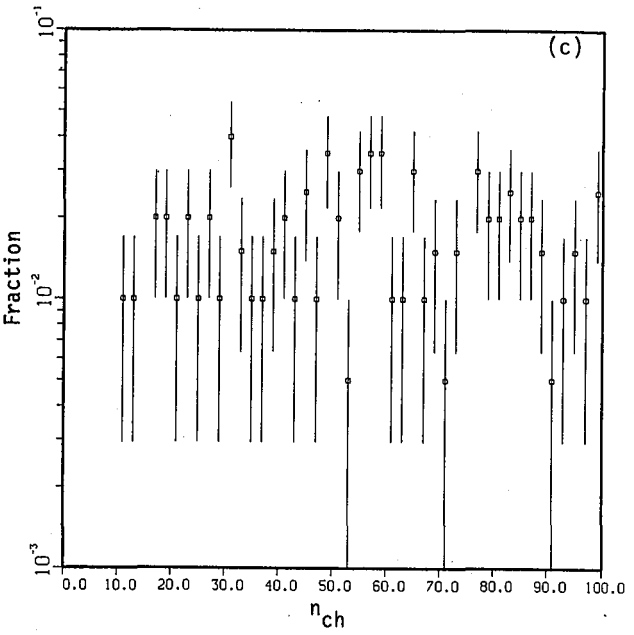

Fig. 5: Pairs vs θ_{12}.

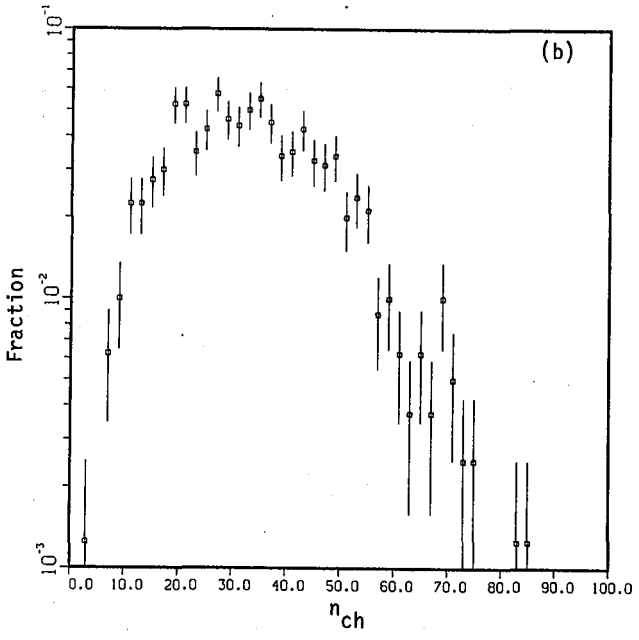

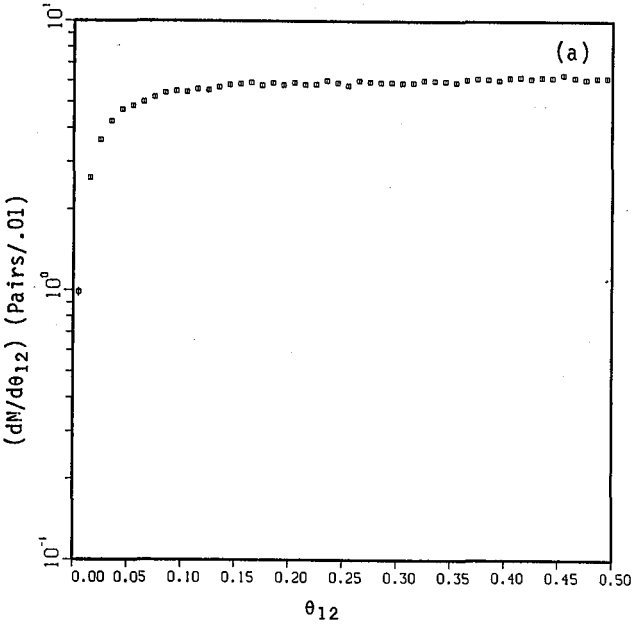

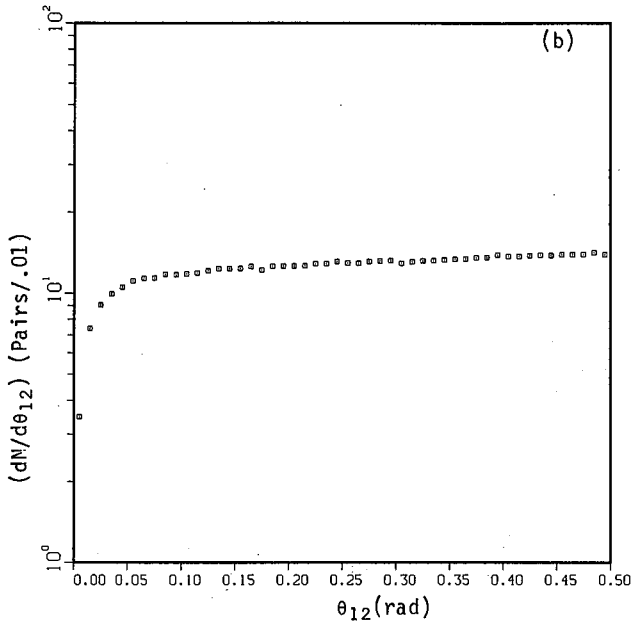

Fig. 6: Pairs each with $p_T > 3$ GeV vs θ.

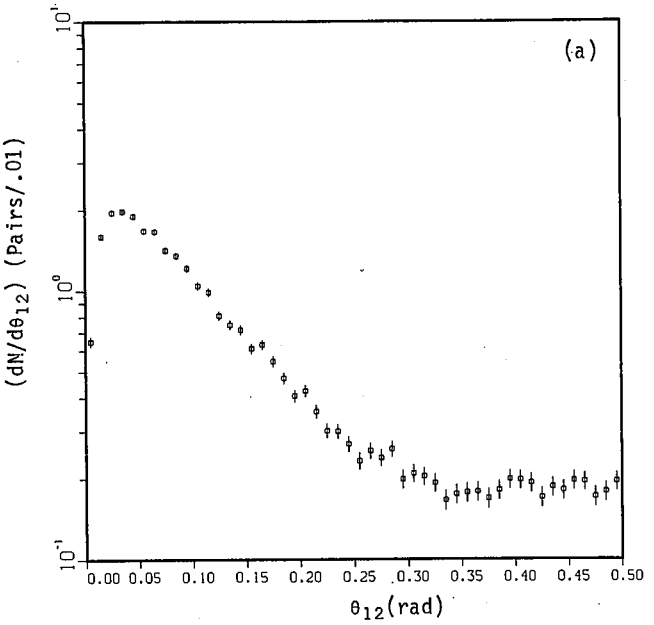

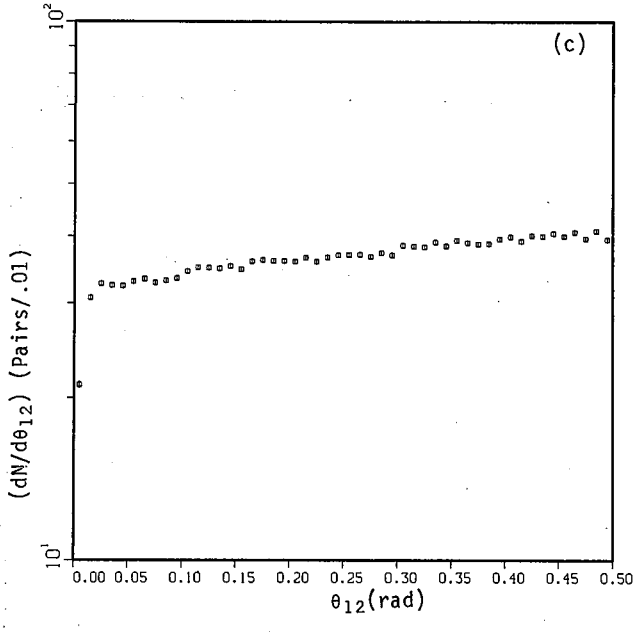

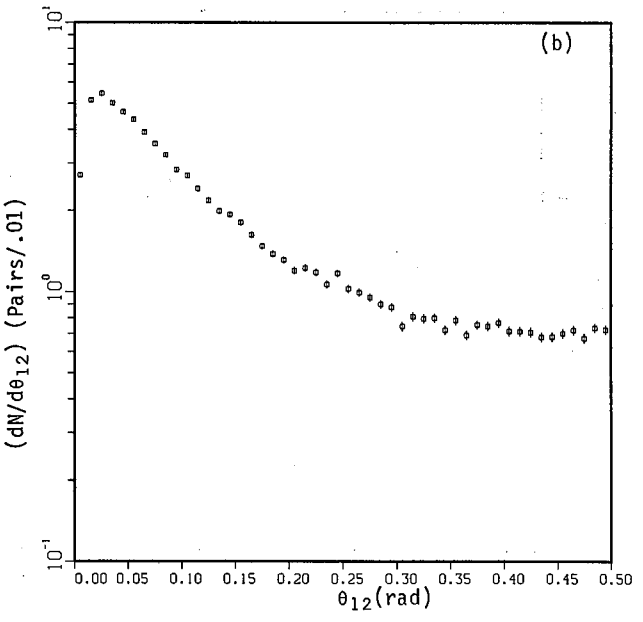

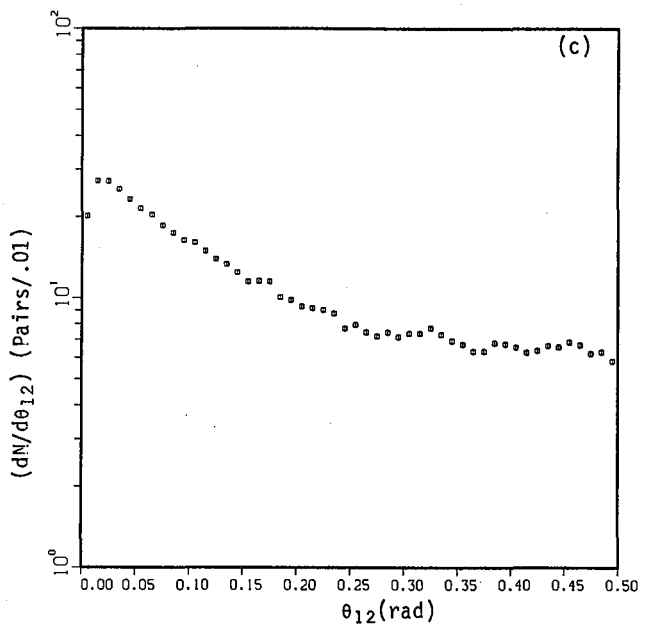

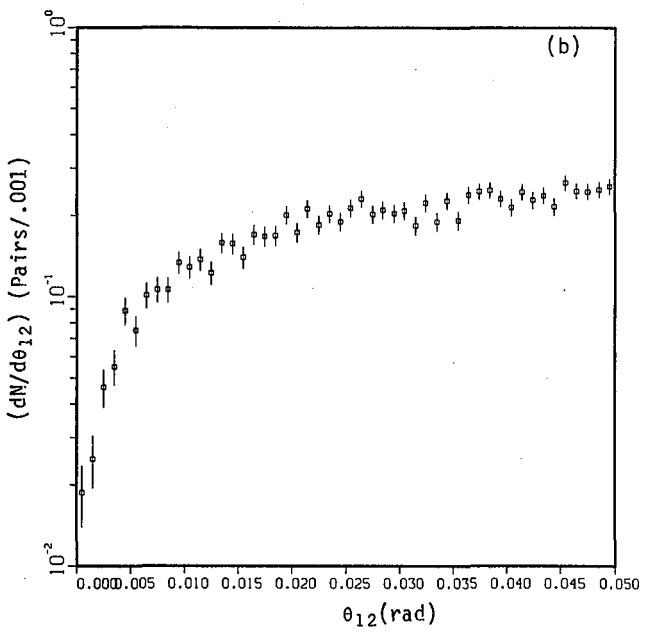

Fig. 7: Charged pairs vs θ_{12}.

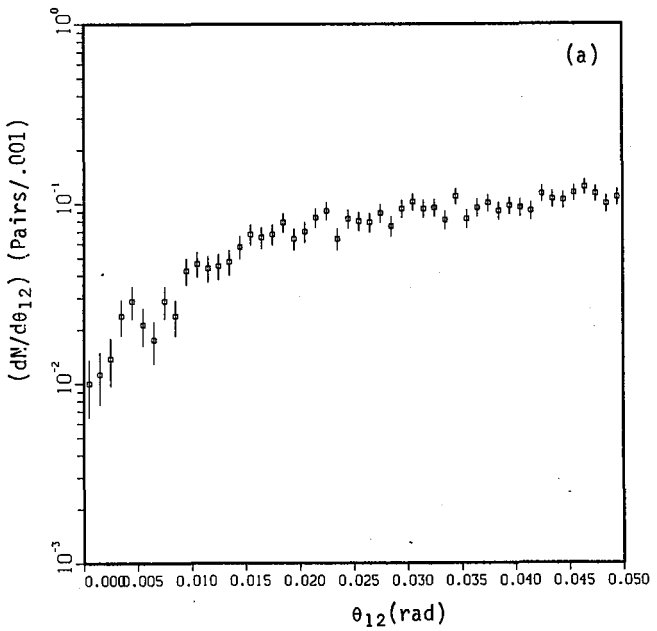

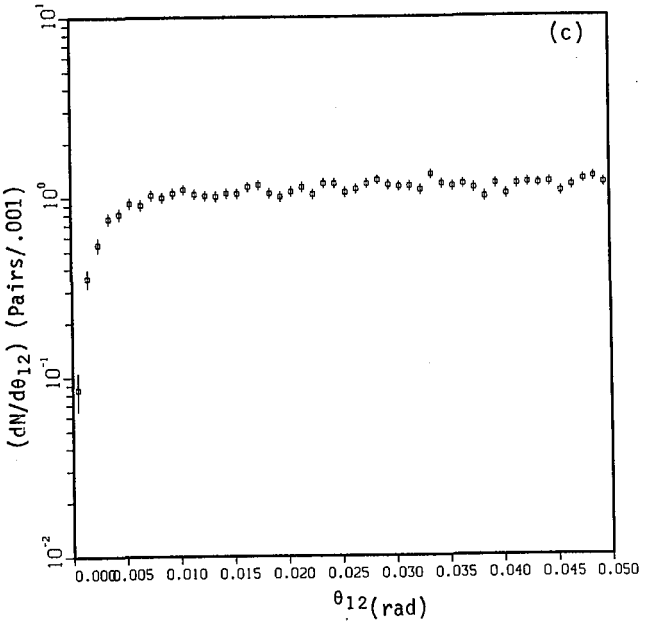

Fig. 8: Charged pairs with $p_T > 3$ GeV vs θ_{12}.

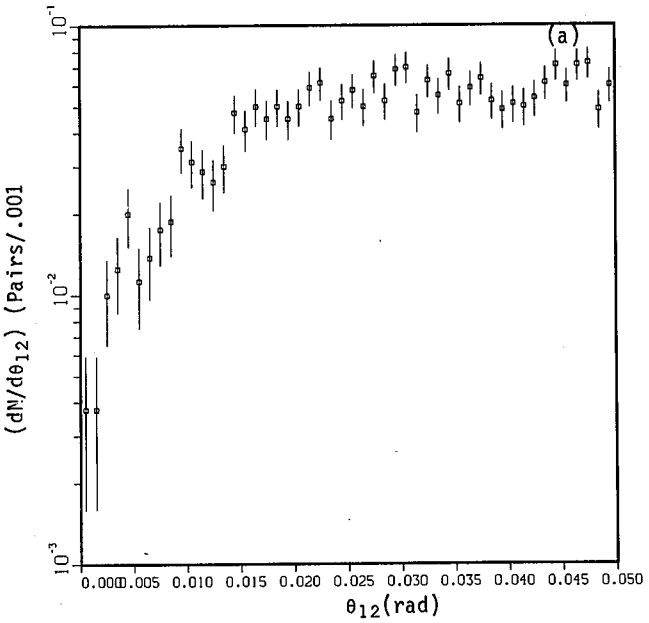

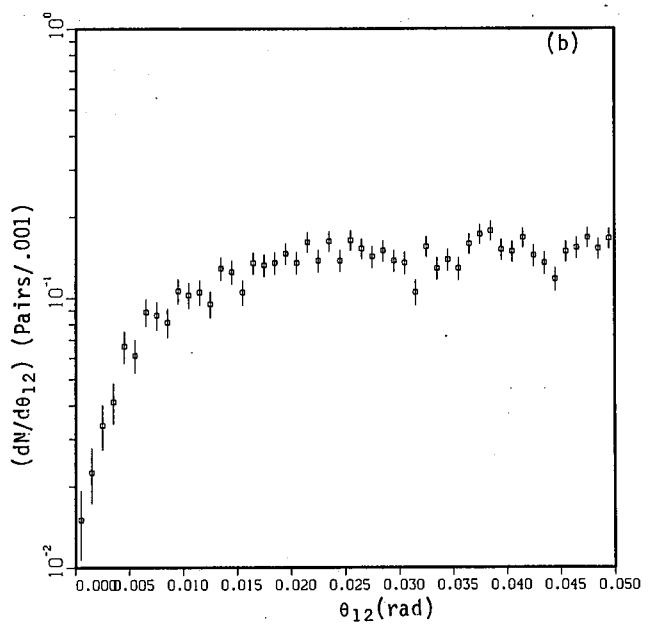

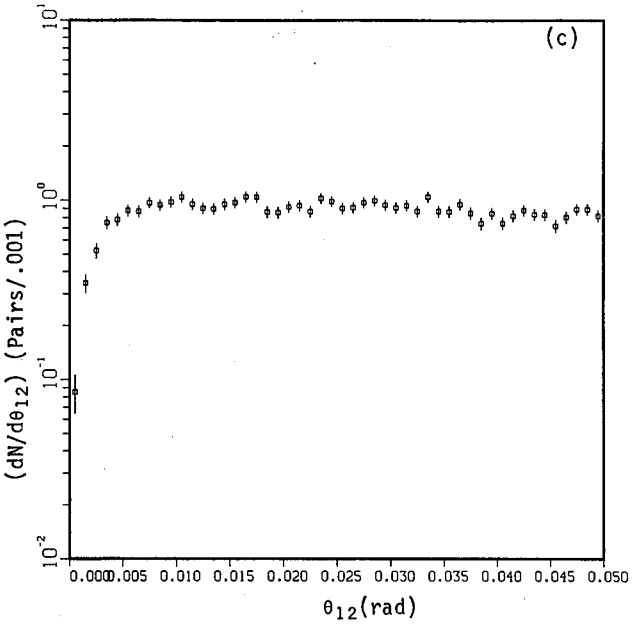

Fig. 9: Calorimeter plots of 10 events with p_T = 1000 GeV.

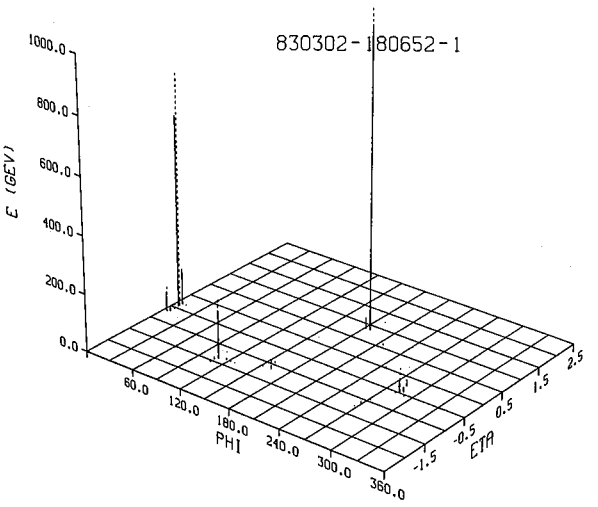

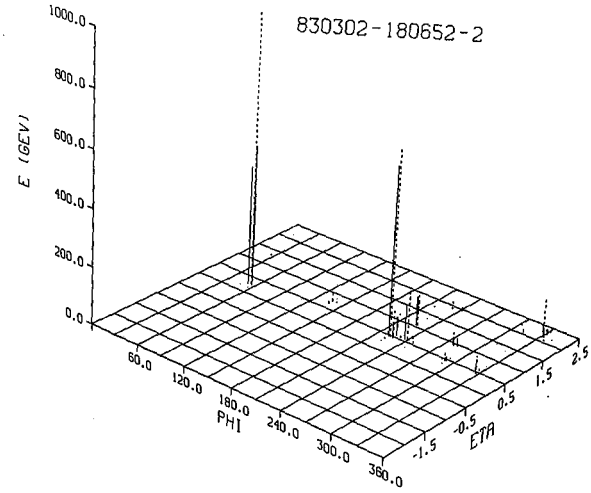
830302-180652-2
E (GEV)
1000.0
800.0
600.0
400.0
200.0
0.0
60.0
120.0
180.0
240.0
300.0
360.0
PHI
-1.5
-0.5
0.5
1.5
2.5
ETA

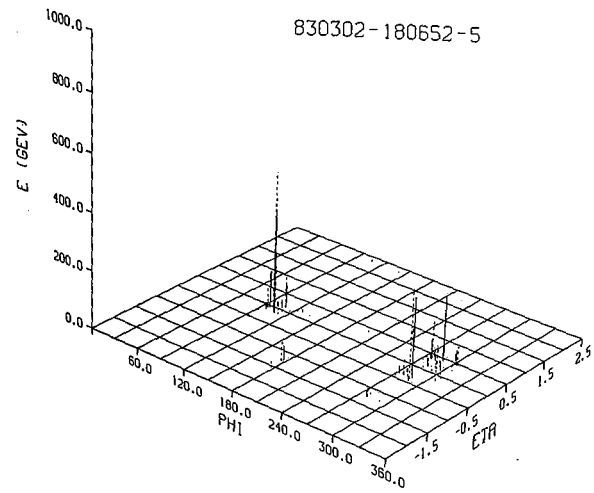
830302-180652-5
E (GEV)
1000.0
800.0
600.0
400.0
200.0
0.0
60.0
120.0
180.0
240.0
300.0
360.0
PHI
-1.5
-0.5
0.5
1.5
2.5
ETA

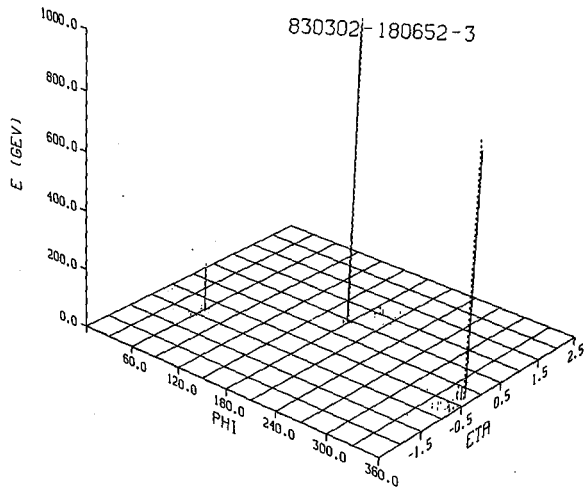
830302-180652-3
E (GEV)
1000.0
800.0
600.0
400.0
200.0
0.0
60.0
120.0
180.0
240.0
300.0
360.0
PHI
-1.5
-0.5
0.5
1.5
2.5
ETA

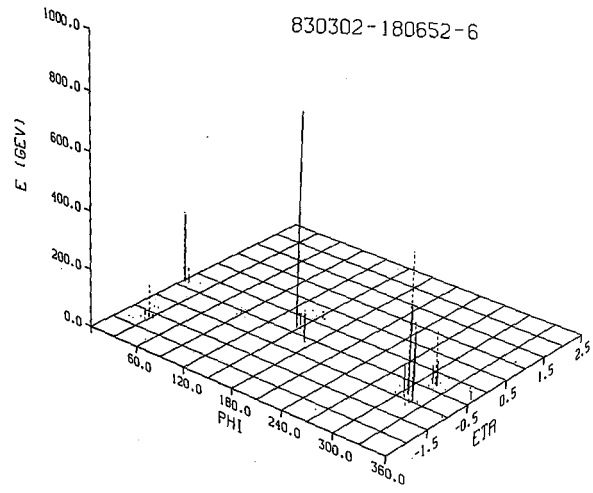
830302-180652-6
E (GEV)
1000.0
800.0
600.0
400.0
200.0
0.0
60.0
120.0
180.0
240.0
300.0
360.0
PHI
-1.5
-0.5
0.5
1.5
2.5
ETA

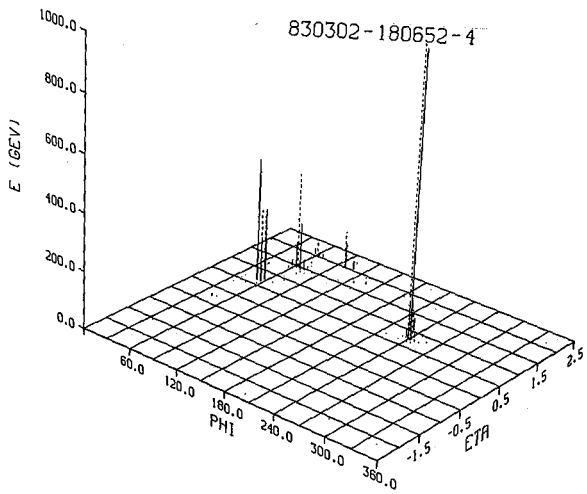
830302-180652-4
E (GEV)
1000.0
800.0
600.0
400.0
200.0
0.0
60.0
120.0
180.0
240.0
300.0
360.0
PHI
-1.5
-0.5
0.5
1.5
2.5
ETA

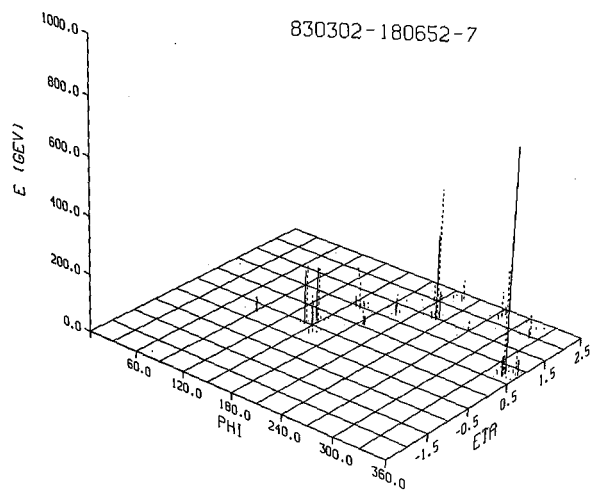
830302-180652-7
E (GEV)
1000.0
800.0
600.0
400.0
200.0
0.0
60.0
120.0
180.0
240.0
300.0
360.0
PHI
-1.5
-0.5
0.5
1.5
2.5
ETA

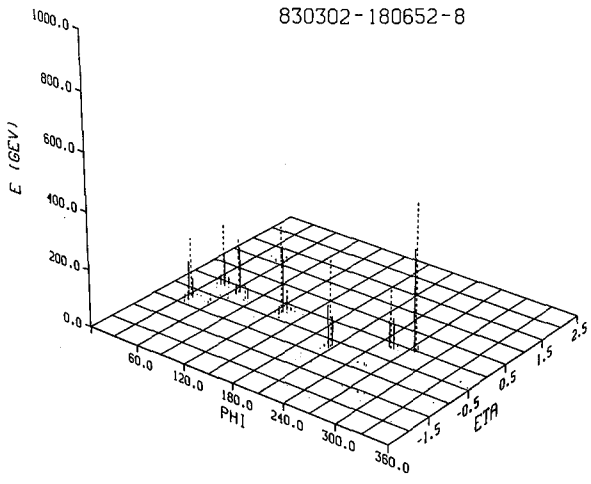
830302-180652-8
E (GEV)
1000.0
800.0
600.0
400.0
200.0
0.0
60.0
120.0
180.0
240.0
300.0
360.0
PHI
2.5
1.5
0.5
-0.5
-1.5
ETA

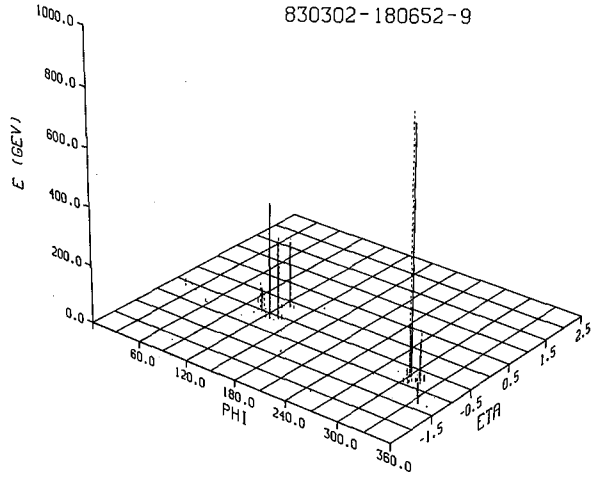
830302-180652-9
E (GEV)
1000.0
800.0
600.0
400.0
200.0
0.0
60.0
120.0
180.0
240.0
300.0
360.0
PHI
2.5
1.5
0.5
-0.5
-1.5
ETA

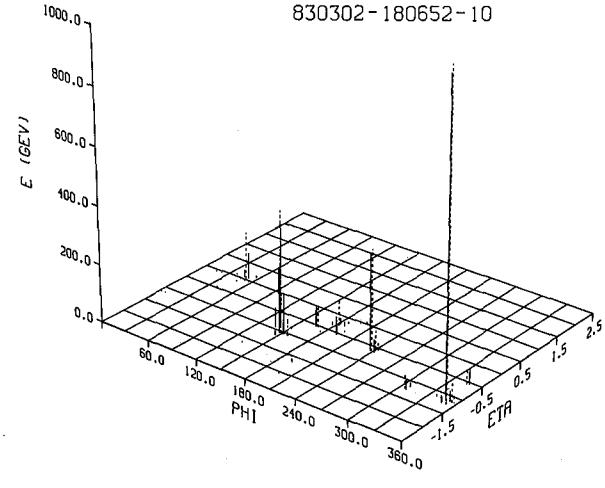
830302-180652-10
E (GEV)
1000.0
800.0
600.0
400.0
200.0
0.0
60.0
120.0
180.0
240.0
300.0
360.0
PHI
2.5
1.5
0.5
-0.5
-1.5
ETA

SECTION II: WORKING GROUP SUMMARY REPORTS

TRACKING DETECTORS

Donald Hartill

Working Group Summary Report

D. Hartill, M. Atac, W. Bartel, M. Breidenbach, A. Bross, W. Carithers,
E. Gatti, D. Greiner, D. Herrup, B. Kephart, D. Levinthal, T. Ludlam,
M. Mestayer, R. Ong, S. Parker, E. Platner, V. Radeka, P. Rehak, F. Sauli,
P. Schlein, K. Shinsky, D. Theriot, and A. Tollestrup

I. Introduction

The problem of tracking charged particles in the cores of high energy jets in a high rate environment is a difficult one and will require a great deal of R and D to solve in an affordable way. During the workshop the tracking group concentrated on three problems to provide a focus for our efforts. These were 1) the general vertex detector, 2) the central and forward regions for 1 TeV pp collider with a luminosity of 10^{33} cm^{-2} sec^{-1}, and 3) possible tracking devices for a 20 TeV hadron hadron collider. The largest effort went into the second problem in order to help assess the desirability of building such a collider. After one day of preliminary work the 20 TeV subgroup joined with the 20 TeV Systems subgroup to form a larger group that could make some progress on a first look at the whole detector question at this energy. Most of their effort was devoted to modelling what jets at 20 TeV might look like in order to determine detector design parameters. Their efforts are summarized in the report from the Systems Group led by Barry Barish. The final section of this report concerns the research and development needs to provide adequate tracking for the next generation collider detectors.

II. 1 TeV with L = 10^{33} cm^{-2} sec^{-1}

The interaction diamond for a pp collider with 1 TeV total c.m. energy and a luminosity of 10^{33} is approximately 40 cm long by a few mm wide.[1] Since the primary physics interest is in high transverse momentum phenomena a magnetic solenoid for the central region has several advantages. Because of the small transverse size of the interaction diamond, it can be used as a constraint (pointlike) for a fast hardware trackfinder for trigger purposes and facilitates using fast software trackfinders to do rapid event filtering to find the interesting high p_T events. The other possibility is to use a dipole field transverse to the beam direction for the central region. This configuration aids the detection of particles in the forward direction by sweeping them away from the beam line so they can be detected. The disadvantage is that the vertex constraint from the beam in the bend plane is now 40 cm in length and hence not very useful as a constraint in fast trackfinding. What seems more sensible is to construct a hybrid system using a solenoid in the central region with open frame dipoles covering the forward and backward directions. The granularity requirements imposed by rate considerations and particle densities in jet cores will be the same with either a central solenoid or a central dipole implying no clear preference. Because of the fast triggering and trackfinding advantages we will choose the solenoid with forward-backward dipoles as the basis for determining the tracking requirements.

A. Central Detector

The minimal requirements for the central tracking detector are:

i. Rapidity coverage $y = \pm 1.5$ ($26^\circ \leq \theta \leq 154^\circ$)

ii. $\Delta p/p = 10\%$ at $p = 100$ GeV/c, sufficient to measure the charge

iii. Operation at L = 10^{33} cm^{-2} sec^{-1}

iv. Efficient detection of individual particles in the core of a 100 GeV/c jet.

The luminosity requirement implies an interaction rate of 50 MHz with an average of 3.6 charged particles per unit of rapidity in the central region. This gives a 500 MHz charged particle rate into the detector. Present drift chamber technology limits particle fluxes to 1 and 2 MHz per sense wire in chambers with $\leq$ 3 mm drift distances.[2] To satisfy this rate limit each layer of a cylindrical chamber must have at least 250 sense wires. The fourth requirement also implies fine granularity as is illustrated in Figure 1 which summarizes the fraction of tracks missed due to overlap in a cell for p_T = 40 GeV/c jet generated by the ISAJET Monte Carlo assuming a total center-of-mass of 0.8 TeV. As can be seen from the graph 300 - 500 cells give a 70 to 80% efficiency for seeing a track in a p_T = 40 GeV/c jet. Figure 2 shows how this tracking efficiency scales with p_T. The other way of determining the granularity is to limit the number of events overlapping during the maximum drift time in the chamber. For a drift distance of 2 mm this drift time is 40 nsec giving an average of two overlapping events for the 50 MHz primary interaction rate.

Figure 3 shows a drift chamber configuration that will satisfy our four design criteria. Assuming a spatial resolution of 200μ in the drift direction, 10% momentum resolution at 100 GeV/c can be achieved by making 45 measurements over a radial path length of 130 cm in a 1.5 Tesla field. The basic design is similar to the AFS drift chamber[3] in use at the ISR at CERN. Figure 4 shows the basic cell configuration in more detail. The sense wires are all parallel to the beam axis and the z-coordinate is obtained by charge division to 1% on every sense wire to aid in pattern recognition. The layers are grouped in four rings with the inner one containing fifteen sense wire layers with the inner most layer at a radius of 20 cm from the beam line. The second, third, and fourth rings contain 15, 10, and 5 layers respectively. To minimize the total number of sense wires, the drift distances also are increased to 3 mm, 4 mm, and 6 mm respectively. The 1% charge division requirement imposes a minimum gas gain of greater than 10^5 giving an avalanche size of $\approx 3 \times 10^6$ electrons. For the inner layers the particle rate is 1.7 MHz per wire which leads to a current of $\approx$1 μA per sense wire and $\approx$.25 μA per sense wire in the outer layers.

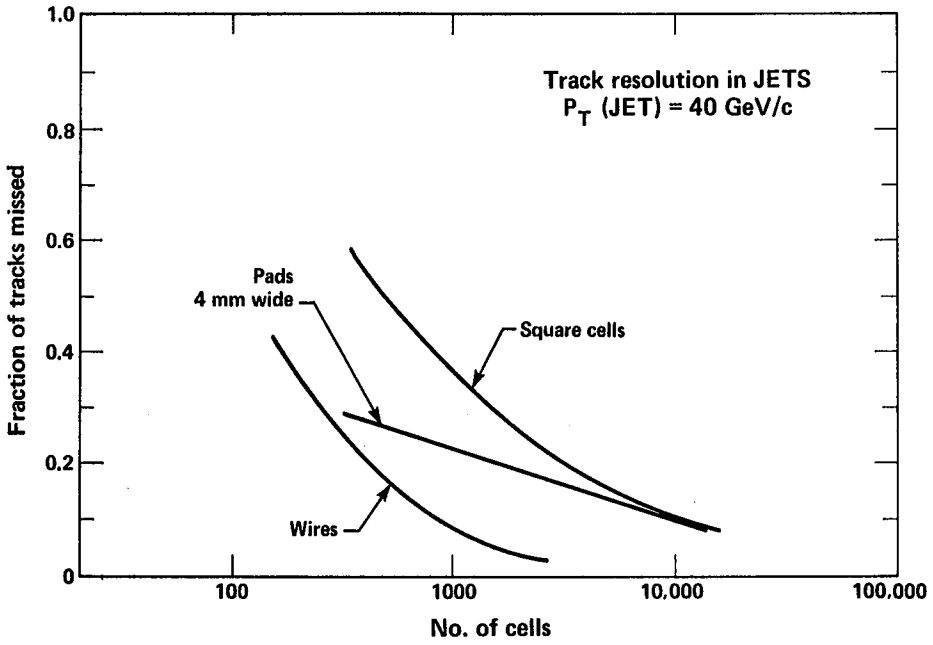

Fig. 1. Track Resolving Inefficiency vs. Cell Density

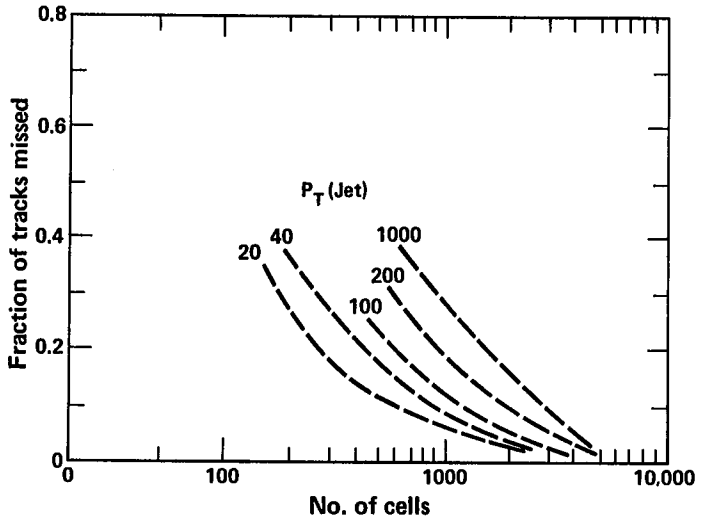

Fig. 2. Track Inefficiency for Different P_T

To improve the z resolution from the ≈1 cm value in the first ring and ≈4 cm value in the fourth ring, one layer in each ring is equipped with a cathode strip system. Figure 5 schematically illustrates this system. The strips are a few mm wide and 16 mm to 48 mm long (covering four sense wires) and connected together by resistors to form a pad. If each end of the resistor chain is connected to a charge sensitive amplifier and the pulse height is measured the avalanche position along the sense wire can be determined to ≈1 mm. Three thousand pads per special layer on the inner two rings and six thousand pads per special layer on the outer two rings would provide useful granularity for high p_T jets.

Table 1 summarizes the number of wires and general properties of each ring. For the sense wires each end must be instrumented with an electronic channel which must measure a time to better than 2 nsec accuracy and a pulse height to a part in 1024 (10 bit resolution) to provide the 1% z coordinate measurement by charge division. The 10 bit precision is necessary to accommodate the large dynamic range of the pulses from the sense wires due to Landau fluctuations in dE/dx and the large angular acceptance of the central detector. Although by existing general-purpose-detector standards, this device is nearly an order of magnitude increase in the number of electronic channels and mechanical complexity, it barely meets our design goals stated in the beginning

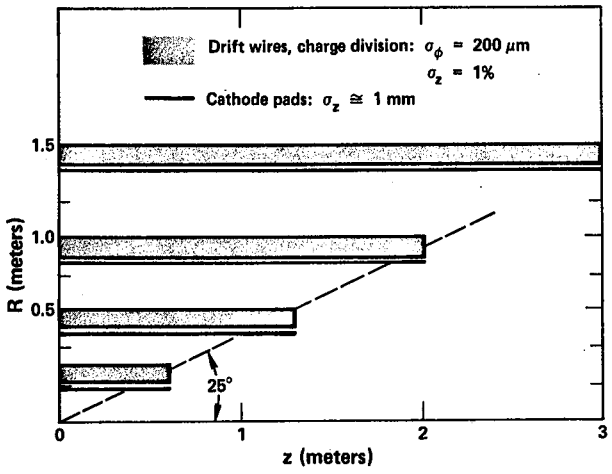

Fig. 3. Quarter Section of Cylindrical Drift Chamber

of this section. The UA1 central detector operating at the CERN $\bar{p}p$ collider with a total cm energy of 0.54 TeV has an effective granularity of 1.5 cm in the drift direction. They plan to decrease that to 5 mm by installing shaping networks on their preamp inputs and feel that this will still be too coarse a granularity to carry out their next round of physics analysis in a reasonable way. Their experience confirms our feeling that the proposed central detector is a minimal detector to do the job. Certainly ease of trackfinding and better particle isolation in jet cores in the off-line analysis would push for even finer granularity and more channels. When planning a detector, the software costs are often overlooked and it is very likely that more complexity in the hardware would payoff in decreased software costs and provide a cheaper overall detector system.

Table 1. Central Tracking Chamber

Ring 1	r_1 = 20cm a = 2 mm	
	314 sense wires/layer	4700 sense wires
	15 layers	3000 pads
Ring 2	r_1 = 50 cm a = 3 mm	
	523 sense wires/layer	7850 sense wires
	15 layers	3000 pads
Ring 3	r_1 = 90 cm a = 4 mm	
	722 sense wires/layer	7220 sense wires
	10 layers	6000 pads
Ring 4	r_1 = 140 cm a = 6 mm	
	1460 sense wires/layer	7330 sense wires
	5 layers	6000 pads

Total sense wires = 27,000
Total pads = 18,000
Total electronic channels = 2 x 45,000 = 90,000

One concern with a chamber system with this number wires is the total thickness in radiation lengths and interaction lengths of the chamber. At $\theta = 90^\circ$ the total thickness is .02 radiation lengths and .003 interaction lengths assuming that the field wires are Al, the sense wires are stainless steel and the gas is 50% A - 50% Ethane. The pulse height measurement will aid in detecting converted photons since they will appear as 2x minimum ionizing particles until the magnetic field separates the tracks.

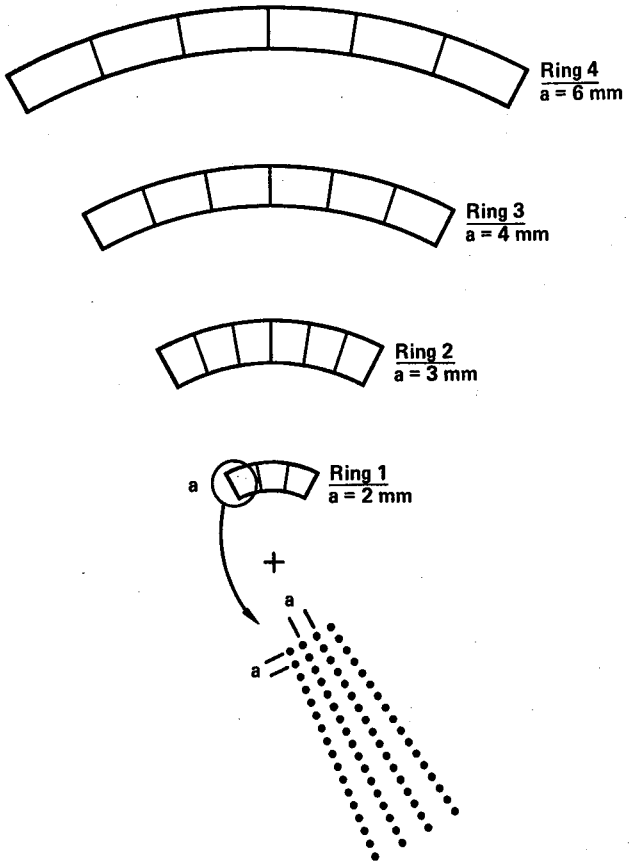

Fig. 4. Partical End View of Drift Chamber with Blow-up of Sector

B. Forward Tracking System

The forward direction covers the rapidity interval from 1.5 to 7.0 (the kinematic limit) corresponding to polar angles from $\theta = 26^\circ$ to $\theta = 0^\circ$ and typically has more than twice the number of charged particles per event as compared to the central region considered in the previous section. In addition, to measure a given $p_T = p \sin\theta$, larger momenta must be accurately measured. As in the case of the central detector, we assume an upper limit of 2 MHz per sense wire, a maximum drift distance of 2 mm, 3.6 charged particles per unit of rapidity and a 50 MHz interaction rate. Transforming from rapidity to distance from the beam line we find that the nearest sense wire in a plane normal to the beam line can never be closer than 20 cm to the beam line. To get to a larger rapidity (smaller θ) you have to go farther from the interaction point. As mentioned previously, a dipole field transverse to the beam line will aid in sweeping the particles from the beam direction in addition to measuring the particle momentum.

Figure 6 illustrates a forward detector which covers the rapidity interval from 1.5 to 5.5 (neglecting the bend of the dipoles) using two window frame dipoles to be used with the central solenoid. If a central dipole is used the smaller first dipole can be omitted since the central dipole provides the sweeping function of this magnet. Figure 7 shows the orientation of the sense wires in the plane perpendicular to the beam line. The design is a mini-drift type similar to the MPS chambers at Brookhaven with a 2 mm drift distance instead of the 3 mm drift used in

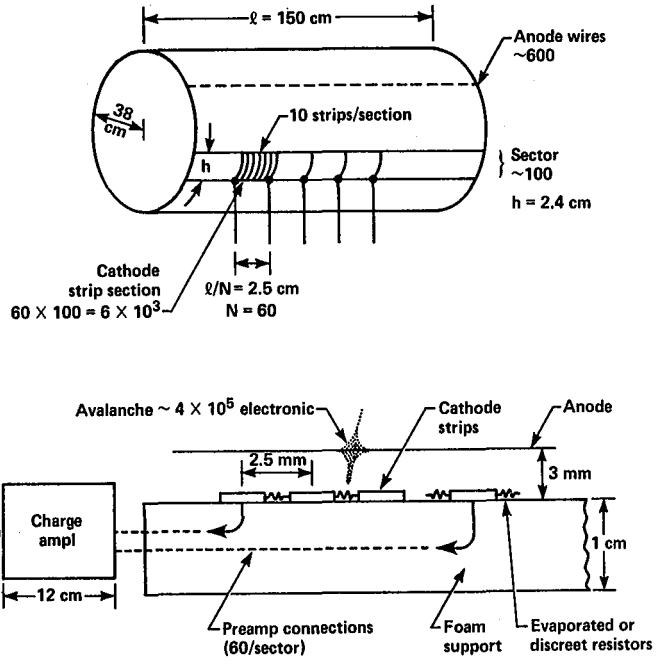

Fig. 5. Schematic Layout of Cathode Strip System

the MPS design. Each module would consist of 2X, 2U, 2Y, 2V planes or a total of eight planes. The tracking system would consist of six modules located as shown in Figure 6. Table 2 summarizes the sizes of the chambers and their sense wire counts for the system. Since charge division is not used, the electronic channels only need to measure the time, so a simple electronic system similar to the one used on the MPS chambers would probably be sufficient.

An identical forward detector system would be required for the other beam direction giving a total of 73.6K sense wires for the forward tracking system. The granularity is probably sufficient for detecting individual particles in high p_T jets since they have roughly constant size in rapidity and $\Delta\phi$. More troublesome is whether the system measures enough space points to carry out the pattern recognition efficiently in complex events. Detailed Monte Carlo calculations similar to the ones carried out for the central solenoid will have to be performed to show that this system is adequate. It certainly is a minimal system and even so it has ≈75K electronic channels.

Table 2

Module	Position	Area	No. of Sense Wires
1	4 m	1.6 x 1.6 m^2	3200
2	8 m	3.2 x 3.2 m^2	6400
3	12 m	4.8 x 4.8 m^2	9600
4	16 m	4 x 2 m^2	3600
5	20 m	5.6 x 2.8 m^2	6300
6	25 m	7.2 x 3.6 m^2	7700
		Total	36.8K

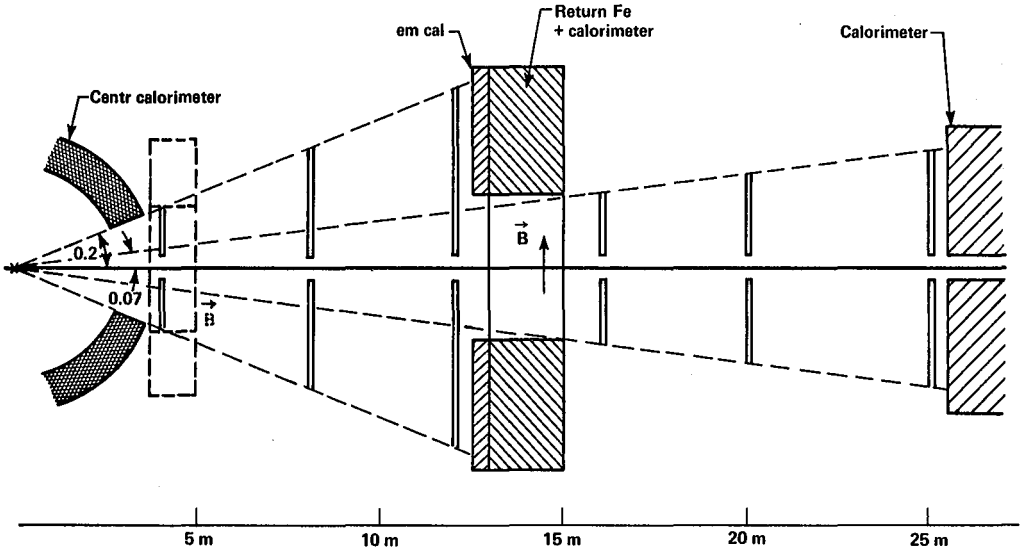

Fig. 6. Layout of Forward Detector Window Frame Magnet is 4 x 2 x $2m^3$, Second Magnet (Dashed Line) is $(2m)^3$.

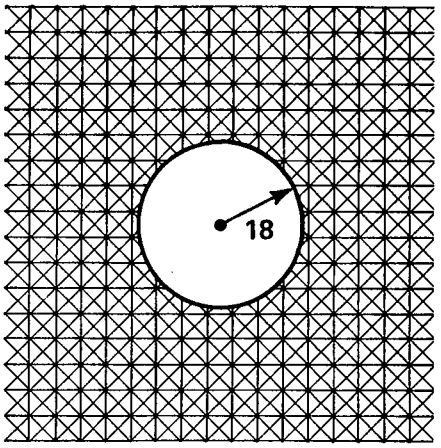

Fig. 7. Sense Wire Orientation: 2x, 2u, 2y, 2v planes

III. Vertex Detector

Constructing a vertex detector with $\sim$ 20 μ spatial resolution and an inner radius of a few cm which will handle the particle rates for $L = 10^{33}$ cm^{-2} sec^{-1} at 1 TeV is impossible with present day techniques. The only realistic possibility is to use a vertex detector with the collider optics adjusted to give a 2 cm long interaction region with a maximum luminosity of 10^{32} cm^{-2} sec^{-1}. If we take the point of view that the main trackfinding will be done by the central drift chamber and that the vertex detector will only be used as a vernier to identify isolated vertices, a reliable vertex detector can be constructed.

Silicon strip detectors can provide spatial resolution of 5 μ or better. The principal drawbacks to using them are their cost of \$300 per cm^2 for the strips and their readout electronics, their thickness in terms of radiation lengths, and their radiation damage sensitivity. Presently available devices can tolerate only 10^{13} minimum ionizing particles per cm^2 before their response is substantially reduced. At 10^{32} cm^{-2} sec^{-1} this corresponds to about six months to one year of operation before the detectors would have to be replaced. Clearly substantial R and D effort should be devoted to trying to produce radiation hardened devices. The Reticon readout electronics fails at about the same radiation exposure and should also be replaced with a radiation hardened system. Figure 8 shows a possible layout along with a more detailed sketch of one of the strips. About 700 strips would be required for the detector in the figure. The total radiation length, thickness of the strips, plus their holders is .03 - .05 at $\theta = 90°$.

A lower resolution option for a vertex detector is a high pressure drift chamber either of the microjet type developed by Va'vra[4] or the minidrift type under development at CERN. Figure 9 shows the possible wire configuration for both the microjet chamber and the minidrift type along with how they might be assembled to form a chamber. Either type will probably give 20 - 30 μ resolution at four to five atmospheres using seven micron diameter sense wires. The pressure vessel will be the major contribution to the radiation length thickness and can probably be limited to a fewer percent of radiation length. Substantial R and D are still required to make either type into a reliable vertex detector with 20 - 30 μ spatial resolution.

Another long range possibility for a vertex detector is a silicon drift chamber. It is a relatively new idea and initial tests will be carried out during the spring of 1983 by Rehak at BNL. It promises 5 to 10μ resolution over mm sizes with simple electronics. At an electric field of 1KV/cm the electron drift velocity in silicon is 13μ/nsec which should give good resolution with fairly simple electronics. The resolution will be dominated by electronic noise and will require fully depleted 300μ thick junctions to provide large enough signals to give 10μ resolution.

VI. Future Research and Development Needs

From the general discussion of the tracking group and from our attempt to outline a realistic tracking system for a 1 TeV $L = 10^{33}$ cm^{-2} sec^{-1} hadron collider several areas which would benefit substantially from increased R and D emerged. These areas are:

i. Longevity of Drift Chambers in a High Rate Environment

The TASSO Drift Chamber operating at PETRA seems to survive with current draws of up to 0.5μA per sense wire which is about a factor of 5 above what other large chambers will tolerate. In the designs considered above an additional factor of at least two is needed. A substantial effort must be devoted to understanding the failure mechanisms and what choice of gas, construction techniques, gas purification systems, etc. produces the most reliable chamber.

ii. Front End Electronics

Because of the sheer numbers of channels, using present day electronics, the electronic costs could easily represent 30 - 50% of the cost of a general purpose detector. In addition, because of the sense wire density the electronics must be integrated and mounted directly on the chamber since there is simply no room to bring out the signals on cables to the outside world. The present MPS integrated electronics is a step in the right direction. However, it only measures the drift time and not both the drift time and the pulse amplitude. In addition, it dissipates more than 400 mW/channel which implies more than 40 kW dissipation for the central tracking system leading to very substantial cooling and longevity problems. The other problem is radiation damage of the circuits. At present, conventional bipolar transistors are the most tolerant to radiation; however, they also consume the most power. Clearly, a coherent and national approach to the front end electronics should be the highest priority item on our R and D list.

iii. The Whole Vertex Detector Question

As mentioned in the section dealing with vertex detectors, there is a strong need to develop radiation hardened silicon strip detectors and their associated readout electronics. The high pressure gas drift chamber options still require considerable R and D before they are reliable detectors. For the future, the silicon drift chamber certainly deserves considerable effort.

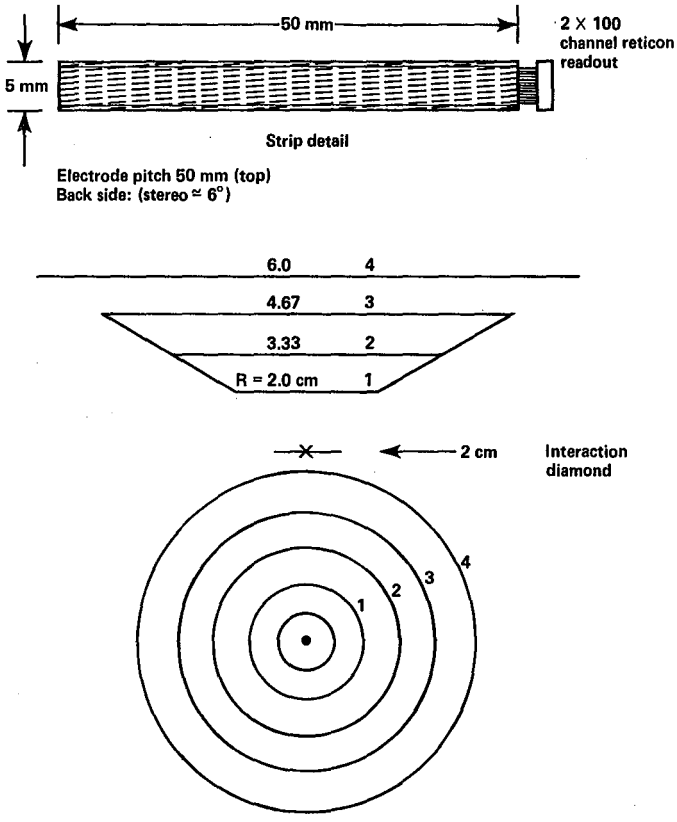

Fig. 8. Silicon Strip Vertex Detector

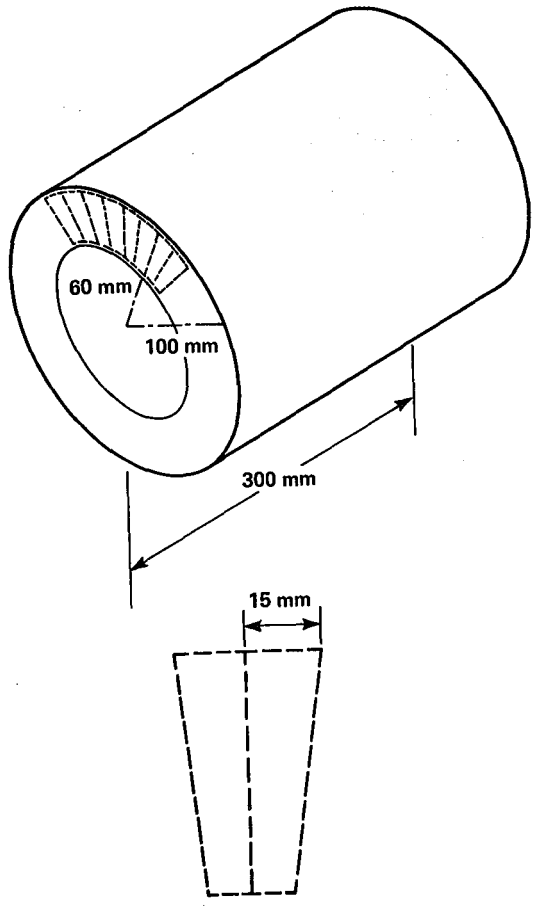

Fig. 9(a). Microjet Vertex Detector

iv. New Ideas

There should be substantial support made available to develop new ideas in detectors. This support should not be entirely attached to particular experiments or detector facilities. However, if there is not some attachment to experiment, one is likely to end up with solutions in search of a problem to solve.

Our future depends on our present R and D efforts and if we don't invest that effort now, we will rapidly lose what remaining initiative we have in particle physics experiments.

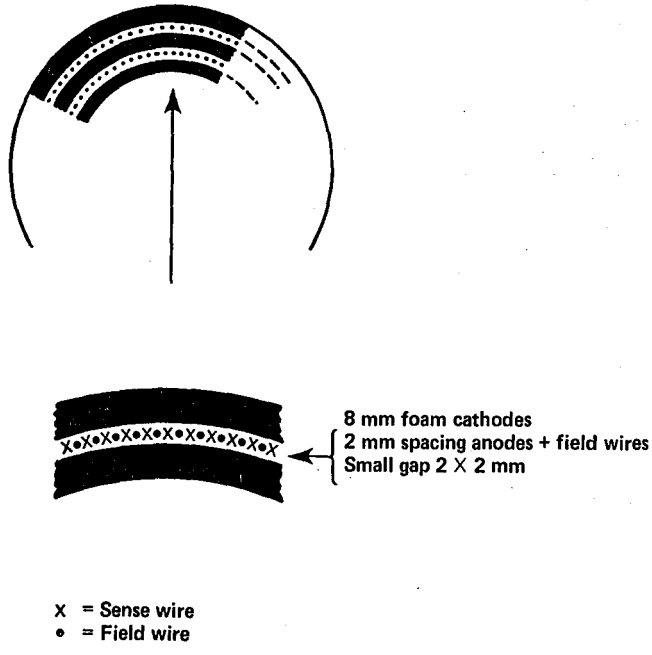

Fig. 9(b). Minidrift Vertex Detector

References

1. Hadron Hadron Collider Group Report, Proceedings of the 1982 DPF Summer Study on Elementary Particle Physics and Future Facilities.

2. E.D. Platner, The MPS II - A Tracking Detector System for Large High Rate Experiments, Proceedings of the 1982 CPF Summer Study on Elementary Particle Physics and Future Facilities.

   P. Schlein, et. al., The Performance of a 16000 Wine Mini-Drift MWPC System CERN-EP/82-198 Reprint.

3. W. Willis, The AFS Detector System at the ISR, this workshop.

4. J. Va'vra, Measurement and Simulation of the Drift Pulses and Resolution in the Micro-Jet Chamber, SLAC-PUB-3045, Jan. 1983.

CALORIMETRY

Bernard Pope

Working Group Summary Report

C. Baltay, L. Camilleri, B. Cox, M. Eaton, G. Finocchiaro,
M. Franklin, M. Gilchriese, H. Gordon, R. Gustafson, R. Huson,
J. Kadyk, R. Palmer, B. Pope, D. Ritson, R. Schindler
W. Selove, L. Spencer, G. Theodosiou, G. Wolf

I. Introduction

We judged that a limited goal that could be achieved in such a short workshop was an overall review of properties of various types of calorimeters with special attention being paid to the challenges of high luminosity and high energy. One difficulty that arose immediately was the perception that the subject could be approached from a number of directions; the performance properties of calorimeters, the physics requirements of calorimeters, various types of calorimeters. It was felt that the group should be divided up into subgroups corresponding to one of the axes of the (at-least-three-dimensional) matrix corresponding to these variables. Each subgroup would then have the task of filling in the two-dimensional matrix corresponding to the subtopic. It was almost as hard to do this as it is to describe!

There was some discussion on the most appropriate direction on which to subdivide. There are good arguments for "starting with the physics" or for comparing a single performance aspect (e.g. energy resolution) for a number of detectors but eventually it was decided that the most logical grouping was to form a subgroup for each of four types of detectors. These subgroups (corresponding to 'continuous' calorimeters, scintillation sampling, gas sampling and liquid sampling calorimeters) would have the task of reviewing the performance properties and, if possible, the physics requirements of each type of calorimeter. Special attention would be paid to new developments in each field with the hope being that areas requiring further study would be singled out for R and D effort.

Section II of this summary contains the reports of the four subcommittees, with particular attention being paid to new developments. Section III explores some limiting factors involved in experiments at high luminosities (or at high energies) and offers some examples of detectors capable of operating at the highest luminosities (energies). Section IV itemizes specific areas where substantial research and development work is needed. The conclusions of the group are stated in Section V.

II. Reports of Subgroups

A. 'Continuous' Calorimeters

A summary table comparing properties of continuous sampling calorimeters is given in Table 1. It is stressed that a direct comparison of all properties of these calorimeters is difficult to make and some of the entries in Table 1 are no more than educated guesses.

In addition to Table 1, this subgroup expressed the following opinions which were believed to hold for all calorimeters in this category. A spatial resolution of $\sigma \sim 5.6\ \text{mm}/\sqrt{E}$ has been measured for 1 cm segmentation placed at depth of 3.5 radiation lengths.[6] A reasonable approach would be to segment with pads of approximately 2 cm x 2 cm at this depth. The resolving power between two showers would then be approximately one pad width. Tower (and projective) geometry appears to be desireable in order to cope with high luminosities and the large multiplicities expected at high energy. Transverse segmentation (tower size) should be approximately 2 r.l. x 2 r.l. Longitudinal segmentation involving at least three samples is thought to be necessary. These continuous sampling calorimeters are most suitable for electromagnetic calorimeters. Using the segmentation suggested above, it is anticipated that π/e rejections at $\sim 10^{-3}$ could be obtained with any of these devices.

B. Scintillation Sampling Calorimetery

Table 2 summarizes the work of the subgroup studying scintillation calorimetry. Some of the entries in this table require some elaboration. Several groups are presently engaged in the development of fast scintillators and waveguides for calorimetery. Bob Palmer described a study in collaboration with the R-807 group of Bill Willis in which he enumerated the various factors contributing to the FWHM of the output pulse of the R-807 uranium-scintillator calorimeter. He measured the following contributions: scintillator (acrylic napthalene) 15 nsec, waveshifter (BBQ) 12 nsec, phototube 5 nsec, effects of shower depth and dispersion in the waveshifter 5 nsec. The overall FWHM thus predicted (by adding in quadrature) is about 20 nsec, in reasonable agreement with a measured value of 23 nsec. Palmer further studies possible improvements in these factors and measured the following: NE111, pilot U or polystyrene scintillator 1.5 nsec, BBOT waveshifter 5 nsec, RCA C31024 phototube 1 nsec. Combined with the shower fluctuations these improvements would suggest that overall FWHM's of 7 nsec are possible. W. Selove and G. Theodosiou also reported encouraging measurements of the light yields and attenuation lengths of fast scintillators and waveshifters.[7] This group used polystyrene doped with 1% B-PBD as a scintillator and experimented with BBOT and POPOP of various concentrations in Plexiglass as a waveshifter. Light yields for these materials were seen to be 20% higher than from NE110. Attenuation lengths were in the range of 80-140 cm and typical times (convolution of scintillator and waveshifter) were 5-6 nsec.

Another development, of particular interest for large area calorimeters were good time resolution properties are required, is a recent series of tests of vacuum photodiodes by the University of Pennsylvania group.[8] These devices, used with scintillators or scintillating glass, would provide good segmentation capability (especially longitudinally), have excellent gain stability, and could run with gates of 30 nsec or less. Such an array could be timed to better than a nanosecond by making special timing runs which would result in a map of timings for each tower. Coupled with a system of multiple gates (or perhaps flash ADC's) energy depositions from events overlapping within 10 nsec could be resolved.

	Lead Glass[1] (SF5)	Scintillation[2] Glass (SCG1-C)	BGO[3]	NaI	BaF_2[4]	Lead Glass/[5] Scint. Composite
Energy Resolution (Statistical Term Only)	$\frac{4.5\%}{\sqrt{E}}$	$\frac{1.1\%}{\sqrt{E}}$	$\frac{1\%}{\sqrt{E}}$	$\frac{1\%}{(E)^{\frac{1}{4}}}$	$\frac{1.7\%}{\sqrt{E}}$	$\frac{9.1\%}{\sqrt{E}}$
Typical Integration Time	40ns	100ns	300ns	250ns		40ns
Possible Integration Time	<10ns				<5ns	
Rad. Length	2.5cm	4.35cm	1.12cm	2.5cm	2.1+cm	3.2cm
Abs. Length	42cm	45cm	23cm	41cm		43cm
Light Output Relative to SFS	1	5.1	10^3	10^4	700	9.5
Radiation Damage (10% loss)	2500rads	8.5×10^4rads	10^4-10^5rads	10^5rads	"Most Resistant Scint."	2500rads
Cost per m^2 per 20 r.l.	$97K	$170K	$2.2M	$1.0M	$400K	$70K
Photodiode?	X	✓	✓	✓	N/A	✓
Number of cells/m^2 Assuming 2 r.l.x2 r.l.	400	130	2000	400	570	250
Problems, Comments	Radiation Damage	New Technique long rad. length	Cost, Temp. Dependent	Hygroscopic	New Technique, Complicated Readout	More like a sampling device

TABLE 1

Performance Properties of Continuous Sampling Calorimeters

C. Gas Sampling Calorimetry

The report of this subgroup is summarized in Table 3. Again, comparisons are difficult and some assumptions have to be made for specific geometries. The essential conclusions are that MWPC systems have the advantage that their timing can be improved by the use of faster gases while non-linearities can be reduced by a reduction in gain.

D. Liquid Ionization Calorimeters

These calorimeters consist of alternating metal plates and liquid gaps. Alternate plates are held at different voltages. Ionization produces electrons in these gaps inducing a current whose time distribution is shown schematically in Figure 1a. Clipping of such a signal, for instance to 1/4 of its length, loses only 50% of the charge (Figure 1b). The drift velocity depends on field gradient as shown in Figure 2 for argon, methane and a mixture. High purity is required for the use of methane or its mixtures. What complications are involved are not yet known.

The induced charge in argon is about 4000 electrons per mm of gap per minimum ionizing particle. Amplifier noise varies as the square root of the gap capacitance and bandwidth. Signal-to-noise thus varies as $\text{gap}^{-3/2}$ $\text{area}^{-1/2}$ $\text{time}^{1/2}$. There is thus a trade-off between low noise and short pulse time. For example, the calorimeter used by the TASSO collaboration[11] has low noise but a 1.4μs pulse whereas the small gap fast SPS calorimeter has 25-50 ns pulses but much higher noise.[12]

Table 4 summarizes the properties of four arbitrarily selected examples; the first two of which have operated and the others are only proposed at this time. In summary the advantages of these calorimeters are a) very good radiation resistance allowing its use in the forward direction, b) ease and stability of calibration allowing realization of high resolution at high energies, c) cracks are not needed for light shifters etc., d) they will work in any magnetic field. Disadvantages include: a) relatively noisy especially if fast pulses are required, b) cryogenic temperatures require thermal insulation which is space-consuming and technically complicated, c) care is needed to avoid shorts.

III. Limiting Factors at High Luminosity and High Energy

Figures 3a and 3b show the results of tests performed by the E-705 collaboration at Fermilab in which samples of SF5 lead glass and SCG1 scintillating glass were exposed to ionizing radiation. It has been determined that a dose of 8.5×10^4 rads will cause a 10% loss in transmission for scintillation glass in comparison with 2.6×10^3 rads which will cause a similar loss of transmission in lead glass. Clearly operation of these detectors at high luminosity machines might pose the problem of radiation darkening simply from the luminosity of the machine i.e. excluding backgrounds caused by beam losses. In order to examine these effects we have developed a simple model for the production of particles as a function of angle, energy and of course luminosity. The model is derived from experimental observations by the UA2 group at the SPS pp collider with assumed scaling of the cross section and rise of the rapidity plateau. The results are shown in Figure 4 as a function of energy and angle for an instantaneous luminosity of 10^{33} cm^{-2} sec^{-1}. Also shown on the curves are estimates of the amount of radiation that would be required to produce a 10% drop in transmission for various sensitive detectors. It can be seen from

TABLE 2

SCINTILLATOR SAMPLING CALORIMETRY

1. Time Resolution

	Width (FWHM)	Resolution (Jitter) (for hadrons)	Gate Width
a) Existing Systems	25ns	±2ns	70-100ns
b) Fast Scint/Waveshifter	8ns	±2ns	20ns
c) Diode Readout	$\leq$8ns	$\leq\pm$1ns	20ns

2. Space Resolution-(Electromagnetic)

	10 GeV	100 GeV	
(Pb or U)/Waveshifter	1cm	0.5 cm	(Diode readout is 50% worse)
1 cm scint. strips or wire plane sampling at 4 r.l.	0.2cm	0.2cm	

3. Space Resolution-(Hadronic)

	10 GeV	100 GeV
Fe	3cm	2cm
U	2cm	2cm

4. Energy Resolution (To at Least 100 GeV)

EM($\frac{1}{4}$ r.l. sampling) $14\%/\sqrt{E}$ Hadronic: Iron (1") $70\%/\sqrt{E}$ Uranium(3mm) $35\%/\sqrt{E}$

5. Cell Size

Coupled to shower size

Towers E-M > $2\times2cm^2$

Hadrons > $5\times5cm^2$

6. Calibration and Stability

Present systems 1%-2%

Diode readout: Needs R & D, but could be <1%

7. Radiation Damage or Other Deterioration

Acrylic is bad (Kienzle; R807; NIM 155, 517 '79)

UA2: 4% Down in 1 year

Polystyrene at 10cm and 2×10^5rad have 10% light reduction

8. Magnetic Field

PMT's shielded to ~1kgauss

Diodes less sensitive (more R & D needed)

9. Dynamic Range and Linearity

no problem to 100 GeV hadrons
40 GeV electrons
(No Measurements Yet Beyond)

10. Cost

a) \$100K to \$200K/m^2
(R807) (E609)

b) Segmentation Costs
1) considerable for mechanically separate towers
2) minimal for diodes

TABLE 3

PROPERTIES OF GAS SAMPLING CALORIMETERS

	MWPC and Proportional Tubes	Saturated Avalanche Mode	Streamer Tubes	HPC (High[9] Density Projection Chamber
Minimum Thickness/Layer	0.7 cm	0.7 cm	0.5 cm	0.9 cm
Pulse Width	200 ns (with faster gas perhaps 50 ns)	200-400 ns	300 ns	3-5 μs
Time Jitter of Rise Time	20 ns (perhaps 10 ns)	20 ns	20 ns	no fast trig signal
Maximum rate for 1 TeV shower hitting same spot	gain 10^5 => 1 MHz gain 10^4 => 1 MHz	1 MHz 10 MHz	1 MHz	~30 KHz
Lifetime (assume 10^{17} e^-/cm)	10-100 years	10-100 years	10-100 years	>10 years
Non-linearity	10% at 100 GeV reduce gain => 10% at 1 TeV	10% at 100 GeV	10% at 20 GeV	no saturat
Energy Res $\frac{n}{}$ for 2mm/3mm/6mm of lead	$\frac{13\%}{\sqrt{E}}$, $\frac{16\%}{\sqrt{E}}$, $\frac{22\%}{\sqrt{E}}$	$\frac{11\%}{\sqrt{E}}$, $\frac{13\%}{\sqrt{E}}$, $\frac{19\%}{\sqrt{E}}$	$\frac{20\%}{\sqrt{E}}$ for 7mm lead	$\frac{11\%}{\sqrt{E}}$, $\frac{13\%}{\sqrt{E}}$, $\frac{19}{\sqrt{E}}$
Rad, Length	2.7, 2.0, 1.3	2.7, 2.0, 1.3	2.0, 1.6, 1.1	3.3, 2.3, 1.
Stability	2%	1%	1%	1%
Effect of Magnetic Field	B perp. =>no effect B parallel => $\frac{\Delta E}{E}$ X 1.4	Same	No Effect	Require $B_\perp \cdot L$ <20 Gauss
Cost per m^2 per layer	$500	$500	$350	
Cost of electronic channel	$25-50[10]	$25-50	$20-50	

TABLE 4

PROPERTIES OF LIQUID CALORIMETERS

	TASSO[11]	R-806	SPS I-144[12]	I-144 + Methane
Material	A/Pb	A/Pb	A/U	A + CH_4/U
Gap	5 mm	2 mm	1 mm	1 mm
Plate Thickness	2 mm	1.5 mm	1.5 mm	1.5 mm
Rad. Length	2 cm	2 cm	0.6 cm	0.6 cm
Abs. Length	60 cm	60 cm	20 cm	20 cm
Volts/mm	0.4 KV	1 KV	-2 KV	-2 KV
Collection Time	1400 ns	600 ns	50 ns	25 ns
Position Resolution EM/Hadronic	3 mm	3 mm	1 mm/5 mm	1 mm/5 mm
Energy Resolution EM/Hadronic	$\frac{9\%}{\sqrt{E}}$	$\frac{12\%}{\sqrt{E}}$	$\frac{9\%}{\sqrt{E}}/\frac{28\%}{\sqrt{E}}$	$\frac{9\%}{\sqrt{E}}/\frac{28\%}{\sqrt{E}}$
Noise per 50 cm^2 EM/Hadronic	5 MeV	10 MeV	100 MeV/800 MeV	30 MeV/300 MeV
cost/m^2	$75K[13]	$75K[13]	?	?

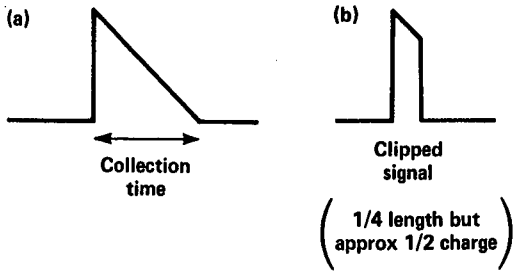

Fig. 1. Charge Collection in Liquid Argon

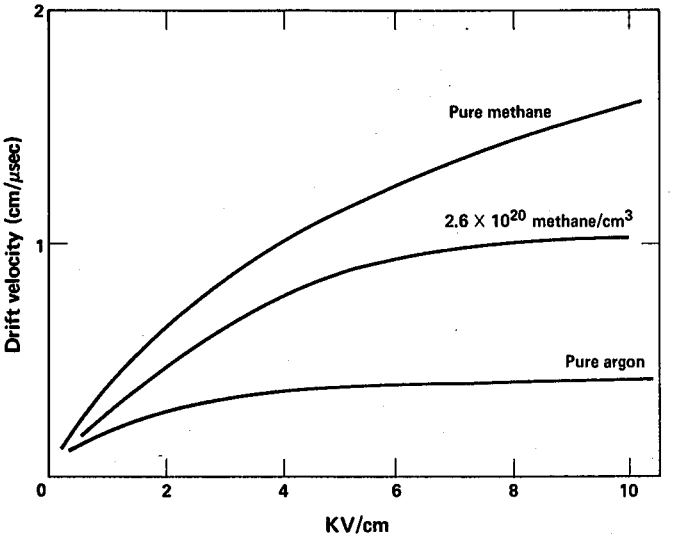

Fig. 2. Drift Velocity vs. Field Gradient

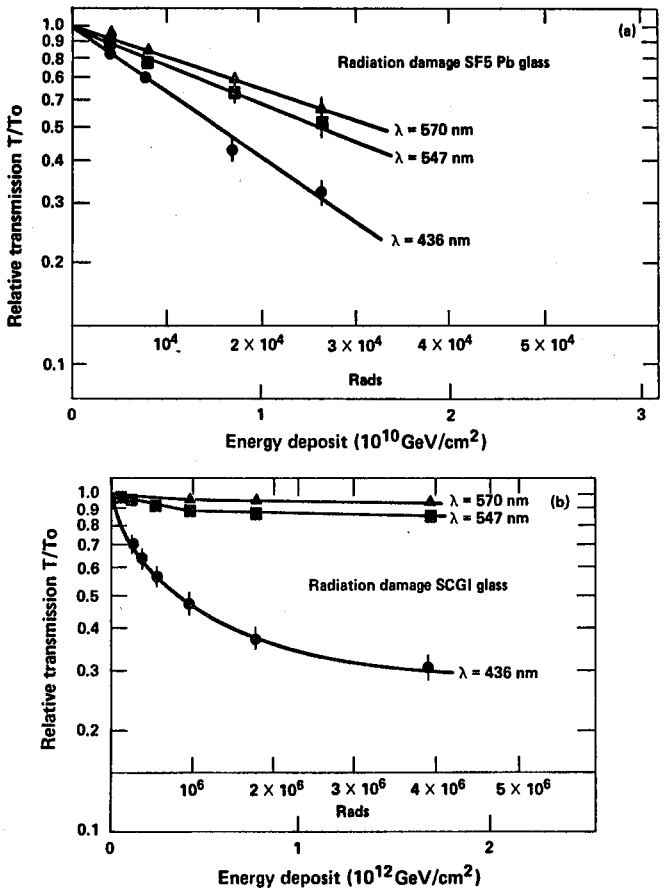

Fig. 3. Radiation Damage (E-705 Collaboration)

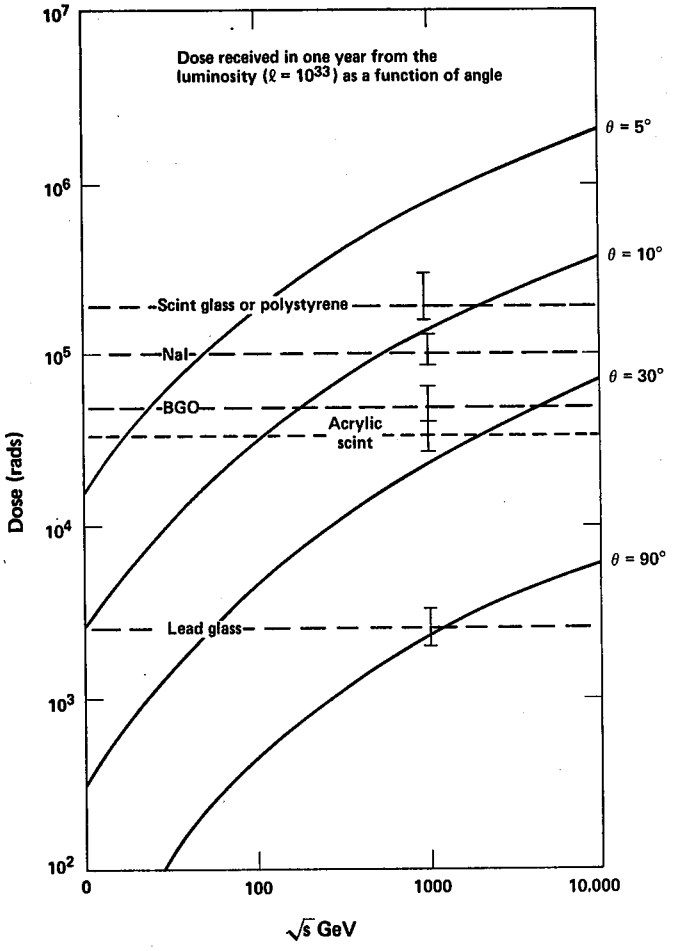

Fig. 4. Dose Limits in Detector Materials

Figure 4 that even for perfectly clean machines there is a limit on the use of these detectors as a steep function of angle and less- steep function of energy. This conclusion is quantified in Table 5. In addition it is cautioned that the estimates of "luminosity-induced" doses for the CERN ISR were low by about a factor of 6 from those that were actually observed.

In a similar way we have attempted to use the integration times for detectors given in Tables 1-4 in order to place further limits on detectors being used at high luminosity machines. These additional constraints are also itemized in Table 5. There is a considerable degree of subjectivity in the conclusions of Table 5.

While Table 5 indicates the angular regions where certain detectors would be able to operate at high luminosities, two of the subgroups chose to 'design' a detector capable of operating at luminosities of 10^{33} cm^{-2} sec^{-1} and energies at 20 TeV. These studies could be taken as an "existence proof" or certain classes of detector and, while they are certainly not definitive or exhaustive proposals they indicate some of the choices that will have to be made. The work is summarized briefly in the next two paragraphs.

The subgroup on gas sampling calorimetery proposed a detector using proportional tubes for the central region i.e. from θ = 30° to 150°. Using 6 mm of lead sampling it is estimated that an electromagnetic energy resolution of $\frac{\Delta E}{E} = \frac{22\%}{\sqrt{E}} + 2\%$ could be obtained. In order to keep saturation below 10% at 4 TeV (maximum energy of a jet) a gain of 10^3 would be used. Using a pulse width of 50 nsec, pile-up would be recognized by recording the time of the leading edge of pulses. This would give a resolving time of about 10 nsec. The center of gravity of the shower could be localized to better than 5 mm. This would be done at three longitudinal depths (each 10 r.l.) giving a measurement of the direction of a photon with an accuracy of about 15 mrad. The hadron calorimeter would also be composed of proportional tubes with 5 cm iron sampling. This would give a hadronic energy measurement of $\frac{\Delta E}{E} = \frac{100\%}{\sqrt{E}} + 2\%$. Tower sizes would be about 300 cm^2 with a total thickness of 12 interaction lengths subdivided longitudinally 3 times. It is estimated that the center of gravity could be located to about 1 cm and the direction of a jet could be measured to 5 mrad. Assuming a bunched beam structure (3 nsec long bunches separated by 10 nsec), 100 mb cross section and a luminosity of 10^{33} cm^{-2} sec^{-1} implies 5 events in a gate time of 50 nsec. The probability of having 2 events overlap would be considerably reduced by imposing a transverse energy requirement of $E_T \times \sin\theta > 2.5$ GeV. Total cost[13] of the detector is estimated to be \$52K per m^2.

A detector proposed by some members of the scintillation sampling calorimeter subgroup[14] is shown in Figure 5. The basic characteristics are as follows. The electromagnetic calorimeter would consist of Barium Fluoride (see later) or perhaps scintillating glass. Three modules in depth would give a total of 30 radiation lengths. The hadron calorimeter would be made of fast scintillator/iron sampling. Polystyrene would be used with vacuum photodiode readout. Three modules in depth would correspond to 10-12 absorption lengths. The essential feature of the detector would be to do very fast gating (10 nsec) accepting that this may degrade the energy resolution because slow neutrons would not be collected. With careful relative timing and mapping within a sector (group of towers) one can

TABLE 5

SUITABLE CALORIMETERS FOR HIGH LUMINOSITY

(At $\sqrt{s}$ = 1 TeV)

Detector	Effect of Rad. Damage	Effect of Integ. Time
Lead Glass	X	N/A
Scint. Glass	θ>10°	θ>30°
BGO	θ>30°	X
NaI	θ>20°	X
BaF_2	θ>10°?	θ>10°
Acrylic Scint.	θ>40°	θ>40°
Polystyrene Scint.	θ>10°	θ>10°
Polystyrene + P.D.	θ>5°?	θ>5°
Prop. Tubes (Fast Gas)	✓	θ>30°
Sat. Avalanche	✓	X
Streamer Tubes	✓	X
High Dens. Proj. Chamber	✓	X
Liquid	✓	θ>10°
Liquid Argon + CH_4	✓	✓?

Conclusions	Region	Candidate
	θ<5°	LA + CH_4
	θ>5°-10°	Polystyrene, BAF_2?, LA
	Central	Scint. Glass, Prop. Tubes

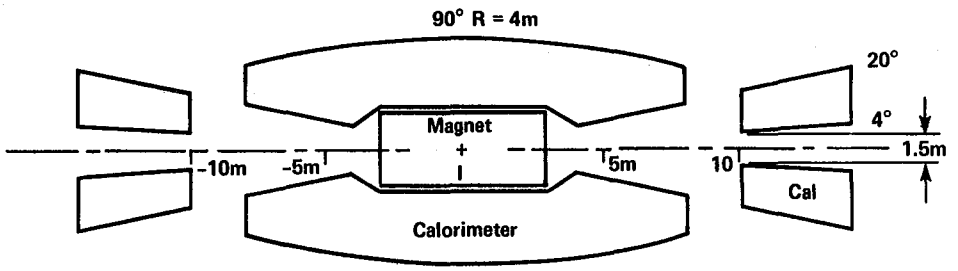

Fig. 5. Sampling Calorimeter Geometry

separate individual events in time using transverse momentum information of individual tower segments. The number of towers would be ~10,000 (each would be 10 cm x 10 cm). A magnet is assumed to cover the central region and the total cost is estimated as $100 M.

Two experiments which actually constitute "existence proofs" for calorimetric experiments running at the highest existing luminosities at colliding beams are ISR experiments R-110 and R-807. R-807 (the Axial Field Spectrometer) has compared triggering rates and cross sections for various triggers at two very different luminosities; a very high luminosity (1.4×10^{32} cm^{-2} sec^{-1}) and a relatively low luminosity (3×10^{30} cm^{-2} sec^{-1}). A jet trigger (E_T in a limited region (cluster) being greater than 9 GeV) was seen to trigger at a rate 50% higher with the high luminosity run. A total energy trigger (E_T > 28 GeV) had a trigger rate for the high luminosity run equal to 5.5 times the rate for the low luminosity run. An analysis of the timing of counters near the beam pipe corroborates the pileup at high luminosities. The group strove to make a direct comparison of cross sections after minimal cuts. For this comparison they chose the jet trigger since a definite signature could be expected. After making cuts on the time of calorimeter hits (20 nsec) the group is confident that they can extract an unbiased jet cross section.

The CERN-Oxford-Rockefeller Collaboration (R-110) has used timing information[15] to deal with multiple event pileup at luminosities up to 6×10^{31} cm^{-2} sec^{-1}. Thirty-two lead-scintillator shower counters and a barrel hodoscope covered ±1.1 units of rapidity and gave times from the average of both ends. These times were found to cluster within a 12 nsec wide window. Multiple interactions could be distinguished on an event-by-event basis by searching for secondary clusters of 2 or more counters falling outside the most populated window. The cross section for a total energy trigger was found as a function of luminosity for luminosities in the range $1.5\text{-}6.0 \times 10^{31}$ cm^{-2}sec^{-1}. The raw data were seen to show strong luminosity dependence with the "cross section" at the highest luminosity being 4.5 times the value extrapolated to L=0. By using the timing information to reject multiple events it was seen that 3/4 of the events at the largest luminosity had an interaction within the trigger resolving time. Obviously for this total energy trigger, one could not successfully insist on single interactions for luminosities beyond 10^{32} cm^{-2} sec^{-1} without better time resolution. The technique could however be extended to individual calorimeter cells. By contrast, a trigger looking for two clusters of $\Delta\phi = 12^o$ by $\Delta\eta$ = ±1.1 units had a maximum 10% contribution due to multiple events at the highest luminosity.

IV. Suggestions for Research and Development

In the course of the workshop several areas were mentioned where either R and D work was actively under progress in a field or it was urgently needed to determine the performance properties of a detector. We itemize some of these promising projects in this section. A brief description of the area is given in some of the cases.

Barium Fluoride

An exciting development for electromagnetic calorimeters is being pursued by D.F. Anderson et al.[4] at CERN coupling BaF_2 with a low pressure wire chamber.[16] This device is shown schematically in Figure 6. There is a fast scintillation component in the UV region (2000-2500 A) which is quite fast (100-500 psec). The wire chamber consists of a metallic cathode surface coated with a liquid layer of TMAE.[17] This layer is deposited by evacuating the chamber and then allowing the vapor of liquid TMAE to enter. The chamber is then filled with ~3 Torr of pure isobutane. The low pressure counter has a gain of $\sim 10^6$ with little time jitter and a time response of 540 ps. Such chambers have been operated in large magnetic fields. Although the quantum efficiency of the TMAE photocathode is only 1%, the number of photoelectrons/GeV is ~3000 which should lead to an excellent energy resolution of better than $2\%/\sqrt{E}$. There has only been a test of a single 26 mm thick crystal but within this year a full electromagnetic calorimeter will be built and tested at CERN. The cost of the BaF_2 is about 3 cents/cc for the raw materials and will probably cost $1/cc for crystals.

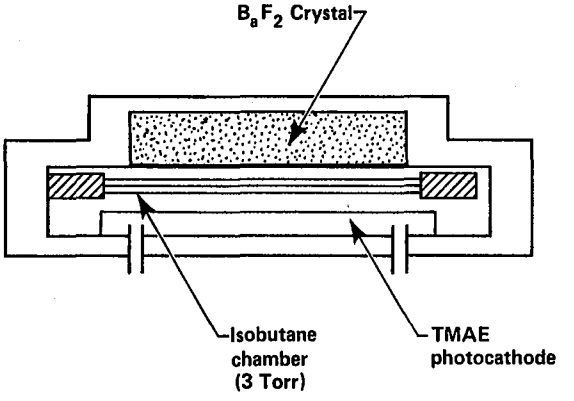

Fig. 6. Barium Fluoride Chamber

During discussions at this workshop two new ideas emerged. First it was suggested that a wavelength shifter could be used (either in the crystal or in a bar adjacent to the crystal) to shift the fast UV component to a longer wavelength so that conventional photodetectors could be used. Second a UV sensitive secondary emission layer of CaF or CeF could be deposited on the crystal. This could be the cathode of a photodiode.

Thallium Formate

Some research is underway on heavy liquids which would replace lead glass as a continuous sampling calorimeter. Thallium Formate ($Te(HCO_2)$) is one such liquid. Its properties are as follows: density = 3.27 gm/cm^3, refractive index = 1.59 and radiation length = 2.57 cm. It has about the same transparency as lead glass but with a 30 nm lower edge. It appears to suffer very little radiation damage, 3×10^6 rads being reported to have had no effect. Its cost is comparable with and probably lower than lead glass but suffers from the disadvantage that it is a toxic liquid.

Xenon

Xenon has been suggested as a liquid scintillator for electromagnetic calorimetery at 180°K. Its density is 3.1 gm/cm^3 and radiation length is 2.8 cm. Its emission spectrum is in the range 150-185 nm with 3 time components (3 ns, 22 ns and 700 ns). Its present cost is about \$4/cm^3 and appears to give approximately the same output as Sodium Iodide.

Use of Methane in Liquid Argon[12]

Faster Scintillator/Waveshifter[7]

Shorter Radiation Length Scintillating Glass

One disadvantage of the new scintillating glass described above[2] is its significantly longer radiation length. Studies are at present underway to reduce this value.[18]

Radiation Resistant Lead Glass

R and D is presently underway by a variety of techniques to improve the resistance of lead glass to radiation.[19] One such technique is the addition of small amounts of Cerium to the melt.

Photodiodes[8] and Phototriodes[20]

Silicon Detectors

V. Radeka has suggested that silicon detectors may be an appropriate device for small areas. The signal is about 13 times higher than that from liquid argon and the signal/noise is 15 times higher. The charge collection time is about 20 ns (for a typical thickness of 300 μ). Ninety-five percent of this charge would be collected with 10 ns. The present cost is estimated as \$20/gm for the material with an additional \$20-40/gm for processing. This would give a total estimated cost of \$100K/m^2 per layer.

Bismuth Silicate[21]

V. Conclusions

I hesitate to use the word 'conclusions' for such a short workshop. Clearly the review of calorimetry undertaken in this report illustrates a rapidly changing field and a strong research effort which has also been reported in many previous reviews.[22] The particular emphasis of this workshop was to explore the challenges posed by high luminosities and high energies.

The difficulties introduced by pileup problems and by high radiation doses were certainly brought out clearly by this workshop. Considerable care will have to be taken with spatial segmentation and with time resolution in order to reduce the problems caused by high rates and high multiplicities. Some energy resolution may have to be sacrificied.

However the consensus of this working group was that it appeared that a calorimeter capable of handling luminosities of 10^{33} cm^{-2} sec^{-1} with (almost) 4π coverage could be built. Such a detector will have many more channels (an order of magnitude?) and will cost considerably more (factor of 2-5) than present day detectors.

Calorimeters will become increasingly important at higher energies. As the statistical term drops (proportional to 1/E), systematic effects will dominate. Sampling calorimeters will suffice and sampling can become more coarse. Paradoxically it may be that calorimeters will become cheaper!

One final recommendation: the short duration of this workshop prevented an in-depth study of the field of calorimetry. The end effects inherent in defining the problems and laying out the guidelines reduced the time even more. Perhaps it would be appropriate to create a "commission" with the charge of centralizing information available on calorimeters, recommending R and D for promising projects, "designing" a detector capable of performing at high luminosity and/or high energy, arranging topical workshops or conferences, and periodically reporting to the high energy community.

References

1. J.S. Beale et al., Nucl. Instrum. Methods 117, 501 (1974).

2. B. Cox et al., Fermilab preprint FNAL Conf. 82/75-Exp.

3. M. Cavalli-Sforza, SLAC Conference on Instrumentation for Colliding Beam Physics (1982), p. 216.

4. D.F. Anderson et al., (Charpak group) submitted to the Vienna Wire Chamber Conference, February 1983.

5. C. Cozza et al., University of Padova preprint, submitted to Nuclear Instruments and Methods.

6. B. Cox et al., Fermilab preprint FNAL Conf. 82/76-Exp.

7. W. Kononenko et al., Nuclear Instrum. Methods 206, 91 (1983).

8. W. Selove, G. Theodosiou, Nucl. Instrum. Methods 186, 585 (1981). See also W. Kononenko et al., University of Pennsylvania Report UPR 0098E (1982).

9. O. Ullaland, SLAC Conference on Instrumentation for Colliding Beam Physics (1982) p. 212.

10. $10 seems possible, see Ball et al., Nucl. Instrum. Methods 197, 371 (1982).

11. G. Wolf talk at this workshop. See also A. Ladage, SLAC Conference on Colliding Beam Physics (1982) p. 180.

12. W. Willis talk at this workshop. Letter of Intent to the SPSC, C.W. Fabjan et al., (CERN/SPSC 83-8 I 144 (1983)).

13. European generated numbers: multiply by 2?

14. W. Selove and G. Theodosiou, private communication.

15. J. Linnemann, R-110 Memo 131 (1983).

16. D.F. anderson, Phys. Lett. 188B, 230 (1982).

17. D.F. Anderson IEEE transactions on Nuclear Science NS-28, 842 (1981).

18. Ohara Optical Glass, Inc., B. Cox, private communication.

19. M. Marx, private communication.

20. M.D. Rousseau, Opal Collaboration at LEP.

21. M. Kobayashi, Nucl. Instrum. Methods 205, 133 (1983).

22. See for example: SLAC Conference on Instrumentation for Colliding Beam Physics (1982), Proceedings of the SLC Workshop on Experimental Use of the SLAC Linear Collider (1982), Proceedings of the 1982 DPF Summer Study on Elementary Particle Physics and Future Facilities. See also the excellent review "Calorimetry in High Energy Physics" by C. Fabjan and T. Ludlam, Annual Review of Nuclear Science (1982).

TRIGGERS

Mel Shochet
Working Group Summary Report

T. Carroll, W. Hoogland, R. Johnson, R. Kass, J. Linneman, S. Loken,
R. Majka, M. Ronan, M. Shochet, M. Tannenbaum, B. Willis, J. Zweizig

The major task of the Trigger Group was to examine the possibility of trigger systems which could operate at a luminosity of 10^{33} cm^{-2} - sec^{-1}. We concentrated on two luminosity related problems: the fast trigger decisions which must be made because of the high interaction rate, and the effect of multiple interactions within the integration time of the detector. Little time was spent on the higher trigger levels where the final selection of events to be written on tape is made, because the difficulty of the problem is very dependent on the specific signature of the physical process under study. If one is looking for events with multiple large $P_\perp$ leptons and jets and significant $\vec{P}_\perp$ imbalance, then the event selection will not be very difficult. On the other hand, if the events of interest are characterized by low $P_\perp$ leptons and hadrons and little $\vec{P}_\perp$ imbalance, then the signal to noise will be poor and the event selection problem will be an extremely hard one.

We concluded that a trigger system for high luminosity operation can be constructed. The system presented here as an existence proof, while not necessarily optimal, will, we believe, work. It is a multi-level trigger system, where the number of events which can be retained at any level is only limited by the requirement that the deadtime at the next level not be excessive. Before describing the overall system, we first discuss multiple event pile-up, tracking, electron identification, and transverse momentum imbalance.

Multiple Event Pile-Up

At a very high luminosity collider, a substantial fraction of events will contain more than one interaction within the integration time of the detector. For example, in a DC machine with a luminosity of 10^{33} cm^{-2} - sec^{-1}, and with an inelastic cross-section of 50 mbarn, interactions occur with an average separation of 20 nsec. For ten percent of the interactions there will be another interaction within 2 nsec of the first.

A crucial question is how the presence of multiple interactions affects trigger decisions. A convolution equation can be written which gives the distribution in transverse energy (E_T) for multiple events in terms of the E_T distribution for a single event. If $P_N(E_{T_{min}})$ is the probability that N overlapping events give a transverse energy $E_T > E_{T_{min}}$, then

$$P_N(E_{T_{min}}) = P_1(E_{T_{min}}) + \int_0^{E_{T_{min}}} dE\, P_1'(E)\, P_{N-1}(E_{T_{min}}-E)$$

The probability of obtaining at least $E_{T_{min}}$ from N events is equal to probability that one event provide the necessary E_T plus the product of the probability that N-1 events give $E_{T_{min}}-E$ and the differential probability that the N^{th} event give E. Using this equation and $P_1(E_T)$, probability distributions for any N can be obtained.

Figure 1 shows a probability distribution, $P_1(E_T)$, which is exponential at low E_T. The effect of multiple interactions within the integration time is seen to be extremely large and to grow with increasing E_T. The difference between low luminosity and an average 5 events per integration time is almost six orders of magnitude at E_T=20 GeV. Fortunately, however, the cross-section at large E_T has a power law behavior. Hence the effect of multiple interactions does not grow with increasing E_T, but rather the effect is a uniform shift in the E_T scale. This shift is equal to the mean number of interactions multiplied by an average E_T per interaction.

Such a shift can be minimized if the incremental E_T from extra interactions is low. This can be accomplished if a cluster algorithm is used in the trigger. Figure 2 shows an ISAJET simulation of hadron jet production. The jet cross-section is increased greatly from its low luminosity level if the full solid angle E_T produced my multiple interactions is included. If E_T is added only from the solid angle near the jet, the effect is greatly reduced. If, in addition, only those calorimeter modules containing E_T > 1 GeV/c are included, the increase in cross-section becomes very small.

This method for limiting the effect of multiple interactions is used in our trigger system.

Central Tracking

Large transverse momentum tracks can be found quickly and easily because of the structure chosen for the central drift chamber (see Tracking Group report). The narrow drift distance not only gives rapid charge collection (<100 nsec), but allows us to use drift cells as simple hodoscope elements. Since the trigger system does not use drift time, the hardware consists of simple digital coincidence logic.

The use of 4 to 6 planes in each of three radial regions provides a local minimum P_T of 4 GeV/c which is determined by the cell size. The minimum P_T for a track can be varied from 4 GeV/c to 20 GeV/c when the local track segments are placed in coincidence. This information is available in a few hundred nanoseconds and thus can be used in the earliest trigger levels. If a few layers of drift wires are equipped for charge division, then the track can be associated with a single calorimeter tower of the first trigger level.

Muon Tracking

We assume that the detector is 8mx8mx10m long and that we have muon detection on the four side walls. If these are four planes of 2.5m long wires with 1cm drift space, then the muon system contains approximately 25,000 wires. In a half cell staggered wire arrangement, the first signal appears within 100 nsec of the interaction. A muon can be correlated with a large P_T inner track and with a single calorimeter module if two muon planes are equipped with charge division read-out.

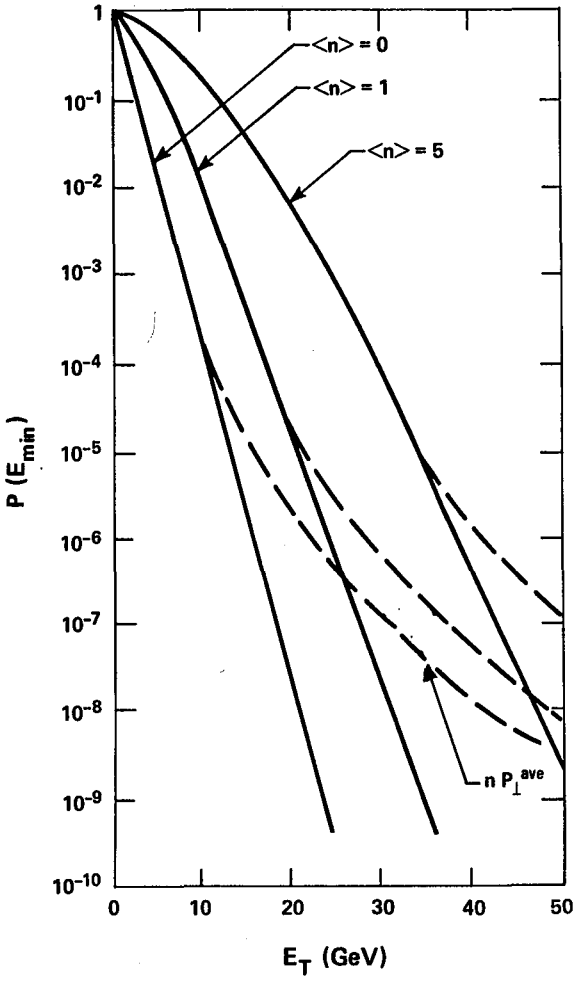

Fig. 1. Probability of exceeding E_{min}^{T} for different event overlaps

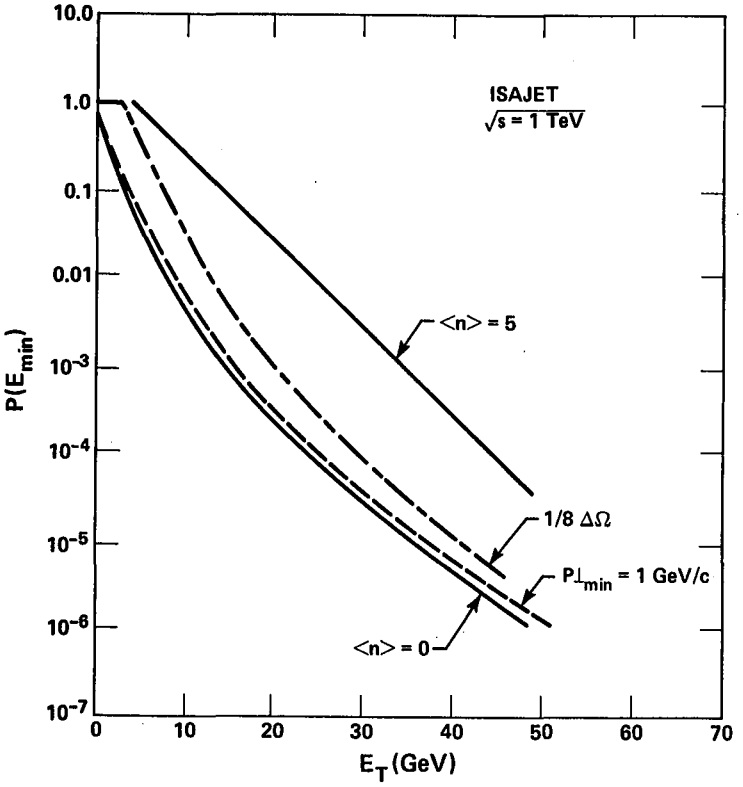

Fig. 2. Isajet Simulation of Jet E_T Probability Distribution

Electron Identification

We have considered two methods for electron identification: traditional calorimetric separation and active electron tagging using transition radiation detectors.

(1) Calorimetric Separation of Electrons

In the early levels of the trigger, the background comes from the uniformly distributed low P_T particle production as well as from particles associated with jets of transverse momentum ~10 GeV/c. Events containing jets of much larger P_T will be retained in the first few trigger levels whether or not there is an electron present. The low P_T particles are not a serious contaminant since they typically deposit less than 1 GeV/c transverse energy in a single calorimeter module. The low to moderate P_T jets are so wide compared to a single calorimeter module, that we can use the single particle inclusive cross-section to estimate the hadronic background.

For charged pions with P_T > 5 GeV/c, the integral cross-section is 4×10^{-29} cm^2 as measured at the SPS collider. At a luminosity of 10^{33} cm^{-2} - sec^{-1}, there would be 40,000 such particles produced per second. If the electromagnetic calorimetry had two segments in depth, we could get at least a factor of 20 pion rejection by requiring most of the energy to be deposited in the first segment. There would then be approximately 2000 fake electrons per second, which is low enough for the first two trigger levels. If the electromagnetic calorimetry were to have no depth segmentation, then the electron P_T threshold would have to be increased by a few GeV/c.

The integrated neutral pion cross-section for P_T > 5 GeV/c is 2×10^{-29} cm^2, giving 20,000 particles per second at 10^{33} luminosity. We estimate that requiring a stiff track (P_T > 4 GeV/c) pointing to the single calorimeter module would give at least a factor of ten pion rejection. Thus, again we would be down to the acceptable level of a few thousand fake electrons per second.

It this appears that for the first few trigger levels, an electron threshold as low as 5 GeV/c might be achieved.

(2) Transition Radiation Detector

If identification of electrons within jets is desired, active electron tagging is required. A transition radiation system can provide both the necessary segmentation and rapid decision time so that the information can be used in the trigger. The assumption here is that the electromagnetic calorimeter cells would be the size of an electromagnetic shower. Several LEP proposals have such segmentation (10^5 elements). To reject π's and K's, the transition radiation detector should have similar segmentation. One of six sections in depth is shown in Figure 3. The electron requirement would be satisfied if at least 4 wires out of the 12 in a line record energy deposition greater than 4keV (five times minimum ionizing).

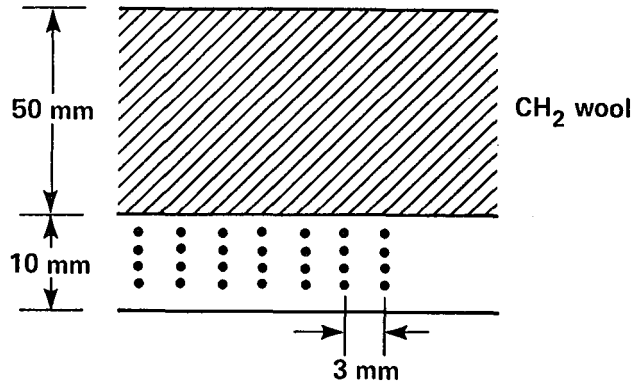

Fig. 3. Transition Radiation Detector

A rough estimate of the electonics cost for such a system was made under the assumption that analog information from the wires would not be read out. Rather there would be a single bit for each segment indicating the presence of an electron. A circuit board would contain the amplifiers and comparators for 48 channels as well as PROM circuitry to perform the majority logic. The estimated cost is \$15/channel or $\$1.5 \times 10^6$ for a 10^5 channel system.

Missing P_T Trigger

There might be a class of events for which the most prominent characteristic is a large transverse momentum imbalance. If events are to be retained at the early trigger levels solely on the basis of P_T imbalance, what thresholds would be required? To answer this question we used UA1 distribution for missing Px or Py, which is well described by a gaussian of $-0.4\ E_T$, where E_T is total transverse energy in the event. We also used the UA1 E_T distribution for minimum bias events and then calculated the missing P_T spectrum when the average number of overlapping interactions is between 2.5 and 5. A threshold of 15-20 GeV/c would suffice for the first trigger level while a 20-25 GeV/c threshold would be required at the second level. Of course these thresholds could be reduced if there were additional requirements of leptons or jets in the event.

Trigger System

The trigger system is an extension of the one designed for the CDF detector. The major difference is that at the Fermilab Collider, beam crossings occur each 3.5 μsec. Thus the first level trigger decision can take a few microseconds without incurring any deadtime. At a CW collider with 10^{33} luminosity, interactions occur on average every 20 nsec. This requires a very fast and deadtimeless first level trigger.

A sketch of the calorimeter level 1 trigger logic is shown in Figure 4. The calorimeter signal first passes through an integrating amplifier. The amplifier output enters a 500 nsec lumped delay line in order to allow time for the level 1 trigger decision to be made. Since the latter stages of the trigger take many microseconds, the calorimeter signals must be held. This is accomplished by the BEFORE-AFTER circuitry which is fed by the lumped delay line. Both switches are normally closed and thus both capacitors follow the output of the integrating amplifier. If the level 1 trigger is satisfied, the BEFORE switch is opened just before the interaction associated signal leaves the delay line. The AFTER switch is opened approximately 100 nsec later. The output of the difference amplifier is proportional to the charge collected by the detector element during that 100 nsec period.

The level 1 trigger logic begins with a difference amplifier connected to the integrating amplifier and to a 50 nsec tap in the lumped delay line. The output, which is the charge collected during the previous 50 nsec, goes to a number of devices. It is connected to two current summing operational amplifiers. The first (second) amplifier has input resistors proportional to the sine (cosine) of the detector element's azimuthal angle. These amplifiers thus give the total Px and Py respectively for the calorimeter cells connected to that circuit board. By adding the signals from the various circuit boards, we get the total Px and Py for the event. If the magnitude of either is above some threshold value, then the P_T imbalance level 1 trigger is satisfied.

The output of the level 1 trigger difference amplifier is also used in a conditional sum to look for large E_T deposition in the detector. If the signal is above a P_T threshold, typically 1 to 1.5 GeV/c, then that calorimeter cell is considered to have large E_T. In that case, a linear switch is closed and the signal enters a current summing operational amplifier with identical input resistors. When these amplifier outputs are added over the entire detector, we get the total E_T for all cells above P_T threshold. If this is above a predetermined value, the large E_T level 1 trigger is satisfied.

The output of the P_T threshold comparator is used for one other purpose. A five bit ring counter has a single one-bit which is shifted each 20 nsec synchronously throughout the detector. When the output of the comparator goes true, the value in the counter is shifted into a storage register. (If this timing is not precise enough, the comparator output can be used to gate the phototube leading edge which would determine the timing.) When the level 1 trigger is satisfied, these timing counters can be used to reduce contamination from multiple interactions. The time from the calorimeter cell containing the largest P_T is defined as the event time. This five bit code is sent to all circuit boards. Only those channels whose time equals the event time are used in later trigger decisions.

The level 1 trigger, which occurs in 300 nsec, must reduce the event rate to 50khz. We have used SPS collider data as well as ISAJET and CDF monte carlo results to estimate the required level 1 thresholds. These studies indicate that if any one of the following is satisfied, the event can be retained and the BEFORE-AFTER switches opened:

1. Greater than 8 GeV transverse energy is deposited in those towers with P_T threshold of 1-1.5 GeV/c.

2. An electron candidate is present with $P_T > 5$ GeV/c. The electron requirement is a large P_T in a single logical calorimeter cell either with a transition radiation count, if such a system is built, or with a high P_T track pointing to the cell and the proper energy ratio in the two depth segmentations of the calorimeter.

3. There is a P_T imbalance greater than 15-20 GeV/c.

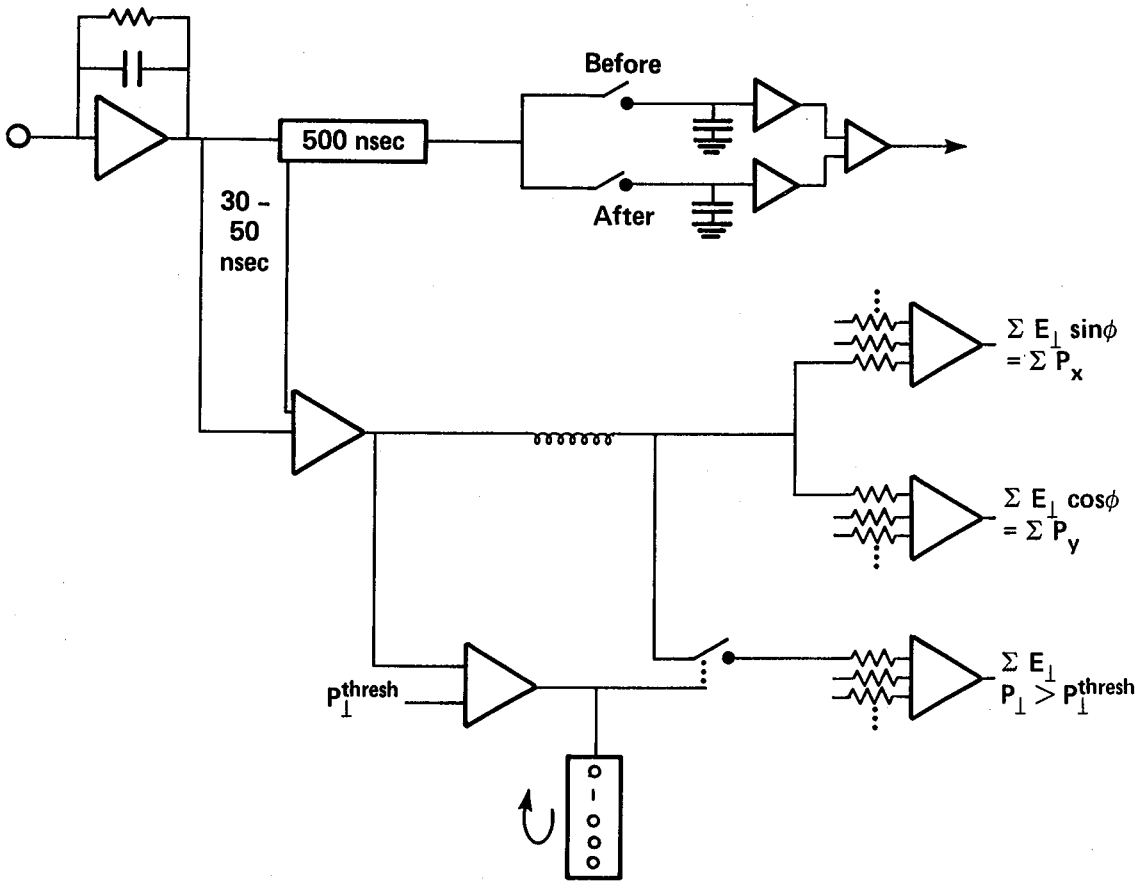

Fig. 4. Schematic of Level 1 Trigger for a Calorimeter

4. Another possible signature is the presence of a high P_T muon candidate in the muon chambers. Details of the steel shield are needed to determine whether this requirement would be restrictive enough.

Level 2 can take approximately 1 μsec and must reduce the rate by an order of magnitude, to 5khz. During this period, cluster finding hardware will locate the largest E_T electromagnetic cluster and hadronic cluster in the detector. The event can be retained if either:

1. There is a jet with P_T > 20 GeV/c;

2. There is an electon (using improved tracking information) with P_T > 5 GeV/c.

3. There is a P_T imbalance of 20-25 GeV/c;

4. There is a muon, as defined by the muon chambers, central tracker and hadron calorimeter, with P_T above a level which depends on the thickness of the iron shield, or;

5. If various combinations of requirements are satisfied such as P_T imbalance 15 GeV/c and a jet with P_T ~10 GeV/c.

Level 3 requires an average of 10 μsec and must reduce the event rate by at least another order of magnitude to a few hundred per second so that the full detector readout which takes 2 msec can be initiated. In this level the overall topology of the event is determined. All the moderate and large P_T energy clusters are found, with hadronic and electromagnetic E_T, mean rapidity and azimuth, and the widths in rapidity and azimuth calculated. Clusters are correlated with high P_T tracks to produce an E_T ordered list of energy clusters with tags for e, , and jet. In addition there is a list of muons in the event.

With the topology thus determined, fast bit-slice processors are used to decide whether it is a topology of interest. Events containing a large P_T electron and missing P_T 180° away in azimuth will clearly be accepted. An event with a multi-jet system of large invarient mass on one side of the detector and a lepton on the other side of the detector is a likely heavy quark decay event and thus also will be accepted. Events with two jets (P_T > 20 GeV/c) approximately 180° apart in azimuth are likely QCD scattering events and because of their abundance will be accepted at a prescaled rate. These are obvious examples of interesting topologies; signatures for other physics processes would also be included.

During the 2 msec required to read out the event, these processors will continue to analyze the information to help determine whether this should be one of less than 10 events per second to be written onto tape.

It is quite possible that additional preprocessing will have to be done to reduce the data to a manageable level. A group of people from the Trigger Group and Systems Group considered this problem. The results are included in the report of the Systems Group.

PARTICLE IDENTIFICATION

David R. Nygren

Working Group Summary Report

S. Aronson, J. Bensinger, C.Y. Chang, M. Goldberg,
M. Holder, R. Kofler, D. Leith, E. Loh
P. Nemethy, D. Nygren, S.J. Smith, R. Van Tyen

I. Introduction

This group addressed a wide variety of subjects within the general context of searching for limitations in capability due to high average rates. The luminosity taken for reference was 10^{33}. The group made an effort to identify areas of technique where inspired R and D effort is especially needed.

Because of the short time scale of the workshop, considerations were limited mainly to the 1 TeV regime. The group felt that the physics of the 20 TeV region is not sufficiently obvious at present to define the relationship between rate questions and particle identification.

Within these constraints, a general conclusion was that no intrinsic "brick walls" for luminosities or the order of 10^{33} were discovered, other than the usual compromises arising from financial limitations. In fact, rates were in some instances rather modest, arising from the high degree of segmentation needed a priori to swallow the high multiplicity jets expected, and evident now at the SPS collider.

Topics receiving attention included the following array of possibilities: Cerenkov ring imaging, transition radiation, synchrotron radiation, time-of-flight (yes!), High $P_\perp$ spectrometer, heavy quark tagging with leptons, general purpose μ and e detector, and dE/dx. The individual reports on these subjects represent the main work of this group. Some comments regarding these contributions are included here to provide a perspective.

II. Cerenkov Counters

Cerenkov ring imaging remains an attractive technique, realized currently in beam line geometries but not yet in collider configurations. Previous studies (1,2) have identified the problems which still remain to be solved before the technique can be accepted as a practical large scale tool. An intrinsic characteristic of Cerenkov effect is the rapid variation of Θ_c just beyond γ threshold, rising to 97% of Θ_i max at only about 3 γ threshold. Therefore, to obtain the widest range of sensitivity to γ, great precision in optical imaging and photon detection is essential. The relatively small number of Cerenkov photons in a frequency interval small enough to avoid dispersion places a severe requirement on the efficiency of photon detection devices. The discovery of superior molecular photoelectron emitters with high quantum efficiency in a wave length regime suitable for quartz windows would advance the practicality of this technique considerably. It is easy to nurture technological fantasies marrying advanced photocathodes with micro-channel plate electron multipliers and CCD imaging arrays in a single device, yet such devices are not likely to be developed with the usual financial resources devoted to instrumentation for high energy physics. Nevertheless, because the γ range can be adjusted through choice of radiator to span a large dynamic range, by cascaded detectors, this technique deserves a larger investment of effort than it has received.

For details, see M. Goldberg and D.W.G.S. Leith, contributed paper in these proceedings.

III. Transition Radiation

An unconventional utilization of transition radiation (TR) was examined, as an alternative to the conventional method of muon momentum measurement by magnetized toroids. The analysis showed that the conventional technique gives better momentum resolution than that obtained with TR, however, the TR method might become interesting if magnetized iron were precluded by other considerations.

IV. Synchrotron Radiation

The use of synchrotron radiation to tag electrons in the multi-GeV regime was evaluated with the conclusion that straightforward techniques such as xenon-filled MWPC's could reliably convert and measure the outboard halo of x-rays emitted by electrons. The magnetic field strength (and hence length) can be tuned for a particular energy range of interest.

See S. Aronson, contributed paper in these Proceedings.

V. Time-of-Flight

Time-of-flight techniques assuming contemporary performance characteristics were studied in the context of a search for new massive, long-lived objects. It was found that a luminosity of 10^{33} could be utilized if some redundancy in measurement is provided.

Details are given in C.Y. Chang, contributed paper in these proceedings.

VI. Jet Spectrometer

Starting with a design developed at an ISABELLE Workshop, the problem of designing a high $P_\perp$ spectrometer to measure jets and identify jet components was reexamined. New insight into the physics of jets at these energies was provided at the workshop by some graphic examples of events produced by ISAJET, a Monte Carlo incorporating the best current theoretical prejudices. The use of a relatively modest magnetic bend region deflects the majority of the particles, i.e. Low $P_\perp$, away from the sensitive elements of the spectrometer. The corresponding rates are on the of a kilohertz/wire, but the bite in rapidity and azimuth must be much larger than was previously thought necessary due to the structure of the jets.

Details are found in S. Aronson, M. Goldberg, M. Holder, and E. Loh, contributed paper in these proceedings.

VII. Quark Tagging by Leptons

The problem of heavy-quark tagging through the identification of the decay leptons was studied. This signature would be observable in relatively low multiplicity jets as an outboard lepton, i.e. a lepton isolated from the core of the jet but close enough to be identified as a jet component. Values of $P_\perp$ expected, relative to the jet axis would be of the order of 10 GeV/c for top in the expected range. Backgrounds from pion and kaon decay limit the usefulness to higher energy jets. Simultaneous muon and electron identification capability enhance the efficiency of this signature considerably since decay chains could be observed.

VIII. Muon/Electron Detection

A general purpose specific muon and electron detector was defined and evaluated. Based on this study, the conclusion was made that systems of the type used for the Fermilab CDF are adequate for $L=10^{33}$, but that single μ and e signatures are sufficiently frequent (a few KH_z) that these have to be used in conjunction with other information or at a higher trigger level. Backgrounds below 10 GeV $P_\perp$ are large.

See J. Bensinger and L, Nodulman, contributed paper in these proceedeings.

IX. Energy Loss Sampling

Finally, a whimsical study of a large solid angle spectrometer employing multiple dE/dx sampling was made to explore the limits of what might be done with brute force. This spectrometer, using the conventional axial-wire soleroid field confirguration requires the stringing of $\sim 1 \times 10^6$ wires and instrumentation of 25×10^5 cells. The strength of the dE/dx techniques lies partly in the fact that the information is contained in the track itself, whereas the weakness comes from the slowly varying logarithmic sensitivity to γ. Furthermore, discrimination is essentially lost above a γ of 200-300 as hadrons and muons merge with electrons. The maximum luminosity supportable by the configuration examined in probably is excess of 10^{32} if machine backgrounds are low. Despite the formidable number of channels, a true optimization might result in a manageable project. An amusing option is the possibility of balancing the several hundred tons force from the wire tension with an overpressure within the chamber volume. The overpressure, on the order of 1/2 atmosphere would improve the dE/dx resolution.

See D.R. Nygren, contributed paper in these proceedings.

X. Conclusion

The time available allowed sufficient progress to establish a belief that particle identification will probably not represent a primary obstacle to utilization of 10^{33} luminosities.

References

1. Proceedings of the Workshop on Possibilities and Limitations of Accelerators and Detectors, FERMILAB, April 1979. ICFA.

2. Proceedings of the Second Workshop on Possibilities and Limitations of Accelerators and Detectors, Les Diablerets, Switzerland, October, 1979. ICFA.

DETECTOR SYSTEMS

Barry C. Barish

Working Group Summary Report

J. Appel, B. Barish, J. Branson, R. Cahn, T. Carroll, J. Christenson, B. Diebold, H. Gordon, W. Hoogland, R. Johnson, L. Jones, L. Lederman, J. Linnemann, M. Nelson, F. Paige, J. Rosen, B. Sadoulet, R. Schwitters, E. Siskind, H. Sticker, A. Tollestrup, J. Yoh

1. Introduction

This report represents a brief review of the work of the "Systems" group for the DPF Workshop on Collider Detector. There are many systems considerations involved in large particle detectors. In this short workshop, only a few select topics could be considered. I have divided this report into two general parts: (1) Detectors at 20 TeV and (2) Detector Considerations for a High Luminosity Hadron-Hadron Machine.

2. Detectors at 20 TeV

2.1 The Character of Events at 20 TeV (F.E. Paige)

In order to get some feeling what events might look like at very high energies, plots of ISAJET events at $\sqrt{s}$ = 10 TeV were made for high P_T jet events.

Two examples are shown in Figures 1A and 1B. Primary jets have

$$1000 \text{ GeV} < P_T < 1100 \text{ GeV}$$

$$-1 < \eta < 1$$

The vertical scale is in GeV. Solid lines are energy deposited in calorimeter cells ($\Delta\eta$ = 0.1, $\Delta\phi = 5^\circ$). Dotted lines are parton energies after QCD jet evolution.

The events contain very sharp jet clusters, but often there are several clusters or side clusters. The central structure is very sharp.

2.2 20 TeV Detectors (B. Sadoulet, F. Paige, J. Bronson, R. Cahn)

Several important physics considerations were noted for doing physics at 20 TeV:

(1) We add high $P_\perp$ $W^\pm$ and Z° to our standard set of indicators of interesting events. For example, four jet events could be used to search for a heavy Higgs.

$$H^\circ \to W^+ W^- \text{ (Reconstruct W-mass)}$$

$$\to 4 \text{ Jets}$$

Note the jets from W have few low momentum particles and are characteristically narrower than QCD jets.

(2) The highest $P_\perp$ leptons which we might expect have $P_\perp \sim 3$ TeV. This is from considering a hypothetical $Z' \to \mu^+\mu^-$ with a mass of 5 TeV and the same dimensionless coupling on the Z°.

(3) QCD subjects may be narrow. We wish to measure jet widths to distinguish W's and τ's.

Detector A. A sample detector was designed by this group and is shown in Figure 2. The main features are the following:

Detect: high $P_\perp$ jets
τ, e
$W^\pm$, Z° jets
missing $P_\perp$

Give up: μ - momentum above ~300 GeV
e - charge above ~50 GeV

It uses calorimetric methods. Note that since e.m. shower and hadronic decay depths do not change rapidly with energy, this kind of detector is very similar to a 1 TeV detector.

The 4π hadronic calorimetry is done with small towers: $\Delta\gamma \sim 0.1$, $\Delta\phi \sim 40$ (10cm x 10cm → 2.5 K cells). The electromagnetic shower counters have finer segmentation (2.5cm x 2.5cm → 45 K cells).

The central tracking is used to identify stiff particles (for electron identification), find the vertex, measure multiplicity, identify W and τ jets. The iron toroids are used to measure muon momentum.

Detector B. (B. Sadoulet) A detector was proposed, somewhat conventional in nature, for a 20 TeV collider.

Physics Goals - (Assume $L \gtrsim 10^{31}$, 10^7 sec $\Rightarrow \int L = 10^{38}$ cm^2)

(1) Heavy new objects in TeV range.

e.g. (i) heavy W or Z° at 4 TeV $\sigma \sim 10^{-36}$
$\to e^+e^-$ $\sigma\beta \sim 10^{-38}$

(ii) Higgs → W^+W^-
If m (H) = 300 GeV $\sigma \sim 310^{-36}$
with W → 2 jets

(iii) new families: jet + e, jet + μ

(2) Extremely violent collisions

e.g. very high $P_\perp$ jet

Fermilab collider will study jets for $P_\perp \sim 400$ GeV

A 20 TeV collider at $L = 10^{31}$ will study $P_\perp \sim 2.5$ TeV

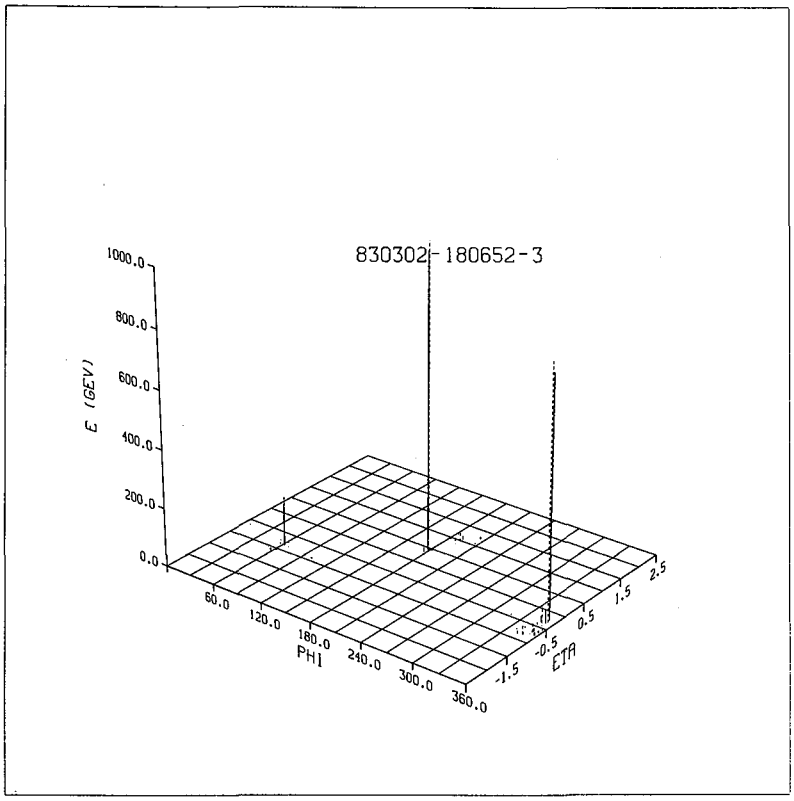

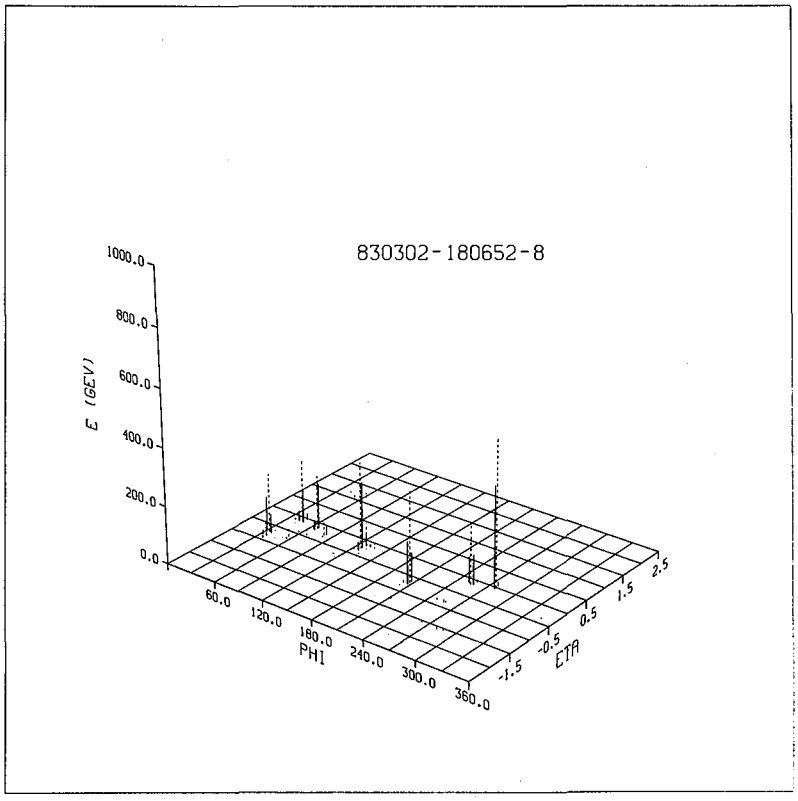

Fig. 1 (a) and (b). Isajet Simulation of $\sqrt{S}$ = 10 TeV events

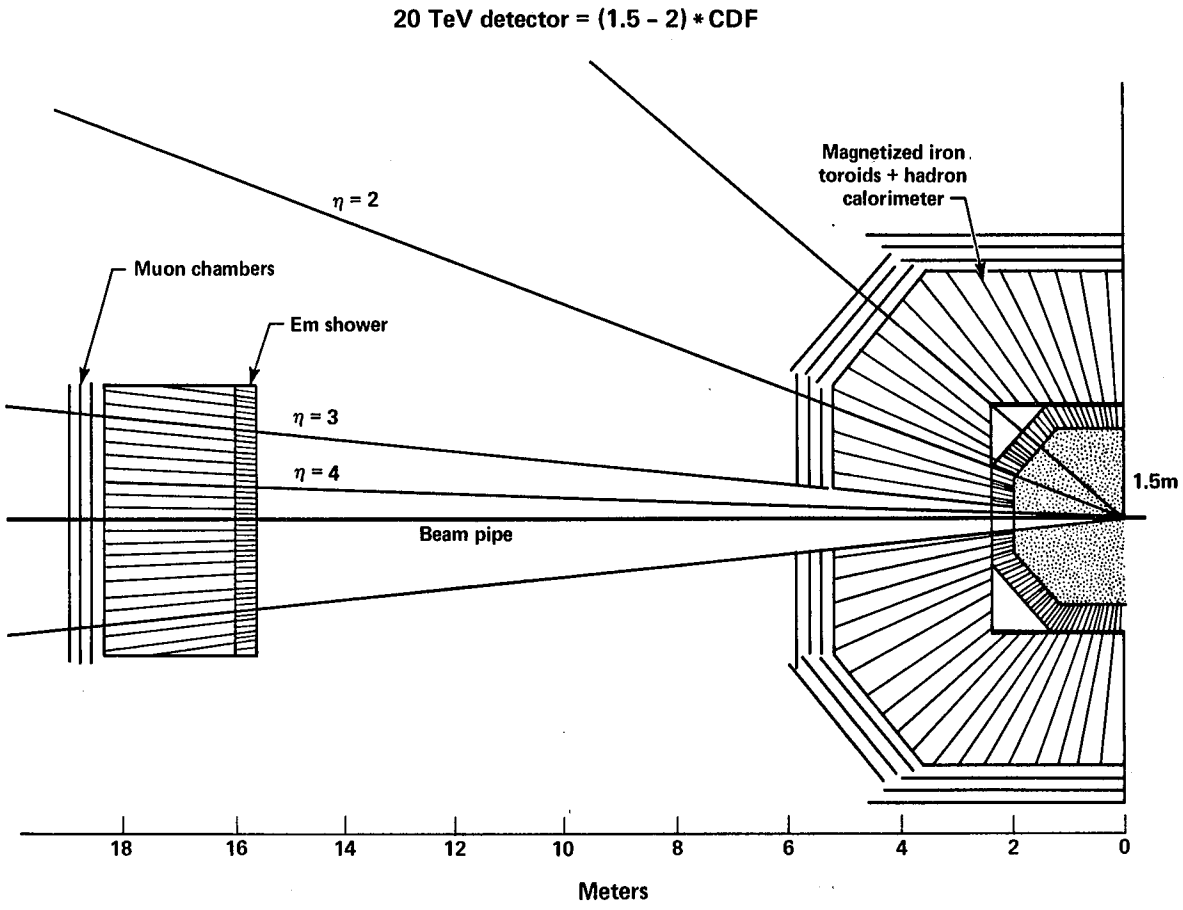

Fig. 2. Calorimetric 20 TeV Detector

Detector Considerations -

(1) The detection of leptons, ν, and single γ's are important for tagging. The electron is easy, single γ maybe hard, μ is extremely difficult above 50-100 GeV, ν is identified by missing transverse energy. To measure $\Delta E^{perp}_{missing}$ to 30 GeV will require coverage down to $\sim$10 mrad.

(2) The presence of the W may be used as tag. For example, W$\rightarrow$ 2 jets boosted gives narrow jets and can reconstruct W-mass.

(3) Jet energy will fragment into "lumps" as we see from the Paige events. The jet "width is $\sim$0.5 rad (½ angle), but many lumps have typical width $\Delta\phi$ $\sim$0.1 rad, Δy $\sim$0.1. These lumps represent the truly elementary objects.

(4) The approximate angular range for a jet of $P_\perp$ is polar angle,

$$\theta > 3 \times \text{kinematic limit} = 3\ \frac{P_\perp}{\sqrt{5}/2}$$

So for 400 GeV, $\theta \gtrsim$ 120 mrad implies $y > 2.6$.

Desired Detector Characteristics

(1) Match calorimetry to jets. The typical hadronic shower diameter ϕ = 0.2m should be matched to Δd = 0.1 and Δy = 0.1.

(2) Making the downstream detector a "reasonable" size yields $|y| < 2$.

(3) Missing energy considerations imply detector must go down to $\sim$10 mrad for $E^{perp}_{missing}$ $\sim$30 GeV/c.

(4) Inside one needs tracking to separate single particles and jets (best two particle resolution available). Magnetic field can be moderate ($\sim$1T), and is needed to identify low energy particles and measure $\Delta P_\perp$ $\sim$0.3%.

An illustration of such a detector is shown in Figure 3. The main feature are summarized below:

Magnet:

coil length 12m

ϕ = 2m external

Field 0.7 - 1T conventional

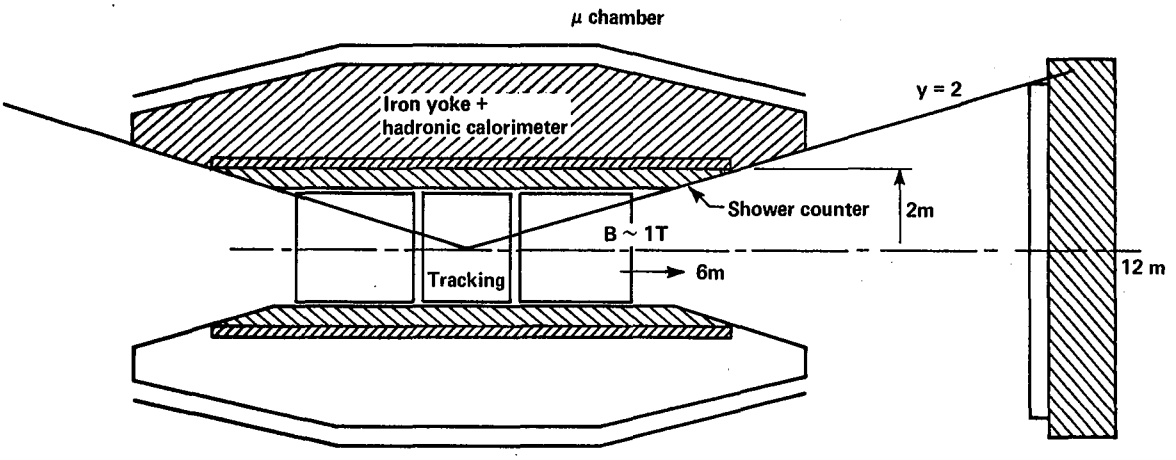

Fig. 3. Solenoidal 20 TeV Detector

Calorimetry-Barrel:

hadron	$\Delta\phi = 0.1$	2500 towers
	$\Delta y = 0.1$	
e.m.	$\Delta\phi = .05$	10K towers x 2 samples in depth
	$\Delta_y = .05$	

Calorimetry-End Caps:

size	$2 \times 25m^2$	
hadron	$\Delta x = \Delta y = 0.2m$	1250
e.m.		5000 x 2 samples in depth

Tracking:

JADE type or UA1 $\sim$ 10K wires

(volume divided by electronics in $\sim 10^6$)

Muons:

$350m^2$ x 2 x,y

2 layers

Conclusions:

A 20 TeV detector is not necessarily a monster and might look a lot like a 1 TeV detector, especially if the role of the magnetic field is restricted to recognizing hard tracks and measuring $P_\perp$ < 50-1000 GeV particles.

Several areas requiring R & D can be noted. There are a large number of cells required for calorimeters (>30K minimum). We need a good idea, similar to time projection for tracking, in order to subdivide the volume electronically. Tracking in a very long solenoid may also present problems.

Other Considerations for 20 TeV Detector A possible alternative to measuring the sagitta of a very high energy track is to use the field free region outside the solenoid coil. The technique then is to measure the straight trajectory in that region, extrapolate to the vertex, and measure the impact parameter.

A schematic view of the end view of such a detector is shown in Figure 4. Consider a coil $2X_0$ thick, ρ = 1.5m, and B = 3T. Then the transverse momentum kick of the magnet is P_T = 0.35 GeV/c and particles of .675 GeV/c will curl up in the solenoidal field.

Consider this method at 90°. Then the impact parameter $b = \frac{\phi\rho}{2}$ (ϕ = angle of bend) and at 1 TeV, $b = \frac{.15B\rho^2}{p}$ = 1mm. Note that the impact parameter b = 4 x Sagitta, so this scheme in principle is simple and more accurate. This, however, depends on limitations from scattering in the coil, and precision of knowledge of the vertex position.

First consider the scattering in the coil = $\frac{15}{p\beta}\sqrt{x_0} = \sqrt{2}\,\mu r$ at 1 TeV. This gives $\delta b = 30\mu$ implying a smearing due to scattering of $\delta p/p$ = 3%. This is, of course, at 90° and becomes worse for more forward angles.

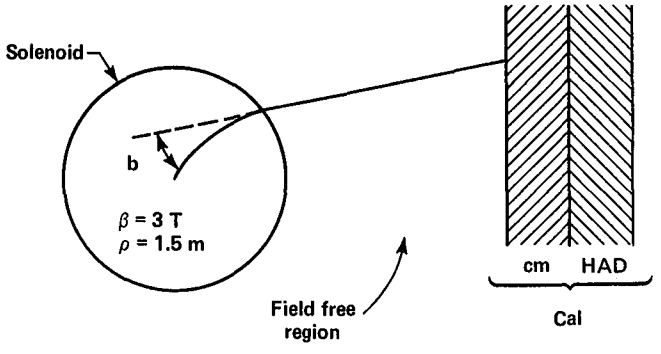

Fig. 4. Momentum Measurement by Impact Parameter

The second limitation comes from the knowledge of the vertex position. The emittance of the beam is invariant $\varepsilon_0 = 20\pi$ mm mr. For $\beta_{machine} = 150$m, $\sigma = 0.2$mm and $\beta_{max} = 3000$m, $\sigma = 1$mm, the size of the beam pipe is $\sim 20\sigma = 2$cm. Consider low β quads at 15m, then $\beta_{min} = 15$m, giving $\sigma = 70\mu$ at the interaction point (correspondingly, $\beta_{min} = 3$m gives $\sigma = 30\mu$ at the interaction point).

Overall, this technique has the advantage of tracking in a field free region, where we have straight line pattern recognition. By this scheme we estimate that all charged particles can be measured to $\delta p/p$ 5-10% to 1 TeV. This technique will only work in the central region where the effective thickness of the coil can be kept small.

3. Aspects of High Luminosity

3.1 State of the Art (L. Lederman)

A relevant question to ask in considering high rate detector systems is what is the "state of the art?". What limits the present generation of experiments and at what effective luminosity? One way to get a handle on this question is to look at a wide variety of high rate experiments at FNAL, ISR, AGS, etc. and try to average over the excuses (i.e. too much halo, trigger death, ...). This has been done in Table I and an attempt has been made to translate these state-of-the-art experiments to a 1 TeV collider in order to find what such a collider detector, built in 1978-82, could have taken in luminosity.

TABLE I

STATE OF THE ART

Experiment	Interaction Sec	Target/ Beam	ABS	Rapidity Ω_{cm}	Effective Luminosity**	Why?
FNAL E-						
400	10^5	Si/400 neutrons	0	1.6 π	$\sim 10^{30}$	trigger dead time
537	1×10^7	W/125 GeV π,p	60"Cu	2 π	$\lesssim 10^{30}$	Beam tagging
326*	10^9c*	Var. 225 GeV π^-	10'Fe	3 π	4×10^{30}	Drift Chambers
615	2.5×10^8	" 250 π^-	8' Be + 16' c	2 π	10^{30}	trigger dead time + PWC's
673	5×10^5	Be 200 π	0	2 π	5×10^{30}	Pb glass pileup PWC, mg.
609	10^5	H_2 400 p	0	2.9 π	2×10^{30} $\rightarrow 10^{31}$	Halo muons Otherwise x5
623	10^5	200π,400p	0	1.8π	2×10^{30}	SC & D.C. jam.
629	10^6	c/200 p, π	0	2π @ 90°	2×10^{31}	Liq A pileup
515	4×10^5	Be/200πp	0	2.5 π	1×10^{31}	Liq A pileup C Confusion
288*	5×10^{11}*	Cu/400 p $p_\perp \gtrsim 2$ GeV/c	22'Be	.007(4π) at 90°	2×10^{31}	Scint. counter +PWC rates
ISR						
I-1 (CCOR)	1.5×10^6	30 x 30	0	2 π	$> 5 \times 10^{31}$	No problems except in E_t
I-6 (AFS)	5×10^5	30 x 30	0	$\sim \pi$	2×10^{31} 6×20^{30} EP83-01 1.4×10^{31} EP82-139 "10% pileup"	
AGS 726	2×10^6	13 GeV π	0	large	4×10^{31}	datahandling triggering beam tagging
732	5×10^6		0	1/5 of 4π	10^{31}	beam tagging

* These experiments correspond to 4×10^{33} and 1.2×10^{34} resp. in a closed geometry with no measurements before the absorber. At 1 TeV these numbers become $\sim 1 \times 10^{33}$ and 3×10^{33} respectively.

** Not yet corrected for multiplicity.

There are four issues that need to be considered in making this decision:

(1) Solid angle or acceptance must be translated to a "standard 4 " collider detector.

(2) Environments may be quite different.

(3) Multiplicity varies with $\sqrt{s}$.

(4) Open versus Closed geometry.

Consider the first issue of translating the solid angle. For a physics thrust of the UA1 or UA2 type, one needs to see correlated jets, leptons, missing P_T, etc. So one must reduce the L by a fraction of solid angle which the fixed target detector subtended. (e.g. Accidentals $A = R^2 \tau\, n(n-1)$ for n separate pieces of a 4π detector. Thus, we must use R/n to keep A tolerable ($P_\perp$ cuts have been neglected).

The third issue is the different multiplicities. (AGS ~5 charged particles, FNAL ~9, ISR ~13, SPS ~25, 1 TeV ~30). Since this burdens the detector there must be corrections. This is partially adjusted for in the solid angle correction.

The fourth issue is how to account for closed vs. open geometry experiments. The closed geometry can be translated to open geometry by correcting for the hadrons absorbed. Absorbers typically give a factor of ~2 10^3 to 10^4 and each experiment needs an adjustment in the luminosity according to the density.

Overall, the results tabulated in Table I, indicate that the present state of the art seem to be that experiments have been rate limited at effective luminosities of $L \lesssim 5\ 10^{30} - 10^{31}$.

3.2 Effects of Multiple Interactions (Diebold, Gordon, Johnson, Linnemann, Paige and Yoh)

A study has been made of the physics consequences of multiple events. The attempt has been to compare single interactions vs. <n> = 10. The characteristics of physics at $\sqrt{s}$ = 1 TeV are $dn/d\eta$ ~6 particles (including neutrals), $\langle \Delta P_T \rangle$ ~.4 GeV yielding $\frac{d\Sigma E_T}{d\eta} \simeq$ 2.5 GeV. The total transverse energy $\Sigma E_T \simeq$ 25 GeV, so that if <n> = 10, $\langle \Sigma E_T \rangle$ ~250 GeV!

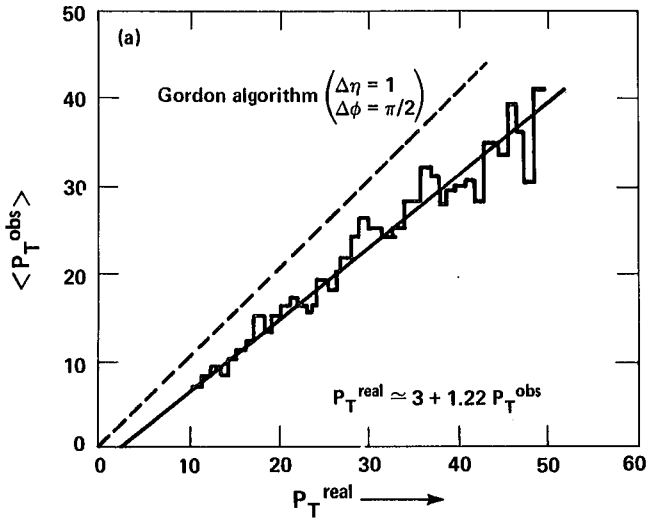

Fig. 5. P_T^{OBS} vs P_T^{REAL}

For the purpose of this study, it is assumed that the calorimetry covers ~4π and is divided into small towers and that tracking is divided into small cells in the B-field. So far this study has included Monte Carlo studies of the effects of multiple interactions on the calorimeter trigger and measurements of $\frac{d\sigma}{dP_T}$ for leading jets. Work is in progress on the effects on multijets (e.g. $W \to T\bar{B}$, QCD Studies) and the effect on tracking for the high P_T trigger. Other interesting questions that could be studied include the effect on measurements of missing E_T, isolated showers, pattern recognition and resolution, processing, multievent tagging, etc.

Calorimetry Studies Consider the question of P_T^{obs} vs. P_R^{Real} and how this is effected by the presence of multiple interactions. The algorithm is to choose the largest P_T inside a window. This has been done for two windows:

$$\Delta\eta = 1, \quad \Delta\phi = \pi/2 \text{ (Gordon)}$$

$$\Delta\eta = .6, \quad \Delta\phi = \pi/6 \text{ (Yoh)}$$

Due to QCD effects, a single window algorithm only picks up ~80% of P_T, even for the narrower of the two "original jets" (see Figure 5).

The effect of multiple events is to give some additional P_T to the observed P_T^{obs} in a jet. Since the algorithm is to maximize ΣP_T inside a window, the center of the window shifts and increases this effect.

Additional P_T Due to <n> = 10

	$\Omega/4\pi$	$\Sigma P_T/4\pi$	Acutal Shift	Ratio
Gordon	1/40	6 GeV	~8 GeV	~1.3
Yoh	1/200	1.2 GeV	~2 GeV	~1.7

This represents the added energy (due to multiple interaction) superimposed on top of a given jet cluster. A second interesting question is how well a detector will respond to hard scattering. For example, consider 50 GeV x 50 GeV P_T and use the simple algorithm of adding all clusters with $E_T \gtrsim 4$ GeV. For single events this works well as is shown in Figure 6. However, the same algorithm gives a very large shift for multiple events. It is evident that the challenge in the presence of multiple interactions is to develop smarter criteria that can determine what energy to keep and what energy to throw away.

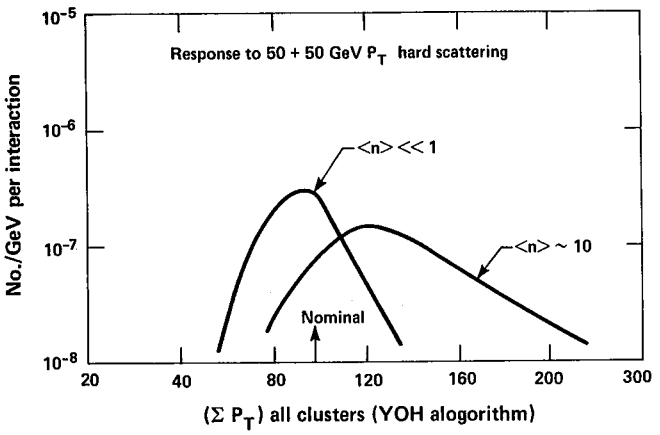

Fig. 6. Overlap effect on Apparent ΣP_T

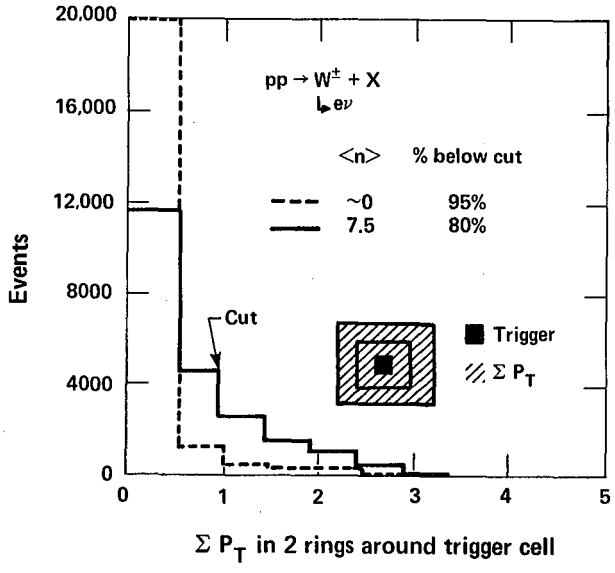

Fig. 7. Overlap Effect on $W^{\pm}$ events

Another physics problem to consider in evaluating the effects of multiple interactions is the reaction

$$pp \to W^{\pm} + X$$
$$\qquad\quad \downarrow$$
$$\qquad\quad e\ \nu$$

Figure 7 shows the added P_T that affects the cuts for isolated electrons. The plot shows that the efficiency of identifying isolated electrons is reduced from 95% to 80% in the example given.

Conclusion for Multiple Events In conclusion, no fundamental difficulty from multiple interactions at high luminosity has been uncovered. Although effects exist, the trigger for hard scattering seems alright; detection and measurement of leading partons is alright, however the detailed picture including gluons has problems for $P_T^{gluons} < 5$ GeV. In the case of tracking, determining the jet core should not be much worse, but the overall tracking will be more difficult.

3.3 Processing Requirements at $L = 10^{33}$ cm^{-2} sec^{-1}

(T. Carroll, W. Hoagland, E. Siskind, H. Sticker)

The experience we start from is from UA1. The fast trigger for UA1 ~1/sec, which scales to ~20 KHz at 10^{33} cm^{-2} cm^{-1}. This trigger includes:

a) electron P > 10 GeV

b) jet E_T > 15 GeV

c) total E_T > 40 GeV, $|\eta| < 1.4$

d) μ

By tightening requirements it should be possible to get a fast trigger that has a rate ~1 kHz (see the Trigger Group summary report). For the purpose of studying the processing problem, we assume that this factor can be obtained by asking for simple signatures in the trigger.

Look For (on-line)	Signature
$W^{\pm} \to e\nu$	e: $P_\perp > P_{\perp\ min}$ & missing $P_\perp$
$W^{\pm} \to \mu\nu$	μ
$W + \gamma$	$e + \gamma$
gluinos	missing $P_\perp$
$t\bar{t}$	e + jet + missing $P_\perp$
-	
-	
-	
new physics	?

Now, let's consider the problem of handling this trigger rate.

Assumption
- 1 event = 10^5 bytes
- channels = $2\ 10^5$
- Channels/ADC = 100
- Channels are 10% occupied

The compaction and digitizing time (ADC) is then 100 x 1 μs (below threshold) plus 10 x 5 μs (above threshold) giving a total time of 150 μs/event. Therefore the readout rate for full events ~5 KHz. This is alright for the assumed trigger rate, but this readout level could be a bottleneck on livetime.

Next, let's consider the data storage limits,

(1) Conventional Technology:

1 25 IPS 6250 Tape Drive

= 5 x 10^5 bytes/sec

= 5 events/sec

(2) Videotape Systems

May go up to 10^8 bytes/sec

= 10^3 events/sec

If videotape systems are used, the problem is shifted to off-line processing. For the purpose of this study we assume a storage rate of ~50 Hz.

The added on-line problem is to do processing to reduce the rate written on the data storage system from 1 KH_z → 50 H_z. Events must be thrown away in a time of 1 ms.

Define: 1 Processor Unit = IBM 168

= 3081 E

= 3-4 VAX 11/780

UA1 Experience: 7 ms = high $P_\perp$ track

1 ms = all μ tracks

~50 ms = general algorithm

So we assume the average processing time to handle and filter these events = 50 msec.

Therefore, we estimate that to handle a 1 KH_z rate requires:

= 50 PO

= 50 3081 E

= 200 VAX 11/780

At first sight, this is an awesome amount of on-line computing. However, this appears technically feasible and even the cost is not outrageous. One could conceive of Fastbus module-processor (3081E) + 1 Mbyte memory (cost ~$10-15K). So the cost of 50 PU = $1M. The array of processors need to be arranged in an array that can pass this rate.

Data Rate = 10^3/sec x 10^5 bytes

= 10^8 bytes/sec

Need ~3 Fastbus segments

~3 Crates of microprocessors

This whole area of microprocessors on a Fastbus card, fast switch, and segment interconnects is an area where R & D could be extremely useful.

The off-line requirements are also very large,

UA1 = 0.1 Hz on CDC 7600

= 0.03 Hz/1 PU

Therefore the analyzed data rate/acquired data rate = 10. This means to process the 50 Hz off-line will require ~160 PU or roughly ~50 CDC 7600.

In conclusion, it appears technically feasible to handle the rates from $L = 10^{33}$ in terms of pre-processing and processing. In order to have flexible triggers and power in data selection and analysis in a general purpose detector without strongly biasing the physics at the trigger level various R & D efforts should be strongly pursued.

a) arrays of microprocessor systems

b) data storage technology

c) software for preprocessing

d) fast ADC's

3.4 Magnet Option (J. Appel, J. Christenson, L. Jones, J. Rosen)

The requirement of using a magnet in a collider detector was examined. The ideal was to determine what a magnet "buys" in terms of physics and what it "costs".

Abilities and advantages with a magnet include:

(1) Momentum Determination

(2) Sign of charge determination (including correlations)

(3) Sweeping of low P_t tracks

(4) Aid in particle identification

Abilities and advantages without a magnet include:

(1) Simplicity of construction

(2) No field effect on photomultipliers

(3) No coil (radiation lengths) before e.m. calorimeter

(4) Reduced need for track length and number of layers in tracking

(5) Opportunity to move calorimeters closer, make smaller

(6) Reduced cost

(7) Reduced smearing of radial lines ($\vec{C}^{\gamma}$ signals, towers)

(8) Reduced decay length (muon backgrounds, and missing energy calorimetry)

(9) Simplified track reconstruction (trigger and off-line).

An example detector was considered that identified jets; measured E_{jet}, $E_{t_{jet}}$, M, Z; measured multiple jets (e.g. $W \to t\bar{b}$, $t \to 3$ jets); found electrons and isolated γ's for special jets and reconstructed "M" $\to W\gamma$, $\gamma\gamma$, WW.

The conclusions of this study were that no overwhelming benefit was found for considering a general detector with no magnet. The cost was estimated to be .5-.7 of a similar capability magnetic detector. No unique physics capability was identified for the nonmagnetic detector. No inherent extra rate capability was found, except for analysis where the number of channels is reduced. Lastly, there probably is an advantage in flexibility or mutability for a non-magnetic detector.

3.5 Cost Considerations for a High Luminosity Detector (B. Barish and R. Schwitters)

Introduction: During this workshop, technical solutions for the various detector components (tracking, calorimetry, triggering, preprocessing, etc.) have been presented. A complete detector utilizing various solutions described by the working groups remains to be done. At that point, the detailed work of measuring the detector against possible physics goals needs to be studied, in order to evaluate the actual ability to do physics. That is probably the most important unfinished job after the completion of this workshop.

In the absence of such a specific detector and physics goals, we have ignored the detailed design of a detector, and instead tried to assess the difficulty of incorporating the technical solutions posed in this workshop into a modern general purpose detector capable of handling the high luminosities. As a guide we have used the Fermilab CDF detector and scaled from the known costs of that facility. We are aware that a new detector would be done differently and do this exercise to identify the scope of such a facility (total cost) and the most costly areas where R & D might be most helpful.

In general most solutions posed at this workshop involve more segmentation, speed, preprocessing power, etc., rather than totally new directions for future high luminosity detectors. The method we have used to cost is to scale all costs relative to CDF. New detector components, like precision vertex detectors, or particle ID methods, have been ignored.

Cost Comparison We have compared the cost of CDF and a high luminosity detector in Table II. The ratio of HLD/CDF cost considerations were the following:

Magnet: Identical (includes coil and cryogenics) Factor x 1.

Tracking-Mechanical: We assume from the cell size 5 times as many cells. Cince the cost in labor dominated we assume 3 times the CDF cost.

(For reference, the CDF central detector has 12K cells, the vertex and intermediate 8K and the forward 8K.)

Shower Calorimeter - Mechanical: The ratio of fast liquid Argon gas we estimate 5: 1 (e.g. Tasso $\$75K/m^2$ x 2 (labor) x 1/2 (mechanical fraction) vs. Gas (CDG $\$500/m^2$ x 30 layers). For the scintillation, we guess 1.3:1 (extra cost for photomultipliers, scintillator, etc.).

The mix of gas:scintillator we assume is 1:1 like CDF. Factor x 3.25.

Hadron Calorimeter - Mechanical: We assume slow gas, fast scintillator and use the CDF mix 1:1. Factor x 1.15.

Muons - Mechanical: We assume 2 x - more cells and complexity. Factor x 2.

Front-End Electronics: For CDF the mix is 1/2 tracking and 1/2 other. For tracking in HLD we have 5 x cells and 3 x complexity (multihit, charge division, etc.). For the rest of the front end electronics, due to short gates, flash ADC's, more channels, we assume an additional x 1.2 for added system complexity for the necessary bandwidth. Factor x 10.

Data Acquisition: Scaling from CDF. Factor x 5.

Level 1, 2 Trigger: Same as level (1,2) plus a factor x 1.2 for increase in system complexity as in front end electronics. Factor x 2.4.

Installation, Administration, etc.: Take overall HLD/CDF ratio. Factor x 3.7.

Conclusions: The overall cost of a CDF type detector built for high luminosity appears to be ~3.7 x CDF in cost (complexity). This gives a total cost of ~$146M. A large general purpose detector facility like this could be considered for a high luminosity machine like (CBA). The detector facility would presumably service ~250 physicists, making its cost/physicist not so different from LEP detectors or CDF. Technological advances and clever design could reduce certain costs.

Two items are of particular interest in terms of pointing out areas most in need of R & D. The large number of channels and complexity have made the front-end electronics inordinately expensive ($69M). A coherent plan for developing cheap front end electronics is urged. Secondly, a total of $18M is estimated for Level Triggers and Data Acquisition. In addition, a large amount of off-line analysis power is needed. R & D on preprocessor systems, data storage, and analysis systems is crucial for meeting our future needs, both in terms of sophistication and cost.

TABLE II

SUMMARY - HLD COSTS ($M)

System	HLD/CDG	CDF Cost*	HLD Cost
Magnet	1	4.1	4.1
Tracking	3	2.6	7.8
Shower Cal.	3.25	5	16
Hadron Cal.	1.15	9	10
Muons	2	1.4	2.8
Front-end Electronics	10	6.9	69
Data Acquisition Electronics	5	1.4	7.0
Level 1, 2 Trigger	2	3.0	6.0
Level 3 Trigger	-	0	5.0
On-line Computers	2.4	1.1	7.6
Cable Plant	2.4	1.0	2.4
Misc.	3.7	3.7	13.7
TOTALS	<3.7>	$39 M	$146 M

*Includes Japanese and Italian Contributions

SECTION III: CONTRIBUTED PAPERS

TRACK CHAMBERS FOR HIGH LUMINOSITY*

T. Ludlam and E.D. Platner
Brookhaven National Laboratory, Upton, New York 11973

I. Introduction

We examine the requirements for wire chambers as large-solid-angle tracking devices in a hadron collider at $L = 10^{33}$ cm^{-2} sec^{-1}. This luminosity corresponds to an event rate of 50 MHz, and we assume an average charged particle density dn/dy = 3.6. We take as a starting point the known performance of the Axial Field Spectrometer drift chamber[1] and the MPS II drift chamber system.[2] The criteria which we have applied for a "safe" extrapolation of these systems are:

i. The rate per wire should not exceed 2 MHz.
ii. The sensitive time of the chambers (i.e. maximum drift time) should be short enough to limit the average number of pile-up events to no more than a few.

These requirements impose a high degree of segmentation: The central and forward tracking systems each require $\approx 10^5$ channels. This fine granularity of detection elements, imposed for rate capability, is also necessary if the tracking system is to have good efficiency for resolving individual tracks in jets.

Since the number of readout channels in such a system is an order of magnitude greater than for existing detectors, the development of new electronics approaches is an R&D item of high priority. The probable cost of a readout system based on custom designed integrated circuits should be much less than estimates obtained by simply scaling the costs of existing detectors according to the number of channels.

II. Central Tracking Chamber

We take a solenoidal geometry, and adopt the basic philosophy of the Axial Field Spectrometer drift chamber (Fig. 1). This chamber, which operates at the CERN ISR with a typical luminosity of $\approx 3 \times 10^{31}$ cm^{-2} sec^{-1}, uses "bicycle wheel" geometry with 42 cylindrical layers of sense wires and 4° azimuthal segmentation in each layer. The active volume extends from an inner radius of 20 cm to an outer radius of 80 cm. With a position accuracy σ_ϕ = 200 μm in the drift plane, and a magnetic field of 5 kilogauss, the momentum resolution is $\Delta P_T/P_T = .02\ P_T$. The sense wires are staggered to resolve left-right ambiguity, and the z-coordinate is determined by charge division. A principal benefit of this design is that the radial geometry and unambiguous space-point measurement makes the pattern recognition extremely robust: The chamber has a demonstrated ability to handle event multiplicities $\gtrsim$ 50 tracks, and has operated at a luminosity of $\approx$ 5 times the design value with no loss of efficiency for the track-finding software.[3]

For a central detector at CBA we require a wider rapidity coverage than is afforded by the AFS detector, and better momentum resoltuion for high transverse momentum tracks. In table I we give the parameters for a conceptual design for a chamber covering ± 1.5 units of rapidity ($25° \leq \theta \leq 150°$). The chamber layout is illustrated in Fig. 2. A space-point accuracy of 200 μm is assumed, in a magnetic field of 15 kilogauss. Drift chamber wires, in the bicycle wheel configuration, are arranged in radial groups, "rings", with 15 layers of sense wires per ring (10 layers in ring 4). Each wire has charge division readout.

If only the first three rings are used, so that the chamber extends to a radius of 1 meter, the momentum resolution is

$$\left.\frac{\Delta P_T}{P_T}\right|_{R=1m} = .0027\ P_T.$$

The addition of the fourth ring, extending the radius to 1.5 meters, provides a 10% momentum measurement at P = 100 GeV/c. We imagine, however, that some compromise might be necessary in the rapidity coverage of the outermost ring, which would otherwise call for wire lengths of 6 meters.

The cell size, a, in Ring 1 is 2 mm, corresponding to a maximum drift time of 40 ns and an azimuthal segmentation of 314 sense wires per layer. In the outer ring the maximum drift time is 120 ns, with 750 anodes/layer. At a luminosity of 10^{33} cm^{-2} sec^{-1}, and dn/dy = 3.6, the rate per wire is 1.6 MHz in Ring 1 and 0.7 MHz in Ring 4. For 1% charge division accuracy we require an avalanche size of 5×10^6 electrons (gas gain $\approx 1.0 \times 10^5$), so that the signal current will be 1 μamp per wire at the innermost layers.

The charge division measurement will be rather coarse, with an uncertainty of several centimeters in the outer layers, but it is also highly redundant and should be adequate for pattern recognition and initial track reconstruction. For precise measurement of the Z coordinate, each ring has one special layer in which the position along the wire direction is determined from the induced charge distribution on cathode pads.[4] These "pad layers" are subdivided into many sections, as given in Table I. Each section consists of a row of pads which are resistively coupled so that the position along the pad row is found by charge division (Fig. 3). The accuracy of the measurement is ≈ 2% of the length of the pad row, provided the section is not occupied by multiple tracks. Thus the number of pad sections is large both because of the desire for millimeter accuracy over large surface areas and the necessity to resolve individual tracks.

Such a chamber is an order of magnitude more complex than those of present generation detectors, approaching 10^5 readout channels each of which involves pulse height measurement of ≈ 8-bit accuracy. Mechanical techniques for assembling alarge device with such a high density of wires are being studied. Feasible solutions, based on methods already used in large chamber construction, have been identified and will be studied further with prototype devices. The readout for such a chamber calls for a major R&D effort. Systems based on miniaturized front-end amplifier circuits and high speed flash encoders for time and pulse height measurement can be designed using existing technology, but a much higher level of circuit integration seems possible, and should be developed. A further discussion of this point is given in Section V.

III. Tracking in Jets - A Study of Segmentation

In order to withstand high rates we are led to a high degree of segmentation, taking the form of a

TABLE I
Parameters of Central Track Chamber

Position accuracy in drift coordinate: σ_ϕ = 200 μm
Second coordinate measurement:
Charge division: σ = .01 L (L = wire length)
Pad layers: $\sigma \simeq$ 1 mm
Avalanche gain: 1.0×10^5
Magnetic Field: B = 15 Kgauss
Momentum Accuracy:
R = 1.0 m (rings 1-3): $\Delta P_T/P_T$ = .003 P_T
R = 1.5 m (rings 1-4): $\Delta P_T/P_T$ = .001 P_T

Thickness of Material at θ = 90°
(wires, gas, pad layers): .02 rad. len.
.003 coll. len.

Ring	Starting Radius (cm)	Cell Size (a,mm)	No. Anodes per layer	No. Layers	Total Anodes
1	20	2	314	15	4,710
2	50	3	523	15	7,845
3	90	4	720	15	10,800
4	130	6	750	10	7,500
					30,855

Charge Division (each wire)			Pad Sections (1 layer each ring)		
Ring	L(cm)	σ_Z(cm)	Section Size	No. Sections	σ_Z
1	120	1.2	2 x 2.5 cm^2	4,000	.5 mm
2	230	2.3	4 x 3 cm^2	6,000	.6 mm
3	400	4.0	5 x 5 cm^2	8,000	1 mm
4	600	6.0	5 x 10 cm^2	10,000	2 mm
				28,000	

very high density of wires. The desire to resolve individual tracks within jets also calls for a fine-grain detector, and for this purpose it is evident that some kinds of segmentation are more effective than others. A jet consists of a high-density cluster of tracks which occupies a small fraction of the detector area. Thus, for a given number of detection elements, it is best to have them as fine-grained as possible in one coordinate, accepting coarse granularity in the other coordinate. This is so because the distance between jets is large compared to the distances within jets:

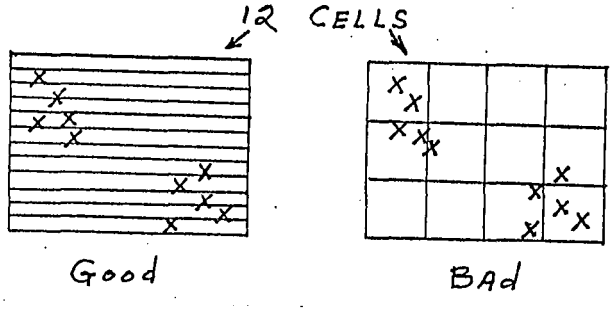

As a quantitative study we have used ISAJET to generate jet events into a cylindrical detector and examined the two-track resolution for three types of segmentation:

i. Squares: The cylindrical surface is subdivided into square detection elements ($\Delta\theta = \Delta\phi$).

ii. Pads: Each detection element subtends 20 mr in ϕ. This would correspond to wires with 4 mm anode-to-anode spacing at a radius of 20 cm. Further subdivision is achieved by segmenting the readout along each wire, e.g. with cathode pads.

iii. Wires: No segmentation in θ. Each detection element corresponds to a wire running the full length of the cylinder.

Our measure of efficiency for resolving tracks is the fraction of tracks missed due to an overlap of two or more tracks in the same detection element ("cell").

The results from 40 GeV jets are shown in Fig. 4. Tracking in jets is best achieved with fine wire spacing, and the wire densities arrived at in Table I (> 300 cells/layer) correspond to efficiencies of $\gtrsim$ 80% for resolving tracks in jets. Figure 5 shows how the results, for segmentation in wires, vary with jet momentum. All results are for a 15 kilogauss solenoidal field.

IV. Forward Tracking Drift Chambers

There is a 25° half angle cone around the beams that is not covered by the central tracking chambers. This cone is most simply filled with high-rate chambers such as those in MPS II which use simple planar frame construction. Here again we impose the constraint that no anode shall have more than a 2 MHz event rate. A simple approximation to the event rate per cm^2 gives $R/cm^2 \approx 3 \times 10^7/r^2$ at $\mathcal{L} = 10^{33}$ where r is the distance from the beam pipe, Fig. 1. The integrated event rate per wire is:

$$2SR/d \tan^{-1} \ell/d$$

where S is wire spacing, 2ℓ is anode length, and d is distance of closest approach. For $\ell \gg d$ and s = 4 mm, this limits d to 19 cm. If chamber modules are employed as in Fig. 2 using 4 mm anode spacing out to 50 cm, 6 mm spacing between 50 and 100 cm and 10 mm spacing outside of r = 1 m the 2 MHz rate limitation per wire will not be exceeded. Applying MPS II experience we would construct modules having pairs of X, Y, U and V chambers as shown in Fig. 3 where each pair is staggered by a drift space. Since these modules are in a field free region, 4 sets of such modules will cleanly generate point slopes and eliminate left-right ambiguities. Table 2 is a listing of the anode wire count.

TABLE 2

Module	Anode Length	Anodes/Plane
D1	3	1.0 K
D2	4	1.2 K
D3	6	1.6 K
D4	7	1.8 K
D5	8	2.0 K
D6	9	2.2 K
D7	10	2.4 K
D8	11	2.6 K

This table adds up to 14.8 K wires per plane for the 8 modules. However there are 8 planes per module or 120 K anodes for the spectrometer. In order to cover the full 4π, including the central detector, one needs 2 spectrometers or a grand total of 240 K channels. This electronics requires only the TDC function so inexpensive MPS II-type electronics is applicable.

V. Electronics Development

Time and amplitude electronics should be deadtimeless and pipeline delayed by at least 1 μs in order to facilitate trigger decisions. Because of the desire to reconstruct jets as well as provide high rate capability, with good efficiency, it is necessary to have fine granularity for both tracking chambers and calorimetry. The number of channels involved is $\approx 10^5$ for both the TDC and ADC functions.

Systems of this size affect the design philosophy in that one can consider substantial investment in custom IC design that can radically reduce the active component count, reduce crate count and improve reliability. As an example, the MPS II drift chamber electronics required the development of 3 custom IC's, the development phase costing about 1/2 the total electronics expeditures. However, due to the design freedom inherent in fully custom IC technology the design goals of a fully pipelined time-to-digital conversion in which there are no adjustable and thus potentially unstable parameters the detectors described in this paper the only further IC development we would recommend would be the engineering and production of a very low noise multichannel amplifier IC. The other active components required have been in use at MPS II for a year. Remaining development would include hybrid packaging of these components since the active circuit power level is low. This should allow a spatial compression of up to a factor of 4 over that of MPS II.

The detector system we describe here will also require a pipelined ADC system probably with sampling rates of 200 MHz. The charge division ADC should have 8 bit resolution with 9 or 10 bit dynamic range. The current state-of-the-art is availability from 3 or 4 sources of 6 bit 100 MHz flash ADC's costing $50-100. There is also an 8 bit 30 MHz ADC with 9 bit dynamic range currently availale for ≈ $8. These are examples of commercial products. It is our belief that with a reasonable engineering budget, i.e. $1-2M, flash ADC's satisfying our requirements can be produced in a time frame of 3 to 4 years. Once such devices are developed, production quantities should be less expensive than the ADC's now available for HEP because of the economics of dedicated IC systems.

The ADC requirements imposed by high speed calorimeters are similar to that of the tracking charge division channels except that the dynamic range is much greater. Here one requires a dynamic range of .1 GeV to 400 GeV with 2 bit resolution at .1 GeV improving to 8 bit accuracy and resolution at 400 GeV. Table 3 shows how 2-9 bit ADC's can be used to cover this dynamic range while contributing negligible error to the measurements in a hadron calorimeter.

The large general purpose detector described above will require 30K TDC channels for the $\Delta Y = \pm 1.5$ detector and 240K TDC channels for the $< 25°$ forward detectors. It will also require 90K channels of 9 bit ADC for the charge division and pad readout in the $\Delta Y = \pm 1.5$ detector. In addition, the Calorimeter with 5K channels each for the electromagnetic and hadronic calorimeters require 2-9 bit ADC's totaling 20K channels. Table 4 is a compilation of this total electronics requirement.

TABLE 3

Energy GeV	√Energy	Hadron Resolution	# of Bits	
400	20	2.5%	9	
100	10	5	7	ADC1
50	7	7	6	
10	3	17	4	9
4	2	25		8
1	1	50		6 ADC2
.5	.7	70		5
.1				2

TABLE 4

Drift Chamber Amplifiers and Discriminators 330K	$ 3.3 M
TDC's 270K	2.7 M
ADC's 110K	11 M
IC Development	2 M
	$19.0 M

The cost estimate of the tracking detector amplifiers and discriminators is a hard number taken from MPS II experience. The ADC cost is an estimate based on an analysis of development costs for other state-of-the-art IC production history. It should be noted that at the 100K part level we are dealing with industrial levels of production which bring very attractive pricing.

References

* Research supported by the Department of Energy under Contract # DE-AC02-76CH00016.

1. O. Botner et al., Nucl. Instrum. Meth. 196, 315 (1982).
2. E.D. Platner, Proc. Int. Conf. on Instrumentation for Colliding Beam Physics, stanford, California, February 17-23, 1982, p. 24.
3. AFS Collaboration, "Operation of the AFS at 1.4 x 10^{32} cm^{-2} sec^{-1}: A First Look at High Luminosity Data From the CERN ISR," these proceedings.
4. V. Radeka, "Centroid Finding of Induced Charge in Gas Proportional Chambers," these proceedings.

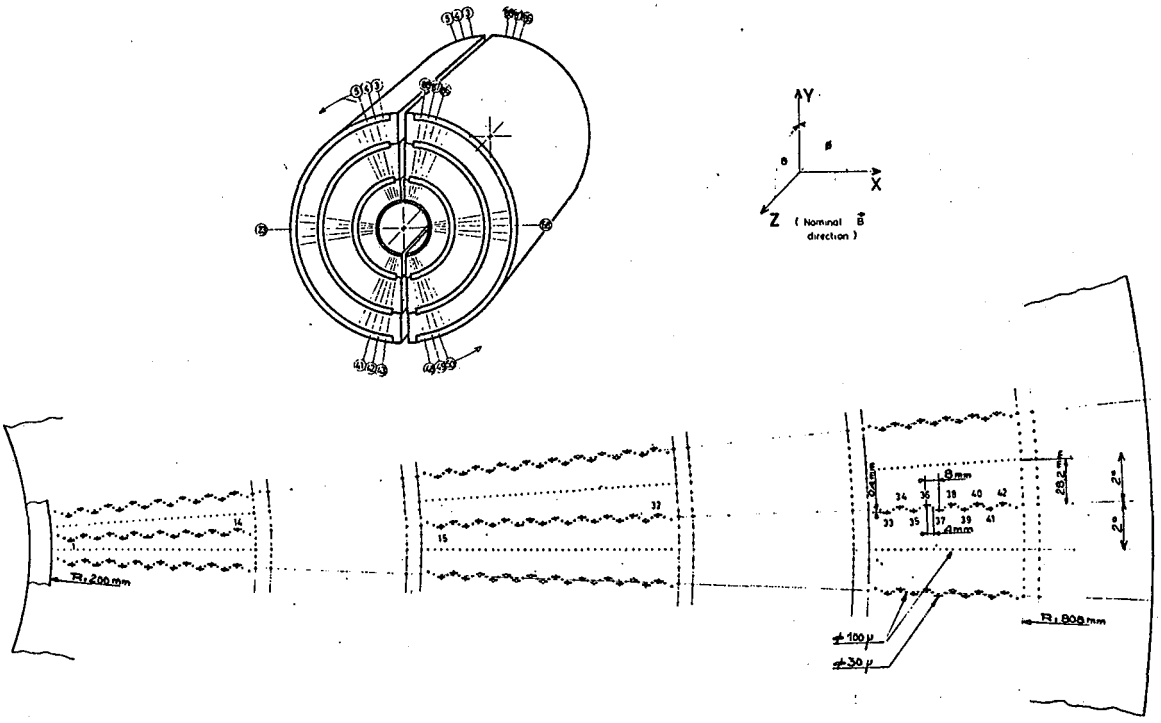

Figure 1
The Axial Field Spectrometer Drift Chamber (Ref. 1).

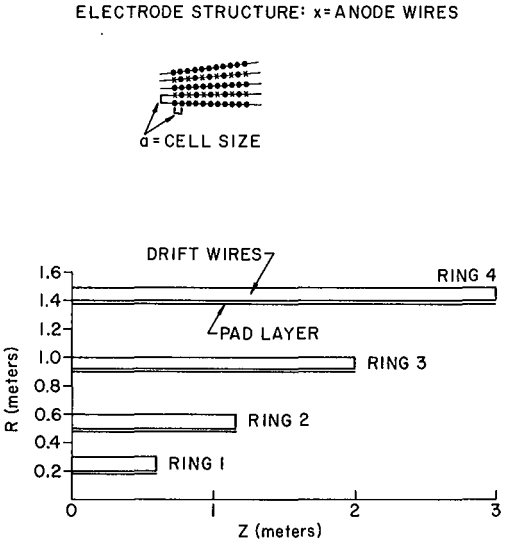

Figure 2
Schematic Layout of the Central Tracking Detector.

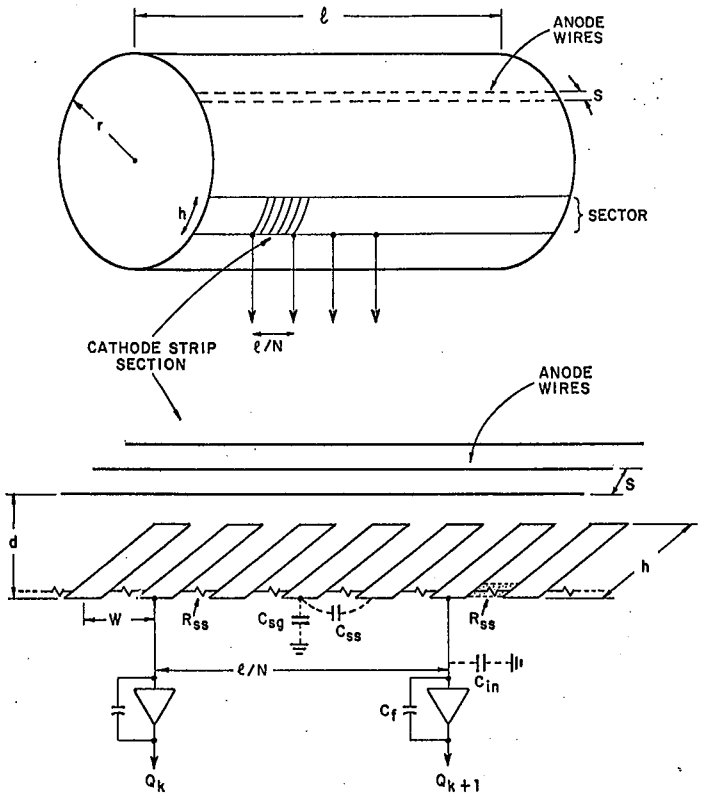

Figure 3
Induced Charge Measurement for Precise Z Coordinate on Pad Layers (Ref. 4).

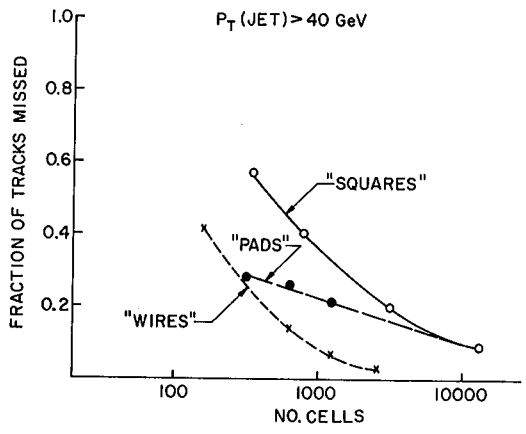

Figure 4
Track resolution in jets, for various kinds of segmentation in the central rapidity region ($y \leq 1.5$). The points are ISAJET calculations for $P_T(\text{jet}) \geq 40$ GeV.

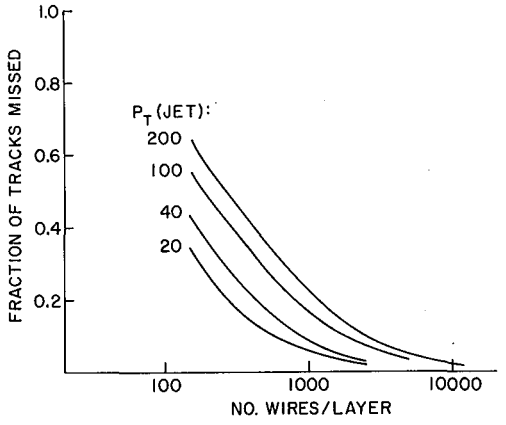

Figure 5
Track resolution in jets, for segmentation by cylindrical layers of wires.

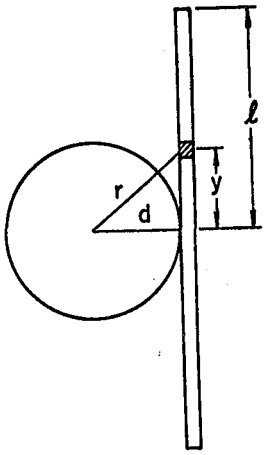

Figure 6
Geometry for flux calculation in forward spectrometers.

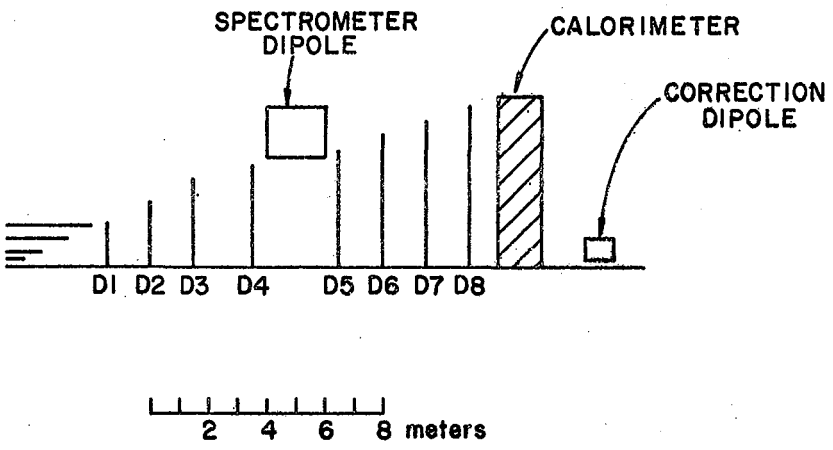

Figure 7
Layout of forward spectrometer.

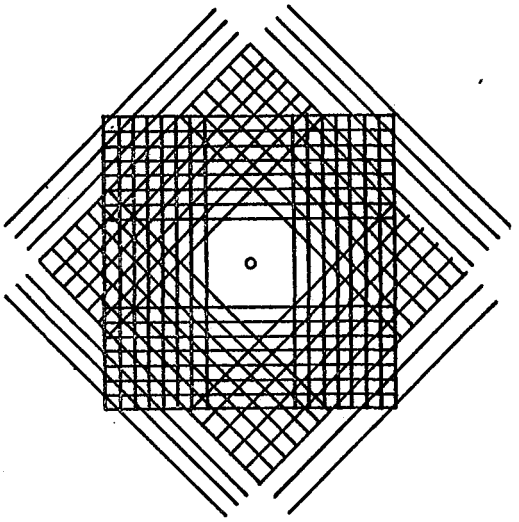

Figure 8
Orientation of wire planes in one module of the forward spectrometer.

THE PERFORMANCE OF A 16000 WIRE MINI-DRIFT MWPC SYSTEM

P. Chauvat, R. Cousins[1], K. Hayes, A.M. Smith
CERN, 1211 Geneva 23, Switzerland.

R. Bonino, J. Ellett, M. Medinnis, A. Russ, P.E. Schlein[2],
P. Sherwood, J.G. Zweizig
University of California*), Los Angeles, California 90024, USA

J. Alitti, B. Bloch-Devaux, A. Borg, J.B. Cheze, A. Diamant-Berger,
I. Giomataris, B. Pichard, F. Rollinger, M. Tararine, J. Zsembery.
Centre d'Etudes Nucleaires-Saclay, 91190 Gif-sur-Yvette, France.

The Mini-Drift chamber system and associated electronics employed in experiment R608 at the CERN-ISR are described. The performance of the system which utilizes 3mm spacing MWPCs produces a spatial resolution of σ = 180 μ under experimental conditions.

INTRODUCTION

While it has been believed since the early days of Multi-Wire- Proportional-Chamber usage that spatial information was available in the arrival time of chamber pulses [G. Charpak et al.-NIM 62, 235(68)], no full-scale experiment has, to our knowledge, made use of this information to improve resolution. This was due partly to the vast amount of electronics necessary to time-digitize signals from a typical experiment with tens of thousands of channels, and partly to the advent of larger cell drift chambers.

Nonetheless, in experimental situations with high rates or high spatial density of particles, one would like to retain the narrow cells of MWPC systems while achieving the σ = 200 μ resolution typical of drift chambers.

In our application at the CERN Intersecting-Storage-Rings, we were faced with a relatively high rate ($\approx 10^6$/sec) and particle density in the forward direction of $\bar{p}p$ and pp interactions. Moreover, the available magnetic field integral was low ($\approx$0.3 Tm), so that σ = 200 μ was needed for good momentum resolution. Thus, the Mini-Drift solution was chosen.

The NEVIS group of Sippach et al. pioneered in the development of a compact 16 channel 6-bit TDC using ECL electronics. In the system described here, we have carried on in this direction in developing a 32-channel 4-bit ECL TDC module. We have also developed a fast readout system and associated multiplicity logic which has a data flow rate of several hundred Megabytes per second. In particular, we have constructed and gained experience with a large system consisting of 514 32-channel amplifier-cable-TDC units.

Besides the electronics demands made by Mini-Drift, the inherent problem of left-right ambiguity resolution is exaggerated because the tracks are always close to the nearest sense wire (1.5 mm in our case). Redundant measurements are necessary to insure a high probability of correct solutions.

The charged-particle spectrometer of experiment R608 at the CERN ISR has been in operation since February 1981. The system performs well even at the highest ISR luminosities, with good multi-track efficiency and momentum resolution. The global spatial resolution, measured to be σ = 180 μ, results in momentum resolution of $\sigma p/p$ = 5.8 % AT 26.7 Gev/c.

SPECTROMETER AND CHAMBER CONSTRUCTION

The layout of the double septum magnetic spectrometer is shown in figure 1. The wire chambers of the spectrometer, constructed at Saclay, consist of five pairs of MWPC packs placed above and below the ISR beam pipe with 3 pairs upstream and 2 pairs downstream of the magnet. The chambers above the pipe and those below the pipe can be thought of as constituting two independent spectrometers, which we refer to as the UP and DOWN spectrometers, respectively. There are 16448 wires in the system.

Each chamber pack has four planes of wires, X, X', Y and U, the latter being inclined at approximately 37 degrees to the vertical. The X' and X wires are vertical and are displaced horizontally with respect to one another by 1/4, 1/2 or 3/4 of the 3 mm wire spacing.

The chambers are constructed with 7 mm between a sense wire plane and each of its neighboring cathode planes. The cathode planes are constructed of mylar with graphite coating on both sides. The chambers are operated with the cathode planes at -3.3 kV giving the potential distribution shown in Figure 2. This distribution is typical of MWPCs, and is different from the standard drift chamber field configuration. In order for the pulse arrival time to measure the distance in the sense wire plane between a sense wire and the traversal point of a track in that plane, the ionization electron nearest the sense wire plane must not be too far from that plane. With 40 or more ionization centers per track traversal and with electronics sensitive to the first electrons, this condition appears to be satisfied. Clearly the velocity is not near saturation in the well-known low-field region midway between the wires but this appears to pose no problem as discussed in section 1.4 below.

The chambers are filled with 60% argon, 39% isobutane and 1% of a mixture of argon containing 1% freon. The argon is bubbled through isopropyl alcohol at 4 degrees celsius. While we have not made extensive tests of the optimal gas mixtures for this application, it is noteworthy that the desired results have been obtained with this rather typical unexotic gas mixture.

CHAMBER ELECTRONICS

The amplifier cards consist of four amplification stages each utilizing a Motorola MC10115 Emitter-Coupled-Logic (ECL) integrated circuit, followed by a MC10116 line-driver stage. The inputs of the 10116's are biassed to 200 mv so that an amplified chamber signal of -300 mv produces a full differential logic swing at the output. With four cascaded stages of amplification, a small change from the nominal VEE of -5.2 V allows the overall gain to be adjusted from a maximum of 1500 down to 800 or less. In our system, the amplifier cards are operated at -4.8 V, resulting in a gain of 1100 and a lower operating temperature for the cards. At this setting, there is a 0.3 mV threshold which produces differential ECL logic pulses of 1.2 V at the end of the 70 meter cable. The cables are Ansley 101-wire flat polyethylene cables with every third wire grounded.

The TDC system, shown schematically in Figure 1, was designed and manufactured at UCLA for this experiment. It digitizes the drift times and encodes the addresses of those wires in the system whose signals arrive during an 80 nsec Level 1 trigger gate. It provides a high-speed path for transfering the wire adresses and drift times to central Randem Access Memory (RAM) on receipt of a Level 2 trigger signal from the experiment. Finally, it makes its own Level 3 trigger decision based on multiplicity logic on the chamber hit data. The Level 3 decision is the computer interrupt.

The TDC cards also have 32 channels so that there is a one-to-one correspondance between TDC and amplifier cards. Up to sixteen TDC cards are mounted in a 19" crate along with their read out module, although a slave crate with up to eight additional modules can also be read out serially by the READOUT module for the larger chamber planes.

The time digitization is accomplished by latching the state of a 4-bit Gray-code counter at the arrival time of a chamber pulse. The Gray-code signals in a given crate are generated by a central clock started by a Level 1 signal from the scintillation hodoscope upstream of the spectrometer. The time bins are 5 nsec wide. Only one "hit" per wire can be registered for each event.

There are 40 READOUT modules, one for each of the wire planes in the system. After an event has been gated into the TDC's, the Level 2 trigger logic either causes the event to be strobed into the MEMORY modules or the entire system is reset. On receiving a good Level 2 ("start readout") signal, the addresses of the wires hit and the digitized times are strobed into the MEMORY modules at the rate of 75 ns/hit with all 40 planes read out in parallel. The total time after a good Level 2 signal to read out all TDC modules to the MEMORY modules is typically 375 nsec for a 5 track event.

There are 20 MEMORY modules, each of which receives data from a pair of wire planes in the upper and lower spectrometers. Each MEMORY module counts the number of wires hit in each plane of the pair separately as the data is received, and compares the hit counts with upper and lower limits which have been previously down-loaded to the modules from the PDP-11 data aquisition computer. Each module also compares the sum of hits from both pairs to a set of upper and lower limits (each plane in the system has its own set of limits).

At the end of the readout process, the results of these comparisons for all MEMORY modules are transferred to a hard-wired processor module called VIRTUS (Very Intelligent Real Time Uvent Selector) which carries out the Level 3 majority logic.

SYSTEM PERFORMANCE

Because of the large size of the system (77,366 IC's), there was initial concern that normal failure rates would make smooth, reliable data acquisition difficult. Experience has shown that this is not the case. The hardware in the system works well. Typically, there are 20 channels dead at the amplifier card level.

Perhaps once or twice a month, a TDC board (or more likely one of the 41 switching supplies that power them) develops a problem. They are easily replaced by spare modules.

The typical drift velocity of 50 μ/ns implies that the time spread of hits in the chambers should be around 30 nsec. A histogram of raw hits recorded on a typical wire for 1000 events (figure 4) shows that most hits occur within 5 or 6 time bins, as expected. Variations from the nominal 5-nsec time bins have been calibrated with a computer-controlled pulser in order to correct for the effects of imperfections in the Gray-code transmission lines.

The small tail at large times in Figure 4 is due mainly to late arrivals from tracks which pass midway between two neighboring sense wires. The drift time-distance dependence has been studied by using tracks which have zero drift time in an X-plane wire over a large range of incident angles. The calculated traversal point in its neighboring X'-plane is compared with the drift time information from the struck wire in that plane. The results are shown in Figure 5, which is seen to be linear up to about 1.25 mm from the wire. The last .25 mm or so, where the curve levels off, corresponds to the very low field region seen in Figure 2. The observed non-linearity presents no analysis problems - large times correspond to large distances - but it is necessary that the Level-1 gate be long enough to have full efficiency. Our measured chamber efficiency is typically 99% with the 80 nsec gate.

About 5% of the time, a particle will cause two adjacent wires to fire (i.e. a cluster). Figure 6 is a scatter plot of the times (in units of tdc bins) for the two adjacent wires in two-wire clusters. It can be seen that both hits have times which lie in the tail of figure 4. Most clusters then result when a track passes through the low field region (see fig. 2) near a cell boundary. (Other mechanisms such as δ-ray production or the presence of a nearby track would usually result in a short time for at least one of the wires. This fact is useful since it allows immediate resolution of the left-right ambiguity (discussed below) of any 2-wire cluster. Closer examination of events in Figure 6 in which both recorded times were less than 30 nsec shows that these are mainly due to the presence of a second track.

OFFLINE ANALYSIS

The offline pattern recognition program finds tracks using only the wire hit information. The momentum is then determined by fitting to the coordinates determined from the drift-time information. The spatial resolution can be illustrated in the following way. Consider the hits in the X and X' planes for one track crossing a particular chamber. The time information can be used to calculate the distances, d_1 and d_2 respectively, of the track from the hit wires in these planes (see Figure 7). If we assume that the track passes on particular sides of its two wires, d_2 can be predicted using the known slope and the measured distance d_1. Figure 7 also shows a histogram of the difference between the predicted and measured d_2 for all hits in one chamber for the case where the track has been assumed to pass on the right side of both wires. The peak centered at zero comes from those instances where this assumption was correct, while the shoulder at larger values contains all the cases where the assumption was wrong. The width of the peak is $\sqrt{2}$ times the actual resolution which is typically σ = 180 μ. The relative areas of peak and background in Figure 7 depends on the relative offsets of the X and X' planes and on the angular distribution of the tracks used. A direct measurement of the momentum resolution is shown in Figure 8, which is a histogram of the reconstructed antiproton momentum in elastic scattering at 26.7 Gev. This distribution has $\sigma p/p$ = 5.8%.

Finally we comment on the question of left-right ambiguity resolution with our system. The solution of the left-right ambiguity in any given plane requires that we can predict, using all the available information for a track, where it passed through that plane. The ambiguity will be solved if one and only one of the two possible solutions is consistent with the data from all the other planes.

We solve the ambiguity problem in two steps. First we calculate the track trajectory using only the coordinates of the hit wires. This gives us, to good approximation, the local direction cosines of the track at each chamber pack. The ambiguities are then simultaneously solved for all four planes in a chamber by exploiting the two constraints which relate the four measurements of the track coordinates in the chamber pack. This is done by considering each of the 16 possible solutions. If only one combination satisfies the two constraints, all four ambiguities are solved. If

two or more solutions satisfy the constraints, then the ambiguities for one or more planes remain unsolved, depending on the specific combinations.

Using this technique, typically 84% of the cases have at least one X or X' ambiguity solved and about 44% have both solved. Hits for which the ambiguity is not solved are usually those where the drift distance is small ($< 400\mu$), but these cases are unimportant as we already know that the track passed close to the wire. Typically 44% of y-view ambiguities and 56% of u-view ambiguities are solved.

We have attempted to resolve the remaining unsolved ambiguities with a global track fit to the 20 hits in the 5 chamber, using the drift-distance corrected coordinates for those hits whose ambiguities were solved using the method described above. We observed only a small improvement in chamber 2 and no improvement elsewhere. This is because at the chamber level, our track measurements are not highly over-constrained; a different choice of solution results in slightly different track parameters, and not necessarily a different χ^2 for the fit. This illustrates the need for redundant coordinate measurements in a chamber pack if a high efficiency of ambiguity resolution is to be obtained.

The time-distance relationship and the resolution are systematically controlled in the experiment using straight tracks recorded with the ISR operating but with the spectrometer magnet turned off.

ACKNOWLEDGEMENTS

We very much appreciate the excellent work at S.T.I.P.E (Saclay) in the design and construction of the chambers. We are grateful to the U.S. National Science Foundation and to the UCLA Physics Department for the support which allowed the development of the chamber electronics. We thank CERN and the ISR Experimental Support Group for their important help in setting up the entire system. P.E.S. thanks Bruce Knapp and Bill Sippach for many invaluable discussions on their experiences with Mini-Drift.

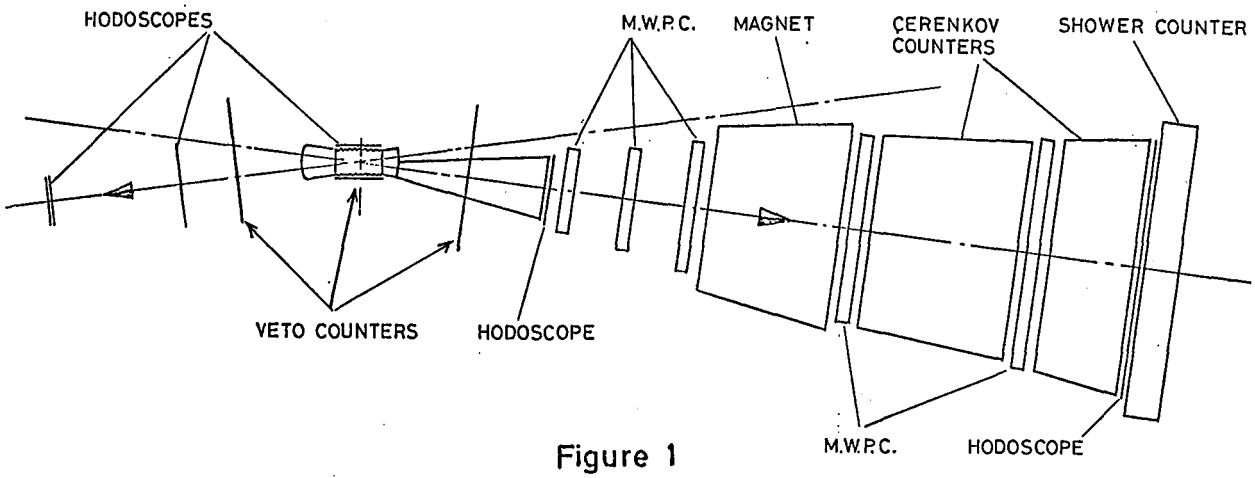

Figure 1

Layout of the R608 spectrometer.

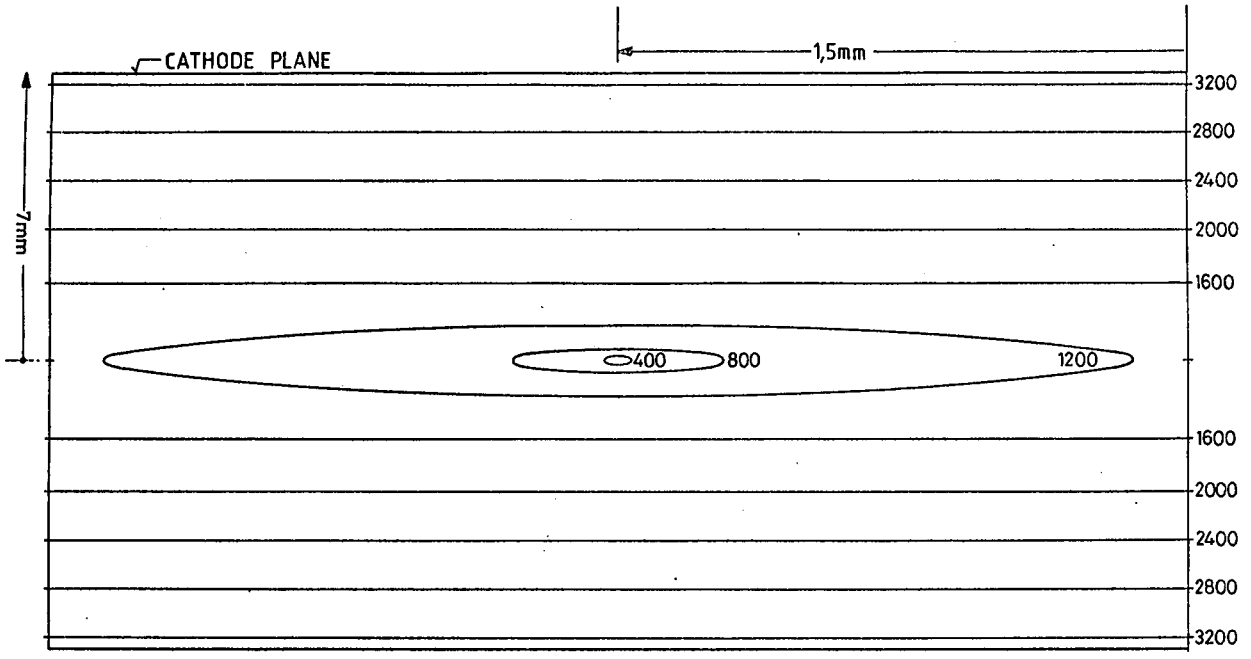

FIELD DISTRIBUTION
3mm WIRING SPACING

2. The electric field distribution around one anode wire.

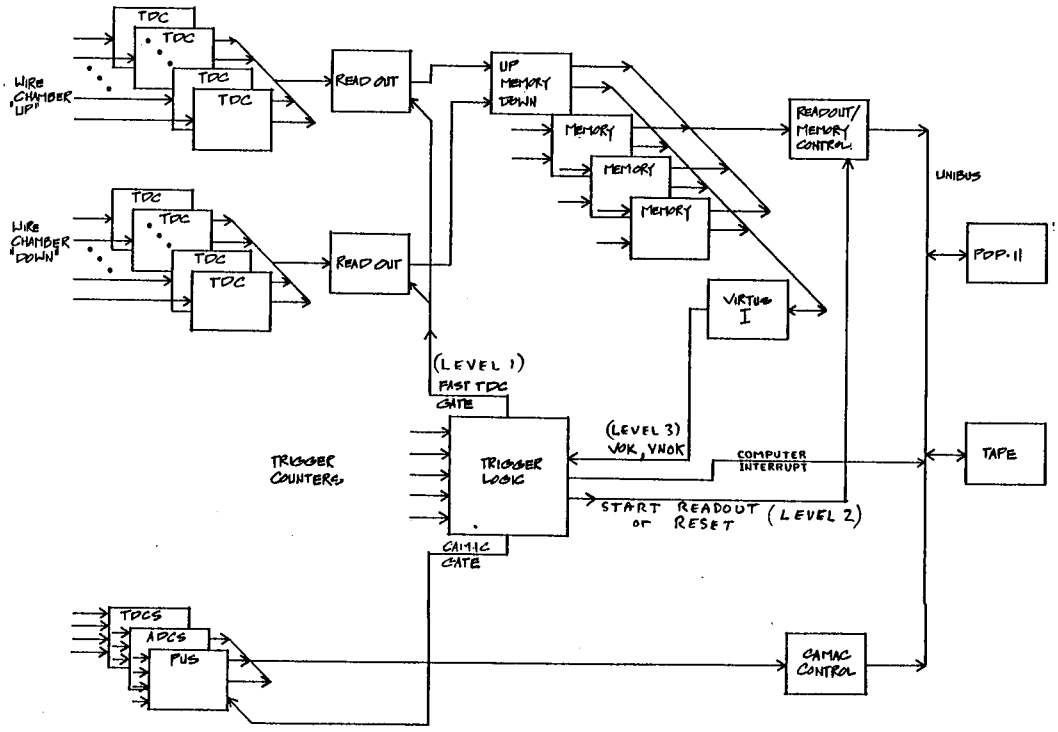

3. Block diagram of the chamber TDC and readout system.

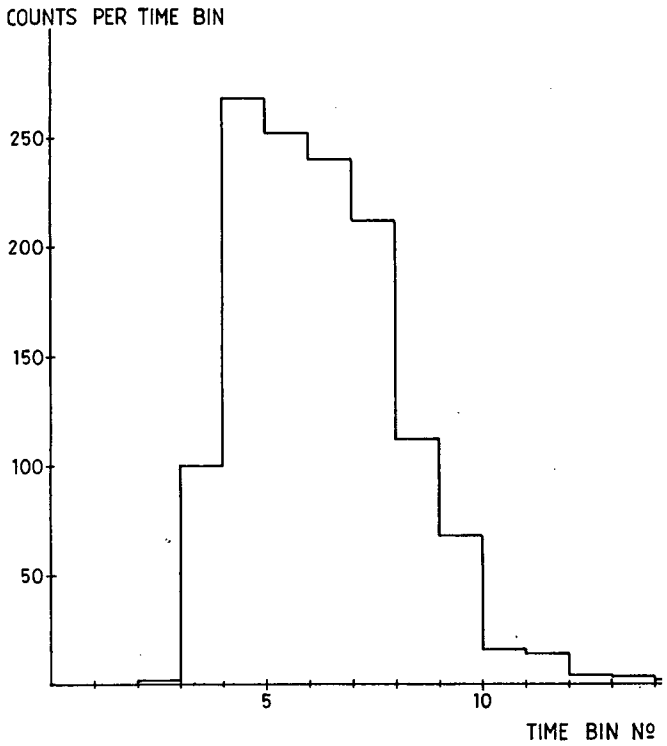

4. A histogram of the times recorded in the TDC's of one chamber.

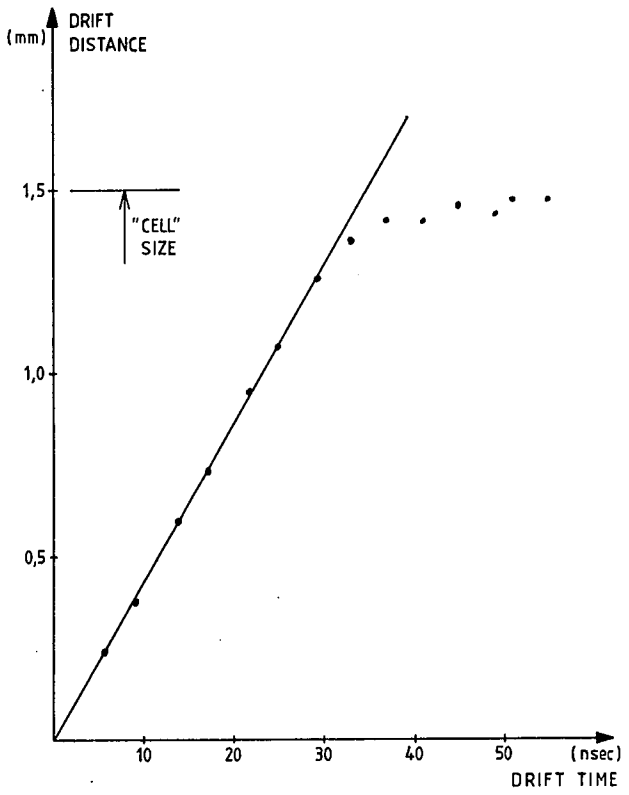

5. The time/distance relationship obtained from fitted tracks.

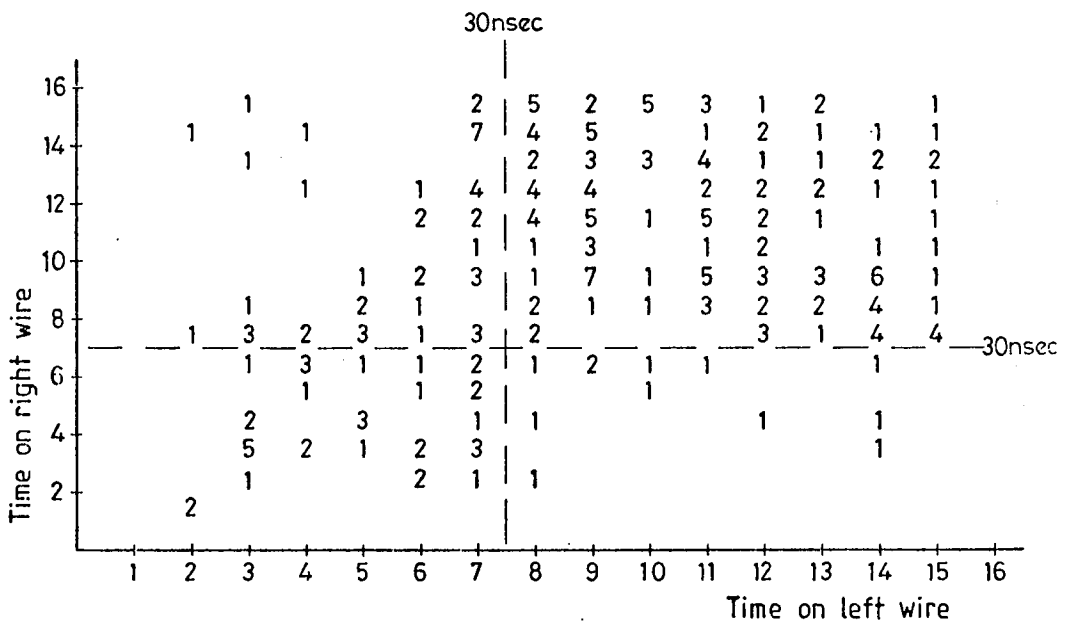

6. A scatter plot of the times recorded when two neighbouring wires both register hits (for hits used on found tracks).

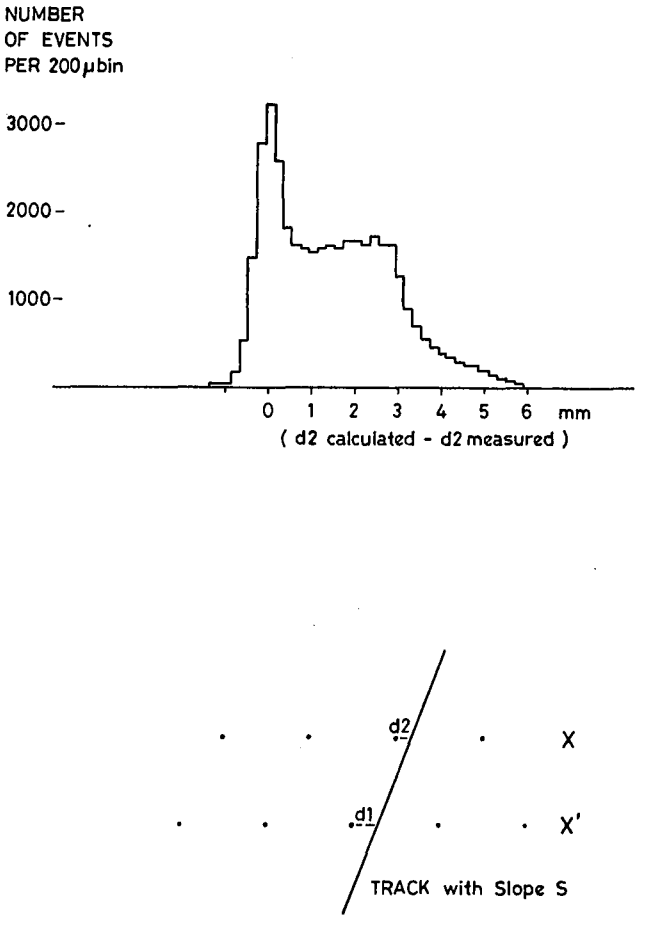

7. An illustration of the method employed to measure the resolution.

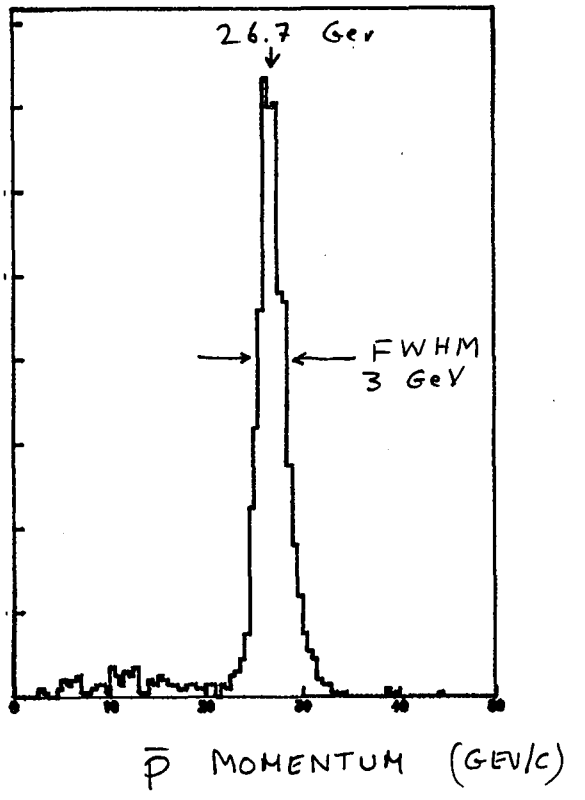

8. Measured momentum distribution of elastic antiprotons at 26 Gev.

BREAKDOWN PROCESSES IN WIRE CHAMBERS, PREVENTION AND RATE CAPABILITY

M. Atac

Fermi National Accelerator Laboratory*

Summary

Breakdowns were optically and electronically observed in drift tubes and drift chambers. They occur at a critical gain for given intensity in a gas mixture when ultraviolet photons are not completely quenched. It was observed that the breakdowns depended critically on average current for a given gas mixture independent of the size of the drift tubes used. Using 4.6% ethyl alcohol vapor mixed into 50/50 argon ethane gas, breakdowns are eliminated up to 7 μA average current drawn by pulses on a 1 cm section of an anode wire under an intense source. Pulses with an avalanche size of 10^6 electron rates above 10^6 pulses per centimeter per wire may be obtained with the elimination of breakdowns.

Introduction

Operation of drift chambers and proportional chambers has been a painstaking struggle for many groups until the end of their experiments. For every case it took a learning period to accomplish satisfactory operation. Some people trained wires by allowing a small current for burning off contamination on cathode wires, some found certain gas mixtures improved the situation, some were able to operate at low gain by reducing pickup noise, thus increasing amplifier discriminator sensitivety, etc. In most cases, especially where beam rates were high, hot wires showed up in a random way. These hot wires had to be replaced or cleaned or disabled. Unfortunately no one has written a few paragraphs to explain what helped them for satisfactory operation. For this reason no references can be given for the above cases. All information was obtained by friendly private communications.

Most of the problems may have been due to arbitrary chamber designs and casual selection of gases. One took someone elses design, because that worked. It may have worked with certain gain and for certain rates, but it may have failed at higher beam intensities. Detailed studies of breakdown processes in gases were done[1] earlier using mainly parallel plate geometry. There has been no methodic study of breakdowns with very commonly used gases in multiwire drift chambers or drift tubes.

This paper is the result of some systematic studies of breakdown processes and prevention of chamber breakdowns related to beam rate and gain.

a. Breakdown in Drift Tubes

The following tests were carried out to help understand intensity and gain related breakdown processes in wire chambers. For simplicity two aluminum tubes of different sizes, a conductive plastic tube[2] and a small drift chamber with a few wires were used for the tests. All the tubes and the chamber had transparent windows for optical observation. These windows were made of In-Sn Oxide transparent film on mylar.[3] The film is sufficiently conductive to serve as a cathode material. The aluminum tubes were 9.5 x 9.5 mm^2 and 12 x 12 mm^2 cross-section, and the conductive plastic tube was 7 mm x 10 mm. Configuration of the drift chamber is shown in Fig. 1. The anode wires in the tubes and of the chamber were 50 μm thick gold plated tungsten. The gas mixture for these tests was 50/50 percent premixed (by volume) argon-ethane flowing through ethyl alcohol (CH_3CH_2OH) at 0°C at a rate of 200 cc/min.

A narrowly collimated (large fraction of the intensity within 5 mm diameter circle) Sr^{90} source of 1 mCi strength was held at a short distance from the tubes. Intensity of the source was regulated by aluminum shim absorbers.

As shown in Figs. 2-a,b and c, independent of the source position along the wires in the tubes, a spontaneous breakdown occurred at a critical gain and a critical intensity. It occurred randomly within a minute (from a few seconds to a minute). Thus the points were taken at three minute intervals. The manifestation of the breakdown is a sudden increase in the high voltage power supply current that slowly reaches to a value around 10 μA which is limited by the gas impedance (there was no current limiting resistor in the circuit). This current is sustained until the high voltage is lowered considerably.

Average dc current drawn through the power supply was monitored. An interesting fact is that the current was approaching 0.4 to 0.5 μA when the breakdown occurred independent of the tube size and intensity. The conclusions from the results are that the breakdown is critically dependent on total average current (i.e., gain x intensity) for this collimation of the source illuminating mainly 1 cm of the anode wire, and the value of the current is 0.5 μA for this gas mixture. It is an important matter to note here that after so many breakdowns the wires held the voltage values at the intensities given. The wires and the cathode surfaces were examined under a microscope showing no observable damage. The gain characteristics of the 9.5 mm x 9.5 mm tube is given in Fig. 3 using a Fe^{55} source to get an idea about the gain values for Fig. 2a. Primary ionization characteristics of the Sr^{90} source is rather different; Sr^{90} results in a wide range of primary specific ionization.

As an exercise let us take Fig. 2a. Breakdown voltage is around 2.4 kV for the source intensity of 1.25×10^5 sec^{-1}. The gain value obtained from Fig. 3 for 2.4 kV is 10^5. 0.5 μA average dc current corresponds to 5×10^{-7} Coulomb of charge. This is $\sim 3.1 \times 10^{12}$ electrons. An average avalanche size (number of total electrons after multiplication) per track is

$$\frac{3 \times 10^{12}}{1.25 \times 10^5} \simeq 2.4 \times 10^7 \text{ electrons.}$$

Then the average primary ionization per track is

*Operated by Universities Research Association Inc. under contract with the United States Department of Energy

$$\frac{2.4 \times 10^7}{10^5} = 240 \text{ electron-ion pairs.}$$

This is a reasonable number for the source.

The same tests were attempted with the small drift chamber using the same gas mixture and the same source strength. No breakdown up to 7 μA dc at 3.1 kV applied voltage was found. Self quenching streamers showed up at a voltage around 2.6 kV and at 3.1 kV mainly streamers were observable.

b. Optical Observations and Rate Capability

Using an image intensifier video camera described in an earlier paper,[4,5] photons from the active area were observed while the average dc current was measured as a function of applied high voltage. Pulses from the anode wires were also observed to detect streamer transitions when the applied voltage was sufficiently high. High voltage versus measured current characteristics is shown in Fig. 4. Space charge saturation begins at 2.3 kV (avalanche saturation). The streamer threshold is around 2.75 kV.

Once the breakdown is eliminated the drift chamber wire can take very high rates. Figure 4 also shows that up to 0.4 μA current gas gain is exponential. This current corresponds to over 2 x 10^6 pulses per second per one centimeter length of the anode wire for a uniform flux of β-rays having gas gain above 10^5:

$0.4\ \mu A = 0.4 \times 10^{-6}$ coulomb/sec, corresponds to

$$\frac{4 \times 10^{-7}}{1.6 \times 10^{-19}} = 2.5 \times 10^{-12} \text{ electrons}$$

Avalanche size of a typical drift chamber pulse is about 10^6 electrons, thus

$$\frac{2.5 \times 10^{12}}{10^6} = 2.5 \times 10^6 \text{ pulses/sec. 1 cm wire}$$

Photon activity around the anode wires of the drift chamber makes the wires visible as shown in Figs. 5a, b and c. The source rate was $\sim 10^5$ counts for each wire per second. The higher the gain the more photons are detectable. Some short streamers are visible at 2.8 kV (Fig. 5b). Many more can be seen at 3.1 kV (Fig. 5c). These and further pictures are the negatives of the polarized photographs for better visibility in copying processes. The photographs are 1/20th second time exposed pictures taken from a video monitor. The author believes that these photons come from some recombination processes not from normal avalanche processes. A hint for this is at low rates (less than 10^4/sec) only streamers can be seen when the voltage exceeds 2.7 kV; no photons could be detected below the streamer transition. A large number of photons are emitted from the space surrounded by cathode wires when the source intensity is high and the gas gain is sufficiently high, and the space is filled by an ion cloud. Even then no breakdown, (i.e., no sustained activity) was observable up to 3.1 kV with the gas mixture when the source was pulled away.

c. Breakdown in the Drift Chamber

This time the 1.4% ethyl alcohol component of the gas mixture was removed; only 50% A - 50% C_2H_6 mixture was used. The β-source was kept at the same place from the chamber, thus providing about 10^5 counts per second per wire over mainly 1 cm of length. In this case, wires were visible at 1.8 kV. A boiling hot circle appeared (Fig. 6) at 1.9 kV. The circle became very visible at 2.1 kV and it stayed active when the source was pulled away. The high voltage had to be lowered below 1.8 kV for the active circle to disappear. This and other phenomena will be explained further in the paper. The high voltage was turned off and on each time the hot spot appeared (at the same place). Each subsequent discharge appeared at successively lower voltages. Thus the first breakdown left a scar on the wires and it was getting worse at each repeated breakdown. Figure 7 shows the relation between the average dc current and the applied voltage. The breakdown current of 0.31 μA is interestingly close to what was found with the tubes previously.

The above results indicate that CH_3CH_2OH is an important element in the gas mixture in preventing the breakdown and probable surface damages related to intensity and gain.

d. Preventing Breakdowns in the Conductive Plastic Tube

More tests were carried out for understanding the effectiveness of the ethyl alcohol component in the A - C_2H_6 gas mixture in preventing breakdowns mentioned in the previous sections. The conductive plastic tube was chosen for the following experiments because of its small size (7 mm gap).

As explained in the previous sections, breakdowns did occur at critical gains and critical intensities (Fig. 2c) with the conductive plastic tube in the gas mixture of 49.3% A - 49.3% C_2H_6 - 1.4% CH_3CH_2OH, but there was no breakdown in the drift chamber until the ethyl alcohol vapor was removed. To help understand these phenomena, the ethyl alcohol vapor concentration was varied from 0 to 4.6% and breakdown current was measured with a source intensity exceeding 1.5 x 10^5 pulses per second. The results are shown in Fig. 8. Breakdown current is very low (around 0.1 μA) without CH_3CH_2OH and the breakdown is practically eliminated with 4.6% CH_3CH_2OH in the gas mixture. There was no breakdown up to 7 μA. This is a very respectable current (i.e. gain x rate per second), therefore no attempt was made beyond this intensity and the gain.

It was clear from the results above that ethyl alcohol did enable the tube run at much higher gain without breakdown. Then the next logical experiment was to study other alcohol vapors, namely, methanol (CH_3OH) and isopropanol ($(CH_3)_2$ CHOH). Figure 9 shows partial vapor pressures of the alcohols mentioned as a function of temperature. The numbers are taken from "Handbook of Chemistry and Physics". From these curves we find that we need to keep CH_3OH at 3°C and $(CH_3)_2$ CHOH at 35° C to have 4.6% of each in the A - C_2H_6 mixture. Clearly, the latter was found not to be practical. Tests also showed that bubbling A - C_2H_6 through $(CH_3)2$ CHOH at room temperature was not sufficient for preventing the breakdown. CH_3OH had to be kept around 10°C to be effective. This may be due to the reason that CH_3OH is a less complex molecule than CH_3CH_2OH, and thus

would have less rotational and vibrational absorption levels for quenching ultraviolet photons which could reach the cathode and knock out electrons. CH_3CH_2OH should also be preferred because it is not an active vapor for plastics, epoxy, etc.

Optical studies also confirmed the results above. Some details are given in the next section.

e. Optical Observation of Geiger Mode

The conductive plastic tube was studied through the image intensifier camera to gather more information about the breakdown processes. As discussed in the previous sections, breakdowns could occur in the tube when the ethyl alcohol concentration in the argon-ethane gas mixture was below 4.6%. Such a breakdown was observed on the video display. Bright spots around the anode wire showed up. After a few seconds more bright spots appeared and then the brightness spread quickly all along the wire. At this time about 10 μA current was drawn through the high voltage power supply even though the source was pulled away. It continued until the voltage was lowered below 1.5 kV. This sequence is shown in Fig. 10a,b and c. Interestingly, the holding voltage of the wire stayed the same after many breakdown tests even after allowing 10 μA of breakdown current to continue for more than 10 minutes with the existence of ethyl alcohol vapor in the gas mixture. After the tests, surfaces of the anode and cathode were examined under a microscope and no visible damage was found.

Is this a true Geiger mode? This question will be discussed further in the paper. There was no observable breakdown on the screen when 47.7% A - 47.7% C_2H_6 - 4.6% CH_3CH_2OH gas mixture was used. Figure 11a and b show the photon activity around the wire at currents of 0.7 and 3 μA, respectively. Figure 11b shows projections of the self-quenching streamers around the anode wire.

The Geiger mode-like spread along the anode wire of the conductive tube could not be seen in the aluminum tubes. The breakdowns were around local spots. A reason for this may be due to the aluminum tubes being considerably larger in size. All the evidence found with this and earlier work[5] indicate that breakdown spread along the wire is mediated by electrons knocked out of the cathode walls by ultraviolet photons, unlike the well known Gieger operation.[6]

f. Epoxy Droplets on Cathode Wires Affect Operation of the Drift Chamber

Some cathode wires of the beam drift chamber (mentioned in Sections a and c) were smeared with epoxy which formed droplets around the wires as shown in Fig. 12. Optical observation on the video display showed that at 2.2 kV (0.16 μA) a hot spot on the wire appeared with 1.6% ethyl alcohol in the gas mixture and it got brighter at 2.7 kV (2 μA) seen in Fig. 13. The hot spot disappeared when the source was pulled away. The position of the spot was in the region where the epoxy droplets were. This could not be observed under the same conditions given above when the same anode wire plane and a clean cathode wire plane were used. A probable explanation for this phenomenon is that the epoxy charges up with the positive ions, polarizes and becomes an electron ejector (Malter Effect). If this is so it could explain why the spot disappeared when the high flux of positive ions stopped (removing the source).

g. More Boiling Hot Circles

It was discussed in Section c that circles showing boiling-like activity in the drift chamber were observed with the image intensifier camera using 50% A - 50% C_2H_6 gas mixture and this breakdown condition was completely prevented by the addition of ethyl alcohol vapor. The tests were done with a newly wired chamber frame. This time identical wire planes of a damaged beam drift chamber were used for the tests. The chamber had some breakdowns while operating with the A - C_2H_6 gas only. There were clearly seen scars on the anode wires.

Hot spots were observed in this chamber up to an ethyl alcohol concentration of 3.3% in the gas mixture. Figure 14a shows the hot spots around the anode wire with the β-source illuminating the chamber (breakdown current of 3 μA). Figure 14b shows that the hot spots remained after removing the source. A boiling circle showed up near the cathode that feeds one of the hot spots on the anode when the camera's sensitivity was increased (Fig. 14c). Hot spots completely disappeared when 4.6% alcohol vapor was used, as seen in Fig. 14d. The conclusion is that even a damaged chamber can be successfully used when complete UV quenching is achieved.

h. Some Hints from the Experimental Results

The following conclusions can be summarized on breakdowns and their prevention from the experimental results given in this paper:

1. The breakdown is strongly dependent upon the average current for a given gas mixture (i.e., higher gain for smaller beam rate).

2. The current = gain x primary ionization x rate can be increased with additional quenching vapor.

3. For all types of the chambers examined here ethyl alcohol, CH_3CH_2OH is an excellent quencher in reducing breakdown probability. 4.6% ethyl alcohol vapor in 47.7% A - 47.7% C_2H_6 mixture appeared to be sufficiently good quenching gas for currents up to 7 μA without any breakdown, even with damaged wires.

4. Epoxy droplets may produce hot spots on anode wires.

5. In conductive plastic tubes of 7 mm size, a Geiger-like mode was observed.

6. There was no detectable damage on the anode or cathode surfaces after successive breakdowns using the Ar - C_2H_6 - CH_3CH_2OH gas mixture.

7. A lifetime test was made with the drift chamber using 49.2 A - 49.2% C_2H_6 - 1.6% CH_3CH_2OH and a high flux Sr^{90} β-source. There was no detectable damage on the wires for integrated pulses of 10^{11} with a gain of 10^5. This amounts to a total of 2.4 x 10^{18} electrons/cm on the wires (see Section a).

8. Electron drift velocity is affected by the addition of ethyl alcohol vapor. This remains to be measured in a systematic way.

9. Last, but not least, there is a great deal more to be learned on the subject.

i. Breakdown Processes

Some explanations can be given on how and why breakdowns occur in wire chambers or drift tubes using the results given in this and the earlier paper.[5] These explanations may be supplementary to the work edited by H. Raether[1] for the parallel plate configuration.

1. In the avalanche process, a critical charge density is reached before the streamer action so that radiative recombination can occur.[5]

2. What makes the streamer grow is most probably a reproduction of electrons near the streamer head by the recombination photons.

3. Another probable way of streamer growth may also occur when a highly intense beam or source is used. Coincidentally, some electrons happen to be present from another track near the tip of an avalanche cone although the critical charge density may not have been reached for regeneration of electrons by the radiative recombination photons. These accidental electrons could in succession enable the avalanche to grow into a full streamer. The streamer may grow close to the cathode. When this happens electron regeneration from the cathode could follow by the photons knocking out electrons. This condition could end up with a continuous feedback from the cathode as found in the breakdown conditions when the quenching was insufficient. This feedback mechanism continues even after removing the source (Sections c and g). Figure 15 shows some of these cathode electrons fed back breakdown circles dramatically (boiling circles). Interestingly, the circles are identical in size, about 3.6 mm in diameter (real size). Top views of some of the individual self quenching streamer pictures[5] very much resemble the circles (Fig. 16).

If this is all correct then the anode cathode separation and cathode configuration play an important role in electron regeneration by photons from cathode surfaces. Wire cathode configuration reduces the probability of such photoelectron production, thus it should be preferred relative to continuous cathode coverage (simple solid angle consideration). Work function of the cathode material may also play an important role in this matter.

Conclusions

A suggestion resulting from this work is that one should do a careful study of gain characteristics of a chamber designed for a specific purpose under an intense source using a gas mixture to match with electronics (mainly amplifier- discriminator circuits). It should not be assumed that even for relatively low intensities one can increase gain arbitrarily.

One should not allow breakdown to occur without a protective vapor like ethyl alcohol, otherwise scars may be left on anode and cathode surfaces. Some tests were done using 70% argon 30% isobutane (instead of ethane) mixture bubbling through ethyl alcohol at temperatures up to 17°C, adding about 4.6% alcohol to the mixture, using the conductive plastic tube. Every breakdown left damage on the anode and the cathode surfaces, thus high voltage had to be lowered. Why couldn't the alcohol prevent breakdown with isobutane mixture and damages? This should be investigated.

Acknowledgement

The author would like to express his appreciation to Dr. M. Mishina for many discussions on the subject.

References

1. H. Raether, Electron avalanches and breakdown in gases, Washington Butterworths (1964).

2. M. Atac et al., IEEE Trans. on Nucl. Sci., Vol. NS-29, No. 1 (1982) 368.

3. M. Atac, Nucl. Inst. and Meth. 176 (1980) 1-8.

4. M. Atac and A. Tollestrup, Fermilab Report, FN-337 (1981).

5. M. Atac, A. Tollestrup and D. Potter, Nucl. Inst. and Meth. 200 (1982) 345-354.

6. S. A. Korf, Electron and Nuclear Counters (Van Nostrand 1955).

Figure Captions

Fig. 1 - Cross section view of the drift chamber.

Fig. 2a - Breakdown curve for 9.5 x 9.5 mm^2 size aluminum drift tube. Independent of source position along the wire there was a breakdown at a critical high voltage (i.e., gain) at the given intensity when average current reached around 0.5 μA. The gas mixture was 49.3% A - 49.3% C_2H_6 - 1.4% CH_3CH_2OH.

Fig. 2b - Same as 2a for 12 x 12 mm^2 size aluminum tube.

Fig. 2c - Same as 2a for 7 x 10 mm^2 size conductive plastic tube.

Fig. 3 - Gain characteristics of the 9.5 x 9.5 mm^2 aluminum drift tube in the saturated avalanche and streamer regions.

Fig. 4 - Gain characteristics of the drift chamber using the high intensity Sr^{90} β-source of 10^5 pulses/sec for 1 cm wire. The gas mixture is 49.3% A - 49.3% C_2H_6 - 1.4% CH_3CH_2OH. Drift chamber wire can take very high rates once the breakdown is eliminated, as indicated in the figure.

Fig. 5 - Photon activity around the anode wires of the drift chamber at 2.5, 2.8 and 3.1 kV. The pictures are negatives of the photographs taken from the video display of the image intensifier camera.

Fig. 6 - Hot breakdown circle in the drift chamber

when the ethyl alcohol component of the gas mixture was removed. Diameter of the circle is about 3.6 mm. It remained there even after removing the source.

Fig. 7 - Average current as a function of the applied voltage with the existence of the breakdown circle shown in Fig. 6. There was no ethyl alcohol vapor in the drift chamber.

Fig. 8 - Breakdown current as a function of ethyl alcohol concentration in A - C_2H_6(50/50) for the conductive plastic tube.[2] It shows that no breakdown occurred up to 7 μA when the ethyl alcohol concentration was 4.6%.

Fig. 9 - Vapor pressure curves of ethyl, methyl and isopropyl alcohol as a function of temperature.

Fig. 10 - (a) Hot spots on the anode wire of the conductive plastic tube when the gain is above a critical value for the hot source (see Fig. 2c). 1.5% ethyl alcohol in the gas. (b) More hot spots appear after a moment. (c) Geiger-like spread along the wire.

Fig. 11 - Breakdown was eliminated in the conductive plastic tube by 4.6% ethyl alcohol in the A - C_2H_6 (50/50) gas mixture up to streamer operation with the hot source. (a) Photon activity at 0.7 μA, (b) streamer photons at 3 μA.

Fig. 12 - One of the cathode wire planes of the drift chamber with epoxy droplets which were deliberately smeared on the wires for the study.

Fig. 13 - A hot spot on the anode wire of the drift chamber in the vicinity of the epoxy droplets. Gas mixture contains 1.6% ethyl alcohol. HV = 2.7 kV. Average current was 2 μA.

Fig. 14 - An identical drift chamber with damaged wires. (a) hot spots on the anode wire even with 3.3% ethyl alcohol vapor in the gas; (b) hot spots remain after removing the source; (c) showing one of the hot spots that was fed by a boiling circle near the cathode wires; (d) hot spots could not be observed with 4.6% ethyl alcohol in the gas.

Fig. 15 - Breakdown circles and hot spots on the anode wire of the drift chamber more dramatically seen when the ethyl alcohol was removed from the gas mixture. (a) The source is on, (b) source is off. At a rather low HV = 2 kV and 2.1 kV, average current is around 0.12 μA.

Fig. 16 - (a) A pair of branched streamers grown like a cone with the cathode fed electrons knocked out by ultraviolet photons. (b) An imaginary cone around (a). Top view of the cone is about the same size as the hot circles.

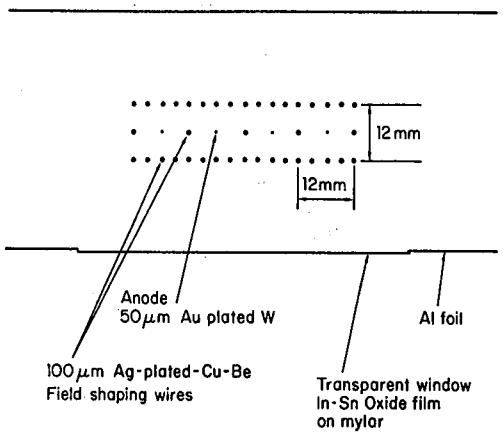

Fig. 1

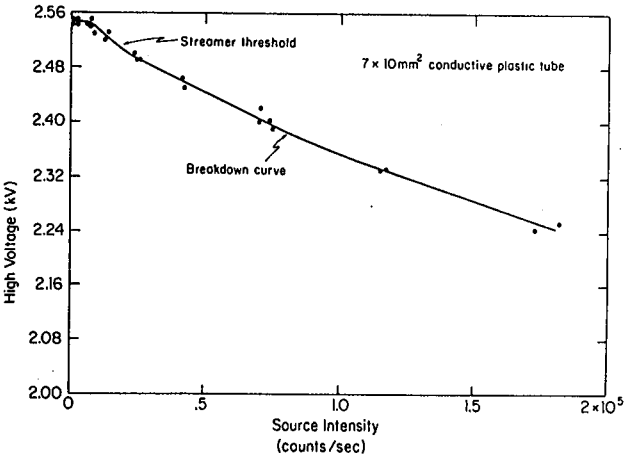

Fig. 2c

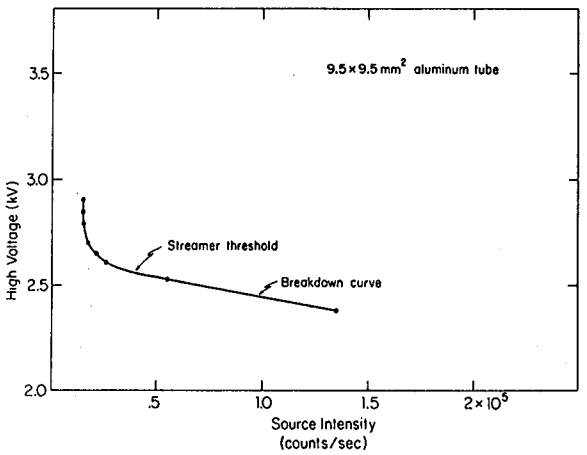

Fig. 2a

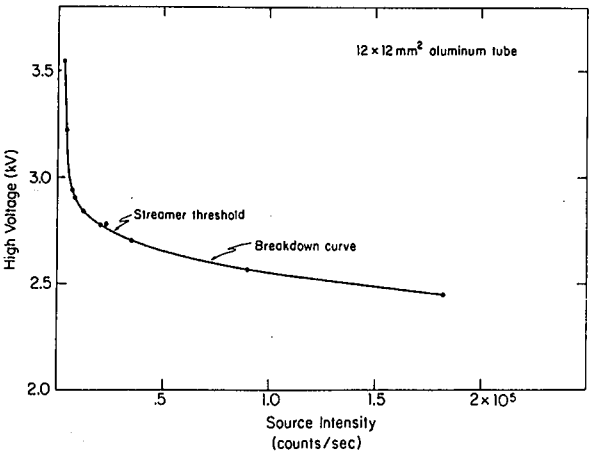

Fig. 2b

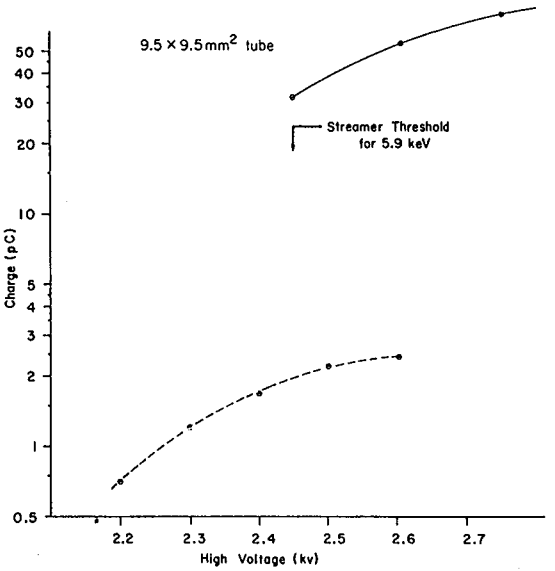

Fig. 3

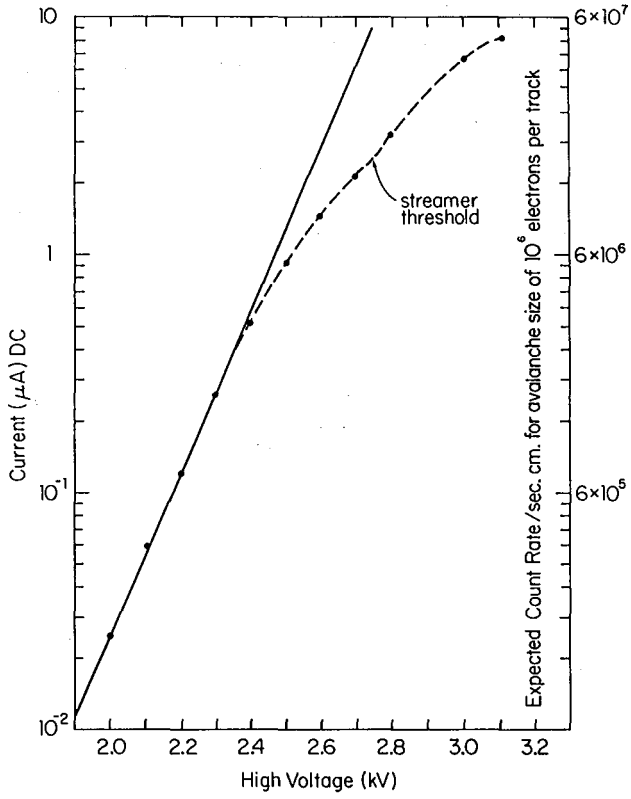

Fig. 4

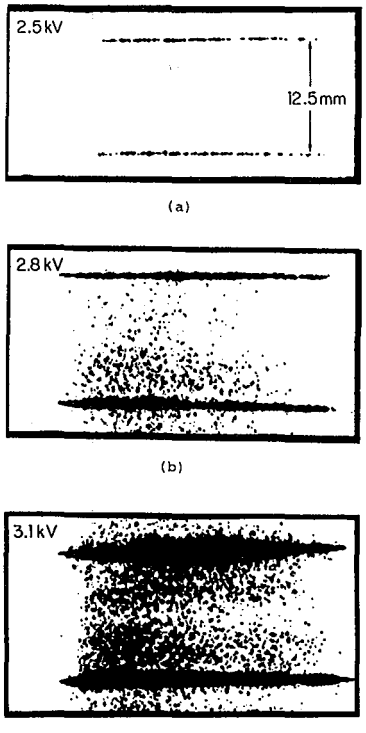

Fig. 5

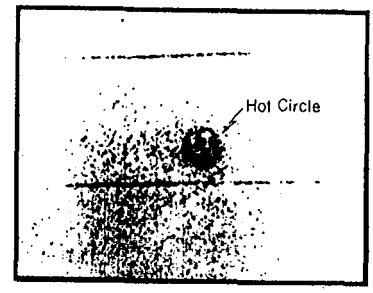

Fig. 6

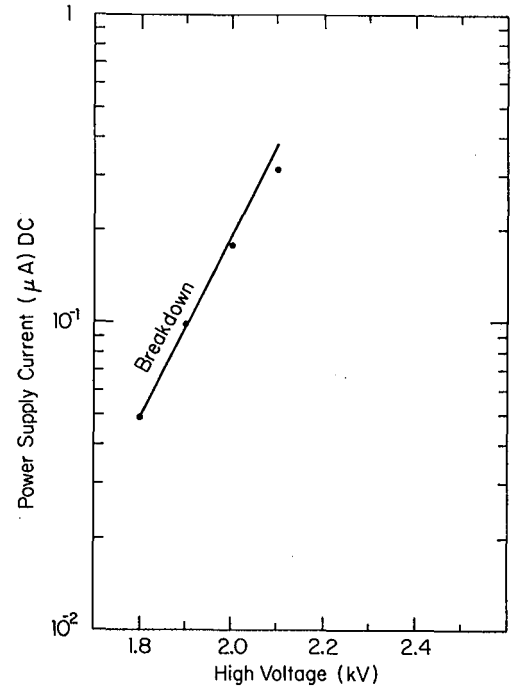

Fig. 7

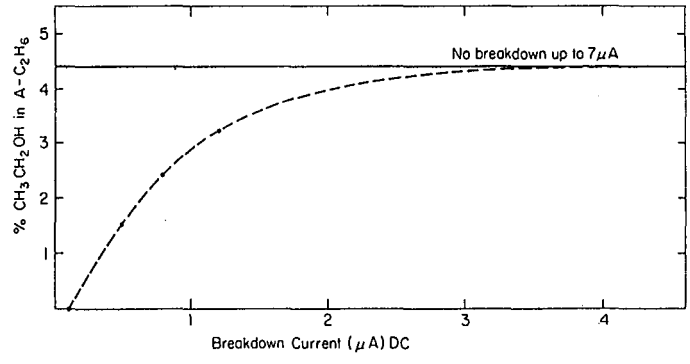

Fig. 8

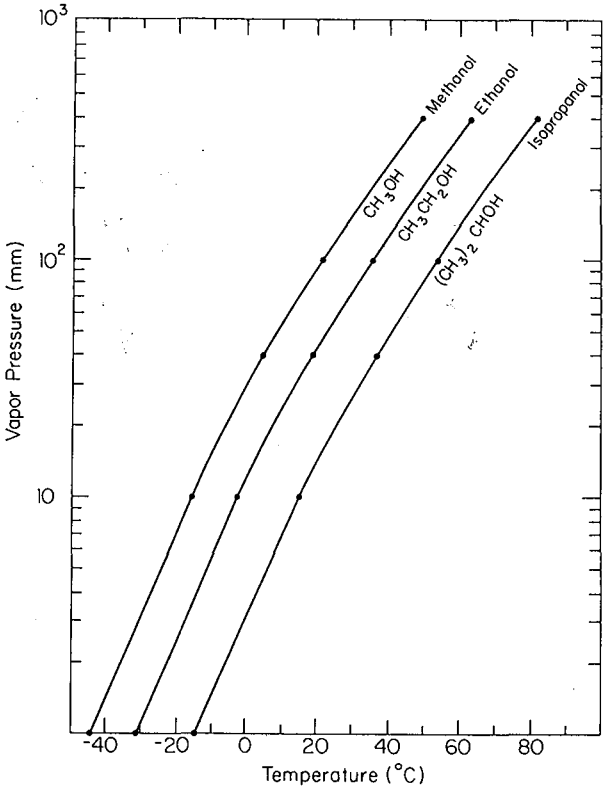

Fig. 9

(a)

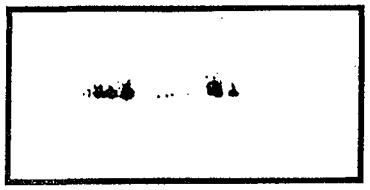

(b)

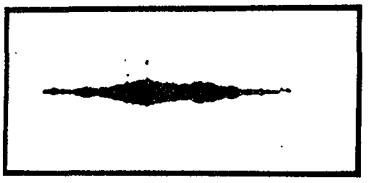

(c)

Fig. 10

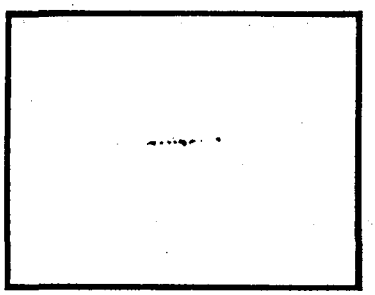

(a)

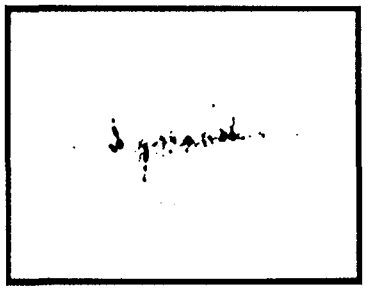

(b)

Fig. 11

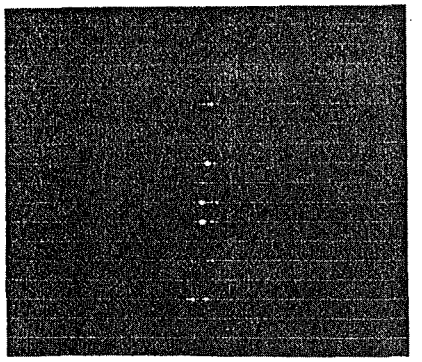

Fig. 12

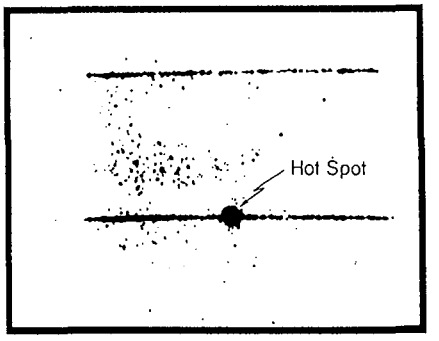

Fig. 13

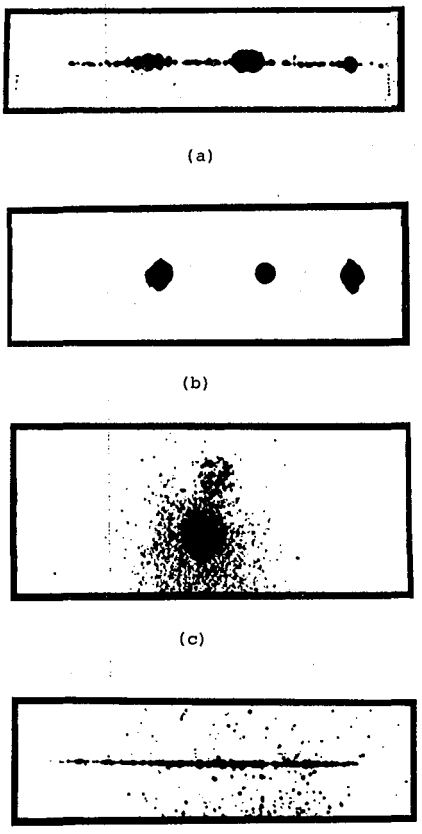

Fig. 14

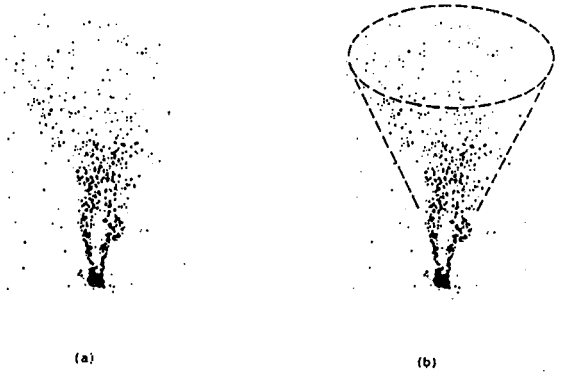

Fig. 16

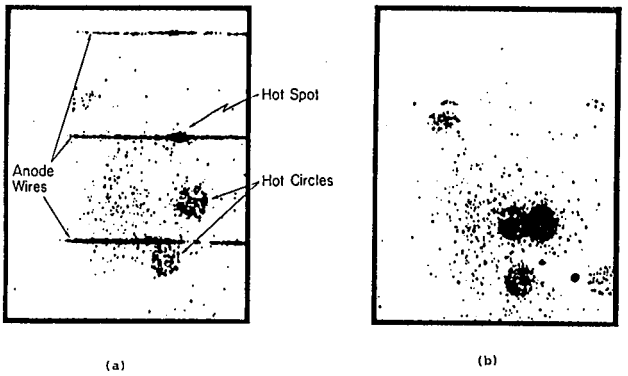

Fig. 15

THE CONCEPT OF A SOLID STATE DRIFT CHAMBER*

E. Gatti†, and P. Rehak

Brookhaven National Laboratory
Upton, New York 11973

I. General Description

The Solid State Drift Chamber (SSDCH) is a thin wafer of a high purity n-type silicon (few cm^2 x a few hundreds μm thick) with a single small-area, small-capacitance anode readout (Fig. 1). The drift voltage is supplied to an array of "drift" electrodes on both sides of the wafer to produce a uniform drift field parallel to the surface of the wafer and to ensure the complete depletion of the wafer.[1]

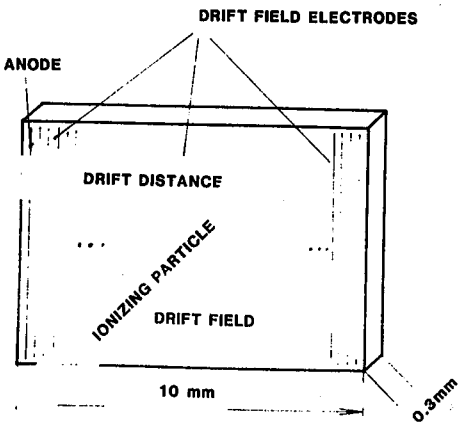

Fig. 1. Solid State Drift Chamber. Silicon wafer is about .3 mm thick and about cm^2 in the front area. The majority of the surface is covered by drift field electrodes (only electrodes at the extremes of the wafer are shown). The ionization produced by a high energy particle drifts toward the anode which is the only readout channel on the wafer.

The wafer is in fact completely depleted through the anode which sits on the highest potential of all electrodes (minimum electron potential energy). By virtue of remaining fixed volume charges and the applied potential to the drift electrons, the potential energy of the electrons inside the wafer has the form of a parabolic "gutter" inclined towards the anode (Fig. 2).

The electrons produced by a fast charge particle inside the wafer moves to the center of the "gutter" and drifts towards the anode. The time difference between the particle passage (scintillation signal) and the arrival of the electrons to the anode is the measure of the drift distance in a similar way as in a gas drift detector.

Due to the much higher density of the silicon compared to the gas, the two fundamental limitations of

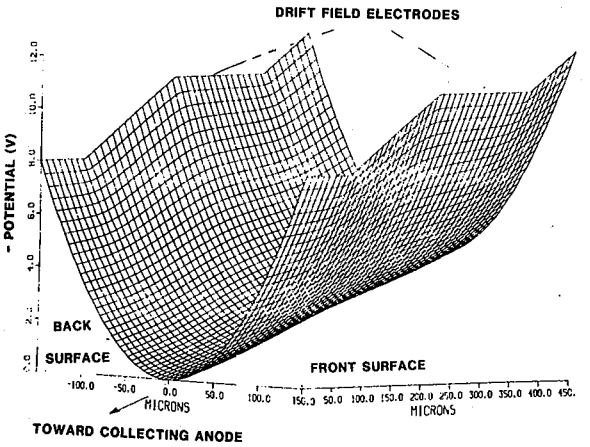

Fig. 2. Profile of the central "gutter" in a SSDCH. The parabolic slope of the channel is due to the remaining fixed charges in the n-type silicon.

the gas drift chamber resolution (δ-rays and fluctuations in the ionization density) are largely reduced.

The following position resolution limiting factors were considered:

i) amplifier noise
ii) electron diffusion
iii) silicon leakage current

The theoretical resolution is expected to be in the region of (2 - 5) μm, i.e., in the region previously obtainable only by emulsion detectors. The test of the devices presently under the construction at BNL will be carried out in the spring of 1983.

II. The Solid State Drift Chamber in High Rate, High Multiplicity Environment.

We would like to evaluate the utility of a Solid State Drift Chamber as a vertex detector for the storage ring experiments.

The ability to measure the position of particles with high precision is not the only requirement of a vertex detector. The multi-particle resolution and the ability to handle the high rate are the additional requirements for a vertex detector.

These additional requirements can be satisfied in a SSDCH by paying a certain price in the degradation of the position resolution. (The drift velocity has to be increased to reduce the memory time of the chamber and also to reduce the diffusion of electrons to facilitate the double track resolution.)

Let us state the merits and limits of a vertex detector for a planned hadron colliding beam accelerator.

* This research was supported by the U. S. Department of Energy: Contract No. DE-AC02-76CH00016.
† Present address: Instituto di Fisica, Politecnico di Milano, Piazza Leonardo da Vinci 32, Milano, Italy.

A special intersection region with the length of a few cms only is required to match the dimensions of the vertex detector. The same beam intensities which produce the luminosities of the order of $10^{33}/cm^2s$ will produce the luminosity of a few times $10^{31}/cm^2s$; still high enough to carry on many interesting experiments. The mean time between two interactions is about .5 - 1. μs.

A drift field of $10^3V/cm$ in silicon corresponds to the drift velocity of 13 μm/ns. With the maximal drift distance of 1 cm the chamber memory time is about 0.7 μs.

The calculated double track resolution is about 100 μm. For tracks closer than 100 μm it is still possible to measure their total number (the total charge measurement) and the center of gravity.

The calculated precision of the position measurement is down to the (5 - 10) μm region limited by the amplifier noise.

The surface covered by a SSDCH is of the order of a few cm^2. The full vertex detector thus would consist of a few thousands SSDCH with the same number of readouts. More resolutions along the second coordinate can be achieved by an anode segmentation at the expense of a larger number of readout channels.

References

1. E. Gatti and P. Rehak, to be published in NIM.

Large Area Non-Crystalline Semiconductor Detectors

V. Perez-Mendez, T. Mulera, S.N.Kaplan, P. Wiedenbeck
Lawrence Berkeley Laboratory, University of California, Berkeley, CA 94720

Summary

The properties of various non-crystalline semiconductors are considered for use as position sensitive detectors. Amorphous silicon and conducting plastic can be doped to form NP depletion regions similar to those in single crystal silicon, but without the limitation of single crystal size. Chalcogenide glassy materials such as Te-Se-Ge compounds as well as some metallic oxides such as the Vanadium oxides have switching and memory properties. They could serve as x,y location identifying devices when triggered by amplified pulses from a parallel plate or multistep gas filled detector stage in order to resolve the multitrack ambiguity for x,y readout schemes.

I. Introduction

Single crystal semiconductor detectors have been widely used in Nuclear Physics research as energy measuring devices. For γ spectrometry in the few KeV to MeV energy range, back biased NP junction Germanium single crystals of ultra-pure germanium have given the highest energy resolution of any device. Position sensitive detection of charged particles has been done with back biased NP junctions in silicon crystals with a plated metallic grid to give the position information. In high energy physics these devices have come into use as vertex detectors in colliding beam accelerators, with spatial resolutions in the few tens of microns range.

All of these applications of silicon and germanium semiconductor detectors are limited to small area usage by the fact that they are slabs of single crystal material. Larger area devices could be made by use of a mosaic of crystals at a high cost and with a great deal of electronic complexity. Furthermore, if the events which traverse the crystal have a high multiplicity, the usual multi-track ambiguity from crossed grid detectors is still present.

We propose to develop the properties of three classes of non crystalline semiconductors for uses as radiation detectors, which would not be subject to the above mentioned limitations. These are (a) Amorphous silicon; (b) semiconducting plastics and (c) chalcogenide - Metallic oxide compounds.

Both amorphous silicon and semiconducting plastics - primarily polyacetylene - can be doped by suitable materials to form N or P type layers and thus create a depletion region by back biasing in the usual manner. Since both of these materials are non-crystalline, the limitations as to size do not apply; however, the difficulty with the multi-track ambiguity still remains.

Amorphous silicon can be deposited in large areas by various proccesses such as the decomposition of Silane-S_iH_4[1]. Doping with trivalent and pentavalent impurities can be done by vacuum deposition, or by sputtering techniques. The mobility of the elecrons and holes in this material is appreciably slower than in the single crystal silicon,[2] and thus there may be serious limitations to the resolving time of such layers if they are more than a few microns thick. Multiple layers can presumably be made in order to have a sufficient stopping power for detection of minimum ionizing particles. Amorphous silicon, being non-crystalline is less susceptible to radiation damage than its crystalline counterpart.

The development of conducting plastics has occurred primarily during the last few years. Among the various types[3] the most promising at this point is Polyacetylene which can be made by vacuum techniques[4] in layers up to a few m.m. thick. Doping with trivalent and pentavalent impurities for PN junctions formation can be done by electrolytic methods[5] or by deposition from the gaseous phase.[6] One present difficulty with the conducting Polyacetylene is that it is unstable in the presence of oxygen; this difficulty can, however, be readily resolved by encapsulation with thin mylar sheets.

A third approach to large area solid state detectors is to use the switching properties of some chalcogenide (Se-Te-Ge-Si) and metallic oxide compounds. These materials switch from a high resistance state to a low resistance state; some under the action of an electric[7] field and some at a critical temperature[8]. The Vanadium Oxides V_2O_3 and VO_2 for example switch at temperatures of 140°K and 68°C respectively. Some of the Se-Te-Ge-Si chalcogenides have been used as electronic latches in prototype computer memory arrays[9]. These devices can be made in large areas by vacuum deposition, sputtering and similar techniques. The temperature switching components are slower than the electronic switching compounds (10-100 μsec compared to 1-20 nsec).

The switching compounds have the following useful features

(a) They are readily made and there is some commercial background on their use
(b) They are more radiation resistant than the semiconducting plastics
(c) The switching properties and their memory can be used to resolve the multi track ambiguity when x,y crossed grid arrays are used.

Figure 1 shows the voltage current relation for typical electronically switched chalcogenides. Since traversal of a semiconducting layer by a charged particle will not produce a net potential difference across the layer, these materials could be used in conjunction with a gas filled chamber and serve as a memory at each node of an orthogonal grid of wires or plated strips similar to a glow chamber memory device[10].

Figure 2 shows the configuration of an argon or neon filled chamber (with a suitable quenching gas), either working as a parallel plate chamber or in a multistep chamber configuration. The pulse of electrons (10^7 to 10^8 electrons) can be drifted onto a plated layer of chalcogenide material, causing switching at locations where charged particles traversed the chamber. A readout scheme in which the n^2 locations are sampled is shown in Fig. 3. Each x line is pulsed sequentially to switch off any conducting elements on that line. The corresponding y locations are read out in synchronism. The speed of such a readout can be as short as 10-20 n/sec per x wire, which is appreciably faster than the corresponding glow memory device.

References

1. W.E. Spear, Adv. Physics 26 (1977) 811.
2. R.S. Grandall, J. App. Physics 52 (1981) 1387.
3. A.G. MacDiaimid and A. J. Heeger, Synthetic Metals 1 (1979/80) 101.
4. C.K. Chiang et al., App. Phys. Letters 33 (1978) 18.
5. Y.W. Park et al., Solid State Commmunications 19 (1979) 747.
6. J.F. Kwak et al., Synthetic Metals 1 (1979/80) 213.
   T. Tani et al., Solid State Communications 33 (1980) 499.
7. N.F. Mott and E.A. Davis, Electronic Processes in Non-crystalline Materials, Clarendon Press, Oxford (1979).
8. J.K. Higgins et al., J. Non-Crys. Solids 18 (1975) 77.
9. S.R. Ovshinsky, Phys. Rev. Lett. 20 (1968) 1450.
10. T. Mulera, M. Elola, V. Perez-Mendez, and P. Wiedenbeck, IEEE Trans. Nuc.Sci. NS-24 (1982) 425.

This work was supported by the Director, Office of Energy Research, Office of High Energy and Nuclear Physics, Divison of High Energy Physics of the U.S. Department of Energy under Contract No. DE-AC03-76SF00098.

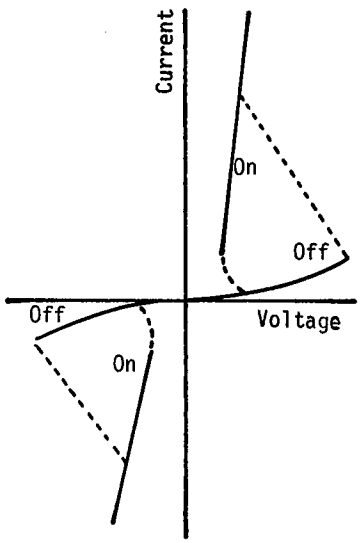

Fig. 1. Current voltage characteristic of a chalcogenide glass switch.

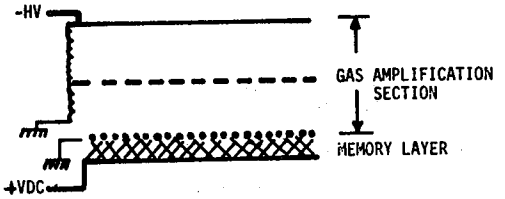

Fig. 2. Schematic of proposed detector. The gas amplification scheme shown here is a multi-step avalanche chamber.

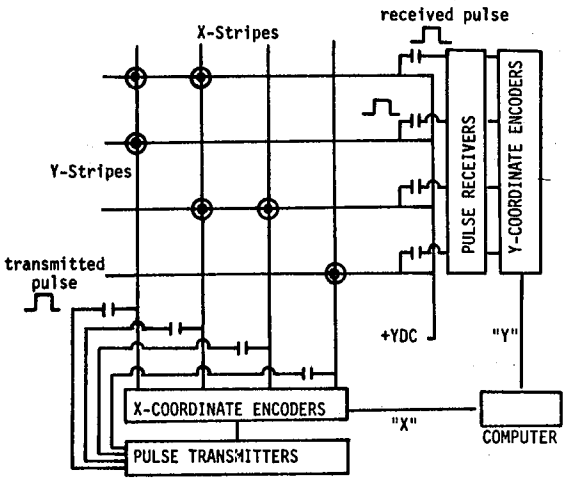

Fig. 3. The correlated x-y readout scheme. The circles represent memory elements which have been switched on by the passage of a charged particle at that location.

THE DESIGN AND EXPECTED PERFORMANCE OF A FAST SCINTILLATOR HADRON CALORIMETER*

R.B. Palmer and A.K. Ghosh
Brookhaven National Laboratory, Upton, New York 11973

I. Introduction

We consider a calorimeter of the type developed by W. Willis, et al., for the ISR 807 experiment.[1] Figure 1 shows the basic concept. The calorimeter consists of a stack of alternating metal (copper or uranium) and scintillator plates 20 cm wide, 120 cm long and 1.5 mm thick. Light generated in the scintillator passes out through the edges and into wavelength shifter bars that lie between the stacks. The light from the scintillator is absorbed in the shifters and excites lower frequency emission that then passes down the shifter to phototubes in the rear. The 807 geometry has in fact separate shifters for the front electromagnetic and rear hadronic parts of the calorimeter but we will not be considering this complication here. We will also restrict the discussion to copper plates.

A typical pulse from the 807 calorimeter is shown in Figure 2. This was generated by 4 GeV electrons but the pulses from hadrons and at different energies are not significantly different. The width and shape of this pulse comes from the convolution of a number of sources:

a. The time spread of energy deposition by a shower including time of flight of slow protons and neutrons,
b. scintillator phosphor rise and decay times,
c. shifter rise and decay times,
d. phototube response,
e. time delays in the light collection from different parts of the calorimeter and time dispersion in transmission.

The objective of the first phase of this study was to isolate these separate contributions, estimate how they could be speeded up and find what costs are involved. For this phase we have run Monte Carlo for (a), made measurements using single photon counting for (b), and (c). Observe (d) with a fast scope, observe (e) and (f). From these observations we estimated that a fast calorimeter could be made with pulses whose full width half maximum would be of the order of 7 nsec.

In the second phase we constructed an extremely crude calorimeter whose pulses should have the same characteristic as in a real device. With this we have observed signals whose mean width was 7 nsec and whose width at 10% of maximum height was 15 nsec. Clipping could reduce these widths to 6 and 12 nsec respectively. We conclude that gate times of less than 20 nsec would be appropriate for such a calorimeter.

A third phase is underway to build a good test calorimeter to confirm these results.

II. Discussion

a. Energy Deposition

A Monte Carlo program used and modified by Alan Stevens has calculated the time distribution of energy deposition for both a copper and a uranium calorimeter. The results in 5 nsec bins are shown below. For copper they are plotted in Fig. 3.

Time Interval	Copper	Uranium
0- 5 nsec	97.2	91
5-10	2.2	6.0
10-15	0.5	2.1
15-20	0.1	0.7
20-25		0.2
25-30		0.1

These results show a fast initial spike 2 nsec wide followed by an exponentially falling slow component whose time constant is 4 nsec and whose total fraction is about 10% for copper and 20% for uranium.

b. Scintillator

ISR 807 uses an acrylic scintillator that contains among other ingredients Napthalene whose published[3] decay time is 96 nsec. We have not measured the response of this scintillator without shifter but the observed long tail on the shifted signal (Fig. 2) is presumably from this decay.

More conventional scintillators contain some combination of fast UV scintillating chemicals such as PBD (emission max ~ 370 nm) and wavelength shifters such as POPOP that lower the emission frequency to a more convenient visible range ~ 430 mm. These scintillators are faster than Napthalene scintillators but slower than scintillators without the shifter. Such scintillators (eg NE111 and Pilot U) emit in the UV (370 and 390 nm respectively) and have shorter attenuation lengths than conventional scintillator but these are not a disadvantage when the light path to a separate shifter is short.

We have looked at the pulse distributions from two fast UV emitting scintillators: NE111 and BC420 (similar to Pilot U). Both give pulses less than 2 nsec FWHM and less than 5 nsec at 10%. Published data[2] gives pulse distribution for NE111 as shown in Fig. 4. We expect that polystyrene scintillators using on the chemical PBD without shifters have similar response at lower cost. The cost of scintillator for a hadron calorimeter using BC420 or Pilot U is about 140 K$ per m^2 in a 0.4 m^2 lot. The cost for polystyrene should be about half this.

c. Wavelength Shifter

Conventional calorimeters (such as that in the ISR 807 experiment) use the shifter BBQ whose absorption maximum at 430 mm matches many conventional scintillators. We measured (see Sec. 3) the response of BBQ illuminated by NE111 and observed a FWHM of 12 nsec and width at 10% of 30 nsec. We also measured the response of POPOP and BBOT each illuminated with NE111 and observed FWHM's of 6.4 and 4.9 nsec respectively and width at 10% of 12.5 and 17.2 nsec respectively (see Fig. 5). Clearly both BBOT and POPOP are much faster than BBQ, with BBOT preferred over POPOP. The absorption maxima for the POPOP and BBOT are at 360 and 398 nm suggesting that good combinations would be NE111 (or Polystyrene UV) and POPOP or Pilot U (or Polystyrene UV-390) and BBOT. The latter combination is preferred because of the faster wavelength shifter

* Work performed under the auspices of the U.S. Department of Energy.

and also because the further UV emitting scintillators NE111 and Polystyrene UV have shorter attenuation lengths (8 cm and 16 cm respectively) compared with Pilot U and Poly UV-390 (100 cm and 20 cm).

Table I summarizes the response time data[2-3] for both scintillators and shifters discussed plus NE110 for comparison.

Table I

	A "Conventional" Scintillator				
	emission λ nm	rise time nsec	fall time nsec	FWHM nsec	Attenuation λ cm
Scintillator					
NE111	370		1.7	1.55	8
Pilot U	391	0.5	1.36	1.97	100
NE110	434	1	3.3	3.3	400

	Published			Measured (w/NE111)
	absorption λ nm	emission λ nm	fall time nsec	FWHM nsec
Shifter				
BBQ	430	505	---	12
POPOP	360	415	1.1	6.4
BBOT	398	432	1.6	4.9

Acrylic is the conventional base for the shifters. It is easy to handle but less radiation resistant than PVT. PVT is harder to handle, being inclined to craze. Polystyrene could possibly be employed although most polystyrene has an unsatisfactorily short attenuation length.

Table II shows attenuation lengths measured by the Penn and ISR groups. For the Penn measurements the bar was 1 cm × 2.5 cm. For the ISR it was 20 cm × 0.3 cm. In both cases the shifters are in acrylic.

Table II

Shifter	Concentration	Attenuation Length cm Penn	ISR
BBQ	80 mg/litre	--	152
POPOP	300 mg/litre	--	114
	100 mg/litre	97	190
	30-40 mg/litre	131	157
BBOT	100 mg/litre	70	---

The concentration of shifter should in general be as high as possible consistent with a sufficient attenuation length. These measurements are critically dependent on the surface condition of the bars and thus show some inconsistencies. The values should thus be taken as lower limits on the bulk attenuation.

d. Phototube

Typical 12 stage phototubes have responses similar to that measured[6] for RCA 8850 and shown in Fig. 6a. FWHM is about 5 nsec and width at 10% about 12 nsec. The width comes primarily from variation in transit time in the dynodes. The RCA C31024 is a tube employing only 5 dynode stages. Gain of over 10^6 is achieved by using Gallium phosphide on all stages. The output from the tube is taken from a special coaxial pin further improving the high frequency response. A pulse from this tube is shown in Fig. 6b. It has a FWHM of only about 1 nsec and at 10% about 3 nsec. The tube has a rather standard 2" photocathode and is very well suited to calorimeter use. Its cost is now just over 1000$ but would be less in quantity.

e. Light Collection Time Delays

The measured mean velocity of light in the wavelength shifter bars is 0.5 times the velocity of light. The velocity of the shower itself is equal to that velocity. As a result light from the back of the shower arrives at the phototube earlier than that from the front. If the calorimeter is 1 m deep this causes a time spread of 3 nsec.

Time dispersion arises because of the finite aperture of the shifter bars. Light traveling straight down the bar takes a time $t = \ell N/C$ (where N is the refractive index), yet the measured mean time was $2\ \ell/c$: slower because of the finite angles of rays in the shifters. For a shifter and light guide about 4 ft long the resultant FWHM time spread is about 3 nsec.

f. Summary of Time Constants

The Table below gives the estimated or measured contributions (FWHM) to the expected output pulses of the ISR 807 calorimeter and a possible faster version.

		807		Fast Cal.	
a.	E. deposition		2		2
b.	Scintillator	Acrylic	~ 15	Pilot U	1.5
c.	Shifter	BBQ	12	BBOT	5
d.	Phototube	standard	5	C31024	1
e.	Light Collection		~ 5		~ 5
	Overall		~ 20		~ 7
	Observed		23		7

Numbers with approximate sign were estimated, the others measured. The observed overall value for the fast calorimeter was obtained from the test reported below.

III. Measurements

a. Single Photon Counting Measurements

The set-up used is shown in Fig. 7. The hole in front of the phototube #2 was adjusted to keep the counting rate from tube #2 to less than 1% of tube #1. The signals from both tubes were taken to constant fraction discriminators. The tube #1 high voltage was set so that the counting efficiency for a minimum ionizing particle passing through the trigger scintillator was about 70%. The tube #2 high voltage was set to obtain a similar efficiency for single photons. The time difference distribution between tubes 1 and 2 were obseved on a "QVT". The distributions obtained are shown in Fig. 5 and reflect effects from the scintillator, shifter and dispersion down the shifter bar, but not from the phototubes except for the jitter in the system (about 1 nsec).

Since the scintillator and this jitter are small compared to the observed width we can interpret this width as that of the shifter without correction.

b. Calorimeter Experiment

In order to check the estimates given in Section II(f) prior to the construction of a full scale test we set up a crude experiment. Sixteen lead bricks (each 3-1/2" × 7-1/2" × 1-1/2") were placed in a row

with 15 4" × 4" × 1/8" pieces of NE111 scintillator between the bricks (see Fig. 8). Two shifter bars were tried: one 30" × 4" × 1/8" of POPOP the other 24" × 8" × 1/8" of BBOT. Both were blackened at the front end. A single RCA C31024 phototube was butted up to the back end of the shifter without a light guide, glue or grease. This device was placed in a somewhat broad (~ 6" diameter) 22 GeV π^- beam. A trigger was formed from the coincidence of one small 1/2" × 1/8" scintillator in front of the calorimeter and a second phototube looking at one of the 4" × 4" × 1/8", 1/3 of the way down the row. The second trigger phototube level was set to fire on at least one minimum ionizing particle at that point in the shower and thus vetoed triggers from a background of low energy tracks not in the beam direction.

It must be noted that this "calorimeter" had a cross section that contains only a small fraction of the approximately 8" diameter of a hadron shower. It also has limited sampling with a very high Z material. It is a very poor calorimeter. It should however provide a reasonable estimate of the pulse length seen by one 4" × 4" tower in a real calorimeter of the same depth.

The observed pulse height distribution is shown in Fig. 9 (for POPOP shifter). The σ for this distribution is 38% corresponding to 180% / $\sqrt{E}$. Under the circumstances this is a surprisingly good energy resolution.

A typical pulse is shown in Fig. 9 (for BBOT). Considerable pulse to pulse variations were observed, as expected in a calorimeter that does not contain the shower. The Table below gives the widths for successive pulses using both BBOT and POPOP.

Widths at half height nsec

POPOP: 5,12,8,14,10,16,11,11; mean 11;
BBOT: 8,9,6,5,7,5,7,10; mean 7.

Figure 10a shows the mean shapes that hopefully approximate the real shape that a larger calorimeter would give. Figure 10b shows the mean shape from BBOT after shaping by a 4 nsec 23% clip. This pulse has only 6 nsec full width at half maximum and only 12 nsec at 10%.

The question was raised as to whether the signal from neutrons at larger distances from the 4" × 4" shower case might be much slower. A further experiment was performed in which the beam was directed at a second stack of uninstrumented lead bricks set up alongside the instrumented stack. Observation of the signals in this instrumented stack showed no indication of signals arriving significantly (i.e., more than 5 nsec) later than had been observed before, i.e., we saw no evidence for a significant slow signal outside the core.

IV. Conclusion

We conclude that a scintillator with suitably chosen available components could give pulses with widths comfortably less than 10 nsec at half height and less than 20 nsec at 10% of height. Gates of 20 nsec seem not unreasonable. Work is needed to confirm this result with a full scale calorimeter and on electronics to digitize the signals. This is underway.

References

1. O. Botner, et al., Nucl. Inst. & Methods 179, 45 (1981); also Ibid 196, 303 (1982), and private communication.

2. J. Pronko, et al., Nucl. Inst. & Methods, 163, 227 (1979); F. Galligaris, et al., Ibid 171, 617 (1980).

3. Catalogs: National Diagnostics, Somerville, NJ, USA; Nuclear Enterprises, Edinburge, Scotland.

4. W. Kononenko, W. Selove, and G.E. Theodosion, UPR96E, U. of Pennsylvania, internal report; RA-Ong, DD23/0G563, Brookhaven Lab internal report.

5. Private communication, W. Willis and W. Wenzel, CERN, Geneva, Switzerland.

6. H.R. Kroll and D.E. Persyk, IEEE Trans. Nuc. Sci. NS19, 45 (1972); B. Leskovar and C.C. Lo, LBL 6456 Lawrence Berkeley Lab internal report.

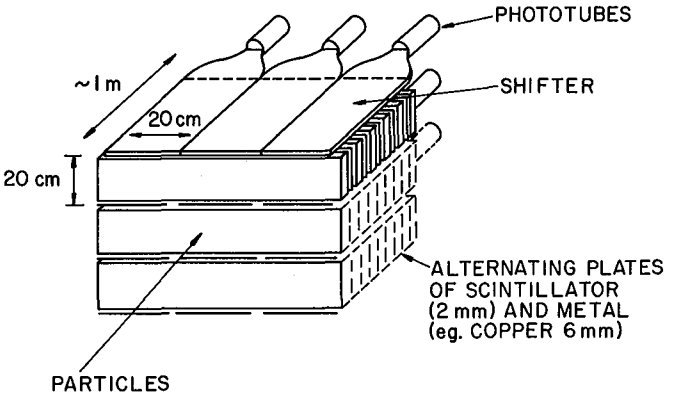

Figure 1. Schematic representation of calorimeter being considered.

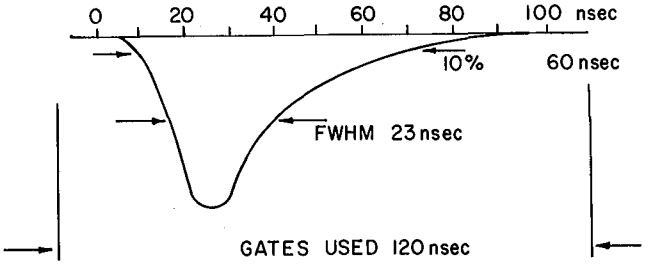

Figure 2. Pulse observed in ISR 807 calorimeter from 4 GeV electron.

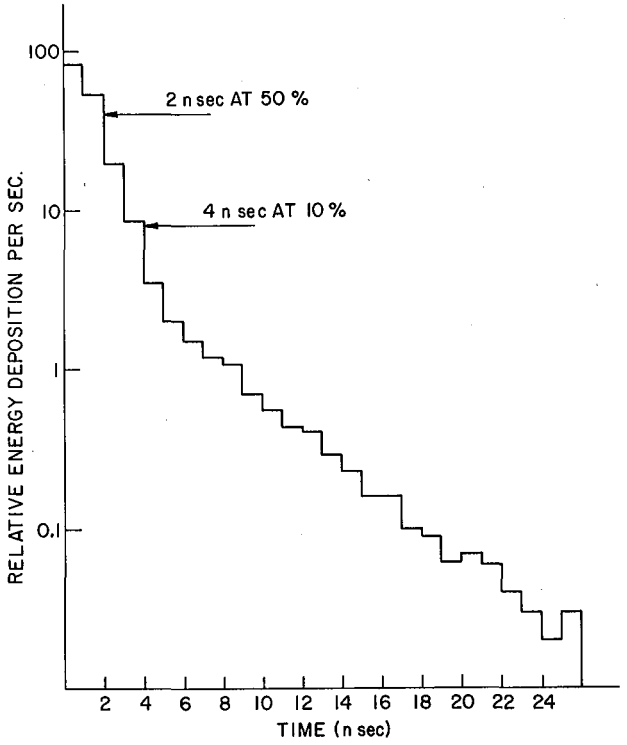

Figure 3. Monto Carlo time distribution of energy deposition from a 5 GeV negative pion in the test calorimeter.

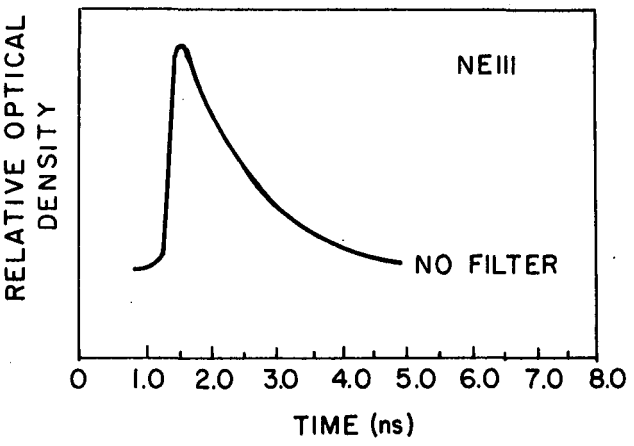

Figure 4. Light pulse from NE111.

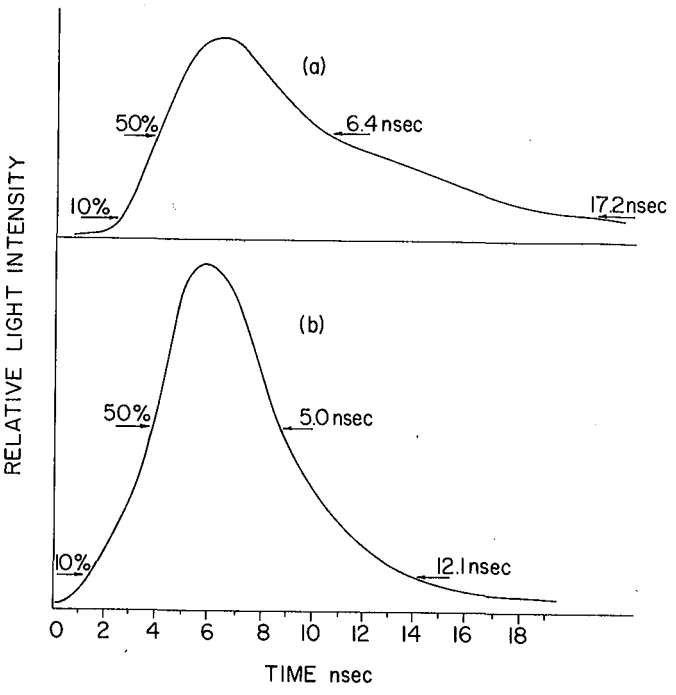

Figure 5. Pulses obtained using (a) POPOP and (b) BBOT shifters together with NE1112 scintillator.

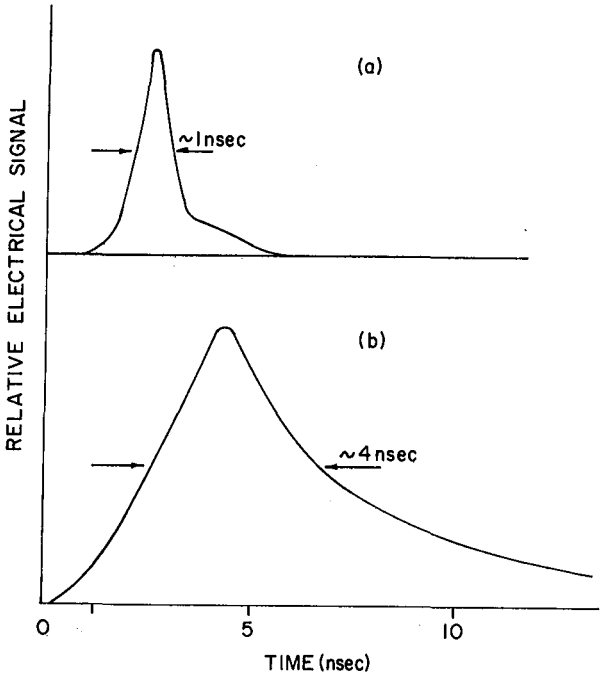

Figure 6. Output pulses from (a) RCA C31024 and (b) RCA 8850.

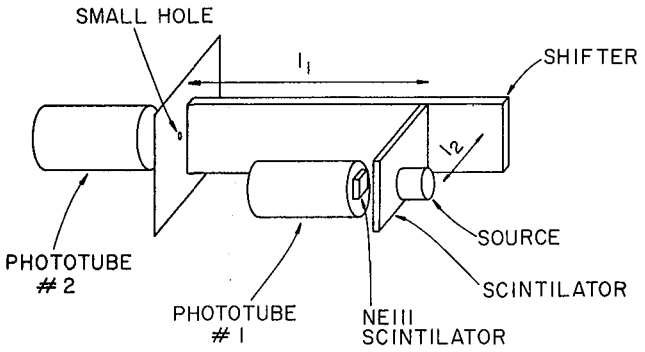

Figure 7. Arrangement for single photon measurement of scintillator and shift pulse length.

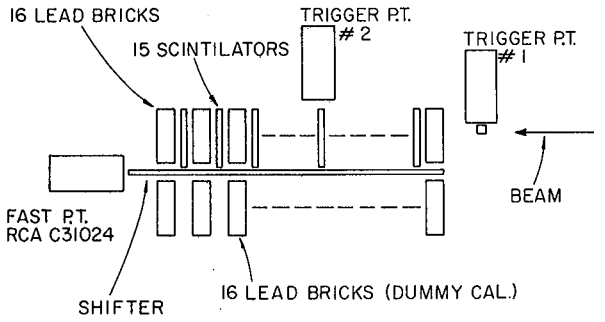

Figure 8. Calorimeter experiment to observe pulse length with fast scintillator shifter and phototube.

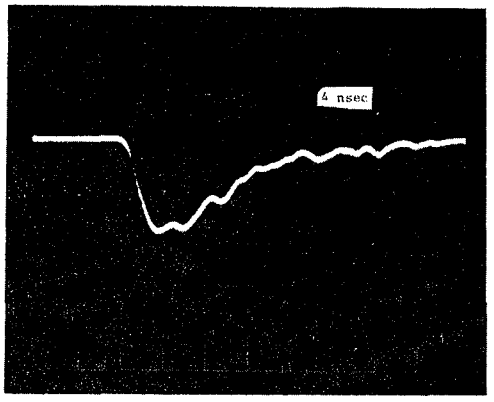

Figure 9. Typical signal from calorimeter experiment using BBOT shifter.

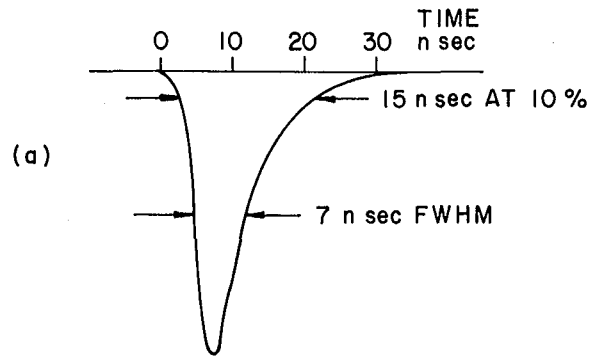

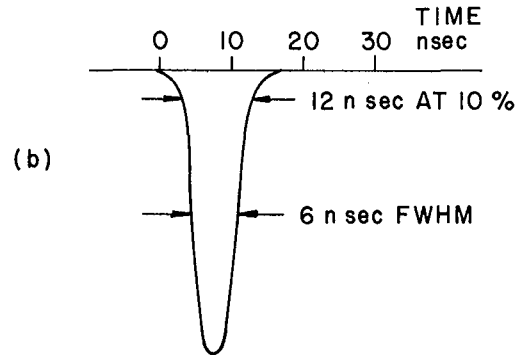

Figure 10. Average pulse shapes from the calorimeter experiment using BBOT (a) without and (b) with a 23% 4 nsec chip.

SCINTILLATION CHAMBER OPERATION OF CALORIMETERS FOR COLLIDING BEAM DETECTORS

Lawrence W. Jones
Department of Physics
The University of Michigan
Ann Arbor, Michigan 48109

Summary. It is suggested that the scintillation chamber, a technique first discussed almost thirty years ago, might find application in colliding beam detector systems, in particular as a means of efficiently extracting detailed spatial and energy information from a sampling calorimeter.

Concept

Using photoelectric image intensification, light from a scintillator can be recorded preserving spatial information of the source of light in the scintillator. In the late 50's the scintillation chamber or luminescent chamber was developed wherein tracks and details of nuclear interactions were photographically recorded from sodium iodide and from plastic scintillators, using photoelectric image intensifiers and cameras. Since those years the image intensifier has evolved a great deal and now finds application routinely in astronomical research, although the scintillation chamber was totally supplanted by spark chambers (and later proportional chambers and other digital readout devices) in high energy and elementary particle physics. One application of the scintillation chamber which is particularly relevant to the present discussion was made by R. W. Huggett and colleagues in a cosmic ray experiment carried out at Climax, Colorado.[1] In this application they had a calorimeter measuring 5m x 1.8m x .9m containing 20 scintillator sheets and this calorimeter was photographically recorded using an image intensifier and photographic film. The concept here is that a sheet of scintillator will pipe the light to its four narrrow edges by total internal reflection. If the edges are cut straight then light which emerges from those edges maintains the spatial information of the coordinate of the source of light in the two dimensions of the scintillator sheet area. A sampling calorimeter containing alternating absorber and scintillator can be viewed from one or two of its side faces using a system of mirrors and a lens to image the light onto an image intensifier and the image will then preserve the profile of the cascade of a hadronic or electromagnetic shower within the calorimeter.

A Prototype System

Consider a downstream or endplug calorimeter with transverse dimensions of about one or two meters and extending along the beam pipe one or two meters, consisting of iron plates of the order of one inch thick and plastic scintillation sheets of the order of one quarter of one inch thick. It is desired to view the plastic scintillator in order to resolve separate hadronic cascades and to determine the separate cascade energies with best possible spatial resolution. If photomultipliers and wave bars and towers are used inevitable compromises must be made. However, the image intensifier system might achieve the best possible separation and resolution of such a system. Strip mirrors could be mounted beside each scintillator and a second set of strip mirrors used to collect the light onto one or more large area mirrors to direct in turn through the objective lens onto the cathode of an image intensifing photoelectric tube. A transfer lens or fiber optics might then bring the light from the image intensifier onto a CCD or similar digital readout device of lesser senitivity. The two sets of strip mirrors might be necessary to make the optical path length from each scintillator edge to the objective lens equal. The set of strip mirrors also serves to collapse the image to eliminate the space occupied by the iron on the image plane, utilizing more completely the photo cathode area of the image device. As an example, the system used in Huggett's cosmic ray experiment of Ref. 1 is reproduced in Fig. 1.

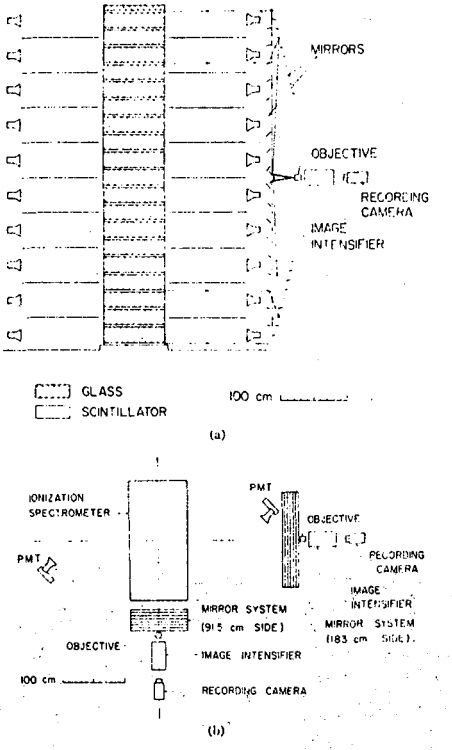

FIG. 1. Apparatus for photographing stereoscopically high energy cascades in a calorimeter. (a) side view, (b) plan view. Taken from Ref. 1.

A scintillator of reasonable quality with 2 MeV per centimeter of energy loss by a minimum ionizing particle produces about 2×10^4 blue photons with one-sixth of these being transmitted to each of the six surfaces of the scintillator. Consider an image intensifier tube with a cathode such that the image from the calorimeter must be demagnified by a factor of 20. Let us also assume an objective lens with an f-stop of 1.5. The fraction of the light this lens will subtend from the scintillator is approximately 1/900 of the light coming out of the scintillator from that surface. The photocathode efficiency of the image intensifier tube may be about 20 percent. For this numerical example, approximately two-thirds of a photoelectron would be recorded per centimeter of scintillator per minimum ionizing particle in the scintillator, and this independent of the depth of the track in the scintillator. This is probably an optimistic figure as there would be at least a factor of two lost in transmission through the optics and in reflection losses. Thus, let us take one photo-electron per three centimeters (or 6 MeV of energy loss) in scintillator. If the calorimeter is made with four centimeters of iron for each centimeter of scintillator, however it is divided, then there will be about 50 MeV of energy loss in iron per centimeter

of scintillator and consequently one photoelectron would be recorded per 150 MeV of energy loss in the calorimeter. The resolution of such a calorimeter based only on photoelectrons statistics would be therefore about $40/\sqrt{E}$ percent, with E measured in GeV. The resolution would, of course, be improved with a faster lens or less demagnification and/or more image intensifier systems. At the very least, one would use two image intensifier systems perhaps looking at the same system of mirrors but from different corners, in order to provide a stereo image. Image tubes could be placed on more than one side of a rectangular calorimeter, but this may not be necessary.

Comments

It is amusing to remark that a scintillation chamber detector was discussed in the context of one the early papers on the experimental utilization of colliding beams.[2] The concept implemented by the Louisiana state group, however, is almost identically that which would be most appropriate for the colliding beam detectors under current discussion. The time resolution of an image intensifier-scintillation chamber system in the applications of the late 50's was determined by the storage time of the phosphor of the first stage of the image intensifier. One can use any number of phosphors with storage times of from a millisecond to much less than a microsecond, however the convenient application of the image intensifier scintillation chamber was made possible by gating a second or later stage of an image intensifier system using the first stage phosphor as a buffer storage, so to speak. A continuously-on image intensifier could use the properties of the CCD or other imaging system in the electronic readout to serve as a buffer store, retaining only information from an event of particular interest. In any case, auxillary triggering, for example from photomultipliers viewing the same scintillators, would probably be necessary, and the time incumbent in this auxillary triggering would be the determining factor in the ultimate time resolution of the system. Greater time resolution might be possible by using image intensifier systems in pairs, one recording a static image as described here, the second utilizing an image intensifier with sweep electrodes incorporated such that the images would be swept across the recording field at a convenient rate. This would produce a displacement of one image in the static system relative to the other in the swept system related to the relative time delay and the sweep rate. In this way, a time resolution might be achieved comparable to the intrinsic time constant of the scintillation process in the plastic scintillator. It is clear that the topology of the scintillator optics image-tube systems could become quite tedious for a central detector, but perhaps not insoluble. Except for such details it seems surprising and indeed amusing that this detector technique, dormant for over twenty years, might find application in the newest and most ambitious detector systems of the next decade.

This work was supported by the U.S. National Science Foundation.

References

[1] R. W. Huggett, T. Sander, and J. E. Webb "Image Intensifier Photography of Ultrahigh Energy Cascades in an Ionization Spectrometer. I. Apparatus," Rev. Sci. Instr. 41, 1007 (1970).

[2] L. W. Jones "The Luminescent Chamber and Other New Detectors," Proceedings of the Intern. Conf. on High-Energy Accelerator and Instrumentation, 561 CERN (1959); L. W. Jones "Recent U.S. Work on Colliding Beams," Intern. Conf. on High Energy Accelerators, Dubna, USSR (1963).

HIGH ENERY ELECTROMAGNETIC SHOWER POSITION MEASUREMENT BY A FINE GRAINED SCINTILLATION HODOSCOPE

B. Cox, G. Hale, P.O. Mazur, R.L. Wagner, D.E. Wagoner
Fermi National Accelerator Laboratory, Batavia, Illinois 60510

H. Areti, S. Conetti, P. Lebrun, T. Ryan
McGill University, Montreal, PQ, H3A 2T8, Canada

R.A. Gearhart
Stanford Linear Accelerator Center, Stanford, California 94305

Summary

We have measured the centroids of high energy electromagnetic showers initiated by positrons in the energy range 2 to 17.5 GeV with a fine grained scintillation hodoscope composed of seven 1 cm wide elements placed behind a 3.6 radiation length (15 cm) converter composed of SCG1-C scintillation glass. A simple first moment calculation using the ionization observed in each element of this hodoscope yields a shower position resolution as a function of energy of: $\sigma(mm) \simeq 0.7 \pm 5.6/\sqrt{E(GeV)}$. We present results on the energy dependence of the shower profiles and the ionization measured by this hodoscope.

Introduction

The determination of the position of a photon by measurement of the profile of its shower in an electromagnetic shower detector is a critical requirement of any experiment which attempts to reconstruct photon energies and directions. In preparation for Tevatron Experiment 705[1] at Fermilab we have tested a fine grained (1 cm wide elements) scintillation hodoscope positioned 3.6 radiation length deep in electromagnetic showers initiated by 2 to 17.5 GeV positrons. We have determined the position resolution attainable by this device as a function of energy. In addition, we have measured the shower shapes and ionization seen by the hodoscope as a function of energy. Comparisons of the measured shower shapes with the EGS electromagnetic shower Monte Carlo[2] have been performed.

Test Beam

This test was performed using the positron test beam 19 in the B end station at Stanford Linear Accelerator Center. The small phase space of the beam (90% of the positrons included within a $\sigma \curvearrowleft 1$ mm spot) allowed us to make a relatively precise determination of the position resolution of the scintillation hodoscope. The momentum of the beam was tunable from 2 to 17.5 GeV and the contamination of the beam by hadrons and muons was less than 10^{-5}. The beam was typically operated at 10 pulses per second with less than 0.3 positrons per 1.6 μsec pulse. Beam pulses with two or more positrons were tagged and later rejected in the off-line analysis.

Experimental Apparatus

The arrangement of the scintillation hodoscope, active converter and SCG1-C scintillation glass/lead glass array[3] used in this test is shown in Fig. 1. The incident positron beam showered in a 15 cm thick (3.6 radiation lengths) SCG1-C scintillation glass active converter. A finger hodoscope composed of seven 1 x 1 x 15 cm^3, NE114 scintillators coupled to 12 stage, 2 inch diameter EMI 9807B phototubes was placed 3 cm downstream of the active converter. Pulse heights from these counters were digitized using a LeCroy 2249W ADC. The main shower detector array,

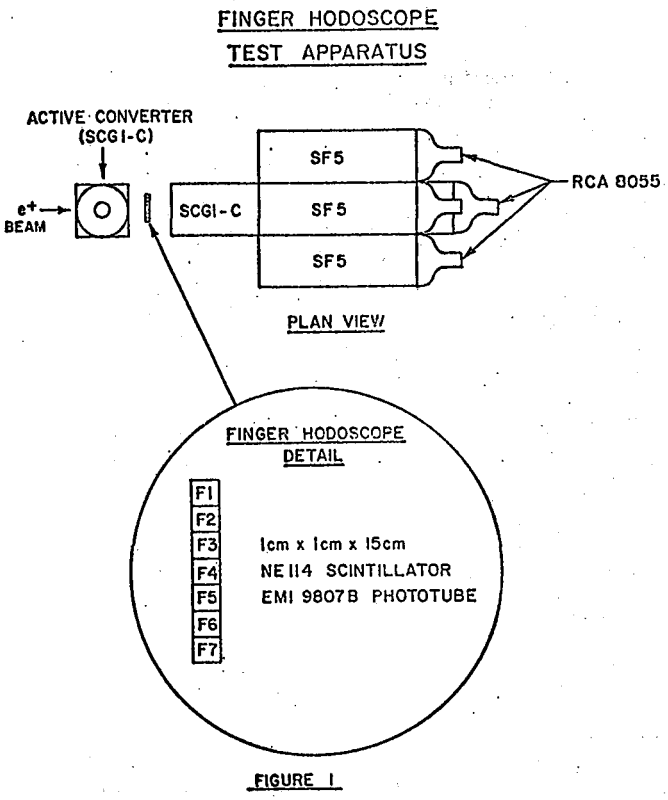

FIGURE 1

which was composed of a central 15 x 15 x 80 cm^3 SCG1-C scintillation glass shower counter surrounded by eight 15 x 15 x 45 cm^3 SF5 lead glass counters, was positioned approximately 4 cm downstream of the finger hodoscope. The entire apparatus rested on a table which could be positioned vertically or horizontally to ± 1 mm.

Test Results

With the active converter removed, the positron beam was scanned horizontally through each of the elements of the hodoscope to locate the hodoscope edges and to determine the pulse height of minimum ionizing particles in each of the finger hodoscope elements. With the minimum ionizing pulse heights determined, all results could be expressed in units of the average pulse height for a minimum ionizing particle. After normalization of the gain of each counter, a 17.5 GeV positron beam was centered in the central finger hodoscope element (F4). Effects of backscatter from the main array were then studied. Less than 5% of the showers had greater than one unit of minimum ionization pulse height in either of the adjacent counters (F3 and F5). This did not significantly change when 2.5 cm of polyethylene

absorber was inserted between the main array and the finger hodoscope.

The active converter was then inserted in front of the finger hodoscope. In this configuration we searched for possible effects of a wide angle, low energy electron component of the 17.5 GeV showers by examining the average pulse heights seen in F1 and F7 (the finger counters most distant from the shower center) as a function of polyethylene thickness inserted between the active converter and the hodoscope. The average pulse height for a 17.5 GeV shower in either extreme counter was approximately 1.5 times minimum ionizing. In comparison, pulse heights averaging approximately 25 times minimum ionizing were observed in the central counter, F4. These results were essentially independent of polyethylene absorber thickness.

The energy of the beam was then varied from 2 to 17.5 GeV. The total ionization observed in the hodoscope is shown in Fig. 2a as a function of energy. The bars on the data points in this figure are not errors in the determination of the centroid of the observed ionization distributions but rather the full width at half maximum of these distributions. Figure 2b shows the ionization in the central counter, F4, as a function of energy.

FIGURE 2a

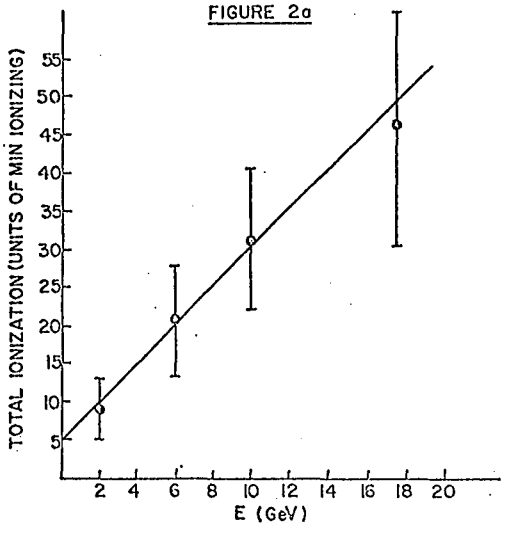

FIGURE 2b

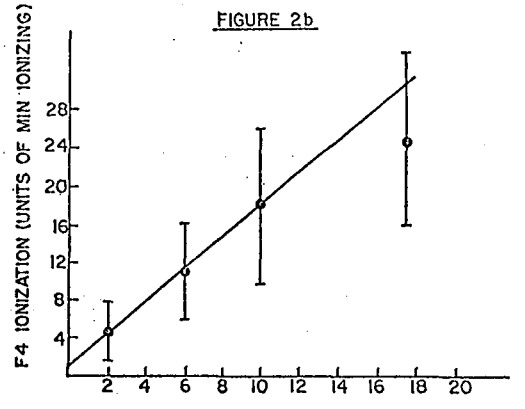

Figure 3 shows the shower profile as seen by this hodoscope for 2.0, 6.0, 10.0 and 17.5 GeV showers. As shown, the shower profiles at a depth of 3.6 radiation lengths are narrow with full widths of less than one centimeter. The shape of the shower was slowly changing with energy. This can be seen in Fig. 3 in the slight tendency of the 2 GeV showers to be less collimated than the 17.5 GeV showers. Figure 4 shows

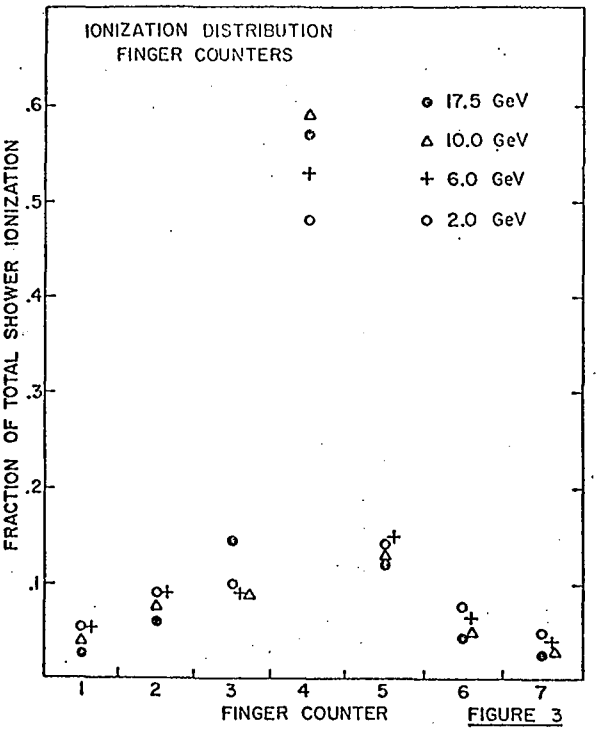

FIGURE 3

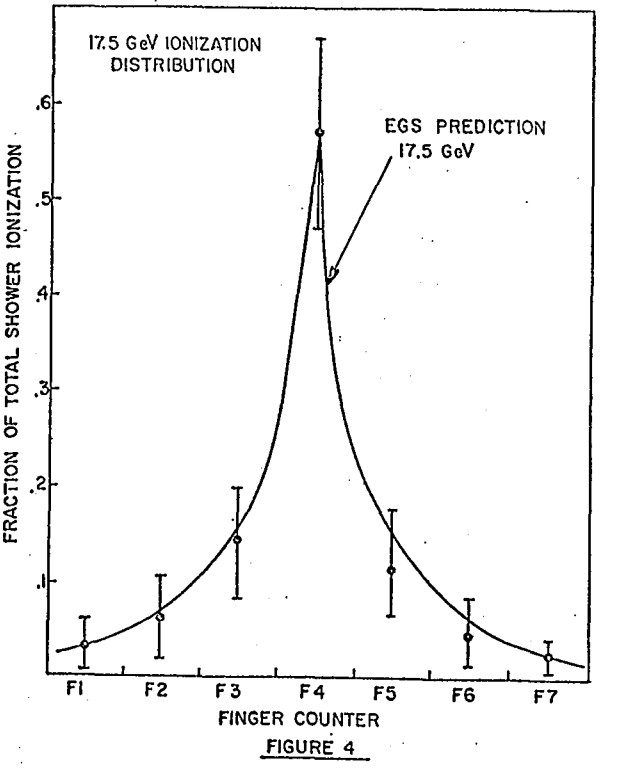

FIGURE 4

the 17.5 GeV shower ionization distribution together with an EGS Monte Carlo[2] prediction of the ionization that the finger hodoscope should detect. As shown the data is consistent with the EGS prediction. The bars on the 17.5 GeV/c data once again are the width of the ionization distributions seen in the various finger counters.

We have performed a first moment calculation of the position of the positron for each shower using the formula

$$\langle X \rangle = \frac{\sum_{k=1}^{7} P_i X_i}{\sum_{k=1}^{7} P_i}$$

where P_i is the pulse height in the i^{th} finger counter and X_i is the position of the center of the counter. The distribution of $\langle X \rangle$ for a set of 2 GeV and 17.5 GeV showers is shown in Fig. 5a and 5b.

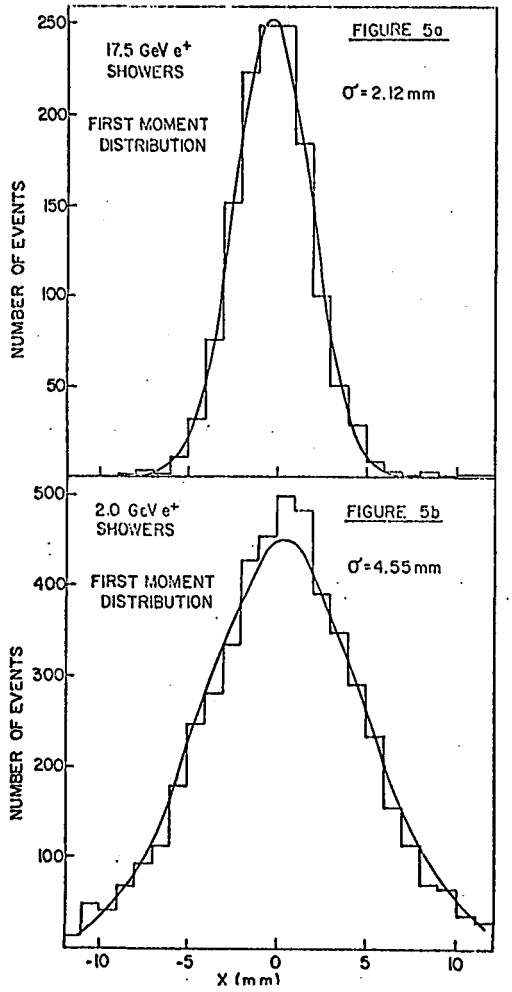

The σ of the distributions of first moment is approximately linear with $1/\sqrt{E(GeV)}$ as shown in Fig. 6. These data are approximately described by σ (mm) $= 0.7 + 5.6/\sqrt{E}$. This σ contains the $\sigma \sim 1$ mm phase space of the incident positron beam which contributes to the energy independent term. The errors assigned to these data points are not the statistical error in the σ of the distributions of first moments but rather the spread in the σ's of these distributions when repeated measurements of the positron showers are done under different experimental conditions.

Conclusions

A fine grained (1 cm) scintillation hodoscope of the type described can be used to determine with precision the centroid of electromagnetic showers when placed behind 3 to 4 radiation lengths of converting

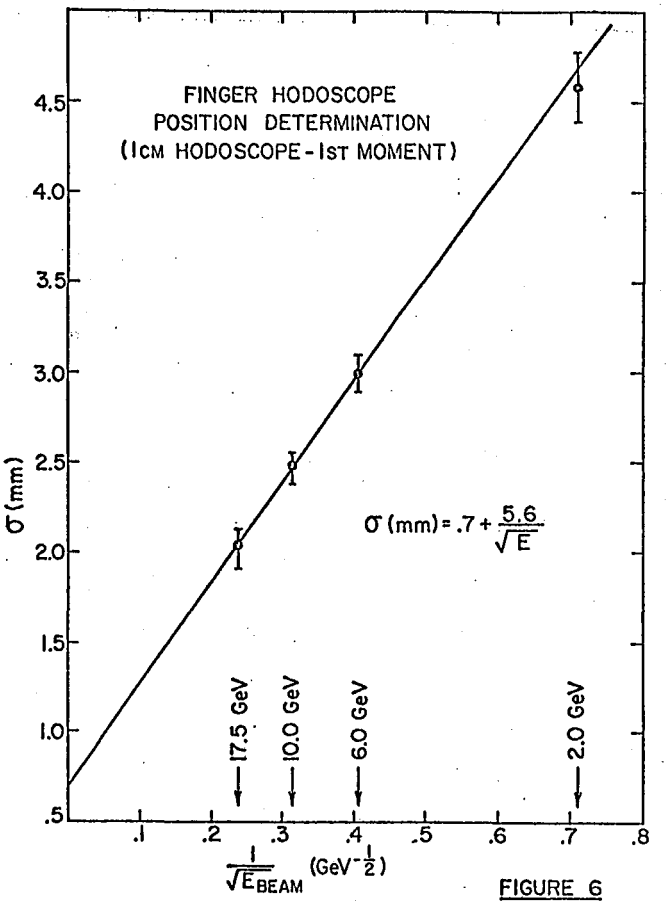

FIGURE 6

material even if the material has a relatively long radiation length ($r\ell$ = 4.35 cm in the case of the SCG1-C scintillation glass). The position resolution which contains the finite size ($\sigma \sim 1$ mm) of the positron beam position is observed to be σ (mm) $\simeq 0.7 + 5.6/\sqrt{E(GeV)}$. The shower shape is less than 1 cm full width at this depth and is slowly varying with energy. The ionization observed in this hodoscope varies linearly with energy with half the ionization appearing in the central element. At 17.5 GeV a total pulse height of approximately 50 times minimum ionizing is observed.

Acknowledgments

We wish to thank Fermilab Physics Department and to acknowledge the considerable efforts of the SLAC operating staff. We would also like to thank the U.S. Department of Energy, the Natural Sciences and Engineering Research Council of Canada and the Quebec Department of Education for their support.

References

1. M. Binkley, et al., Fermilab Proposal E-705, 1981.
2. R.L. Ford and W.R. Nelson, SLAC-210 (1978).
3. B. Cox, et al., A Measurement of the Response of an SCG1-C Scintillation Glass Shower Detector to 2-17.5 GeV Positrons, Paper 2H7, 1982 Nuclear Science Symposium, Washington, D.C.

SCINTILLATORS AND WAVESHIFTERS FOR FAST SCINTILLATOR-WSB CALORIMETRY

George E. Theodosiou
Department of Physics
University of Pennsylvania
Philadelphia, PA 19104

Abstract

We discuss some properities of fast scintillators and waveshifters, and their use and limitations in calorimetry using the wavelength shifter bar(WSB) read-out technique.

Introduction

The BBQ WSB readout technique in scintillator calorimetry, developed recently[1,2], has been up to now the dominant calorimetry method for experiments at high energies. The high event rates in future high luminosity Colliders necessitate the development of calorimetry with scintillators and waveshifters faster than BBQ. We have carried out, more than two years ago, extensive studies[3] on the light output and attenuation length of several inexpensive acrylic and polystyrene (fast) scintillators[4] coupled with fast waveshifters (POPOP, BBOT) with very encouraging results. We briefly present some of these results and discuss their implications on fast calorimetry.

Measurements

Figure 1 shows a test set up with a Ru^{106} source, the scintillator and waveshifter bar test samples and an 8850 Quantacon photomuliplier.

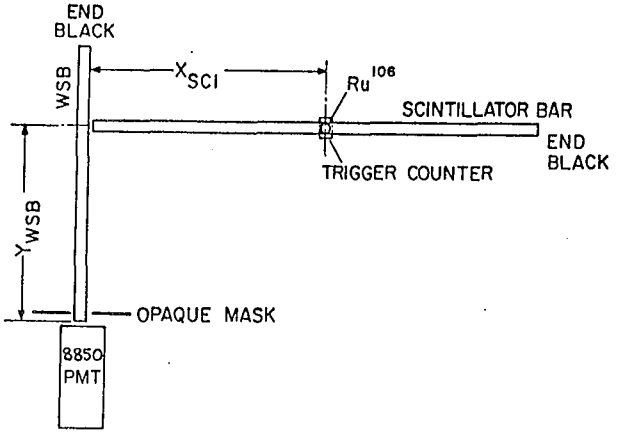

Figure 1

Figure 2 shows the number of photoelectrons plotted (Npe) as a function of light travel distance in the WSB (Ywsb) for a fixed position of the source relative to the scintillator(X_{sci})for a 6.3 mm thick polystyrene scintillator sample, S1, and several kinds of 10mm thick WSB's (1,2,3): UVT acrylic doped with different kinds of wavelength shifters of varying concentrations.

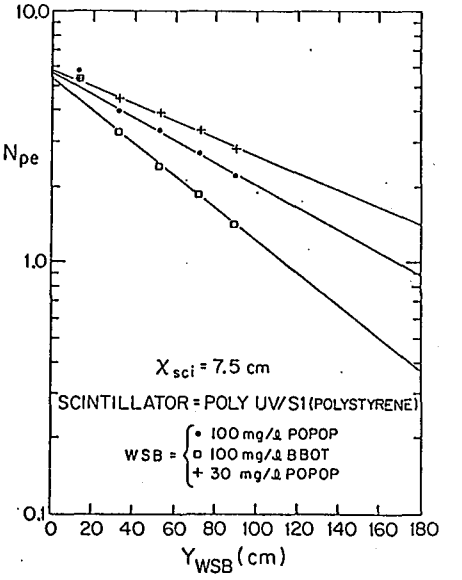

Figure 2

Figure 3 shows the same thing, but for an acrylic scintillator sample, ACR3, which is considerably slower than polystyrene[4].

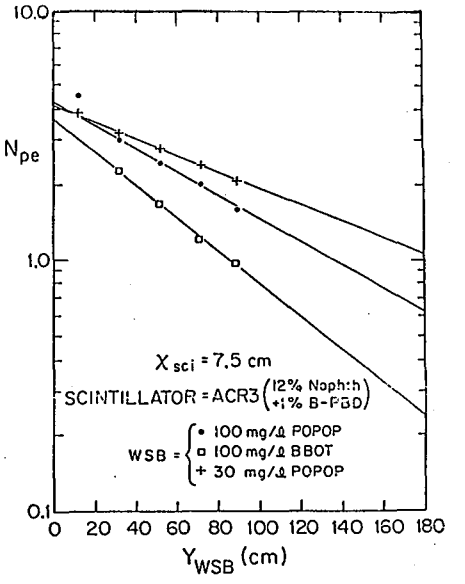

Figure 3

A much more detailed and complete account for the tests and the results is given elsewhere[3].

Discussion of Results

The table below gives Npeo, the number of photoelectrons extrapolated to $Y_{wsb}=0$ and the attenuation length(λ_{wsb}) for each scintillator + wsb combination as well as the composition of each of the materials.

Scintillator (X_{sci}=7.5cm)	Waveshifter	Npeo	λ_{wsb}(cm)
Poly UV	WSB1	5.7	131
	WSB2	5.5	101
	WSB3	5.0	71
ACR3	WSB1	4.1	131
	WSB2	4.3	93
	WSB3	3.5	68

Poly UV = 99% Polystyrene + 1% B-PBD
ACR3 = 87% PMMA + 12% Naphthalene + 1% B-PBD
WSB1 = PMMA + .003% POPOP
WSB2 = PMMA + .01% POPOP
WSB3 = PMMA + .01% BBOT

We note that the attenuation length increases as the waveshifter concentration decreases so that with POPOP concentrations of .001% - .002% one might be able to obtain attenuation lengths of 1.5m or more. The polystyrene scintillator is best in the number of photoelectrons (pe) produced. With a 1 cm thick scintillator sample and at a distance of X_{sci} = 5cm, from our data we can calculate that one should expect about 10 pe(Npeo)instead of 5.7.

Materials and Costs

Cast acrylic and extruded polystyrene scintillators have been routinely produced in large quantities in recent years for several experiments at FNAL and CERN and they are relatively cheap. Their cost is several times lower than that of PVT aromatic scintillators.

Calorimetry Considerations

The large signal levels and attenuation lengths measured by us with the polystyrene and POPOP combination make its use for fast calorimetry quite feasible. A 100 cm^2 area, 10 gap sampling calorimeter module with the proper polystyrene + POPOP combination, read out two meters away could produce as many as 40-60 p.e. per minimum ionizing particle.

The feasibility of fast calorimetry has also been investigated recently in tests at BNL by R.B. Palmer, where calorimeter pulses shorter than 10 nsec have been obtained with a small prototype sampling calorimeter module[5].

The WSB readout technique has however some limitations pertinent to experiments with high luminosities: The difficulty to obtain very fine granularity, the high light attenuation with distance, of fast waveshifters, and its sensitivity to radiation damage.[4,6] However, all three limitations can be greatly reduced if this technique is used for the outer parts of a calorimeter detector surrounding an interaction region and vacuum photodiodes (VPD) are used for read out[7] for the inner part of the calorimeter, located closer to the beams and the interaction point. This combination is quite attractive at present, since VPD readout is considerably more expensive than WSB readout and the volume of a spherical-like detector grows as R^3 (R = distance from the interaction point).

Acknowledgements

The tests were planned and performed with W. Kononenko and W. Selove. We are indepted to B. Musgrave and L. Nodulman for providing to us the KSH polystyrene samples, to V. Fischer and U. Widham of Roehm GmbH Chemische Fabrik for the WSB samples and to DOE for support. We would like to thank the Workshop Organizers for providing the appropriate climate for exploration of such ideas. The exchange of important information and ideas with R.B. Palmer, C. Baltay and R. Gustafson is gratefully acknowledged.

References

1. G. Keil, N.I.M. 87(1970)111 and references therein.
2. W. Selove et.al, NIM 161(1979)233; B. Barrish et.al, Preprint, CALT68-623.
3. "Scintillator-Waveshifter Light Measurements". W. Kononenko, W. Selove and G.E. Theodosiou, University of Pennsylvania Report UPR-0096E, March 9, 1982. To be published in NIM.
4. C. Aurouet et.al., NIM 169(1980)57; J.C. Thevenin et.al, NIM 169(1980)53.
5. R. B. Palmer, Proceedings of this Workshop.
6. UA1 Collaboration, private communication.
7. "Scintillator Calorimetry with vacuum photodiode readout" by W. Selove and G. Theodosiou, Proceedings of this Workshop.

SCINTILLATOR CALORIMETRY WITH VACUUM PHOTODIODE READOUT

W. Selove and G.E. Theodosiou
Department of Physics
University of Pennsylvania
Philadelphia, Pennsylvania

Abstract

Vacuum Photodiodes (VPD) are discussed as a new readout technique for fast scintillator sampling calorimeters.

Introduction

The feasibility of this technique has been demonstrated with light yield measurements using polystyrene scintillators and diodes[1] and measurements with a prototype scintillator sampling e-m calorimeter[2]. Some of its properties and results are presented here. The amplifier noise levels and the possibility of the use of fast signals are briefly discussed as well as the sensitivity of the technique to radiation damage effects. Finally, the numerous virtues of the technique are reviewed pointing to the urgency of rapid manufacturing development of low cost VPD's.

Measurements

Figure 1 illustrates the basic principle of the technique, called SPED, where thin, large area vacuum photodiodes(PED) are used to collect light produced in the scintillator(S) in each cell of a sampling calorimeter. The diode signals of several layers are added together and fed into an amplifier/shaper for readout.

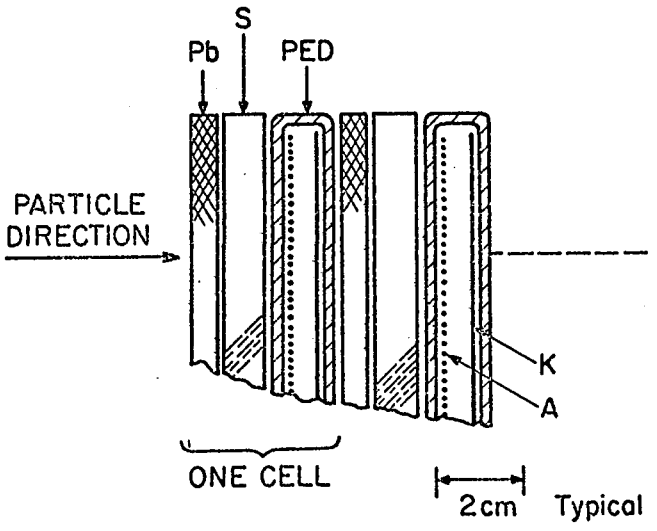

Fig. 1

Figure 2 shows an e-m calorimeter prototype, which was used to measure muons and 20-38 GeV electrons at FERMILAB. The apparatus description, tests and measurements are given elsewhere, in detail.[2]

Figure 3 shows, for this prototype, muon and pedestal pulse-height distributions with a ratio of Signal/Noise=2.4 and Fig. 4 a 20 GeV electron pulse-height distribution, with a pulse rise time of t_{rise} = 150 nsec and a 1 μsec gate, consistent with an energy resolution of $\sigma/E = 0.22/\sqrt{E}$ (1 r. l. Pb plates).

PROTOTYPE SPED e-m CALORIMETER MODULE

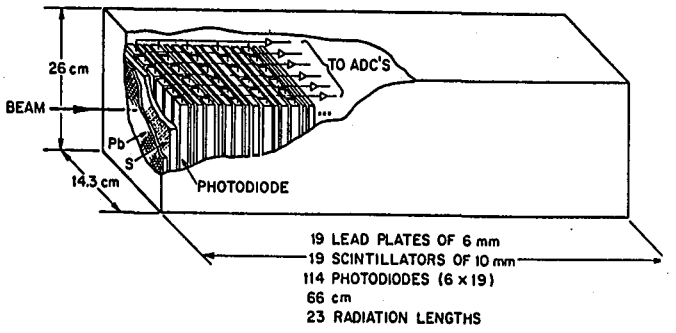

Fig. 2

MUON PULSE HEIGHT DISTRIBUTION

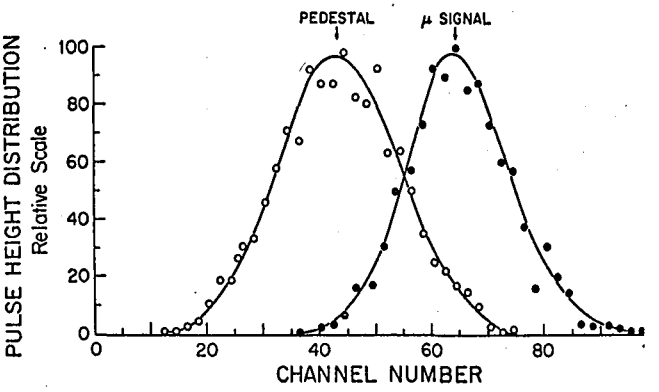

Fig. 3

20 GeV ELECTRONS

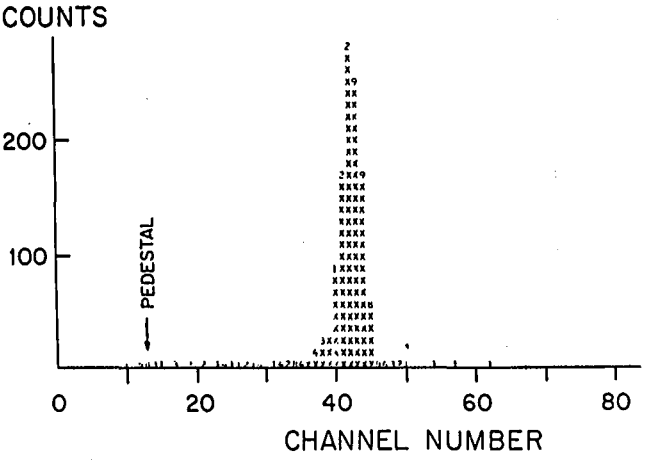

Fig. 4

Signal And Noise

The muon signal measured in this prototype was about 20000 photoelectrons (pe) and corresponds to a 0.2 GeV signal equivalent energy loss or 100k pe/Gev. Then the rms noise is 85 MeV or 30 MeV per 10 diodes per amplifier. From these measurements we estimate that, with properly designed VPD's (1 cm anode-cathode separation) and amplifier electronics, a 25 cm squared, 10 gap, calorimeter module, read out by one amplifier, will contribute a noise of 15 MeV per module, or 30-40 MeV per tower consisting of 4 such modules. Therefore the noise contribution to e-m or hadronic showers of a few GeV energy is negligible. In order to be able to handle the high event rates of a high luminosity Collider, i.e., $L = 10^{33}$ cm^{-2} sec^{-1} (DC mode), it would be necessary to use pulse rise times shorter than the 150 nsec used here. The VPD readout technique seems quite promising in this respect, if very fast pulse shaping is used and the signals are large. If faster signals are used, the noise increases as $1/\sqrt{t_{rise}}$.[3] With optimization of parameters it appears feasible to go to rise times much shorter than 150 nsec and still have reasonably small noise levels for high energy hadrons or jets, for example 50 GeV and higher.

Radiation Damage Effects

Measurements made with polystyrene scintillators by J.C. Thevenin et al.,[4] show that the amount of light loss due to radiation damage is less than 2% for a 2×10^5 rad dose for light travel distances of the order of 1 cm, but increases rapidly as the light travel distance increases (20% for 20cm travel). This indicates that the effect of radiation damage on the signal can be expected to be considerably smaller with the use of the VPD readout technique than with WSB readout.

Merits

The VPD readout technique, applied to fast scintillator sampling calorimetry as well as to high resolution "continuous media" e-m calorimetry, is of high potential at high luminosity machines, mainly because:

1) Calorimeter pulses can be read out very fast.
2) Pulse time resolution can be very good, of the order of 100-200 psec (rms).
3) Radiation damage effect on light yield is expected to be minimal.
4) High segmentation capability.
5) High gain stability.

Other important properties, not directly related to high luminosities, include :

6) Readout compactness.
7) Low sensitivity to magnetic fields.
8) Good energy resolution.
9) No high voltages.
10) Simplified calibration/monitoring.
11) Relatively simple construction and operation.

Cost and Development

At the present time, VPD's with the desired properties can be available at $600 per sq.ft. for quantities of the order of 10k sq.ft. This cost must go down to $150-200 in order for the overall calorimeter cost to be very competitive with that of gas calorimeters.

We also note a very important development need for thin, large area vacuum photo-"triodes" with a gain of 10 or so. With such devices, virtually all amplifier noise problems would become negligible.

Acknowledgments

This work has been carried out all along with W. Kononenko. We would like to thank B. Robinson for exchange of important ideas, R. Van Berg for work on the prototype design and the electronics and R. Ruland for help with the diode tests. We are indebted to J. McCormick and T. Hayashi of the Hamamatsu Co. for the VPD development, to R. Boie and V. Radeka for essential discussions and for providing the amplifiers and to DOE for vital VPD development support.

References

1) W. Kononenko et al.,, NIM 186(1981) 585-591.
2) IEEE Trans. on Nucl. Sci., Vol. NS-30, No. 1, Feb. 1, 1983; Univ. of Pennsylvania Report UPR-101E, to be published in NIM.
3) V. Radeka, private communication.
4) J.C. Thevenin et al., NIM 169 (1980) 53-56.

A MEASUREMENT OF THE RESPONSE OF AN SCG1-C SCINTILLATION GLASS SHOWER DETECTOR TO 2-17.5 GeV POSITRONS

B. Cox, G. Hale, P.O. Mazur, R.L. Wagner, D.E. Wagoner
Fermi National Accelerator Laboratory, Batavia, Illinois 60510

H. Areti, S. Conetti, P. Lebrun, T. Ryan
McGill University, Montreal, PQ, H3A 2T8, Canada

J.E. Brau,† R.A. Gearhart
Stanford Linear Accelerator Center, Stanford, California 94305

Summary

We have measured the response of an electromagnetic shower counter constructed from the new scintillation glass (SCG1-C, Ohara Optical Glass, Inc.) to positrons in the energy range 2 to 17.5 GeV. We have measured the energy resolution of this 18.4 radiation length detector plus its attendant SF5 lead glass shower counter array to be $\sigma/E = (1.64 \pm 0.14)\% + (1.13 \pm 0.33)\%/\sqrt{E}$ with the constant term dominated by variations in the conversion point of the positron and shower leakage. We found this counter to be linear over the energy range examined. We have also measured the light output of the SCG1-C counter relative to light output of the SF5 lead glass guard blocks using 17.5 GeV positrons. We find that the SCG1-C counter produces 5.10 ± 0.30 more light at the phototube than the SF5 lead glass counters.

Introduction

A new type of high density glass (SCG1-C from Ohara Optical Glass, Inc.) has recently been developed[1,2] which can be used in electromagnetic shower counters for high energy physics. This glass differs in two major ways from the various types of lead glasses which have been used for over a decade in high energy physics in two major ways. This glass has barium oxide rather than lead oxide as the high Z material and contains Ce_2O_3 which acts both as a scintillator and a wavelength shifter for Cerenkov radiation. The blue and near ultraviolet Cerenkov light is absorbed and reemitted at longer wavelengths which survive absorption by the glass. The observed net gain, relative to that possible with lead glass, in the number of photons which reach the photomultiplier results in an improvement in the part of the energy resolution due to photon statistics.

This scintillation glass, along with earlier versions, has been tested[3-6] with low energy photons and electrons (< 300 MeV). We have constructed an electromagnetic shower counter which is suitable for high energy shower measurements from this new glass and have tested it using high energy (2 to 17.5 GeV) positrons at the Stanford Linear Accelerator Center (SLAC).

Beam

This test was performed using the positron test beam 19 in the B end station at SLAC. This positron beam had a momentum bite, $\Delta p/p$ (FWHM) = 0.25%, and a small phase space with 90% of the beam particles contained within a beam spot of radius 1 mm. The contamination of this beam by pions and muons was less than 10^{-5} over the entire momentum range. The momentum of this beam was tuneable from 2 to 17.5 GeV/c. We typically operated the beam at 10 pulses per second with an average of less than 0.3 positrons per 1.6 μs pulse. Beam pulses with two or more positrons were tagged and later rejected in the off-line analysis.

Experimental Apparatus

The arrangement of shower counters used for this test is shown in Fig. 1.

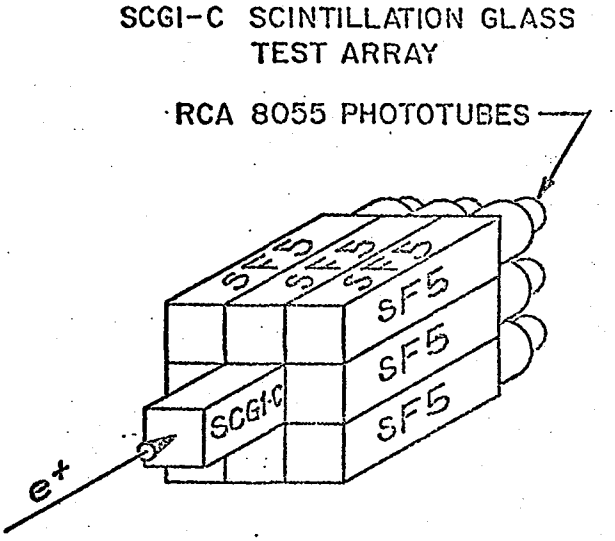

FIGURE 1

The array consisted of a central counter composed of the scintillation glass, SCG1-C, surrounded by eight SF5 lead glass guard counters to capture the transverse leakage of the high energy showers. The SCG1-C counter was 80 cm in length (18.4 radiation lengths) and 15 cm x 15 cm in cross section and had the composition shown in Table I.

Table I

Composition of SCG1-C Scintillator Glass[2]
(by weight)

BaO	43.4%
SiO_2	42.5%
Li_2O	4.0%
MgO	3.3%
K_2O	3.3%
Al_2O_3	2.0%
Ce_2O_3	1.5%

The heavy compound which is the major contribution to the 4.35 cm radiation length is BaO and the scintillating, wavelength shifting component is Ce_2O_3. This particular counter, constructed from two 40^2 cm

†Present address: Department of Astronomy and Physics, Univ. of Tennessee, Knoxville, Tennessee 37916.

pieces, was viewed toward the incoming positron beam by an RCA 8055 photomultiplier. Epotek 305 epoxy was used for the glass-glass joint and for the tube-glass joint in this counter. The eight SF5 guard blocks were 45 cm in length (18.0 radiation lengths) and 15 cm x 15 cm in cross section. These counters were also viewed end on by RCA 8055 tubes. The shorter guard blocks were positioned so that their upstream ends were 25 cm from the upstream end of the SCG1-C counter. This positioning was chosen for the maximum containment of the transverse shower leakage from the SCG1-C counter. Each of the nine counters of the array had a red LED (Monsanto MV10B) mounted on the end of the counter opposite to the phototube for purposes of gain monitoring.

Experimental Results

The pulse shape obtained from the SCG1-C counter resulting from a 17.5 GeV positron shower is shown in Fig. 2 along with the counter's response to a 40 ns pulse from a green LED (Monsanto MV5252).

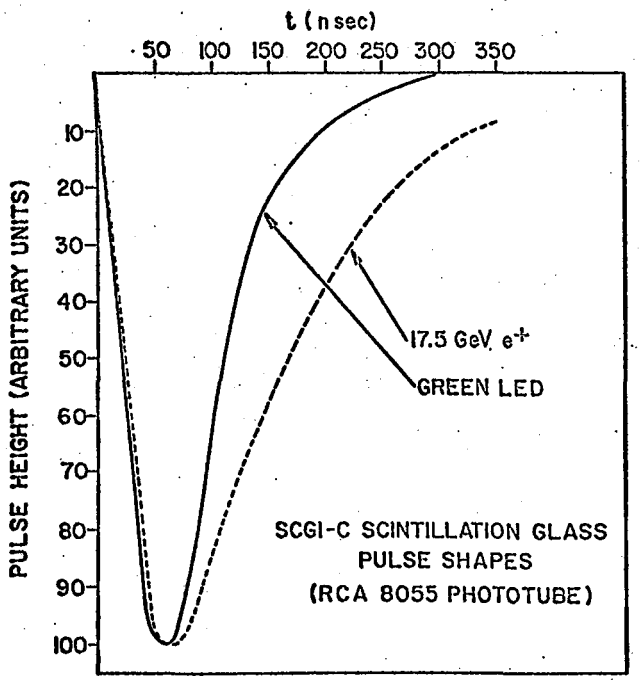

FIGURE 2

The time response of the RCA 8055 tube is a major contributor to the 300 ns length of these pulse shapes. We have estimated the exponential fluorescent decay time of the glass from the difference of the two pulse shapes to be approximately 70 ns. Both 400 ns and 1 μs gates were used with a LeCroy 2249W ADC with no observed difference in the energy resolution. The measurements reported in this paper were performed with the 400 ns gate.

The calibration constants, C_i, for each element of the array were defined by $E_{ik} = C_i P_{ik}$ where E_{ik} is energy deposited and P_{ik} the observed pulse height in the i^{th} counter for the k^{th} shower. These constants were determined from a set of 4.0 GeV runs using an iterative, bootstrap technique. Initially, a starting estimate was made for the calibration constant of each of the nine counters. For the i^{th} individual counter the calibration constant C_i was then determined by minimizing the chi-square

$$\chi^2 = \sum_{k=1}^{N} (E - \sum_{j=1}^{9} C_j P_{jk})^2 \qquad E = \text{beam energy}$$

with respect to C_i. The minimization leads to the formula for C_i:

$$C_i = \frac{\sum_{k=1}^{N} (EP_{ik} - \sum_{\substack{j=1 \\ j \neq i}}^{9} C_j P_{jk} P_{ik})}{\sum_{k=1}^{N} P_{ik}^2}$$

Using this formula and a data sample of N showers with a 4.0 GeV beam centered in the i^{th} counter, the C_i calibration constant was calculated. This C_i then replaced the initial (or the current iteration) value for the i^{th} counter for the next iteration through the array. Using this technique, the calibration constants for the array stabilized after three iterations.

The resolution and linearity of the SCG1-C counter and its accompanying guard counter array were determined by positioning the positron beam at the center of the SCG1-C counter (to ± 1 mm) and recording a few thousand showers at energy settings of 2,4,10 and 17.5 GeV. Pulse height spectra for 2 and 17.5 GeV energies obtained by summing the pulse heights above pedestals in the array are shown in Fig. 3a and 3b.

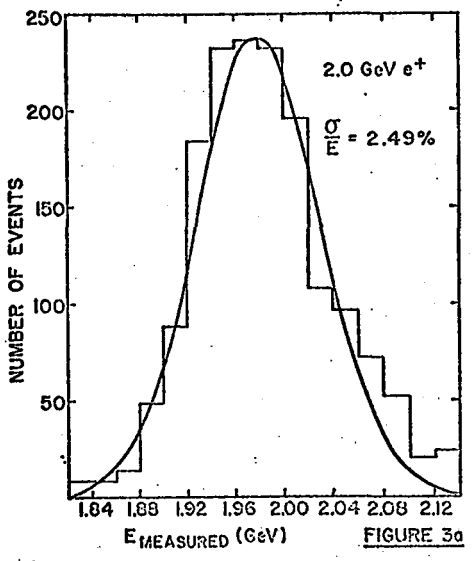

FIGURE 3a

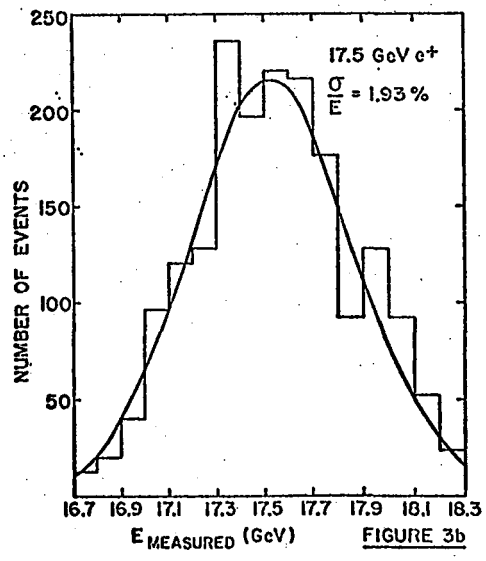

FIGURE 3b

The majority of the energy of the showers was

contained in the SCG1-C counter with only approximately 3.6% of the visible shower leaking into the guard blocks. (This fraction was nearly independent of energy.) The linearity of the array with the beam centered on the SCG1-C counter is shown in Fig. 4.

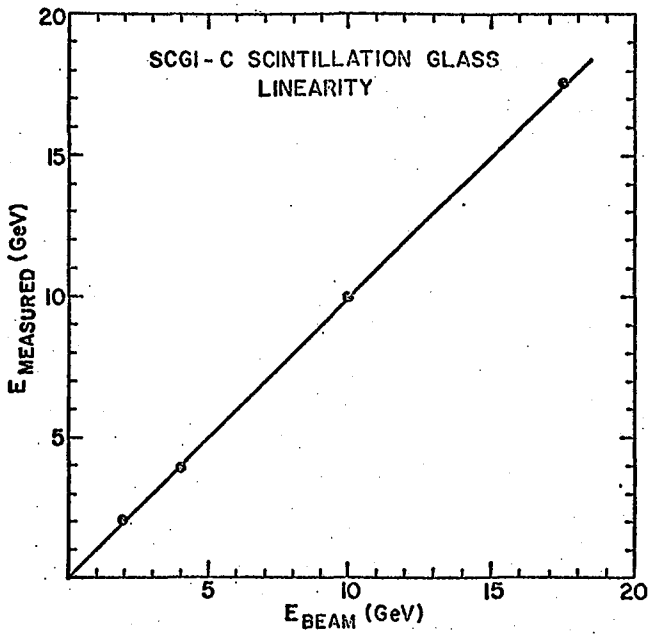

FIGURE 4

We find that these data fit a straight line with a χ^2 of 3.4 for 2 degrees of freedom.

The energy resolution of the test array (which is dominated by the SCG1-C counter response) is shown in Fig. 5 plotted against $1/\sqrt{E}$.

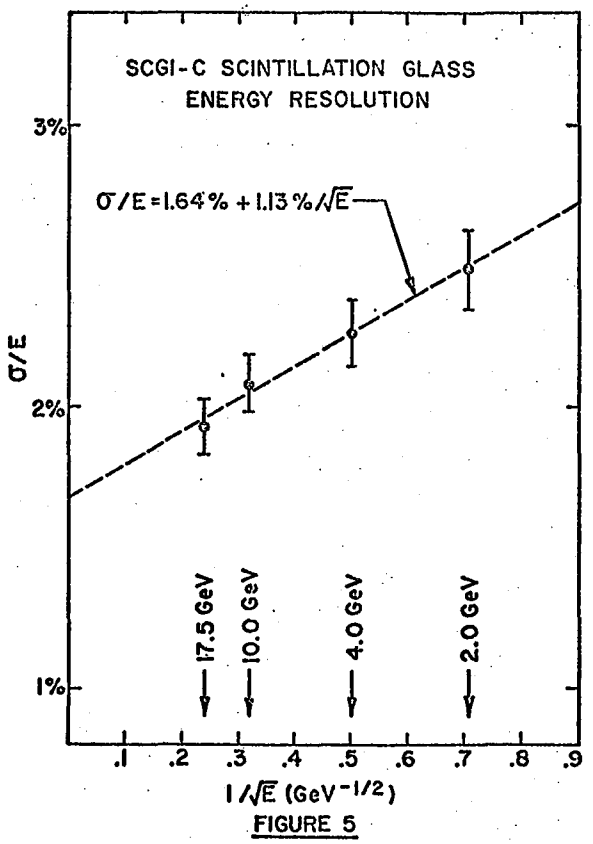

FIGURE 5

These data fit the form $\sigma/E = a + b/\sqrt{E}$ with $a = 1.64\% \pm 0.14\%$ and $b = 1.13\% \pm 0.33\%$. This resolution is to be compared with the result $\sigma \backsim 1.65\%/\sqrt{E}$ obtained by Bartalucci[3] using 60 MeV photons and $\sigma \backsim 2.5\%/\sqrt{E}$ obtained by Chiba[8] using 20 to 120 MeV electrons. These experiments were in the energy regime in which sensitivity to a constant term was small. We have used the EGS shower Monte Carlo program[8] to estimate various sources of contributions to the constant term. Of the 1.6% which we observe, 1.4% can be expected from the sources listed in Table II.

Table II

Estimated Contributions to the Energy Independent Term of the SCG1-C Resolution

Conversion Point Fluctuations	1.1%
Undetected Energy Leakage Fluctuations	0.8%
Resolution of Guard Blocks for Detected Transverse Leakage	0.3%
Momentum Spread of Test Beam	0.1%
Fluctuation of Shower Across Glue Joint	0.1%

Each of these sources of the energy independent term are to the first order independent and therefore can be added in quadrature to get the 1.4% estimate of the constant term. The largest contribution comes from the different optical attenuation of the light from positrons converting at different depths in the glass. This contribution may be minimized by an appropriate filter at the phototube to cut out the component of the light at short wavelengths which fluctuated because of differential absorption. In addition, corrections for the position of the conversion point may be applied on a shower by shower basis if the longitudinal development of the shower is sampled by use of an active converter. The second largest contribution to the constant term, the undetected energy leakage fluctuations, can be reduced by increasing the length of the SCG1-C counter and by proper matching of the lengths of the guard counters to the central counter in order to minimize undetected transverse shower leakage.

Finally the relative light yield of the SCG1-C counter and one of the SF5 guard counters was measured. The relative gain of the phototube of the SCG1-C counter and the guard counter was determined by comparing the pulse heights from a red and green LED which were viewed by both these counters. The relative gain determined in this manner has been corrected for the different absorption of the LED light by the SF5 and SCG1-C glass. The two counters were then exposed to a 4 GeV positron beam and the resulting pulse heights adjusted for the relative gains of the tubes. The ratio of the light outputs of the SCG1-C counter to the SF5 counter determined in this way was found to be 5.10 ± 0.30. Most of the error in this ratio originates in the mechanical reproducibility of the gain measurement which required moving the LED's from one counter to the other.

Conclusions

A counter constructed from Ohara SCG1-C scintillation glass has been tested in a high energy positron beam and has been found to have resolution ($\sigma/E = 1.64\% + 1.13\%/\sqrt{E}$) and good linearity. For comparison the resolution for lead glass measured by other experiments[1,9] is of order $\sigma/E \backsim 1\% + 4.5/\sqrt{E}$. In a complete scintillation glass detector the energy independent term can be reduced by reducing leakage and by compensation for conversion point variations. The intrinsic decay time of glass is consistent with an exp(-t/70 ns) behavior. The light from a 4 GeV

shower arriving at the photomultiplier of this counter is larger by a factor of 5.10 ± 0.30 than that for a comparable SF5 counter. We were encouraged by these results and are designing a larger scintillation glass detector for Fermilab Experiment E-705.[10]

Acknowledgments

We wish to thank Fermilab Physics Department and to acknowledge the considerable efforts of the SLAC operating staff. We would also like to thank the U.S. Department of Energy, the Natural Sciences and Engineering Research Council of Canada, and the Quebec Department of Education for their support.

References

1. Y. Yoshimura, et al., Nucl. Inst. and Methods, 137 (1976).
2. Ohara Optical Glass, Inc., private communications.
3. S. Bartalucci, et al., Laboratori Nazionali di Frascati preprint, LNF-80/10(P), (1980).
4. M. Kobayashi, et al., KEK Preprint 81-8 (1981).
5. M. Kobayashi, et al., Nucl. Inst. and Methods, 184 (1981).
6. M. Chiba, et al., Nucl. Inst. and Methods, 190 (1981).
7. J.E. Brau, et al., Nucl. Inst. and Methods, 196 (1982).
8. R.L. Ford and W.R. Nelson, SLAC-210 (1978).
9. J.A. Appel, et al., Nucl. Inst. and Methods, 127 (1975).
10. M. Binkley, et al., Fermilab Proposal E-705 (1981).

CALORIMETRY AT L = 10^{33}

W. Selove and G. Theodosiou

Department of Physics
University of Pennsylvania
Philadelphia, PA 19104

Abstract

We show that existing scintillation calorimetry techniques make operation at collision rates of 10^8/sec feasible for most rare events. Thus for pp colliders at L = 10^{33}, with DC operation, most such events will be analyzable. The question of possible misleading effects due to pile-up is discussed.

Contents.
1. Introduction and summary
2. Handling events of small time separation
3. Time resolution of an individual event
4. Calorimeter segmenting considerations
5. Timing considerations for triggering
6. Some final comments

1. INTRODUCTION AND SUMMARY

To work efficiently at collision rates of 10^8/sec, calorimeter signal duration, including any jitter, must be short enough to fit into an ADC gate of order 10 ns or less. Moreover, one must be able to cope with the fact that more than one interaction will normally contribute to the set of ADC signals resulting from a single trigger.

Both of these requirements can be met. First, very fast scintillation calorimeter signals are now available. Secondly, we describe a technique whereby one can expect to recognize very easily whether a second interaction (or more) occurs within the gate time, at least in 80% of the cases and probably in 99% or more of the cases. This same technique can be expected to allow one, in most cases, to use the triggering event with little or negligible interference from the second event.

Finally, for very rare events, which might be of unusual physics interest, we discuss briefly pile-up effects. Pile-up effects may be extremely small if the event signature is sufficiently unique (as for example the signature for $W \to e\nu$); if they are not that small, then pile-up contamination can of course be readily recognized by taking runs at different luminosity.

Our conclusion is that as far as calorimetry is concerned, luminosities up to 10^{33} cm^{-2} sec^{-1} are likely to be highly usable to search for rare processes. One might find that rare processes found in this way are in fact simply due to pile-up effects--but it is also possible that pile-up effects will play no significant role.

2. HANDLING EVENTS WHICH OCCUR WITH SMALL TIME SEPARATION

Consider an event occurring in the interaction diamond at some coordinate z along the length of the diamond. (Define z = 0 at the center of the diamond.) This event sends out particles in various directions. The particles reach different angular regions of the calorimeter at different times (unless z = 0).

The fundamental point is this: In any given sector of the calorimeter--say e.g. some 0.5 sr sector, with several hundred towers--the timing signals from these particles will form a tightly bunched group on a time plot--a group of FWHM of order 0.3 to 0.5 nsec. (The σ in this group will be much smaller than the pulse duration from each calorimeter module--see below.) If two events occur, within say a 10 nsec ADC gate, they will in general form two groups on a p_T-vs.-time plot; and for most triggers these two groups will be (a) quite distinct, (b) very different in integrated p_T.

We illustrate this point in Figure 1, which represents a scatter plot of p_T(tower) vs. time, for two events both delivering particles into one sector. This Figure shows what will typically be seen if the two events have a) 1.5 nsec time difference in the average arrival time of the particles, b) total integrated p_T values of 100 GeV/c for event A (a

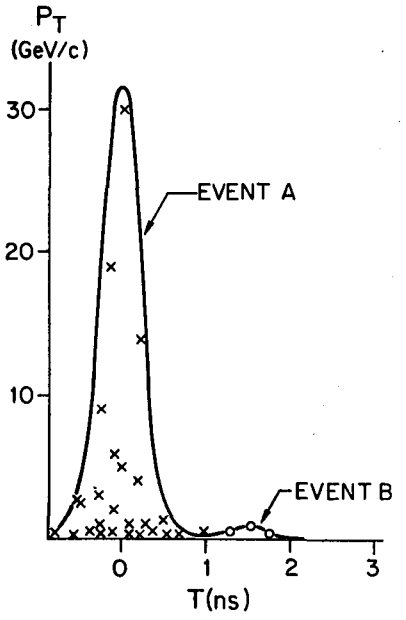

Fig. 1. Expected scatter plot for tower p_T vs. time, for an example with 2 events depositing particles in a 0.5 sr group of towers. Event A is a jet with 100 GeV/c total, carrying many high-p_T particles; event B has only 3 particles in this sector, carrying a total of 1.5 GeV/c. (Only tower signals of 0.2 GeV/c or more are shown.)

typical jet) and 1.5 GeV/c for event B (a typical non-jet set of particles). Clearly if the high-p_T event was the event of interest, and caused the system to trigger, than from this plot one would know that there was a second event present in the gate--and that it was separable, if not in fact ignorable.

In the following sections of this note we treat further details of the time resolution of an individual event. Here we make only a few further comments. (1) The two events which would typically correspond to Figure 1 will in general occur at different z's. Thus recognition of 2-event occurrence, and separation of the events, is possible not only by p_T-vs.-time analysis, but additionally by tracking, given a tracking system of comparable time resolution. Time analysis alone would allow one to interpret some 80% of high-p_T triggering events as probably clean, for the timing resolution indicated above; time and tracking analysis together would probably allow over 99% of high-p_T triggering events to be given an initial interpretation as probably clean. (2) The time separation between two events, shown as 1.5 nsec for the example in Figure 1, will be different in different parts (sectors) of a 4π calorimeter array, since the relevant collisions occur typically at different z's. This variation is in general helpful in showing whether two (or more) events did occur within the gate time.

The point to be emphasized in connection with Figure 1 is this:

> Most collisions result in relatively small total E_T into the calorimeter array--but more particularly they produce mainly low-p_T particles. Hence if the events of interest have a major part of the information carried by high-p_T particles, then a second event occurring within the ADC gate will generally give virtually no distortion of an event of interest.

A plot like Figure 1 merely facilitates recognizing that the 'second' event, in this example, is of almost negligible p_T, at least in this region of the calorimeter.

3. TIME RESOLUTION OF AN INDIVIDUAL EVENT

We remark here on two separate points: a) The duration of sampling calorimeter signals, and b) the pulse timing accuracy.

a) Two techniques have been reported at this Workshop which can give signals of 3 to 6 nsec FWHM. (There is a longer duration pulse "tail" effect, which we discuss below.) One is the convetional SC-WSB--scintillator-waveshifter bar--technique, used with materials having very short decay times and with PMs which have fast rise time.[1] The second is the VPD--vacuum photodiode--technique.[2] Other potentially very fast techniques have also been reported, but are not discussed here.

The fast SC-WSB technique is discussed in reference 1. Here we make a few further comments on the VPD technique. The VPD readout system uses inexpensive fast scintillator and relatively inexpensive thin large-area diodes. The major part of the signal can be obtained as a pulse of a few nanoseconds duration. The low noise amplifiers used with such a device have normally been used with shaping circuits which give rise times of order 100 ns or more, which would require ADC gate lengths of 200 ns or more. However, very much faster shaping circuits can be used, and gates as short as 10 ns or less, at the cost of higher noise in proportion to $T^{-1/2}$, where T is the gate length. The noise level, at 10 ns, would still be reasonably small in a hadron calorimeter working with high p_T events, involving say jets of 50 GeV/c or more.[3]

There is a longer time "tail" component, in any calorimeter, due to long-lasting physical processes in the development of the cascade energy. Restricting the signal collection time by use of a short gate will thus generally worsen the energy resolution. This effect will vary substantially according to the detailed calorimeter design and operating conditions. For non-uranium calorimeters, at high p_T, the resolution worsening can be expected to be relatively small; for uranium calorimeters, particularly at modest p_T, the effect can be a factor of perhaps 1.5 to 2.[4]

b) Pulse timing accuracy. We remark principally on the VPD technique. Signals of say several GeV in a tower correspond to 200,000 p.e. or more. Thus using zero-crossing discriminators the time jitter for a TDC comes entirely from amplifier noise and not from photostatistics. For 0.1 GeV noise per module, and say 4 nsec rise time, the time jitter would be less than 0.1 nsec for 5 GeV energy deposition, and would vary like E^{-1}.

For the SC-WSB Technique one expects about 100 to 200 p.e. per GeV; in this case the TDC jitter comes from photostatistics rather than noise. For 4 nsec rise time the time jitter for this technique would also be about 0.1 nsec, and in this case would vary like $E^{-1/2}$.

Other sources of time jitter include internal time jitter in a module, and, for a calorimeter sector (say 30° in theta and 60° in phi), variation in the flight time for particles from events with the vertex z different from zero. With suitable design all of these effects, combined, can be kept down to 0.2 to 0.3 nsec, rms, thus providing the tight time grouping, for events of say 20 GeV or more, indicated in Figure 1.

4. CALORIMETER SEGMENTING CONSIDERATIONS

Individual tower size should be minimized, consistent with shower sizes, so as to reduce the probability that the two events indicated in Figure 1 will both deliver particles into the same tower. Precise granularity design will depend on the exact machine energy, physics objectives, and overall detector design. For a design in which at 90° the shower maximum occurs at about 150 cm from the beam interaction point, and in which steel plates of 3 to 5 cm thickness form the main part of the calorimeter, we estimate that 200 to 500 towers per steradian at 90°, and about 2000 towers per unit rapidity elsewhere, would probably be appropriate. This would give about 30,000 towers for a 10 TeV + 10 TeV collider.

To carry out the event separation indicated in Figure 1, the analysis of each event, whether on-line or off-line, must be performed using "sectors" corresponding to a limited theta-band, so that the varying flight distances for different particles from the interaction vertex will not unduly broaden the

peak in Figure 1. The tolerable size of each theta-band depends on the ratio of interaction diamond length to radius of the calorimeter, as well as on whether the calorimeter array is spherical or cylindrical. Theta-band widths of order 30 degrees appear satisfactory for the case of diamond lengths of +/- 25 cm and calorimeter radius (spherical case) of 150 cm to the cascade shower peak.

5. TIMING CONSIDERATIONS FOR TRIGGERING

We have been discussing pulse durations of order 5 nsec FWHM. For an interaction vertex which may have any z value in the diamond, there can be substantial variation in the signal time for "forward" particles relative to "backward" particles, up to +/- 2 nsec. If triggering is to use a combination of forward and backward segments, as is the case e.g. for a missing-p_T trigger, and if the trigger is to operate on the combined amplitude of the calorimeter signal rather than on the combined area, then the signals providing the trigger may have to be re-shaped to have a flat top of length roughly 3 nsec. The signals which go to the ADC need not have this shaping--the ADC gate length simply has to be wide enough to allow roughly +/- 1 nsec variation in the signal location relative to the gate, from event to event.

6. SOME FINAL COMMENTS

The approach we have described requires pushing present techniques to about the limit, to permit working with 10 nsec gate lengths. One might fail to reach this limit, by a factor of 2 or perhaps even 3. On the other hand, if the technology improves one could reach this mode of operation without serious problems. A particularly important development in this connection would be the development of thin vacuum photo-"triodes," with a gain of 10 or so.

We have discussed the fact that p_T-vs.-time analysis, combined with tracking information, would probably allow some 99% of all high-p_T events to be analyzed even though additional interactions, but of low p_T, overlap in the ADC gate. The remaining 1% involve events in which there are two interactions so close together in both z and time that they cannot be separated by the techniques described here. For those events one can indeed mis-interpret the character of the event--the multiplicity of jets, the effective masses of combinations of jets, etc. Ultimately, any such mis-interpretation can be identified only by the technique described in section (1): take runs at different luminosities. This limitation, on doing clean physics analysis at the highest luminosity, will always exist at some level, at any luminosity. As one pushes toward higher energies, and searches for ever higher masses and/or processes with weaker coupling constants, one can only try to develop techniques to improve the prospects for clean analysis at higher luminosity. It is in that spirit that we have written this note.

7. ACKNOWLEDGMENTS

We wish to thank the organizers of the Berkeley Workshop--A. K. Mann et al. of the DPF, and Peter Nemethy, Melissa Franklin, and the other members of LBL, for the stimulating atmosphere at this Workshop. We also thank B. Pope, R. B. Palmer, and W. Willis for several interesting discussions.

REFERENCES

1. R. B. Palmer, this Workshop.

2. W. Kononenko et al.: NIM 186, 585 (1981); IEEE Trans. on Nucl. Science, Vol. NS-30, No. 1, p. 125 (1983); U. of Pa. Report UPR 101E, Dec. 1982, to be published in NIM. See also Proceedings of this Workshop.

3. W. Selove and G. Theodosiou, Proceedings of this Workshop, report about 5000 electron equivalent noise charge for 20 cells of 20 cm^2, in a test setup, at 150 nsec rise time, with a signal of 20,000 p.e. from a muon. With optimization of parameters, one could expect that with 5 nsec rise time amplifier noise equivalents of 0.1 to 0.2 GeV could be obtained in hadron modules of this size.

4. W. J. Willis, this Workshop.

TRIGGERING AT HIGH LUMINOSITY: FAKE TRIGGERS FROM PILE-UP

Randy Johnson
Brookhaven National Laboratory, Upton, NY 11973

Triggers based on a cut in transverse momentum (p_t) have proved to be useful in high energy physics both because they indicate that a hard constituent scattering has occurred and because they can be made quickly enough to gate electronics. These triggers will continue to be useful at high luminosities if overlapping events do not cause an excessive number of fake triggers. In this paper, I will determine if this is indeed a problem at high luminosity machines.

The trigger probability for high p_t processes with n additional overlapping events can be calculated as follows. Let $P_n(E_{min})$ be the probability that n overlapping events give an energy $E \geq E_{min}$ with $P_n(0) = 1$. (E can be total energy, transverse momentum along an axis in a hemisphere, or any other continuous parameter of an event which is positive and additive among overlapping events.) $P'_n(E) = dP_n/dE$ = the differential probability for getting n overlapping events between E and E + dE.

$$P'_0 = \frac{1}{\sigma_{TOT}} = d\sigma/dE$$

and

$$P_0 = \frac{1}{\sigma_{TOT}} \int_{E_{min}}^{\infty} d\sigma/dE \, dE$$

= trigger probability of an individual event.

Then

$$P_n(E_{min}) = \int_{E_{min}}^{\infty} dE \int_0^E d\varepsilon \, P'_1(\varepsilon) \, P'_{n-1}(E - \varepsilon).$$

Changing the order of integration gives

$$P_n(E_{min}) = P_1(E_{min}) + \int_0^{E_{min}} d\varepsilon \, P'_1(\varepsilon) \, P_{n-1}(E_{min} - \varepsilon).$$

The probability that n interactions give a trigger is the probability one interaction triggered the system plus the convolution integral for the probability that one interaction combined with the group of (n - 1) interactions to give a trigger. With this formula, the probability for n interactions can be calculated by successive convolutions of the single interaction probability distribution.

Convolutions of exponential distributions get equal contributions from all portions of the integration interval; convolutions of distributions which fall less steeply will tend to get the most weight from the limits of the integration. Therefore, it is not surprising that the most probable high p_t trigger from n overlapping events will come from one moderately high p_t event plus (n - 1) low p_t events.

For triggering purposes, the mean number of interactions during the integration time of the analog sum is the appropriate measure of the luminosity. High luminosity at the ISR has meant .2 to .4 interactions per trigger integration time. At a luminosity of $10^{33}/cm^2/sec$ the mean number of interactions might be between 1 and 5. The trigger probability for an average multiplicity of $\bar{n}$ and trigger threshold of E_{min} is the sum of $P_n(E_{min})$ weighted by the Poisson statistic for n with a mean of $\bar{n}$.

Before moving on to some examples, let me make a disclaimer. I am not trying to predict rates for any specific experiment in a high rate environment with these examples, although they are taken from ISR experiments and the ISAJET Monte Carlo calculations.[1] Instead, I will show what generic types of cross sections can and cannot be measured, and what can be done at the trigger level to reduce the pile-up trigger rate.

The first example is a pure exponential: $P_1(E_t) = .84\ e^{-.84E_t}$ (shown in Figure 1). As can be seen in Figure 1, any amount of pile-up during the measurment is disastrous. Increasing the trigger threshold reduces the fraction of interesting triggers (triggers from single events with $E_t > E_{min}$).

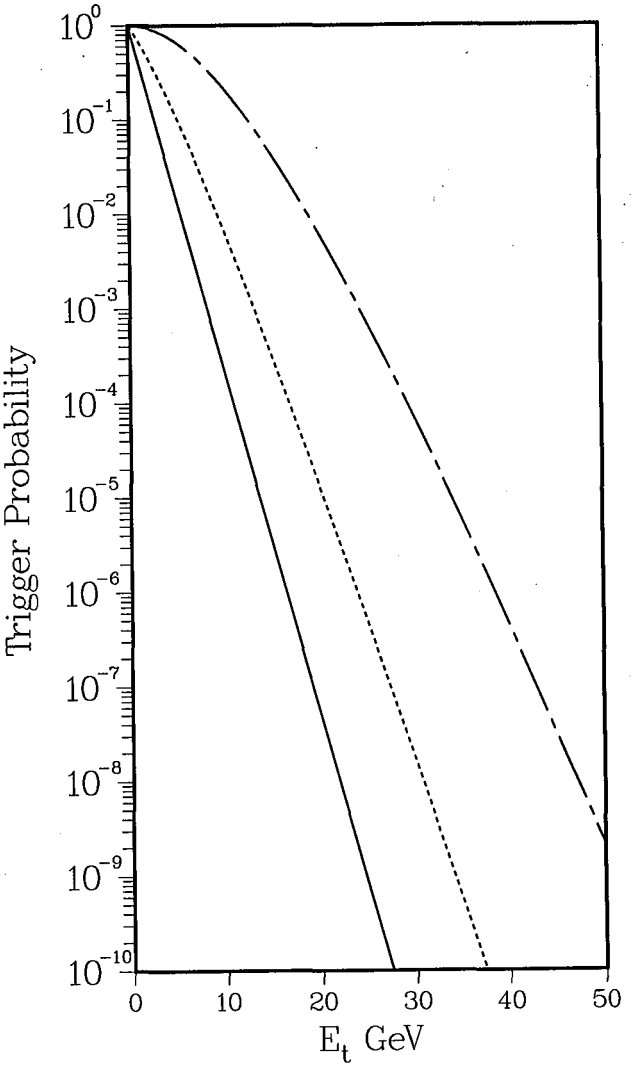

Figure 1. Trigger probability per interaction for the cross section $P'_0(E) = .84\ e^{-.84E}$. Solid line is the integral production cross section (n = 0). Dashed line is for n = 1 and dashed-dotted line for n = 5.

A parton picture of the nucleons implies that the high p_t scattering cross section eventually deviates from a pure exponential. As the second example, let the cross section follow the exponential to E_t = 10 GeV/c and then fall like E_t^{-8} beyond that. The triggering probability distributions for this cross section are shown in Figure 2. The low E_t portion is still dominated by pile-up from multiple events from the exponential region, but, as E_t goes up, the trigger rate eventually deviates from this exponential pile-up and stays at approximately a constant factor above the true cross section. In the high E_t region, the pile-up just lowers the effective threshold from E_t to $E_t - \bar{n}\ E_t^{average}$.

These first two examples are consistent with the E_t cross section measured by R807 at the ISR.[2] They observed an increase in the trigger rate of about 5 when going from a mean multiplicity of 0 to .2 with an E_t threshold of 10 GeV/c. The exponential distribution of example 1 gives a factor of 3.3 increase for these parameters.

At higher energy storage rings, the flattening of the E_t cross section is expected to begin sooner. The E_t cross section predicted by ISAJET for E_{cm} = 800 GeV is shown in Figure 3 along with the trigger rates for n = 1 and n = 5. Because the cross section is flatter, the deviation from exponential pile-up occurs at a lower E_t. The $E_t^{average}$ per event has not changed, however, and the shift in the effective trigger level is about the same as in Figure 2.

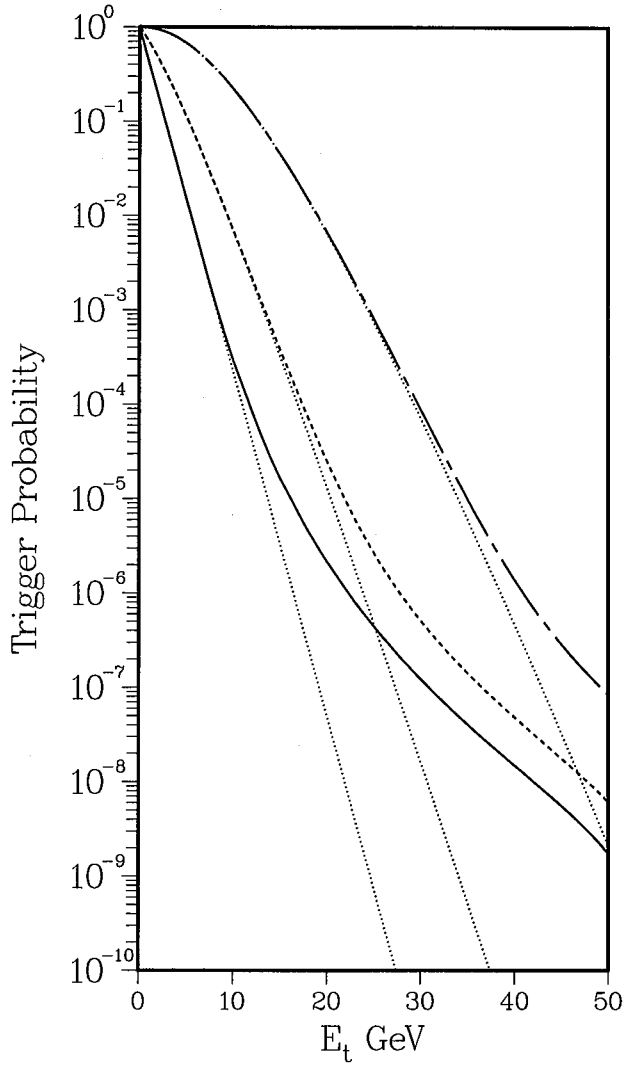

Figure 2. Trigger probability per interaction for the cross section $P'_0(E) = .84\ e^{-.84E}$ for $E \leq 10$ GeV and $P'_0(E) = 1.8 \times 10^4 \cdot E^{-8}$ for $E > 10$ GeV. Solid line is the integral production cross section, dashed line for n = 1 and dashed-dotted line for n = 5. The dotted lines are the curves from Figure 1 for the pure exponential distribution.

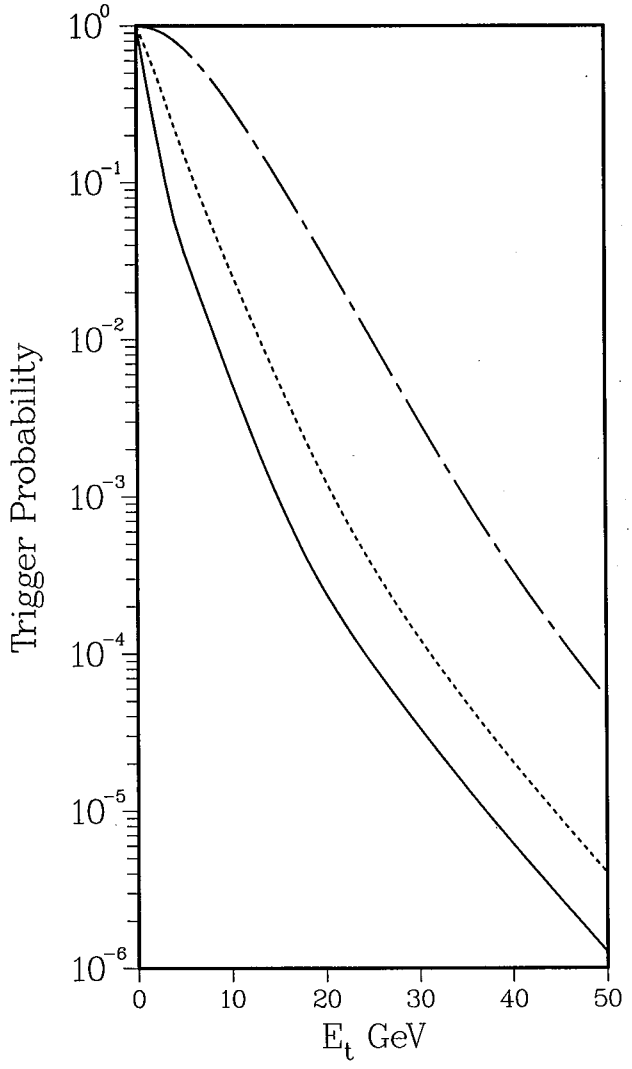

Figure 3. Trigger probabilities per interaction for the ISAJET production cross sections at E_{cm} = 800 GeV/c. Solid curve is for the integral production cross section, dashed curve for n = 1 and dashed-dotted curve for n = 5.

The way to reduce the number of pile-up triggers is to reduce either $\bar{n}$ or $E_t^{average}$. Obviously, better time resolution and smaller integration times will reduce $\bar{n}$. $E_t^{average}$ can be reduced in a number of ways. Rather than summing the E_t over the entire solid angle, just the E_t in the small area around the jet need be summed. Then the E_t from the jet would be unaffected, but the ambient E_t would be reduced (Figure 4). The probability distribution for one jet is the same as in the previous example, but the probability distributions for all subsequent events are reduced. By reducing the integration area from $\Delta y = 4$, $\Delta\phi = \pi$ (as in Figure 3) to $\Delta y = 1$, $\Delta\phi = \pi/2$ the average E_t for an accidental coincidence is reduced from 3 GeV/c to .7 GeV/c. With this technique, the accidental to actual rate is 1:1 down to 30 GeV/c for 5 overlapping events. Placing a threshold requirement on the subelements of the detector reduces the average E_t even further. Although this technique cannot be calculated analytically as the previous examples have, Howard Gordon and Dennis Weygand have written a Monte Carlo program using ISAJET to simulate this process.[3] They find that with a minimum cut of 1 GeV/c the high luminosity trigger rate ($\bar{n} = 10$) is only 30% more than the low luminosity rate down to $E_t = 10$ GeV.

What do these examples teach us? First, the amount of pile-up is dependent on the cross section to be measured. Exponential cross sections are very difficult to measure at anything but extremely low luminosities; cross sections which flatten out at high p_t are easier. For those flatter cross sections, the ambient background from multiple events tends to shift the energy scale of the trigger. A trigger set for 50 GeV/c will trigger, on events produced at $p_t = 50 - \bar{n}\, p_t^{average}$. $\bar{n}$ can be reduced by reducing the resolving time of the apparatus. $p_t^{average}$ can be reduced by reducing the area covered by the trigger, or by summing only the showers generated by particles coming from a given vertex region. If these techniques are used, triggering on high p_t events can be quite efficient even at high luminosities.

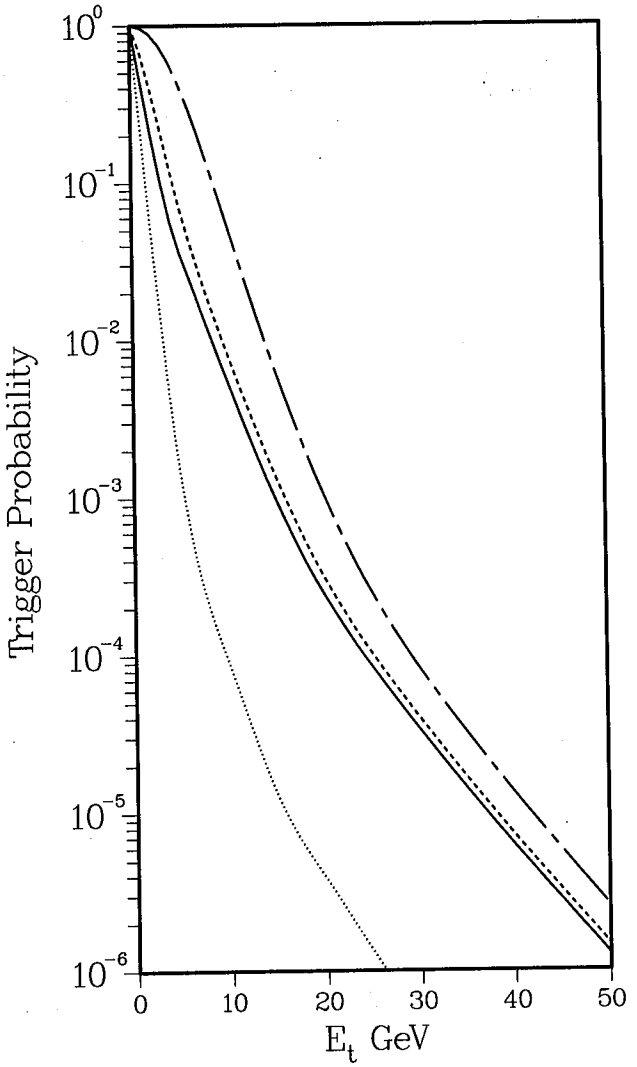

Figure 4. Trigger probabilities per interaction for the reduced solid angle trigger described in the text. The solid line is the integral production cross section used for $P_0(E)$; the dotted line is the random jet probability distribution used for the convolution integrals. The dashed curve is for n = 1 and the dashed-dotted curve for n = 5.

References

1. F.E. Paige and S.D. Protopopescu, ISAJET: A Monte Carlo Event Generator for pp and $\bar{p}p$ Interactions, Version 3, Proceedings of DPF Summer Workshop on Future Facilities, 1982, Snowmass, Colorado.

2. The AFS Collaboration, Opertion of the AFS at 1.4 $\times 10^{32}/cm^2/sec$: A First Look at Data at High Luminosity from the CERN ISR, these proceedings.

3. H.A. Gordon, M.J. Murtagh, R.A. Johnson and D.P. Weygand, Monte Carlo Simulation of the Effect of Pile-up, these proceedings.

FAST ASYNCHRONOUS LEVEL 1 PRE-TRIGGER FOR ELECTRONS AT L = 10^{33} cm^{-2} sec^{-1}

Michael J. Tannenbaum
Brookhaven National Laboratory, Upton, NY 11973

Asynchronous Triggers have long been used at fixed target accelerators and the CW High Luminosity CERN ISR. Bunched beam colliders have tended to use triggers which were synchronized with the time of the beam crossing. The CDF trigger scheme[1] has 3.5 μsec between such crossings to decide whether to further process any events which occurred during the crossing. The level 1 trigger can accept a rate of 50 KHz without appreciable dead time.[1] The level 2 trigger uses fast bit-slice processors to select event topologies in 10 μsec and thus can accept a trigger rate of 5 KHz[1]. Readout of the system which takes 1/2 msec is required for level 3, thus limiting the triggering rate at level 3 to ∿ 100 Hz.[1] The purpose of this note is to show that this same trigger scheme would work at a CW luminosity of 10^{33} cm^{-2} sec^{-1} by the addition of a conventional hard-wired asynchronous pre-trigger.

A pre-trigger for relatively low p_T electrons is discussed, since electrons have long been used as a signature for interesting hadron interactions. Low p_T is emphasized, since such interesting particles like J/ψ and T tend to produce electrons with p_T ∿ 1 GeV/c and ∿ 4 GeV/c respectively. If these electrons are lost at the trigger level there is no hope of getting them back afterwards.

One imagines[2] a typical central region detector as covering the full azimuth, a rapidity range $-2 \leq y \leq +2$ and being segmented into 40 × 40 = 1600 calorimeter towers each covering Δφ = .16, Δy = 0.10. The calorimeter will be divided into electromagnetic and hadronic compartments. For the purpose of the low p_T electrons discussed here, a 17 radiation length counter is superior in charged pion rejection to the 26 radiation lengths used in UA1,[3] so it is assumed that the electron compartment will be subdivided into at least 2 compartments, with the first ∿ 17 radiation lengths being used in this trigger.

It is important to distinguish the time resolution required to obtain analog information with precision suitable for triggering from the time required to integrate the signal for the ultimate energy resolution. For the R-807 calorimeter[4], the pulses could have been clipped to ∿ 20 nsec for triggering, although a 125 nsec integration time was required at the ADC. A high impedance fanout near the photomultiplier would tap-off, clip and distribute the fast signals for the hard-wired trigger while the main signal would proceed to the precision ADC through a delay of ∿ 500 nsec. During this time the main signal would have its rise time degraded by the long delay but this predominantly dispersive process would have little effect on the pulse area.

The tower size of the calorimeter discussed above[2] is well matched to single particle detection for $p_T < 15$ GeV/c. CCOR[5] used a tower size of Δφ = 0.10, Δy = .10 for single particle studies at the ISR. Furthermore, the jets at these low p_T values are much wider than those at higher p_T. It is expected that the background conditions for single particle triggers with $p_T < 15$ GeV/c will be very similar to conditions at the ISR where extensive data exist on single particles and jets with $p_T < 15$ GeV/c.

The pre-trigger is made as follows: A single particle solid angle cell is defined by linearly fanning-in (100) independent groups of 4 × 4 towers in the 40 × 40 array. The output of each fan-in goes to a discriminator with several thresholds and also to the next level linear fan-in (3 × 3 cells of the 4 × 4 towers, for a total coverage Δφ = 0.6π, Δy = 1.2 which is suitable for a jet trigger, etc.). Each of the cells of 4 × 4 towers is fully efficient for single particles in the central 2 × 2 towers, and less efficient in the outer 12 towers. Thus for full efficiency over the whole array, four sets of cells of 4 × 4 towers can be formed, each centered on the intersections of the edges of alternate rows and columns.

The trigger will have a time slewing of 20 nsec due to the dynamic range so that it will have to be retimed with a zero-crossing or constant fraction discriminator to a precision of ∿ 2 nsec. At this point other fast trigger information like Transition Radiator Electron identification[1] or a nearby track[1] with $p_T > 2$ GeV/c can be added. Leading edge timing from the calorimeter[1] can be used to determine which towers were struck in-time (5 to 20 nsec) to avoid pile-up during the longer ADC gate.

The triggering cell size is sufficiently small that triggering rates can be estimated by integrating the measured[6] single π^0 cross section at $\sqrt{s}$ = 540 GeV.

$$E\,\frac{d^3\sigma}{dp^3} = \frac{4.9 \times 10^{-25}\ cm^2}{(p_T + 1)^{8.31}}$$

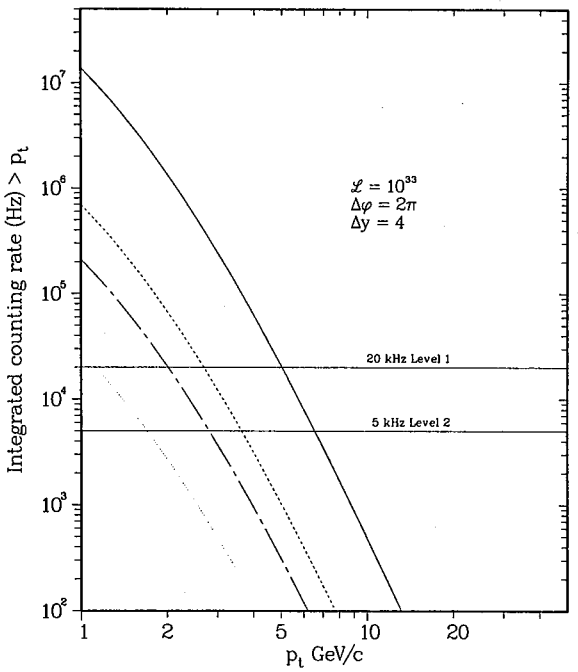

Figure 1. Trigger Rates for Low p_T electron triggers.

1. M. Shochet, Trigger Summary, These Proceedings.
2. H. Gordon, et al., "Reasons Experiments can be Performed at L = 10^{33}," DPF Snowmass Proceedings.

For a detector covering $\Delta\phi = 2\pi$, $\Delta y = 4$ and for $L = 10^{33}$ cm^{-2} sec^{-1}, the π^0 production rate is shown as the solid curve in Figure 1. If there were no tracking or particle I.D. information, this would be the trigger rate. The threshold is determined by either the 20 KHz maximum trigger rate at level 1 or the 5 KHz of level 2. With tracking, or particle I.D., the threshold can be reduced.

The principal background is due to charged hadrons, π^+, which deposit most of their energy in the electromagnetic calorimeter. For a fixed energy deposition, this background is down by a factor of 20 from π^0 (dashed line). This would be the limit of the trigger improvement with fast tracking.[1] A similar but smaller background is a π^0 which deposits its energy accompanied by a charged track with $p_T > 2$ GeV/c coming from the same jet and landing on the same 4×4 cell. This is at the level[5] of $\sim 1.5\%$ and is less of a problem (long-short dashed curve). The dotted curve shows the real electron background[7] due to Dalitz and external conversions (1.5% X_0) which is down a factor of 500 from the π^0 rate. If the electron energy is not measured independently of the parent π^0, then the relevant rejection factor is only 5% which is the probability that the energy of a π^0 includes any conversion electrons. With a magnetic field to sweep away soft electrons, a Segmented Transition Radiator[1] could provide a trigger level rejection of 1% (long-short dashed curve). This would allow a threshold of[8] 4 GeV/c for single electrons at 5KHz triggering rate. Level 2 can then be used to find interesting event topologies like 2 or more electrons, electron + jet, electron + missing E_T etc.

3. C. Rubbia, These Proceedings.
4. B. Pope, Calorimeter Summary, These Proceedings, quoting R.B. Palmer.
5. A.L.S. Angelis, et al., Physics Letters 79B, 505 (1978); Physica Scripta 19, 116 (1979).
6. UA2, J,P. Repellin, Paris Conference 1982, as quoted by R. Cahn, These Proceedings.
7. G. Bunce, et al., W, Z^0 Production, DPF Snowmass 1982
8. N.B. the threshold of 3 GeV/c from Figure 1 was multiplied by a factor of 1.3 to allow for systematics. This factor will be refined with further investigation.

PROSPECTS FOR ĈERENKOV RING IMAGING AT HADRON COLLIDERS

Marvin Goldberg

Syracuse University, Syracuse, New York 13210

David W.G.S. Leith

Stanford Linear Accelerator Center, Stanford, California 94305

Summary

The developing techniques of Ĉerenkov ring imaging detectors are reviewed, with emphasis on their performance in high luminosity environments.

I. Introduction

Ĉerenkov ring imaging is a rapidly developing technique which may be used to identify charged particles over a wide momentum range. Such detectors have recently been utilized in E605 at Fermilab[1], and have been proposed for detectors at LEP[2] and the SLC[3]. The requirements of high quantum efficiency have led to the use of gaseous detectors containing photoionizing vapors.

Since the ring imaging detector can measure the angle of radiation of the Cerenkov photons, the direction of motion of the radiating particle and the number of radiated photons, it can extract far more information than conventional Ĉerenkovs, and needs only two-dimensional readouts as opposed to dE/dx techniques which require far larger numbers of wires. These features lead to relatively compact detectors of large dynamic range.

II. Geometry

Fig. 1 illustrates the "classic" geometry where the interaction region is surrounded by a mirror of radius R_M. Charged particles of velocity β or Lorentz factor γ radiate Cerenkov photons at an angle θ which is focused on a sphere of radius $R_M/2$.

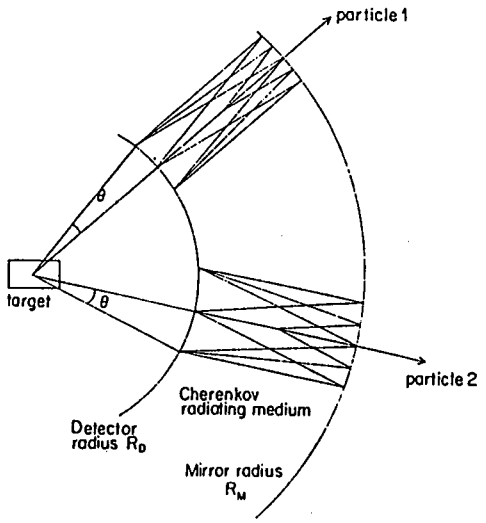

Fig. 1. Schematic view of the ring images produced by two different particles emerging from a target or an interaction region.

The imaging properties of the mirror can easily be understood by realizing that the two sets of parallel Cerenkov rays in the plane of the page look like a source at infinity, and thus form two points on a ring of radius $R=f\tan\theta$ where $f=R_M/2$ is the mirror focal length. A photon detector sits in the focal plane of the mirror.

The above arrangement can be inconvenient when other apparatus is needed. This leads to a "retracted" geometry where segments of the mirror are moved away from the interaction region. More mirror surface area is required at the larger distance, but the total area of the photon detectors can remain esentially the same due to the focusing of rings from non normally incident particles. This arrangement is used in the SLC and LEP proposals (see Fig. 2) where isobutane is the gas radiator.

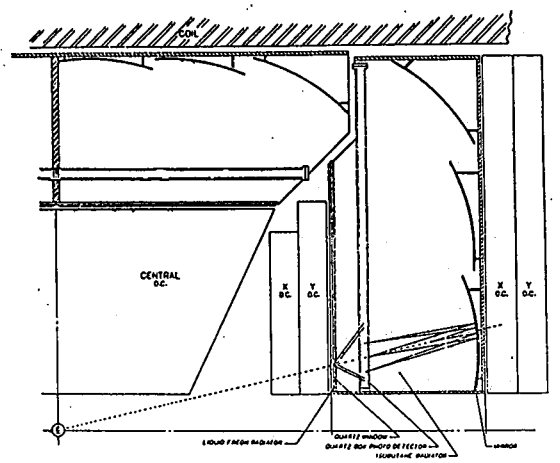

Fig. 2. Detector of SLD proposal at SLC. The DELPHI detector at LEP will have individual photon detectors associated with each mirror. A liquid Freon radiator is shown in addition to gaseous isobutane.

The fixed target E605 arrangement at Fermilab is shown in Fig. 3. Here the radiator (length 16m) is longer than the focal length of the mirror segments, which focus the U.V. photons on the outboard detectors, which never see the beam particles. Helium is the radiator of choice in this experiment.

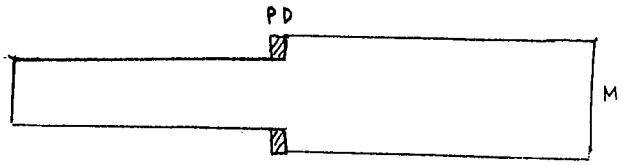

Fig. 3. Schematic of 16m Helium radiator of E605 at Fermilab. Photon detectors are shaded.

One can also imagine a "hidden" geometry, where the photons are reflected to a detector shielded from particles emerging from the interaction region. This technique could be useful at small angles in conjunction with high Cerenkov thresholds (Lorentz factor γ_T) in cases of high luminosity, so that only high momentum particles are seen by the detector (see Fig. 4).

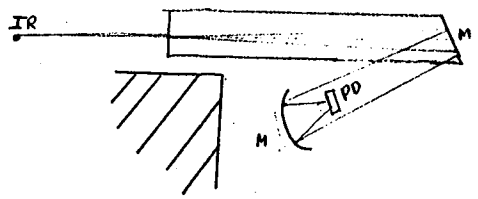

Fig. 4. Schematic of possible "hidden" geometry, where photon detector is hidden by shielding from interaction region.

III. Useful Equations and Approximations[4]

With β the particle velocity and n the radiator index of refraction, then

(1) $\cos\theta = 1/\beta n$ and small θ then

(2) $\sin\theta \simeq \tan\theta \simeq \theta$ For relativistic particles

(3) $1-\beta = 1/2\gamma^2$.

Then for small n-1

(4) $\theta_\infty = \sqrt{2(n-1)} \simeq 1/\gamma_T$ where γ_T is threshold γ, θ_∞ is θ as $\gamma \to \infty$.

The number of detected photons per cm of radiator is then

(5) $N_\infty = N_0 L\,\theta_\infty^2 = N_0 L/\gamma_T^2 = 2N_0 L(n-1)$

where

(6) $N_0 = 370\,eV^{-1}cm^{-1} \bar{\varepsilon}\,\Delta E$ where ΔE is the energy interval for detected photons and $\bar{\varepsilon}$ an overall efficiency.

For slower particles (7) $N = N_\infty (1 - \gamma_T^2/\gamma^2)$.

The ring radius is (8) $R = f\theta$ where (9) $f = L = R_M/2$ is the focal length for a radiator of length L in the classical configuration with mirror radius R_M. For two particles of the same momentum where γ_{max} refers to the heavier particle

(10) $\Delta R/R_\infty \simeq \Delta\theta/\theta_\infty \simeq \gamma_T^2/2\gamma_{max}^2$

IV. Dynamic Range

The curves of Fig. 5 illustrate[5], in a radiator independent manner, the angle of emission of Cerenkov radiation as a function of γ. The detected ring size is used to measure the Cerenkov angle, and so a kaon, for example, can be identified from just above its threshold γ_T up to γ_{max}, the energy where $1-\theta_K$ is too small to measure with precision. The range for kaon identification, γ_T to γ_{max}, or correspondingly E^K_T to E^K_{max}, yields a range of "complete" π-K-p separation. Equation (10) indicates that a 1% measurement in radius yields a range in energy from E_T to $E^K_{max} = 7\,E^K_T$ for such separation.

Additional particle identification is possible over other energy intervals. Pion-electron separation is available as long as the pion ring is distinguishable from that of the electron. The energy interval range is then from E^π_T to $7\,E^\pi_T$.

V. Precision of Position Measurement

Fig. 6 shows the contributions to the uncertainty $\Delta\theta$ due to various sources[6] for an Argon radiator. For regions of interest here, chromatic dispersion is a significant limitation. We note that an uncertainty of $\Delta\theta = 0.3$mrad will provide the upper limit to the dynamic range. Since $\theta_\infty = 26$mrad, we conclude that a 1% angular measurement is possible. Since gases with less inherent dispersion (smaller $\Delta\theta/\theta$) generally

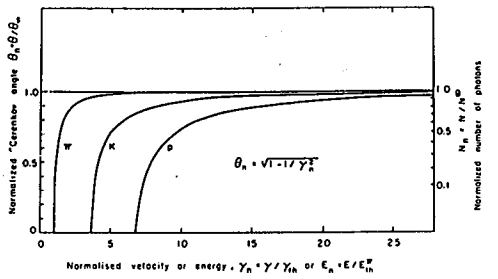

Fig. 5. In this plot the left curve shows how the normalized Cerenkov angle $\theta_n = \theta/\theta_\infty$ grows from zero at the normalized velocity $\gamma_n = 1$ up towards the maximum value 1 at large velocities. Taking the ordinate to be a relative energy scale normalized to the threshold energy for pions, the three curves correspond to π, K, and p as indicated. The ordinate on the right-hand side shows the normalized number of emitted Cerenkov photons.

have lower indices of refraction and are therefore longer, the required position resolution does not vary substantially with the choice of gas radiator in the classic or retracted geometry.

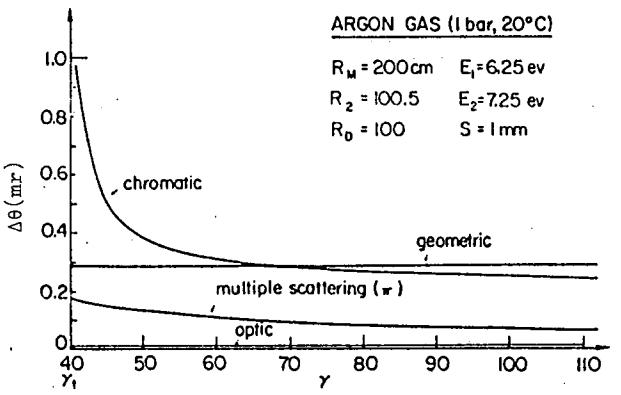

Fig 6. Aberrations of an argon gas radiator with the listed geometry and detector condition versus the Lorentz γ factor. The threshold of such a counter is $\gamma_T = 40$; s is the wire spacing or equivalent.

VI. Readout

A collider detector suited to study narrow jets should maximize the number of radiated photons so that overlapping rings are clearly resolved. While two dimensional readout could accomplish this task, the number of elements and complexity of readout required does not presently allow this technique. Electron positron collider detectors have chosen to drift electrons perpendicular to the direction of incident photons, determining the associated co-ordinate from

the drift time and anode wire position. (See Fig. 7) A third co-ordinate could be determined by cathode readout. This technique is not suited to high luminosity colliders because of the large time aperture associated with the long drift distance (>10cm). Constraining ourselves to reasonable numbers of MWPC wires leads to a system of electron detection below the conversion region of Fig. 7, instead of on the side. Fig. 8 illustrates this type as used in the detector of Fermilab E605. The preamp plus PWC combination allows sufficient gains while minimizing problems due to avalanche produced photons. The two required co-ordinates are measured by a combination of anode and stereo cathode wires. Fig. 9 shows an example of this type of readout. Even photons distant from the ring of interest can cause confusion, and the number of photons per ring must be limited to ~6. Improvements in this readout may be achieved by: charge division for the distant photon problem; pulse height correlations for ring overlap problems; time slicing to improve the resolution on non-normally drifting electrons.

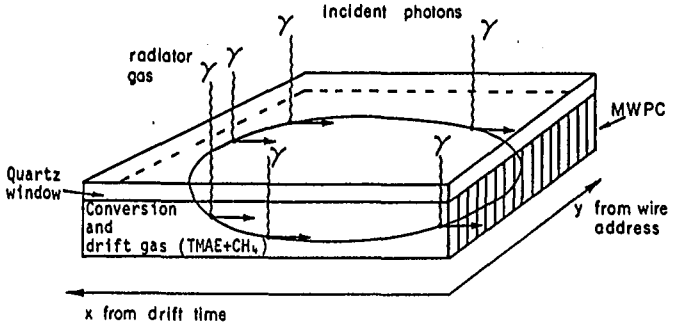

Fig. 7. Schematic view of the single-photon drift detector, Delphi proposal.

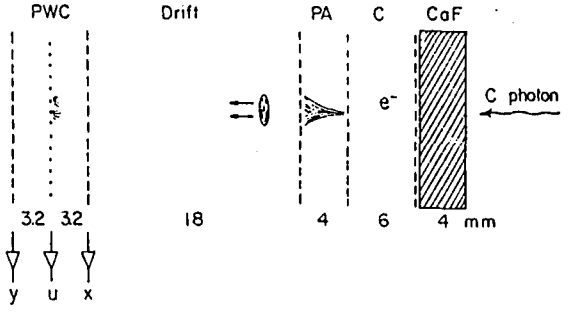

Fig. 8. Photon detector structure.

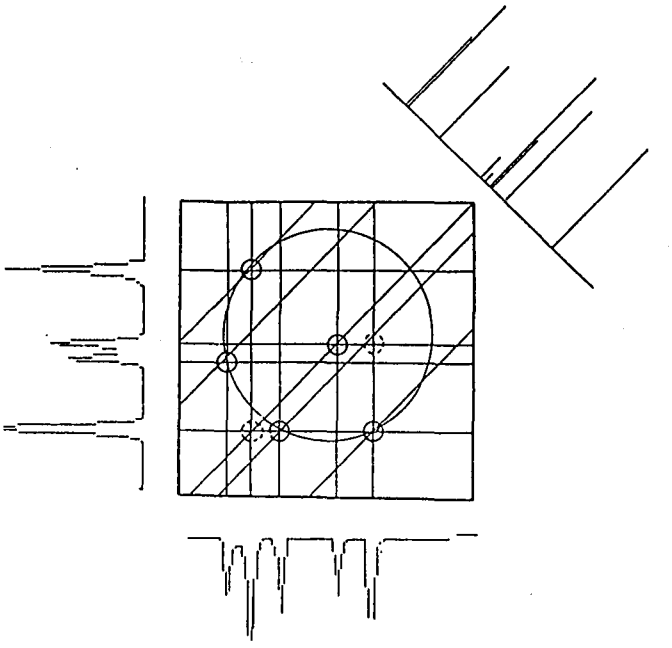

Fig. 9. An example of photon reconstruction for an event with four photons and a beam track. The beam track is not at the center of the Cerenkov ring which is determined by the particle direction. Two ghost points appear, but they are easily eliminated because three coordinates are required for other, real points.

VII. Choice of Radiator-Detector System

A luminosity of $10^{33}cm^{-2}sec^{-1}$ at 1TeV will produce ~3.5 particles/interaction in a unit rapidity interval (or 2πster) for polar angles $30° < \theta < 150°$ at an interaction rate of 50 MHz. If we consider a detector of solid angle ~1str, a flux of $\sim 3x10^7$Hz must be handled.

With current materials, we have a choice of two photoionizing vapors, TMAE and TEA. The time aperture of a TMAE system is 0.5-1usec due to the 0.5-1cm mean free path of photons in the gas, while a TEA system can provide a mean free path of 0.5-1mm and a corresponding time aperture of 50-100nsec.

The above considerations have led to a choice of a TEA detector for E605, and TMAE proposals for electron positron colliders. As Fig. 10 indicates, TMAE has the advantage of quartz windows, variety in liquid and gaseous radiators and higher quantum efficiency. If heated to increase its vapor pressure, the time aperture may be reduced somewhat. A magnet may be placed in front of the detector, reducing the flux to $\sim 5x10^6$Hz, and if a cell of photon detector sees 10mstr, the flux through it could be $5x10^4$Hz. Very few of these particles will produce rings in the gas detector due to the radiation threshold. Providing that other detector elements label tracks from previous events, a TMAE system like that of the Delphi proposal with the addition of E 605 type readout with time slicing, may work. The limits for π-K-P separation are indicated in Fig. 11 for a system of liquid freon and isobutane ($n-1 = .277$, $1.7x10^{-3}$ respectively).

A TEA detector could have a time resolution an order of magnitude better than that for TMAE: calcium fluoride windows with special mountings (cost $200 for 10cm x 10cm window) are then necessary, and noble

gases must serve as radiators.

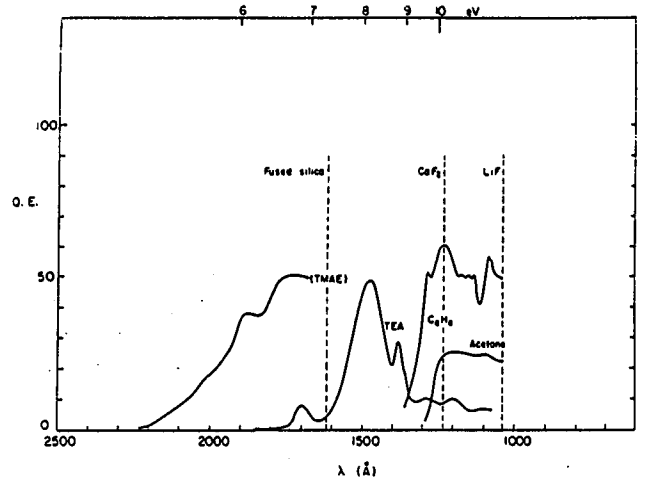

Fig. 10. Quantum efficiency of various photoionizing vapors and window cutoff frequencies.

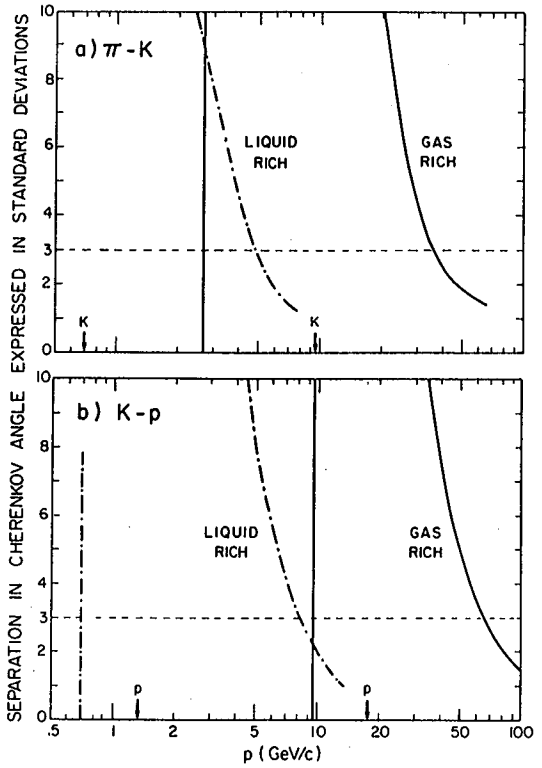

Fig. 11. Pion-kaon and kaon-proton separations given by the forward Delphi counters. For both pairs of particles the two counters match, giving many more than the conventional three standard deviation separation in wide momentum ranges: 0.3-35 and 0.7-60 GeV/c respectively. The thresholds (i.e. the vertical lines) correspond to 95% detection efficiency for the lighter particles. The arrows indicate the threshold for the heavier particles.

Realizing that the energy range for π-k-p separation is ~E_T^K to 7E_T^K, and that the upper limit of interest at proposed hadron colliders is <100 GeV, Table I would suggest Argon as the preferred radiator. A 10 mstr cell at ~3 meters from the intersection would enclose most rings.

The above detection can help identify electrons up to E^{π}_{max}=37GeV, or distinguish pions from K's and protons from 6 GeV, and provide complete π - K-p separation from E_T^K=20GeV to the highest momentum of interest.

Table I

Noble Gas Characteristics[7]

	$(n-1)\times10^{-5}$	γ_T	Length for 8 detected photons assuming No = 80cm^{-1} cm	E_T^{π} (GeV)	E_T^K (GeV)	Classic Geometry cm
He	3.7	116	1340	16	56	12
Ne	7.2	83	690	12	42	8
Ar	34	38	147	5.3	19	4
Kr	55	30	91	4.1	15	3

Extending the momentum convergence downward with TEA presents unpleasant choices: pressurized Argon (where γ_T varies as (pressure)$^{-1/2}$, or liquid Helium (n-1=0.02). The cryogenic problem may be easier to live with than high pressure on CaF_2 windows. The simplest solution seems to be a series of threshold counters[8].

VIII. Cell Content on Triggered Events

If the density of rings per event per cell is more than 1, reconstruction will be difficult with the type of readout proposed. In the gaseous radiation detectors, preliminary ISAJET studies indicate that a jet trigger will provide a mean number of ~1 ring plus ionization of ~1 extra particles if used in combination with a sweeping magnet in front of the detector. This type of ring density will also be encountered in LEP and SLC detectors.

IX. R & D Activities

The following items would clearly be of interest

A. TEA matched radiators with indices of refraction larger than isobutane but with no cryogenic or pressure requirements.
B. Thin photocathodes of high quantum efficiencies (CsI and liquid TMAE are under study).
C. Two dimensional[9] fast and efficient readout schemes (needles, pads, CCD's).
D. Other TEA matched windows.

Additional studies should be done to assess the feasibility of long liquid helium ring imaging detectors near the beam lines.

X. Conclusions

Although there are difficulties, one can conceive of a detector with freon, isobutane and argon radiators, covering a momentum range from less than 1 to over 100 Gev with π-K-P separation abilities. We wish to thank F. Sauli for many valuable conversations.

References

(1) Paper submitted to IEEE Transactions on Nuclear Science, E605, Fermilab. Also see R. Boucher et al CERN EP 82-83. A. Breskin et al IEEE Transactions on Nuclear Science NS-28, 1981, 429. G. Coutrakon et al IEEE Transactions on Nuclear Science NS-29, 1982, 329

(2) DELPHI 82/1 and COLLEPS 82/23, Proposals to CERN for the LEP detector.

(3) The SLD proposal of Cal. Tech, Johns Hopkins, MIT, SLAC, U. of ILL., U. of Wash.

(4) Proc of 1981 Summer Workshop, Isabelle, BNL 50885

(5) T. Ekelof et al Phys Scripta 23, 718, 1981

(6) T. Ypsilantis, Phys Scripta 23, 371, 1981

(7) T. Ekelof, ICFA Workshop, 1979, Ed by U. Amaldi (CERN, 1980) P 396

(8) Proc of 1978 Summer Workshop, Isabelle BNL 51443

(9) B. Robinson, Phys Scripta 23, 716, 1981

USE OF SYNCHROTRON RADIATION FOR ELECTRON IDENTIFICATION AT HIGH LUMINOSITY

S. Aronson
Brookhaven National Laboratory, Upton, NY 11973

Introduction

Synchrotron radiation has been used successfully to identify electrons of 10 to 30 GeV traversing a field length of 30 kG-m.[1] Since comparable field lengths are a feature of many proposed collider detectors, and since this is an electron energy range of interest at $\sqrt{s} \approx 1$ TeV, we consider whether such a device could be useful in the $L = 10^{33}$ environment.[2]

Figure 1 shows the arrangement. The electron track and its "tail" of X-rays are detected in a

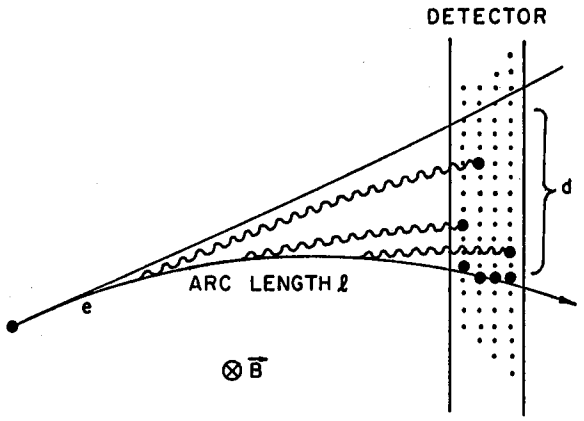

Fig. 1. Schematic depiction of electron identification by synchrotron radiation. The length of the X-ray "tail" is denoted by d. The detector is a multilayer wire chamber, the large dots represent hits.

Xenon-filled MWPC. Figure 2 shows the spectrum of X-rays produced in a 1 meter distance at 30 kG for several electron energies. The total energy emitted in a distance ℓ and field B is given by

$$\Delta E_x \approx 0.013\, E_e^2 B^2 \ell,$$

where ΔE_x is in keV, E_e is in GeV, ℓ is in meters and B is in kG. Despite the fact that the total energy is proportional to E_e^2, the number of detected photons peaks at $E_e \approx 5$ GeV (see Fig. 3). This is due to the detection efficiency of Xenon and to the shift of the spectrum with E_e depicted in Fig. 2.

The electron identification depends on the spatial correlation between the electron and X-ray hits; the X-rays lie in the bend plane of the electron, spread over a distance d(mm), where

$$d \approx 15\, B\ell^2/E_e.$$

For example d is 15mm for a 30 GeV electron with B = 30 kG and ℓ = 1m. The width of the X-ray tail is determined by the spatial resolution of the detector in the direction perpendicular to the bend plane.

Rates and Particle Densities

We assume a detector which covers about 2 units of rapidity (centered at y = 0) and is composed of 4mm mini-drift cells at 1m from the interaction diamond,

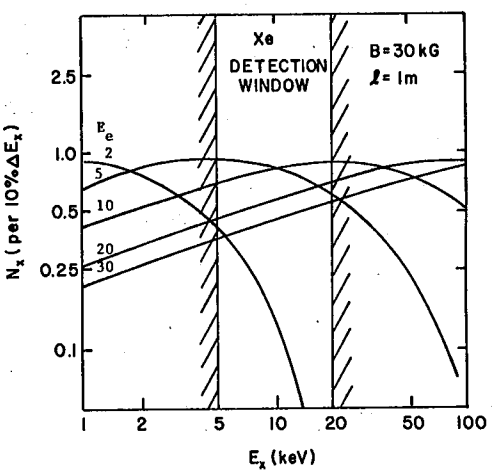

Fig. 2. The number of X-ray photons produced versus photon energy, E_X. The curves are labelled according to electron energy in GeV. The shaded vertical lines delimit the region of good X-ray detection efficiency in Xenon.

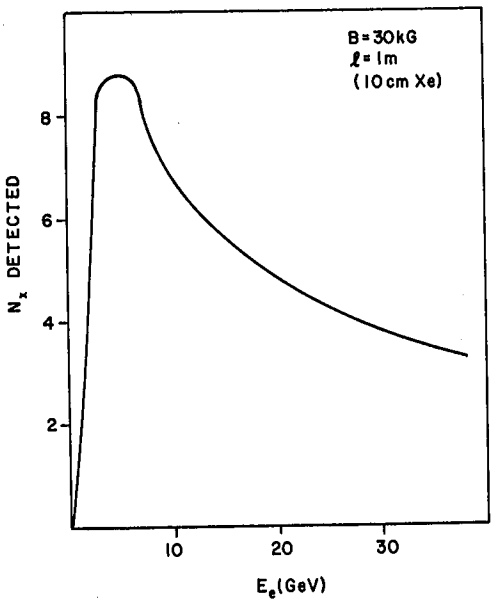

Fig. 3. The number of photons detected in 10 cm of Xe as a function of electron energy.

with 2.4m long wires parallel to the magnetic field. The charged single particle rate at $L = 10^{33}$ (taking into account the p_T cutoff of the field) is about 0.25 MHz/wire (or 4 μsec mean separation). Since one should be able to operate such a chamber with a gate < 100 nsec, rate does not appear to be a problem in this configuration.

A more serious question (albeit independent of luminosity) is that of fake electron triggers or trigger losses due to the spatial overlap of particles within the same event. To investigate this question we use predictions of particle densities within 100

GeV jets from ISAJET.[3] To estimate the resolution perpendicular to the bend plane, we assume this is done with cathode strips which yield 5mm localization of the hits. Taking any spatial coincidence of two charged particles within an area = 5mm x d to be an "electron," we find about 0.1 fake electrons above 10 GeV per 100 GeV jet. This can be suppressed significantly by seeing if the tracking system finds 1 or more than 1 track pointing to the "electron." Further suppression could be based on the fact that a charged track and a collection of X-rays would produce very different energy depositions on the drift wires. With dedicated processors these reduction factors could probably be obtained in the few μsec available. A crude estimate of these factors yields $< 10^{-3}$ fake electron triggers above 10 GeV per event.

Using the same input from ISAJET one can determine the loss of real electrons due to overlaps of other charged tracks. In 100 GeV jets this loss is 1 to 2% for 10 to 30 GeV electrons. (A brief look at 1000 GeV jets reveals that for comparable values of $E_e/E(\text{jet})$ the losses are at most a factor of 2 worse.)

Compatibility with Other Detector Components

Note that $\Delta E_x \propto B^2\ell$ and $d \propto B\ell^2$. Thus one benefits (at fixed $\int Bd\ell$) from larger B and smaller ℓ. This yields more X-rays in a smaller impact area. Tracking systems, on the other hand, prefer large ℓ and smaller B. This gives larger sagittas (also $\propto B\ell^2$) and fewer trapped soft tracks. Thus compromises need be made in a system that includes both. It should be kept in mind that if the tracking chamber is carefully designed to keep the mass low, then it will be transparent to those X-rays which can be detected in the Xenon chamber. Thus tracking and electron identification can coexist in the same field volume.

Research and Development

At E_e = 10 GeV the number of detected X-rays is already falling (albeit slowly) because the X-ray spectrum peak has shifted out of the Xenon detection window. The energy range of identifiable electrons could be expanded (or the B,ℓ requirements lowered) if a detector with good efficiency for $E_x > 100$ keV could be used. Thus development of a practical liquid or solid detector might be very useful.

This research supported by the U.S. Dept. of Energy under Contract No. DE-AC02-76CH00016.

References

1. J. Dworkin, Univ. of Michigan Ph.D thesis (unpublished). In this case electrons from Λ-β decay in a neutral hyperon spectrometer were identified with a Xe-filled proportional chamber following the analysis magnet.
2. J. Kirz and H. Walenta, Proceedings of the 1981 ISABELLE Summer Workshop, BNL 51443, p. 1406.
3. F.E. Paige and S.D. Protopopescu, "ISAJET: A Monte Carlo Event Generator for pp and pp Interactions, Version 3," BNL 31987 (Sept. 1982).

TOF FOR HEAVY STABLE PARTICLE IDENTIFICATION

C. Y. Chang
University of Maryland
College Park, Maryland 20742

Searching for heavy stable particle production in a new energy region of hadron-hadron collisions is of fundamental theoretical interest. Observation of such particles produced in high energy collisions would indicate the existence of stable heavy leptons or any massive hadronic system carrying new quantum numbers.[1] Experimentally, evidence of its production has not been found for PP collisions either at FNAL[2,3] or at the CERN ISR[4] for $\sqrt{S}$ = 23 and 62 GeV respectively. However, many theories beyond the standard model do predict its existence on a mass scale ranging from 50 to a few hundred GeV.[5] If so, it would make a high luminosity TeV collider an extremely ideal hunting ground for searching the production of such a speculated object.

To measure the mass of a heavy stable charged particle, one usually uses its time of flight (TOF) and/or dE/dX information. For heavy neutral particle, one hopes it may decay at some later time after its production. Hence a pair of jets or a jet associated with a high P_t muon originated from some places other than the interacting point (IP) of the colliding beams may be a good signal. In this note, we examine the feasibility of TOF measurement on a heavy stable particle produced in PP collisions at $\sqrt{S}$ = 1 TeV and a luminosity of 10^{33} cm^{-2} sec^{-1} with a single arm spectrometer pointing to the IP.

To measure the time of flight (TOF) for the stable heavy particles produced at large angles, we shall use the β = 1 muons as a reference. Figure 1-a shows the TOF for a 100 GeV/c^2 mass particle with 50 GeV/c momentum in comparison with that of β = 1 reference particles. At 1 TeV C.M. energy and 10^{33} cm^{-2} sec^{-1} luminosity, the PP system collides at an average rate of ~80 MHZ. It is not infrequent to find a second event occurring within 10 to 20 nsec after the current event took place. To distinguish the TOF of heavy particle from that of the β = 1 background arising from different collisions, we shall sample a set of TOF measurements for the particles at different stages of the spectrometer. Figure 1-b shows the time separations among heavy particles and the β = 1 background with respect to the reference β = 1 muons at various distances. It is clear that the TOF of the heavy particle is highly constrained. While at small angles, the acceptance of the spectrometer will be severely reduced, because every particle, light or heavy, moves with a high speed, one has to depend on a nicely bunched beam and a very long flight path for measuring the TOF of the heavy particles. Figure 2-a shows the angular distribution of a 100 GeV/c^2 heavy lepton produced by pp collisions at 1 TeV. This result is obtained for PP $\rightarrow L^+L^-$ + anything via ordinary Drell-Yan process. When a TOF window cut (e.g. $3 < \Delta$ (TOF) < 20 nsec at 6 meters from IP) and a mass weighting factor $[(Q^2-4M_L^2)/Q^2]^{1/2}$ are applied to the produced events, one noticed that in Figure 2-b, the small angle enhancement of events attributed by the kinematic collimation of $L^{\pm}$ in the forward region is lost due to poor time separation between the signals and the β = 1 reference muons. In the 90° region, presumably, a few meters of path length would be sufficient to identify the heavy particles. However, there are too many slow junks flooded in this region, one may not be able to deal with it at such a high rate. An optimum angle for the spectrometer axis to be oriented with respect to the beam axis of the collider is probably 40°.[6]

We would like to thank Dr. R. G. Glasser for providing us many handy routines to generate various spectra of Drell-Yan process at Maryland.

Footnotes and References

1. New and Unthinkable Ideas, Summarized by L. M. Lederman, Proceedings of the 1975 ISABELLE Study, July 14-25, 1975 (BNL 20550) page 84. See also page 356 for detail calculations by Chang and Samios.
2. D. J. Bechis, et al., Phys. Rev. Lett. 40, 602 (1978).
   D. Antreasyan, et al., Phys. Rev. Lett. 39, 513 (1977).
3. J. A. Appel, et al., Phys. Rev. Lett. 32, 428 (1974).
   D. Cutts, et al., Phys. Rev. Lett. 41, 363 (1978).
4. M. G. Albrow, et al., Nucl. Phys. B97, 190 (1975).
5. Beyond the Standard Model, G. L. Kane and M. L. Perl (See it for references); Proceedings of the DPF Workshop on Future High Energy Physics and Facilities, Snowmass, Co., July (1982).
6. In reference 2 (D. J. Bechis, et al.), we have dumped 10^9 protons per beam spill at 400 GeV onto a 5 meter long stainless steel beam dump plugged inside the sweeping magnet of the FNAL neutral hyperon beam. We found a 72% dead time for the down stream p.w.c. read out system because of the existence of the high energy muons. At 45° c.m. of angle, we believe that we have enough β = 1 muons for reference.

Figure Captions

Figure 1-a. TOF for a 100 GeV/c^2 massive stable particle with momenta 10 and 50 GeV/c in comparison with that of a β=1 bunch of particles.

Figure 1-b. Time separations observed among heavy particle and the β = 1 background arising from different event. One can sample the Δ(TOF) measurements at various locations of the spectrometer.

Figure 2. Angular distribution of stable heavy leptons produced via Drell-Yan mechanism. We assume $\sqrt{S}$ = 800 GeV, m_L = 100 GeV/c^2, distance from IP is 6 meters.
   a) All $L^{\pm}$
   b) Weighted by $[(Q^2-4M_L^2)/Q^2]^{1/2}$ and in the TOF window ($3 < \Delta t < 20$ nsec.)

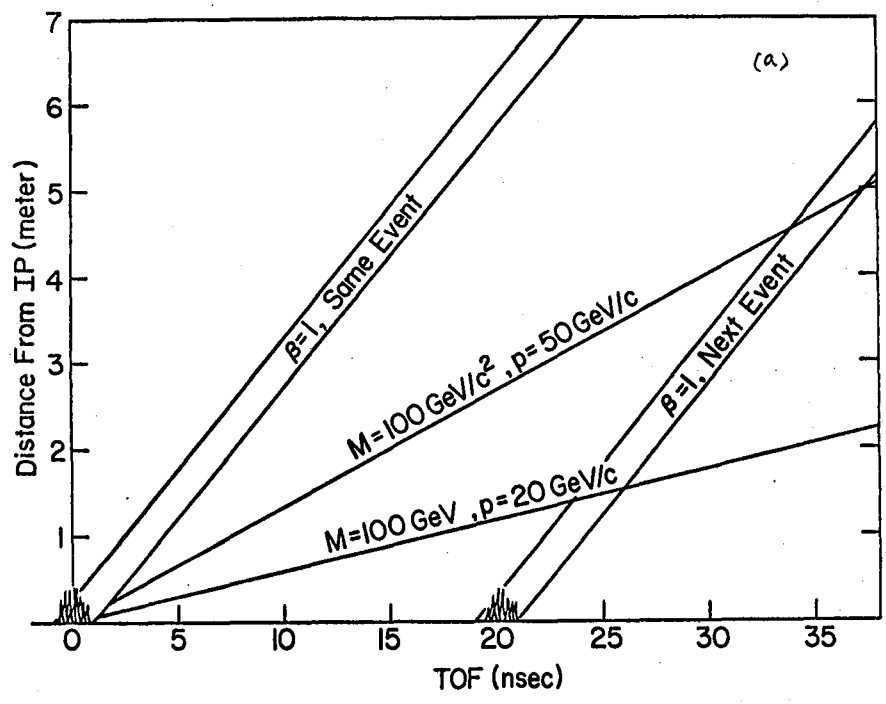

Figure 1-a

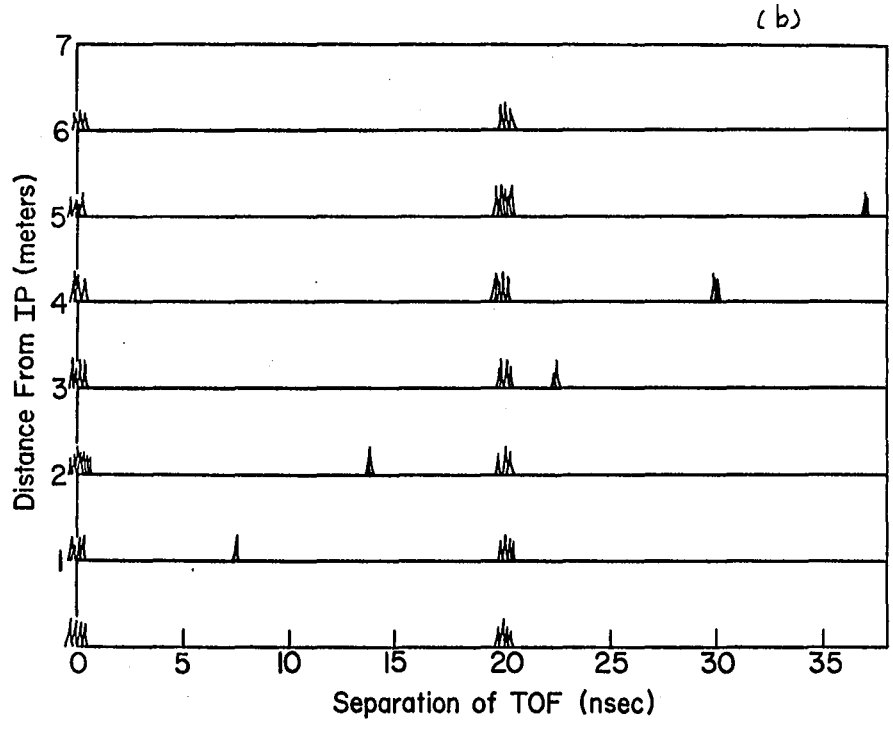

Figure 1-b

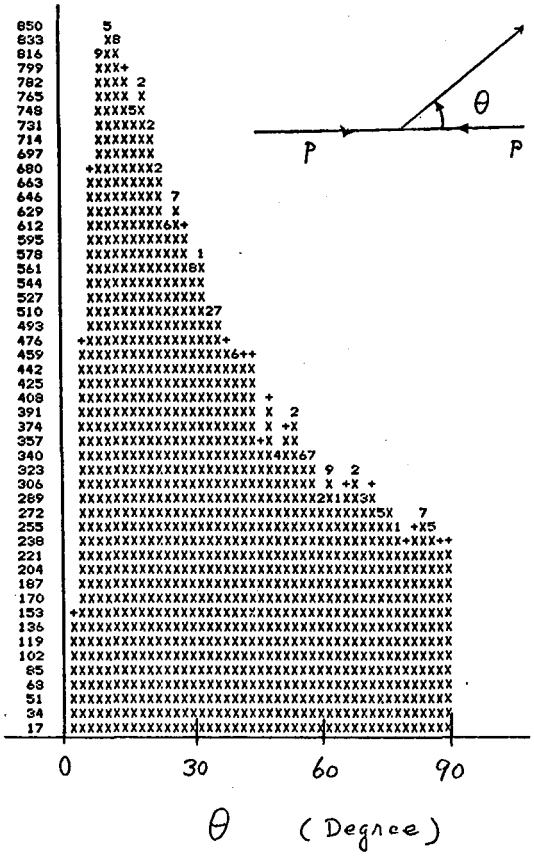

Figure 2-a

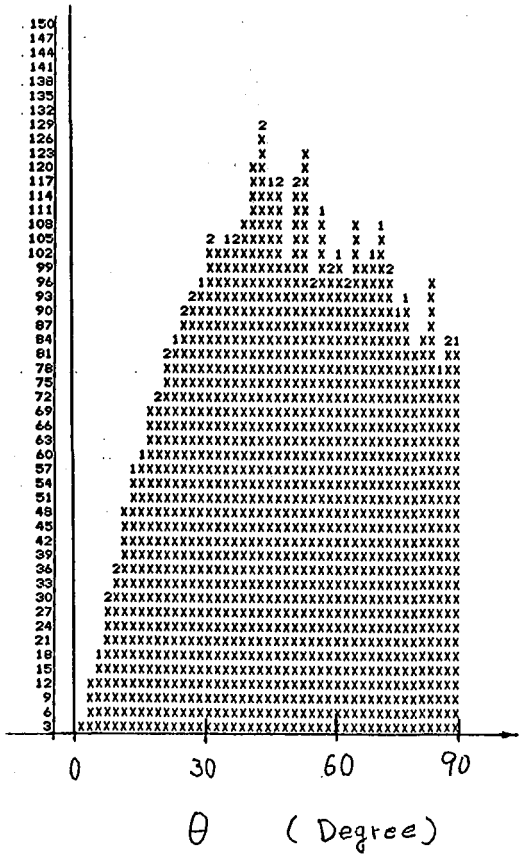

Figure 2-b

OPERATION OF A HIGH-p_T SPECTROMETER ARM AT $10^{33}cm^{-2}sec^{-1}$ WITH PARTICLE IDENTIFICATION

S. Aronson
Brookhaven National Laboratory, Upton, NY 11973

M. Goldberg
Syracuse University, Syracuse, NY 13210

M. Holder
University of Siegen, D5900 Siegen 21, W. Germany

E. Loh
University of Utah, Salt Lake City, UT 84112

I. Introduction

In the Proceedings of the 1978 Isabelle Summer Study[1] a high-p_T spectrometer pair is presented as a prototype high-luminosity experiment. We consider here an updated version of this apparatus with the following questions in mind:

1. What rate capabilities are required to cope with $L = 10^{33}cm^{-2}sec^{-1}$?
2. What segmentation is needed to deal with the particle densities expected in high p_T jets?
3. Is the resulting device within the reach of present technology?

Section II presents the current version of the device and the expected rates. Section III discusses the rates and segmentation of the components. Section IV contains the results of calculations related to event pile-up and triggering. The main conclusion, that particle identification appears to be quite feasible at these rates, is discussed in more detail in Section V.

II. Spectrometer Components and Total Rates

We consider a single arm of the apparatus. Physics considerations will dictate the most efficient use of the rest of the solid angle. Some choices are an identical arm in the opposite direction as in Ref. 1, a larger acceptance arm with more modest particle ID and tracking, or an "energy-flow" device (i.e., mainly segmented calorimetry) covering as much of the remaining solid angle as possible.

Figure 1 shows the spectrometer arm. The acceptance, as defined by the magnet aperture, is as follows:

$$\Delta\Omega \simeq 0.9 \text{ steradians}$$
$$\Delta y \simeq \pm 0.5 \qquad (1)$$
$$\Delta\phi/2\pi \simeq 0.15$$

The total rate is estimated with the assumptions $L\sigma_{inel} = 50 \times 10^6/sec$, and $dn/dy(ch) = 4.1$ on the plateau at $\sqrt{s} = 800$ GeV. For the aperture given, we find the rates

$$R_{ch} \simeq 30 \times 10^6/sec \simeq R_\gamma.$$

With a 30 kg-m field integral all charged particles with $p_T < 0.45$ GeV/c are swept out of the aperture. Assuming $dn/dy\, dp_T^2 \propto \exp(-6p_T)$, actual rates reaching the spectrometer are

$$R_{ch} \simeq 5 \times 10^6/sec;\ R_\gamma \simeq 30 \times 10^6/sec. \qquad (2)$$

Since $1/\sin\theta$ varies by only 10% over the aperture, we can treat this flux as uniform over the solid angle.

For present purposes, it is assumed that the spectrometer performs tracking, momentum analysis, calorimetry and particle identification of all particles in the aperture. We use ISAJET[2] predictions of particle multiplicity and density within $p_T = 100$ GeV/c jets produced in $\sqrt{s} = 800$ GeV pp collisions. The cross-section for production of 100-110 GeV/c jets into the spectrometer aperture is $\approx 10^{-7}$mb (i.e. 0.1/sec at $L = 10^{33}cm^{-2}sec^{-1}$). The spectrometer elements are as follows (see also Table I):

Tracking

Interspersed in the detector are MWPC or drift planes as shown in Figure 1. These are relatively sparse, as only straight-line tracking is involved. Sufficient information to resolve left-right and x-y ambiguities is available at each wire chamber location. Momentum analysis is derived from the apparent miss distance in the bend plane of the track and the interaction point.[1]

Calorimetry

Electromagnetic ($\geq$ 20 r.l.) and hadronic ($\geq$ 6 int.l.) is provided over the whole aperture, plus wide angle coverage for charged particles with p_T down to 2 GeV/c which are bent away from the spectrometer axis.

Particle ID

1. Electrons and photons: The electromagnetic calorimetry is assumed to be finely enough segmented in depth to reject hadrons relative to electrons at the 10^{-3} level. Independent electron identification is provided by either transition radiation[3] or synchrotron radiation.[4] For this purpose the first tracking chamber following the magnet is assumed to be filled with Xe for good X-ray detection efficiency. In the transition radiation case this would be a stack of several fiber or foil layers interleaved with Xe-filled MWPC's.
2. Muons: The hadronic calorimeter is followed by 6 more interaction lengths of steel with interleaved proportional drift tube arrays for muon identification.
3. Hadrons: A system of 3 ring-imaging Cherenkov counters,[5] provide $\pi/K/p$ separation from about 1 GeV/c to over 50 GeV/c.

III. Component Segmentation

The charged particle flux given in Eq.(2) is not large by accepted standards for fixed-target spectrometers of comparable area. For example, the first [Xe-filled] MWPC, with 2 mm wire spacing to keep gate widths to $\lesssim$ 50 ns, would be comprised of $\lesssim$ 1000 wires/plane. The charged particle rate is then $\approx$ 5kHZ/wire. The photon flux is about an order of magnitude higher so some care must be taken to minimize the mass of detectors. If the Xe-filled chamber is part of a transition radiation detector ($\approx$ 5% of a radiation length) then the flux per wire from conversions is $\approx$ 3kHZ, still giving a very manageable total rate. In this front-most chamber it is seen that segmentation is driven by the desire for speed, not by the singles rates on individual wires. This is, if anything, more true of the tracking chambers.

From the stand-point of calorimetry also, rate is not the driving force behind fine segmentation. The transverse size of showers gives a natural area segmentation in the calorimeters, say 4 x 4 cm^2 in the electromagnetic and 10 x 10 cm^2 or larger in the hadronic parts, respectively. The density of particles in high p_T jets likewise gives a natural angular segmentation for calorimetry on individual particles. Using the angular correlations between jet particles from Ref. 2, we find

$\Delta\theta_{em} \approx .01$ (all particles)
$\Delta\theta_{had} \approx .025$ (charged particles)

In other words, for calorimetry on individual particles in jets of $p_T \approx 100$ GeV/c, 4 cm/.01 = 10 cm/.025 = 4 meters is a natural distance between source and calorimeters. For the aperture of this spectrometer we then get the following rates in individual towers:

Electromagnetic:
$\approx 10^4$ towers; rate $\approx$ 3kHZ/tower(all particles)
Hadronic:
$\approx 10^3$ towers; rate $\approx$ 5kHZ/tower(charged particles)

For the ring-imaging counters there is also a natural element size, based on the density of tracks and on ring size.[5] In this case 10 mstr cells (i.e. about 100 per counter in this aperture) are appropriate. This gives a small probability for 2 or more rings per cell and an average of 1 additional (soft) charged particle per cell within the jet. The total charged particle rate (assuming the photoionization detectors cover the aperture) is about 50 kHZ/cell and not all of these produce Cherenkov light. This rate is further divided among the ($\gtrsim$100) sense wires per detector.

In all of the detector components associated with particle identification there are 1-2 x 10^4 elements and rates 1-50 kHZ/element. These numbers are not daunting; in fact the detector is not different in scope from many existing fixed target experiments.

IV. Event Pile-Up

Table II gives the contribution to E_T of minimum bias event pile-up as a function of gate width. Due to the field, a small fraction of charged particles from pile-up events contribute to E_T, while photons (with half the $\langle p_T \rangle$ of charged particles) contribute in full force. Per pile-up event about 0.6 photons and 0.15 charged particles enter the aperture, contributing on average $\approx$ 0.24 GeV to E_T per pile-up event. From the table one can see that even for a 100 ns gate pile-up at the $\lesssim$ 1% level (i.e. 18 events in the gate 1% of the time) produce only about a 4 GeV addition to E_T. Since one may expect E_T of 50 GeV or more into the aperture for a 100 GeV jet down the axis of the spectrometer, the effect on the trigger is manageable. One will be able to do even better off line. Event pile-up in the Cherenkov counters is potentially the most serious problem for the particle ID components, because of the relatively coarse segmentation (100 cells) and the memory time ($\lesssim$ 1 μsec) for the TMAE photoionization detector. At 1 μsec the mean pile-up is 50 events; these contribute < 0.1 charged particle per Cherenkov cell and so constitute less of a problem than that of particle density within jets mentioned above.

V. Summary

The technologies employed in the particle identification components of this detector are either available or very close at hand. In particular, rate and particle density are not issues of fundamental importance in a limited solid angle apparatus such as this. The price paid for this rather intensive particle identification and analysis over $\approx$ 1 steradian is in numbers of detector elements (i.e. complexity). However detector systems with thousands of calorimeter cells and tens of thousands of wires are already in routine use. Extending a system such as this to cover a larger ϕ range and a somewhat larger y range (centered around y = 0) is only a matter of cost and complexity.

This research supported by the U.S. Dept. of Energy under Contract No. DE-AC02-76CH00016.

References

1. S. Aronson, et al. Proceedings of the 1978 Summer Workshop, BNL 50885, p 278.
2. F.E. Paige and S.D. Protopopescu, "ISAJET: A Monte Carlo Event Generator for pp and $\bar{p}p$ Interactions, Version 3," BNL 31987 (Sept. 1982).
3. M. Holder and E. Loh, these Proceedings. Transition radiation is presented there in a different context; see references contained therein.
4. S. Aronson, these Proceedings and references contained therein.
5. M. Goldberg and D. Leith, these Proceedings and references contained therein.

Table I. Spectrometer Components

Component	# of Elements	Comments
A. Tracking Chambers	5×10^4 wires	MWPC's or minidrifts (2-4 mm drift)
B. Calorimeters (e-m)	1.5×10^4 towers	Liquid argon with pad readout, lead glass bars with interleaved patch chambers, etc.
(hadron)	2.5×10^3 towers	Iron-scintillator with wave shifter bar readout.
C. Particle ID (e)	4×10^3 wires	Transition radiation modules (carbon fibers or plastic wool), or synchrotron radiation detector.
(μ)	1.5×10^3 wires	1 m iron with interleaved proportional drift tube planes.
(π/K/p)	300 cells	3 ring-imaging Cherenkov counters: Liquid Freon (2 cm), Isobutane (50 cm), Argon (150 cm). TMAE photoionizing gas detectors.

Table II. Event Pile-up Contributions to E_T

Δt Gate	$\bar{n}$	n(CL≃.005)	ΔE_T
20 ns	1	4	0.6 GeV
40	2	6	1.2
100	5	11	2.4
200	10	18	4.0

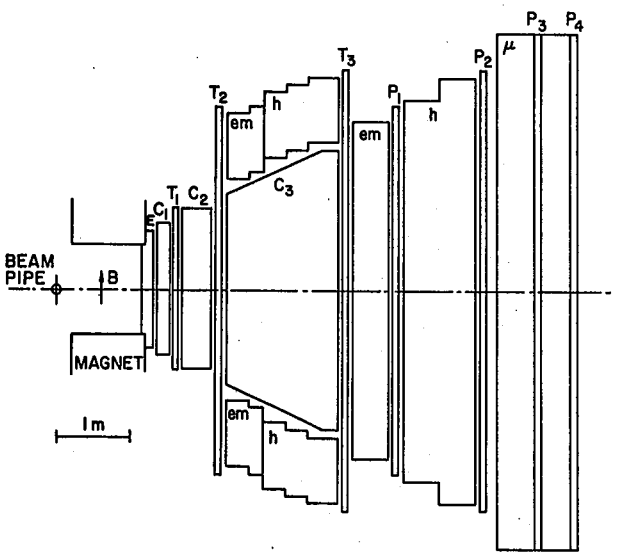

Fig. 1. Schematic representation of the high-P_T spectrometer. The components discussed in the text are labelled as follows: E = electron identifier; T_i = tracking chambers; C_i = ring imaging Cherenkov counters; em = electromagnetic calorimeters; h = hadronic calorimeters; P_i = proportional drift tube arrays; μ = iron muon filter.

MUONS AND ELECTRONS IN GENERAL

L. Nodulman
Argonne National Laboratory, Argonne IL 60439

J. Bensinger
Brandeis University, Waltham MA 02254

We address the problem of simultaneously identifying electrons and muons in a general purpose detector at a luminosity of $10^{33}cm^{-2}sec^{-1}$. Those discoveries and important measurements which are reasonably well predicted now are under way and likely to be fairly complete before turn on. The signatures of new effects to be found at high rates are not well predicted, and for flexibility it may be necessary to look simultaneously for some combination of jets, missing E_T, electrons, and muons. This leads immediately to an open geometry with magnetic tracking and calorimetry. At high luminosity, getting out trigger information quickly is a prime concern. Note that if a given signature requires isolating individual events then even for an optimistic integration time of 20 ns, the optimal luminosity is about $2x10^{32}cm^{-2}sec^{-1}$. We have not had the opportunity to be very specific in design or to consider the extended momentum range implied by 10-20 TeV collisions.

In order to be specific, we have assumed a detector which is a variant of the CDF design.[1] Detailed calorimetry design, and solving the problems of magnetic tracking at high rates are left to others. We assume a solenoidal detector with an open flight path of 1.5 m at 90° and calorimetry of 100 radiation lengths corresponding to 1.5 m of iron 2 m thick. The calorimeter is separated with the electromagnetic portion preceding the hadronic. The electromagnetic calorimetry is assumed to be in a tower geometry with separate front and back segments with x-y strip chambers near shower maximum.

The muon system we consider is a variant of the CDF system.[2] We add scintillators with similar segmentation to the calorimetry in order to provide fast trigger information and in order to eliminate cosmics immediatly in a situation where, in effect, there is always an event. The system involves accurate tracking in azimuth to enable a fast projection to the beamline to give an implied p_T cut. This reduces decay background and cuts out shower splatter. The increase from 1 (CDF) to 1.5 m of iron equivalent reduces both splash and punchthrough, with no claim to being optimal.

The dominant source of background for muons is decay in flight of $\pi^{\pm}$ and $K^{\pm}$. Extrapolating from a CDF study by G. Ascoli,[3] the decay probability at 5 Gev/c p_T is 1.4% varying as $1/p_T$. An effective threshold of 10 GeV/c p_T should give a trigger rate of about 1000/sec with overall misidentification probability improving from about $7x10^{-3}$ at 10 GeV/c. Lesser backgrounds are from punchthrough, about $2x10^{-4}$, and splash. The splash probability increases from $2x10^{-2}$ at 10 GeV/c to $1.3x10^{-1}$ at 30 GeV/c.[4] Splash is readily removed by tracking, and both punchthrough and splash make little contribution to the rate seen by the muon system. The 1.8 GeV/c p_T cut given by the 1.5 m of iron will keep the interaction related muon system counting rate down to about 10^4/sec, roughly comperable to cosmic rays. Radiation damage is no problem, but the muon trigger runs much too fast to be used alone.

A fast coincidence, strobed by beam/beam counters or whatever, is available for muons for an initial pipelined deadtimeless trigger level. This would require an outside scintillator corresponding to mimimal calorimetry signals. Note that this tends to antiselect muons in a jet. This fast information should be sufficient to allow reasonably long drifts in muon tracking. Staggered pairs of wires in drift tubes, aligned to the beamline, can be put into time coincidence corresponding to an azimuthal impact parameter. The drift time and coincidence time and possibly charge division ratio can be made available for sample and hold even if no coincidence trigger pulse is produced. Perhaps central tracking can produce a stiff track signal in rough alignment, also on the time scale of a few microseconds. At a still higher level, a detailed track match may be required.

The details of the system are dominated by multiple scattering considerations. The rms projected impact parameter to the beamline at 10 GeV/c p_T is 5.6 cm. The softness of the resulting p_T threshold can be aided by the stiffness required of the track. The rms misalignment in azimuth of the inside track projected to the back of the calorimeter with the outside track is 1.9 cm at 10 GeV/c. This gives an ultimate limit to picking out a muon in a jet, although the few $x10^{-3}$ rejection may not be generally sufficient.

The electrons are identified by a combination of momentum measurements of incoming track in central tracking chambers, proper electron signature in the electromagnetic calorimeter, and small energy deposition in the hadron calorimeter. In a CDF test a setup[5] similar to the one described here, and assuming a central tracking momentum measurement of $\sigma p/p = .002 \times p$ (GeV/c) achieved a pion rejection factor of $7x10^{-4}$ for 30 GeV/c electrons and pions, with a 70% effieiency for electrons. This level is sufficient since there is no point pushing this beyond the level set by Dalitz decays and photon conversion.

Overlap between a charged pion and a photon can be eliminated if position resolution of both the charged particle track and the shower are better than 1 cm at a radius of 1.5 meters. In that case even in a jet if the particle density is 100 times background (assumed to be 5 charged tracks and 2.5 neutral particles per unit of pseudorapidity) the probability of an overlap is $\sim 10^{-4}$.

Triggering involves several levels of information. At the first level pulse height from each calorimeter can be compared with a predetermined p_T. A second level can identify clusters and compare information between electromagnetic and hadronic calorimeters. A third level could match stiff tracks from central tracking with calorimeter towers.

Time limitations prevented more than a superficial look at forward muons, but between say 35° and however small an angle may be tolerated, a toroid system such as has been proposed for CDF[2] can give similar rejection and fixed $\sigma p/p$ of less than 20%.

Although we did not give adequate consideration to 10 TeV collisions, the problems are apparent. How to measure even the sign of the high end of the available lepton momentum spectrum is a problem. Also, more dense jet cores will make picking out leptons even less likely.

In conclusion, a muon and electron system similar to that of CDF can provide single lepton tag rates of order 10^3/sec at $10^{33}cm^{-2}sec^{-1}$. The muon misidentification probability is a few $x10^{-3}$ above 10 GeV/c, dominated by decay. This would be improved by higher quality tracking allowing shorter flight paths, probably to the detriment of electron triggering.

References

1. CDF Design Report, CDF-111 (unpublished).

2. Ibid, section 6.

3. G. Ascoli, CDF-57 (unpublished).

4. Gabrial and Bishop, NIM 155, 81 (78), quoted in CDF-151.

5. L. Nodulman et. al., NIM 204, 251 (83) and R. Diebold et. al., CDF-106 (unpublished).

LARGE SOLID ANGLE SOLENOID SPECTROMETER WITH PARTICLE IDENTIFICATION BY DE/DX

David R. Nygren

Lawrence Berkeley Laboratory

Summary

In this note we consider a brute force approach to achieve simultaneously useful particle identification for hadrons and electrons, good momentum resolution and 100 nsec sensitive time apertures. The configuration envisaged is a cylindrical gas volume (with solenoid magnetic field) sampled in entirety by axial-wire drift cells instrumented for pulse height measurements as well as timing. The 100 nsec aperture implies a drift length of 1 cm or less, depending on gas choices and on the cell geometry.

The conventional lore[1] about dE/dx implies a trade-off between number of samples and sample thickness for a given resolution (Fig. 1). To achieve a satisfactory level of particle identification it is necessary to obtain at least 6% FWHM in the usual truncated mean estimator. For this performance, a choice can be made between the extremes of 500 samples of a total of 4 meter-atmospheres and 100 samples of 8 meter-atmospheres. Minimizing the physical size of the detector pushes the choice toward the large number of samples. With the further choice of inner radius of 0.5 meters and outer radius of 4.5 meters, the 500 sample configuration implies nearly 5 x 10^5 individual cells.

This number is perhaps a little uncomfortable, so another tactic can be considered: reduce the number of cells and wires by ~2, and pressurize to regain the requisite product of atmosphere-meters. An amusing although potentially very practical by product of pressurization is the possibility of balancing the rather formidable force on the endcaps due to the wire tension: ~200 tons. This possibility implies that wire stringing would be done with very low tension; pressurization would then provide most of the wire tension. Thus the cylindrical structures would need to be equipped with a bellows to permit the endcaps to move about ~5 cm or 1/2-1% of the total wire length.

The pressurization needed is about 1/3 of an atmosphere to provide the balancing force. The combination of 250 samples and 4. x 1.3 = 5.2 meter-atmospheres falls handily on the 6% resolution contour. It is worth pointing out that R&D effort to ensure the absence of snapping wires on first pressurization is a very good investment! Pattern recognition should be a tractable problem because of the very high degree of segmentation.

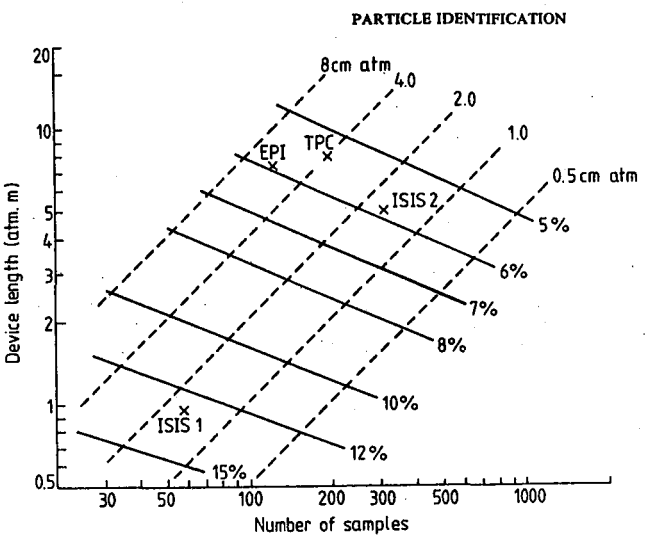

Figure Caption

Figure 1. The ionization resolution (% FWHM) of a multisampling detector filled with pure argon, calculated with the photo absorption-ionization model described in reference 1. The dashed lines are Loci of constant sample thickness.

References

1. W.W.M. Allison and J.H. Cobb, "Relativistic Charged Particle Identification by Energy Loss", Annual Review of Nuclear and Particle Science, Vol. 30 p. 253 (1980).

DETECTING HEAVY QUARK JETS

G. Benenson, L.L. Chau, T. Ludlam, F.E. Paige,
E.D. Platner, S.D. Protopopescu, P. Rehak
Brookhaven National Laboratory
Upton, New York 11973

I. Introduction

The ability to identify c, b and t jets and to separate them from the much more abundant u, d, s and gluon jets could lead to a wealth of new physics. A very promising technique is the possibility of measuring vertices near the interaction region with a resolution of the order of 10 μm, making one sensitive to decay lifetimes of a few x 10^{-13} sec and so tagging charmed particles and possibly τ's.

The immediate result, of course, would be the measurement of $d^2\sigma/dp_t dy$ for such jets. This could be compared with QCD predictions, and it would also shine some light on the question of the amount of intrinsic $c\bar{c}$, $b\bar{b}$ and $t\bar{t}$ in the $q\bar{q}$ sea of the proton. Detailed study of these jets may allow us to separate t, b and c jets. At sufficiently high p_t (high compared to the t mass) the relative cross sections are expected to be 1/1/1; significant deviations from the expected ratios could lead to the uncovering of new phenomena.

Another interesting possibility is to attempt full reconstruction of B mesons. Given the large background and multiplicities this may seem utopic; however, at $L \sim 10^{32}$ cm^{-2} sec^{-1}, close to 10^{10} B mesons are produced in a year (10^7 sec). This is to be compared with $<10^5$ expected at LEP. So any scheme that selects b jets with $\geq 10^{-4}$ efficiency produces $\geq 10^6$ events for further study. A good example of an interesting decay mode is $B^{\pm} \to K^{\pm}e^+e^-$, which is expected from the standard model to have a branching ratio $\sim 10^{-6}$. While such a small branching ratio may be impossible to observe, horizontal gauge symmetry models[1] can raise the branching ratio to $\sim 10^{-4}$, which may be possible at CBA but out of reach at LEP. A branching ratio substantially higher than 10^{-6} cannot be explained in the standard model and would be a very important discovery. Since in this case the decay does not involve charm, one could look for it in the jet accompanying the tagged one; having an identified heavy quark jet will give a tremendous reduction in background. The study of two or more jets will require the capability of doing electromagnetic and hadronic calorimetry over a large solid angle, but the charmed particle tag may be more restrictive in solid angle without a very detrimental effect on efficiency.

Another observation of interest is that of $B^\circ\bar{B}^\circ$ mixing. An initial state of $B^\circ(\bar{B}^\circ)$ can have a finite time-integrated probability of becoming a $\bar{B}^\circ(B^\circ)$. The mixing is maximal when there is equal probability for the final state to be B° or $\bar{B}^\circ$ irrespective of the initial state (as is the case for $K^\circ\bar{K}^\circ$). There are reasons to believe that, although the mixing for $D^\circ\bar{D}^\circ$ and $T^\circ\bar{T}^\circ$ is small, the mixing for $B^\circ\bar{B}^\circ$ could be maximal.[2,3] In this case one finds:

$$\sigma(pp \to BB^\circ X) = \sigma(pp \to \bar{B}\bar{B}^\circ X) \sim (1/5\text{-}1/10)\sigma(pp \to B\bar{B}X)$$

the factor is 1/10 if only B_d° or B_s° have maximal mixing and 1/5 if both do. Thus, one can expect that between 20% and 40% of back-to-back b jets end up as $b\bar{b}$ or $\bar{b}\bar{b}$ rather than $b\bar{b}$. It is sufficient to separate $b\bar{b}$ from bb or $\bar{b}\bar{b}$ jets clearly (at the 10% level) with 10^{-7} efficiency to observe mixing. The simplest way to accomplish this is to detect equal sign leptons that come from semi-leptonic B decays in back-to-back jets.[4]

CBA will also produce enormous numbers of τ's ($>10^9$) compared to 10^5 at LEP. For most decays they will be impossible to distinguish from $D^\pm$ or $F^\pm$. Nonetheless there are some decay modes worth looking for, such as $\mu^\pm e^+e^-$ or $\mu^\pm\phi$. These decays are forbidden in the standard model but could be as large as 10^{-4} with horizontal gauge symmetries, and efficiencies as low as 10^{-4} will be sufficient to reach that level. Finding a signal into such a mode would have momentous impact.

In this exercise we examine the performance of a detector specifically configured to tag heavy quark (HQ) jets through direct observations of D-meson decays with a high resolution vertex detector. To optimize the performance of such a detector, we assume the small diamond beam crossing configuration as described in the 1978 ISABELLE proposal,[2] giving a luminosity of 10^{32} cm^{-2} sec^{-1}. Because of the very large backgrounds from light quark (LQ) jets, most triggering schemes at this luminosity require high $P_\perp$ leptons and inevitably give missing neutrinos. If alternative triggering schemes could be found, then one can hope to find and calculate the mass of objects decaying to heavy quarks. A scheme using the high resolution detector will also be discussed in detail. The study was carried out with events generated by the ISAJET Monte Carlo[3] and a computer simulation of the described detector system. Many of the results that follow were presented at the DPF Summer Study at Aspen.[4]

II. A Heavy Quark Detector

In Fig. 1 we show what a "modest" size heavy quark detector (HQD) may look like. It needs basically five sections: an inner vertex detector as close to the beam as feasible, a charged particle detector consisting probably of drift chamber planes interleaved with transition radiation detectors to help identify electrons, an electromagnetic calorimeter, a hadronic calorimeter and a μ detector. Because the expected angular spread of jets is large ($> \pm 5^\circ$) we require calorimeters covering $\phi = \pm 45^\circ$ and in rapidity $y = \pm 1$.

The inner vertex detector is shown (actual size) in Fig. 2. It consists of four planes of high resolution position sensing elements. We give a detailed discussion of this device in Sec. IV. To be effective, this detector must be extremely close to the beams. We assume that the first plane is 1 cm from the beam axis. We have discussed this with ISABELLE accelerator physicists and it does not seem to be a fundamental problem provided the chamber is placed either above or below the beams (i.e., not in the horizontal plane). The chamber would be in a rough vacuum separated from the beam by a thin skin (<250 μm) of titanium. It would have to be retracted during stacking and acceleration of the beams.

It is natural to imagine repeating the detector arm shown in Fig. 1 four times to achieve full azimuthal coverage, particularly to be able to detect

more than one jet. However, for the reason given above, it does not seem feasible to achieve full azimuthal coverage with the vertex detector.

The detector sketched in Fig. 1 will have excellent tracking capability --the vertex detector alone measures track angles to an accuracy $\lesssim 1$ millirad. It is designed to handle high densities of low momentum tracks. Thus a very modest magnetic field will suffice for adequate momentum measurements. It may be argued that no magnetic field is necessary, supplanting momentum measurement with calorimetric energy measurement. However, some momentum information will be useful for evaluating multiple scattering errors in the precise vertex measurements; it will be helpful to have measured muon momenta; and information on the signs of tagged leptons may be crucial in some studies. For the present study we have not included the effects of a magnetic field in our calculations.

III. Trigger

The philosophy here is to implement a total energy (E_T) trigger with a calorimeter, and examine the response of the vertex detector for events thus triggered -- i.e., the effectiveness for tagging D meson decays. As we shall see, this effectiveness increases with increasing momentum of the trigger jet. In order to maximize the yield of B mesons, however, we wish to keep the E_T threshold as low as possible.

With the calorimetric trigger alone the major background is due to light quark jets. Therefore we consider a "low" E_T trigger (15 GeV in the calorimeter) with lepton triggers in coincidence. Since the leptons of interest are relatively soft, triggers on leptons are not straightforward, and will require some real-time processing. The choice of 15 GeV E_T threshold is guided by our estimates of lepton trigger capability, for the luminosity of 10^{32} cm^{-2} sec^{-1}. We also consider a "high" E_T threshold of 30 GeV, and a "low-low" threshold of 8 GeV.

Calorimeter Trigger

The hadron calorimeter is 1.5 meters from the interaction diamond and is 3x3 m^2 in area. Fine segmentation is important. It is subdivided into 20x20 cm^2 towers ($\sim$250 cells). The electromagnetic shower detector (approximately the first 10 radiation lengths of the calorimeter) is subdivided into 1000 cells. The full calorimeter is 6 absorption lengths deep.

Since we are triggering at relatively low E_T, the energy resolution of the calorimeter is a critical determinant of trigger rates. A calorimeter with hadronic energy resolution $\sigma_E = .8\sqrt{E}$ (typical of iron/scintillator devices) would give a trigger rate several times the rate at E_T = 15 GeV. Using the "best" hadron calorimeter, with $\sigma_E \simeq .3\sqrt{E}$ (e.g. uranium/scintillator), the trigger rate will be 30-50% higher than the true rate. For the results presented here we do not include the effect of calorimeter resolution on the rates.

At L = 10^{32} cm^{-2} sec^{-1} we have 6x10^6 interactions/sec, most of which send something into the calorimeter. Hence the mean time between events is $\sim$200 nsec for a calorimeter trigger. For reasonable calorimeter gate widths ($\sim$100 nsec) this results in a substantial contribution to the trigger rate due to pile-up. If, however, we require that each cell of the calorimeter have a minimum energy before adding it to the trigger sum (250 MeV for the EM part, 500 MeV for the hadronic part) the rate due to pile-up of "minimum bias" events is suppressed well below the jet trigger rate for $E_T \gtrsim 5$ GeV.

The calorimeter trigger rates for our 3 chosen E_T thresholds are given in the first line of Table I. The corresponding rates for b-quark jets among these triggers is given on the second line. It will be seen that the ratios of triggers/b-quark jets are $\sim$2000, 800, 600 for E_T thresholds of 8 GeV, 15 GeV, 30 GeV, respectively. For the 15 GeV threshold we have $\sim$1 b-jet/sec among the triggers, and we need to bring the trigger rate down by another factor of 10-20 to reach a reasonable rate for data recording.

Fig. 3 shows the multiplicity of charged tracks into the detector for minimum bias events and for a trigger threshold of 15 GeV. These include only tracks which traverse all four planes of the vertex detector. Because of the small diamond size the fraction of tracks which do otherwise is small: For E_T > 15 GeV the mean number of hits in the first plane of the vertex detector is 9.8.

In Fig. 4 we show the momentum spectra of charged tracks in the detector for the 15 GeV threshold setting. Note that the leptons shown in 4b and 4c come from both B meson and D meson decay. (Fig. 4b also includes Dalitz electrons.)

Muon Trigger

For the detector configuration shown in Fig. 1, with a 6 absorption length calorimeter, the energy loss suffered by a muon is 1.5 GeV. Thus a trigger on muons traversing the calorimeter is limited to $P_\mu \gtrsim 2$ GeV/c, or about 70% of the muons from B and D meson decay (see Fig. 4).

The probability for a pion to traverse the calorimeter without interacting (punch-through) and thus fake a muon is .0025. The probability for a pion (kaon) to produce a decay muon before absorption in the calorimeter is $.029/P_\pi$ ($.22/P_K$). We take a K/π ratio .2, and assume that only particles with P > 2 GeV/c will produce a fake muon trigger by punch-through or decay.

For calorimeter-triggered events, the mean number of charged particles entering the calorimeter is $\sim$9 (see Fig. 3), of which 18% have P > 2 GeV/c for a calorimeter threshold of 30 GeV.

Given these numbers we can construct the following table of minimum background rates for a muon trigger in coincidence with the calorimeter trigger (at luminosity = 10^{32} cm^{-2} sec^{-1}):

E_T Threshold	Punch-Through	π,K Decay Muons
8 GeV	10 sec^{-1}	62 sec^{-1}
15	1.5	9
30	.05	.5

Thus the trigger rate can, in principle, be reduced by a factor of 30-40 from that given by the calorimeter alone (Table I). To achieve this, however, we must deal with additional severe background due to leakage of shower particles out the back of the calorimeter. This can be reduced to levels comparable to those in the table above by the following two means, both of which require a fast processor if they are to be implemented at the trigger level:

i) Require a minimum ionizing signal in the calorimeter segments traversed by the "muon."

ii) Require that the position and angle of the track exiting the calorimeter match, within multiple scattering limits, the trajectory of a charged particle incident on the calor-imeter.

For lack of a detailed study (but guided by a similar study done by the R807 Group) we take the muon trigger rate to be roughly twice the "minimum" rate due to punch through and decay. This crude estimate of rates is entered in Table I for calorimeter plus muon trigger. Note that the addition of a muon trigger is useless for $E_T > 30$ GeV (for this detector configuration) and in fact the signal-to-background ratio is not greatly improved by the muon trigger for any of the three E_T threshold settings.

Electron Trigger

For the e-trigger we choose transition radiation detectors (TRD) because of the high degree of segmentation required and the desire to separate electrons from hadrons over a wide range of energies with a compact device.

We assume a total length of $\sim$80 cm of TRD, subdivided into two separate modules as shown in Fig. 2. Each module is made up of $\sim$5 planes of radiator (Li foils or Carbon Fibers), each with MWPC readout. Such a device should be capable of reducing the π/e rate by a factor of $\sim 10^3$, with good efficiency for electrons of momenta $\gtrsim$ 1 GeV/c. (We are specifically guided by the configuration tested in Ref. 5). Such a device, coupled with the EM calorimeter will give a very powerful electron tag. At the trigger level, however, the counting rate will be dominanted by conversion electrons, as the TRD thickness will be $\sim$5% of a radiation length.

We estimate that $\sim$1/20 of the calorimeter triggered events will have a conversion electron with $p > 1$ GeV/c. This background can be virtually eliminated by requiring that the electron track appear in all four planes of the vertex detector, but it is unlikely that this can be accomplished at the trigger level. Some improvement can certainly be had with an on-line processor, e.g., by requiring the electron track to appear in the first of the two TRD modules. Guided by these considerations, the entries in Table I are based on the assumption that the electron trigger reduces the calorimeter trigger rate by a factor of 30, and is 90% efficient for electrons.

IV. Vertex Detector

The use of semiconductor detectors as very high resolution tracking devices in high energy physics experiments has been a subject of intense development over the past few years.[6] A number of such detectors are being constructed (one is operational)[7] which give $\sim$10 μm space-point resolution in the high track density environment of heavy quark searches at fixed target machines. These "microstrip" detectors consist of silicon wafers whose surface area is finely subdivided into strips; each strip may be read out as a separate detection element. The strip-to-strip spacing is typically 20-50 μm. This gives the characteristic position resolution, which is achieved along one coordinate of the detector.

The signal charge for a minimum ionizing track is $\sim 8\times10^4$ electron-hole pairs per mm of detector thickness, with charge collection time $\lesssim$ 50 nsec for a 300 μm thick detector. This, coupled with the intrinsically high degree of segmentation, leads to excellent rate capability. The lifetime of such detectors has been measured to exceed $10^{14}/cm^2$ for fluxes of relativistic charged particles. For the detector geometry discussed here, the innermost plane of the vertex detector would see an integrated flux of $\sim 2\times10^{12}$ charged particles/cm^2 in a year of running at a luminosity of 10^{32} cm^{-2} sec^{-1}. The effects of background radiation need more study: slow neutrons and heavily ionizing particles are much more damaging than minimum ionizing particles. Tests carried out with silicon surface-barrier detectors placed near the beam crossing at the ISR indicate that these backgrounds will not be a problem, however.

The most serious technical difficulty for implementing these detectors in colliding beams is the extremely high density of output connections in a situation where we need to cover (relatively) large area. An output on each strip implies thousands of connections per centimeter along the detector edge. One way out, which is being studied at BNL, is to use resistive charge division to interpolate the position among groups of strips. An analysis by V. Radeka[8] gives the following formula for the optimal number of outputs as a function of detector characteristics:

$$N = \xi_a^{2/3} \frac{A}{t(\sigma_x w)^{2/3}} \qquad \text{IV.1}$$

where

σ_x = resolution

A = detector area

t = detector thickness

w = strip length

$\xi_a^{2/3} = 1.4\times10^{-2}$ $cm^{1/3}$ for silicon detectors

N = number of signal outputs.

For $\sigma_x = 10$ μm and t = 300 μm (a standard wafer thickness for semiconductor devices) one obtains

$$N = 47 \frac{A}{w^{2/3}} \qquad \text{IV.2}$$

For the detector illustrated in Fig. 2 this gives, for the four planes,

$$170 + 317 + 462 + 640 \simeq 1600$$

total readout channels.

Note that our detector measures one coordinate only. We take this to be the azimuthal coordinate. To obtain space points in 2 dimensions (using strip detectors) would require at least 3 times as many detector planes. As we shall see, the cost in multiple scattering errors would outweigh the usefulness of such a scheme. Thus the proposed detector really provides a tag for charmed particles and not a fully reconstructed vertex.

It should be pointed out that other schemes for realizing semiconductor devices as track detectors of this type are being considered and developed by various groups. For instance, CCD devices could, in principle, solve both the "connection" and the 2-dimensonal readout problems; however, these (as track detectors) are in a very early stage of development

and are fundamentally unsuited for the rates encountered in CBA experiments. A device with strip electrode geometry but serial readout (hence few connections) is being developed at the University of Pittsburgh.[9] This is based on a very interesting technique in which signal charge is stored in shallow impurity traps in the i-region of a PIN diode detector at cryogenic temperatures. These and other developments may point the way to better devices than that proposed here. For the moment, we confine our analysis to the "known" technology of microstrip detectors.

For a 4-plane detector, the error (σ_v) in the extrapolation of a track to the vertex position is given by (see Fig. 5):

$$\sigma_v^2 \simeq \frac{\sigma_x^2}{4} + \left(\frac{\sigma_x}{\sqrt{3}}\frac{L_1}{L_2}\right)^2 + \left(\frac{8.7 \times 10^{-4}}{\beta\ P\ (\mathrm{GeV})}\ L_1\right)^2 .$$

The first term is the position resolution, the second is the effect of the angular resolution and the last is the multiple scattering contribution. For σ_x = 10 μm, L_1 = 1 cm, L_2 = 2 cm:

$$\sigma_v^2 \simeq (5\ \mu\mathrm{m})^2 + (3\ \mu\mathrm{m})^2 + \left(\frac{9}{P\beta}\ \mu\mathrm{m}\right)^2 .$$

Multiple scattering dominates for P $\lesssim$ 2 GeV/c even though we have been at some pains to place the detector as close to the beams as feasible (L_1 = 1 cm). Nonetheless, for the average momenta of tracks through the detector in E_T-triggered events (Fig. 4) we obtain $\sigma_v \simeq$ 10 μm.

The average multiplicity of charged tracks into our detector, for calorimeter triggered events, is $\curvearrowright$9 (Fig. 3), and the distribution ranges up to about 20. From these tracks we must reconstruct the primary vertex and determine which, if any, tracks originate from a secondary decay vertex. For our Monte Carlo simulations we conservatively included only $D^{\pm}$ decays and used a lifetime for them of 8×10^{-13} sec. The distribution of projected miss distance, δ, is shown in Fig. 6. The criteria for resolved decays were as follow: (Note that σ_v is momentum-dependent.)

i) If only a single decay track is visible, it must have

$$\delta > \max\ (100\ \mu\mathrm{m},\ 4\ \sigma_v)$$

ii) If two decay tracks are visible,

$$\delta > \max\ (50\ \mu\mathrm{m},\ 4\ \sigma_v)$$

iii) If more than two decay tracks are visible,

$$\delta > \max\ (50\ \mu\mathrm{m},\ 3\ \sigma_v)$$

iv) If a decay lepton is tagged,

$$\sigma > \max\ (50\ \mu\mathrm{m},\ 3\ \sigma_v)$$

for all visible track multiplicities.

The results are shown in Table II for various decay topologies and E_T thresholds. Roughly 40% of the charged D mesons entering the vertex detector are resolved. This means that $\curvearrowright$20% of the triggered HQ jets have a visible decay. The rates for accumulating events with resolved decays are shown in Table I.

Cut (i) is the least restrictive; a 4 σ cut keeps only $\curvearrowright$1/16000 tracks. However, since the average number of tracks per event is 10, the probability of a fake decay is $\curvearrowright$1 per 1600 events. Since the cuts reduce the signal by a factor of 6 (a factor of 2 by requiring $D^{\pm}$ and another factor of 3 from lifetime cut) the overall improvement in signal-to-background ratio (S/B) is $\curvearrowright$200. From Table I we can see that once a lepton trigger is used the vertex detector cuts increase S/B to 1/2. Off-line the lepton identification can be substantially improved, particularly for electrons by correlating TRD and shower counter information. Therefore, it is possible to reduce the LQ jet background to the 10%-20% level. The only significant background to b jets at this point is from c jets.

V. Physics with Two Detectors

Two detectors, like the one shown in Fig. 1, placed opposite each other, offer very interesting physics possibilities. In Table III we give the rates for various triggers using both detectors. The triggers require a minimum total energy (E_T) deposition in the calorimeter and in triggers, 3, 4, 5 there is also an electron with P_e > 1.0 GeV/c (two in trigger 5).

Consider, for example, trigger 4, which has a comfortable trigger rate (8 sec^{-1}). After a vertex cut on the jets in the detector with an electron trigger the signal-to-background ratio S/B is 1/1. This can be reduced by at least another factor of 5 to 10 by additional off-line requirements on the electron, such as matching momentum measured in the drift chambers with energy deposition in the electromagnetic calorimeter. This gives an unbiased sample of b jets in the opposite detector with a background of c jets only (roughly 2 to 1). In 10^7 sec we have then 10^5 heavy quark jets of which 3×10^4 are b jets. This is to be compared with $\curvearrowright10^5$ b jets that are produced at LEP in a similar period of time before <u>any</u> selections are made.

As will be discussed in the next section, it is possible to reduce the data rate by a factor of $\curvearrowright$10 by using information on the multiplicity and pattern of space points in the vertex detector at the trigger level. If so, then triggers 2 and 3 can ultimately provide as many as 10^6 tagged b jets.

Trigger 5, which requires 2 electrons in one detector, is not very efficient for b jets, but it is of great interest for searching for rare decays, such as $B^{\pm} \to K^{\pm}e^+e^+$ or $\tau^{\pm} \to \mu^{\pm}e^+e^-$. If all $B^{\pm}$ decayed to $K^{\pm}e^+e^-$ we would have 2.2 events/sec (trigger 1). Requiring P_e > 1.0 GeV/c and P_K > 1.5 GeV/c reduces the rate to 0.20 sec^{-1} so after a vertex cut on the detector opposite to the one triggering on 2 electrons we would collect $\curvearrowright3\times10^5$ Kee decays in 10^7 sec. The only significant background at this level are the few percent of b jets which produce 2 electrons. After requiring P_K > 1.5 GeV/c (no K identification), P_e > 1.0 GeV/c and m(Kee) = m(B) ± 50 MeV the b jet background is down to $\lesssim$ 1/40,000. Thus a branching ratio for $B^{\pm} \to K^+e^+e^- > 10^{-5}$ could be observed. A slightly higher branching ratio could be seen for τ → μee (using τ's from B and F decays).

In the search for $B\bar{B}$ mixing we can use trigger 3 with the additional requirements of observing a lepton in both arms. Because of the chain decays b→c→ℓ and b→ccs with c→ℓ the leptons observed could be of equal sign even in the absence of mixing. However, the leptons that come from b→ℓ have substantially higher momentum than the secondary leptons, as

shown in Fig. 7. We make the requirements that both leptons have $P_\ell > 4.0$ GeV/c, that a D be tagged in each arm, and finally that the leptons be within 30μ from the primary vertex (to reduce the number of leptons from D decay). Then the equal sign pair are reduced to less than 10% of the direct pairs.

With the above cuts one expects ∿20,000 pairs from direct $B\bar{B}$ leptonic decay and less than 2,000 where one lepton comes from the decay chain $B \to c \to \ell$ (in 10^7 sec at $L=10^{32}$ cm^{-2} sec^{-1}). Unequal sign leptons can also come from cc pair; however, the simultaneous requirements that a D be tagged and that the lepton be within 30μ of the primary vertex reduce the expected number to ∿3,000. This number can be reduced further by studying the P_T distribution of the leptons with respect to the jet axis, so they are not a significant background. A possible source of background of equal sign leptons is due to cc or $\bar{c}\,\bar{c}$ jets. For $|y|<1$ these are expected to have a much smaller cross section than the $b\bar{b}$ jets and thus negligible.

Given the large number of lepton pairs from direct B decays (∿20,000) satisfying the selection criteria described above and the relatively low background, detailed studies of the characteristics of these events are possible and should enable one to show convincingly the existence or non-existence of $B\bar{B}$ oscillations.

VI. Vertex Trigger

a) Motivation

Because of the large backgrounds from light quarks and gluon jets (LQ jets) the limiting factor in studying heavy quark jets (HQ jets) is the ability to trigger selectively. The cross section for HQ jets increases rapidly with decreasing E_T (as long as E_T > mass of the heavy quark); therefore, to get large numbers, it is important to trigger with the lowest feasible E_T in the calorimeter. As one can see from Table I to keep the trigger rate at a manageable level with an electron trigger the lowest E_T in the HQD is $\gtrsim$ 15 GeV. The electron trigger requirement improves the ratio HQ/LQ from 1/800 to 1/150 while the rate goes from 600 sec^{-1} to 20 sec^{-1}. This is a substantial improvement but still leaves an enormous number of background events that need to be rejected before one can analyze HQ jets. A very significant reduction in the background level is obtained using the high resolution Si detectors near the interaction diamond to tag charm particle decays as discussed in Sec. IV. Obviously, there is much to be gained if one could use these detectors at the trigger level.

In the next section we will describe an algorithm and a scheme for implementing the algorithm that selects HQ jets with high efficiency in less than 2 msec. Using the vertex trigger and requiring E_T > 15 GeV in the HQD gives a rate of <10 sec^{-1} and roughly 0.2 b jets/sec. Further offline cuts lower this to $\gtrsim 10^6$ b jets with HQ/LQ $\gtrsim$ 1/2 - 1/3 after using only the vertex detector information. This is to be compared to 2×10^5 jets with an electron trigger -- however, with better HQ/LQ ($\lesssim$ 1). Although the background level is still high this system gives a large number of events which could be studied in conjunction with other detectors. The limitation on E_T comes mainly from the trigger rate before using the vertex trigger, i.e. 500 sec^{-1} which forces E_T > 15 GeV (Table I). If additional requirements are imposed, E_T can be lowered. Let us, for example, use two detectors (as discussed in Sec. V) and demand that each Si plane have at least 4 hits, then a 500 sec^{-1} rate is obtained with E_T > 8 GeV in each arm and now adding the vertex trigger to either arm gives a rate of <10 sec^{-1} while the HQ rate is 0.25 sec^{-1}, i.e. HQ/LQ $\gtrsim$ 1/40 at the trigger level. This setup gives for $\int L dt = 10^{39}$ cm^2 sec^{-1} a sample of 10^6 unbiased b quark jets in the arm that did not use the vertex trigger. A great advantage in keeping E_T low is that the track multiplicity in the jet is also low, consequently the combinatorial background when reconstructing either D or B mesons is less severe. This is to be contrasted with roughly 10^5 b jets at LEP (in the same amount of running time) with E_T = 45 GeV. In Fig. 8 we show the type of event that triggers the vertex detector: a) shows all the charged tracks from the event, b) an expanded view of only those tracks which are reconstructed in the vertex detector. Figure 8 illustrates the point that although the track multiplicity in the event is high, only a small number of tracks go through each vertex detector and are used for triggering.

b) Algorithm

For the trigger consider three planes with hits x_1^i, x_2^k, x_3^ℓ. If those hits lie on a straight line they must satisfy the requirement

$$x_2^k = a_1 x_1^i + a_3 x_3^\ell \qquad \text{VI.1}$$

where a_1 and a_3 are fixed constants. For all pairs, i,ℓ we can calculate a corresponding $x_2^{i,\ell}$. The distribution of $|x_2^{i,\ell} - x_2^k|$ is shown in Fig. 9. It is obvious that imposing $|x_2^k - x_2^{i,\ell}| < 70$ μ will remove all the wrong combinations. Note that inside a magnetic field of 5 Kgauss the sagitta for tracks through 3 detectors (separated by 2 cm) is <40 μ for p > 200 MeV/c; so only soft particles will fail the cut. Since they also have large errors from multiple scattering and for a linear extrapolation to a vertex, this is not unwelcome. If redundancy is felt to be necessary the chosen pairs can be checked against a 4th plane.

The second part of the algorithm makes use of the fact that the beam is all contained within ±200 μ. The intersection x_n^k of the selected lines through 5 or any small number of planes in the interaction diamond can be quickly computed using equation VI.1 with the appropriate constants a_1^n, a_3^n. The average $\bar{x}_n = \sum_{k=1} x_n^k/N$ and a pseudo chisquare $\chi^2 = \Sigma(\bar{x}_n - x_n^k)^2$ can then be calculated for each plane.

The third part of the algorithm is to choose the plane n for which χ_n^2 is smallest and keep the event if $50\ \mu < \max|\bar{x}_n - x_n^k| < 1000\ \mu$.

The algorithm was checked with Monte Carlo events (generated with ISAJET) and seems quite effective in rejecting LQ jets by a factor of 50-100 while accepting $\gtrsim$20% of the HQ jets. To eliminate confusion one must require that two readouts with signals be followed by at least one with none; this implies that the hits must be separated by at least 300 μ before they can be used in the trigger. Table I gives the rates for LQ and HQ with one and two detectors. In Appendix A we give an example of how the previously described algorithm can be implemented so as to keep the time required for calculations to less than 2 msec.

c) Backgrounds

There are two effects that can increase the background from LQ jets: Multiple scattering tail (hard scattering) and multiple events in the time win-

dow needed to read the information from the Si detectors. The procedure for selecting straight tracks tends to eliminate from consideration tracks with noticeable scattering in any plane except the first one. Limiting the range for maximum deviation between 50 μ and 1000 μ also substantially reduces the probability of selecting an event in which one of the tracks underwent a hard collision. It, incidentally, also reduces the probability of triggering on K decays, less than 4% of the $K_s^o \to \pi^+\pi^-$ decays will satisfy the trigger. Multiple events can be a more serious problem. The readout time for the Si detectors is unlikely to be less than 50 nsec. At L = 10^{32} cm^{-2} sec^{-1} the average time between events is 200 nsec, so 25% of the time there will be another event in the 50 nsec window. One could veto those events using a device with faster response such as a scintillator hodoscope. Another approach is to orient the readout along the beam direction as shown in Fig 8. Since the interaction region is 2 cm long and tracks are selected with deviations less than 1 mm only $\sim$ 1/20 of the double events will satisfy the trigger requirement, i.e. 1/80 of the LQ jets will trigger. Better timing off line will still be required to reduce the background further. The multiple events problem then can be eliminated by suffering a 25% loss. The disadvantages of orienting the readout along the beam direction (Z) are: 1) the vertex detector can no longer be used as part of a momentum measurement in a solenoidal field; 2) it is impossible to join tracks in the vertex detector to the rest of the system if that system does not have good resolution along Z. The natural field with this arrangement is a dipole with field lines parallel to the ground.

VII. Conclusion

We have shown that it is possible in principle to design a detector of modest dimensions capable of detecting heavy quark jets with good rejection of light quark (and gluon) jets. In order to achieve this, good lepton identification and the ability to tag a charmed particle decay with a high resolution vertex detector are indispensable. To keep the vertex detector within realistic dimensions we make use of the possibility at CBA of a small interaction diamond (± 2 cm full width) with high luminosity, L=10^{32} cm^{-2} sec^{-1}.

With two detectors placed opposite to each other it is possible to collect at least 10^5 unbiased heavy quark jets (in the detector opposite the tagged jet) in a year of running with practically no background from other processes. More sophisticated on-line data processing can raise this number to 10^6. The ratio of c to b jets in this sample is 2 to 1. With such large numbers of B mesons it is conceivable that some decay modes may be fully reconstructed. Of particular interest is the decay $B^{\pm} \to K^{\pm}e^+e^-$ for which an upper limit of 10^{-5} is achievable, easily an order of magnitude better than what is possible at LEP. The standard model predicts 10^{-6} for this branching ratio; however, horizontal gauge symmetries can increase it to 10^{-4} which would be observable with the detectors envisaged here.

This research was supported by the U.S. Department of Energy under contract DE-AC02-76CH00016.

Appendix A

The trigger would be implemented as a front-end processor of data from a silicon strip detector array. The proposed architecture makes use of data-flow hardware processor techniques.[10,11]

Approximate system requirements are as follows:

1. Input data originates from 3 detector planes, and is linearly encoded with 10 μ resolution over a maximum range of 5 cm.

2. Average track multiplicity = 10/event; maximum = 30.

3. Total dead-time is not to exceed 2 ms.

The proposed algorithm separates neatly into 2 parts:

1. Find all tracks which pass through all 3 detector planes, and project back the intersection region. Calculate the intercepts of each track with a series of planes ($\sim$5) parallel to the detector planes, but within a narrow decay band of the intersection region.

2. Analyze the sets of decay-band intercepts for the signature of a secondary vertex. An example algorithm would be as follows: For each projected plane, calculate the chi-square of the intercepts. For the plane with lowest chi-square, apply a window test to the maximum deviation from the mean; if the maximum deviation for that plane is within limits, produce a trigger; otherwise, reset the detector for the next event.

The problem of high-speed, high-multiplicity track-finding in a segmented multi-plane detector system has been studied extensively,[12] and a system is currently under construction for experiment 766 at the AGS. The first part of the algorithm could be implemented using essentially the same techniques, although perhaps at lower speed and cost. Figure 10 shows a possible configuration. The cost of such a processor is estimated to be $20-$30K. Processing time is dominated by production and testing of all pairwise combinations of hits from planes 1 and 3. Assuming the maximum multiplicity N=30, there are N^2 $\sim$ 1K combinations, so that even at TTL cycle times, only about 200 μs are required for track finding.

Hardware processing techniques are not as appropriate to the second part of the algorithm. For one thing, the speed requirement simply is not there: The processing time scales with N, rather than N^2. Furthermore, there are multiplication and division operations, which would be expensive in hardware, but not well justified. Finally, a hardware vertex finder would incur high design costs for an algorithm which is relatively untested. For these reasons, the second part of the algorithm is better implemented using an array of microcomputers, each executing the same algorithm on one of the projections (see Fig. 11). The output of each microcomputer will consist of two pieces of information: chi-square for the projection; and maximum deviation (or, more compactly, the result of the limit test: yes or no). The microcomputer outputs would be made available via a bus structure to a hardware trigger logic box and/or a host minicomputer.

Each microcomputer would have 2 ms to perform approximately 10 N arithmetric operations per event; or about 300 maximum. Assuming 1.5 ms for this task, a high-performance device, such as Motorola 68000, would be required. The cost would be roughly $5K per micro, or about $25K for 5 projection planes in the decay region.

Table I

Rates with One Detector at $L = 10^{32}$ cm^{-2} sec^{-1}

	$E_T > 8$ (sec^{-1})	$E_T > 15$ (sec^{-1})	$E_T > 30$ (sec^{-1})
Calorimeter Only:			
Trigger rate	7000.	560.	12.
B Jets	3.0	.7	.02
$B \rightarrow$ Resolved $D^{\pm}$	0.5	.24	.004
Calorimeter + Muon Trigger:			
Trigger rate	350.	40.	2.
B Jets	.7	.16	.004
$B \rightarrow$ Resolved $D^{\pm}$	.1	.03	.0012
Calorimeter + e Trigger:			
Trigger rate	250.	20.	.4
B Jets	0.5	0.12	.0035
$B \rightarrow$ Resolved $D^{\pm}$	.08	.02	.0007
Calorimeter + Vertex Trigger:			
Trigger rate	120.	10.	0.2
	1.5	.3	.01
	.8	.15	.007

Table II

$\frac{\text{Resolved } D^{\pm}}{\text{Total } D^{\pm} \text{ in Trigger Jet}}$ vs. E_T Threshold

	$E_T > 8$	$E_T > 15$	$E_T > 30$
1 Visible Track	20%	24%	25%
2 Visible Tracks	11	9	8
>2 Visible Tracks	7	8	14
Total	38%	41%	47%
Visible Lepton	12%	12%	13%

Table III

Rates with Two Detectors at $L = 10^{32}$ sec^{-1} cm^{-2}

	Trigger Configuration Detector 1	Detector 2	Trigger Rate sec^{-1}	b jet Rate*
1	$E_T > 8$	$E_T > 8$	7500	1.1
2	$E_T > 15$	$E_T > 15$	130	0.12
3	$e+E_T > 8$	$E_T > 8$	120	0.20
	$E_T > 8$	$e+E_T > 8$		
4	$e+E_T > 15$	$E_T > 15$	8	.02
	$E_T > 15$	$e+E_T > 15$		
5	$2e+E_T > 8$	$E_T > 8$	4	.0025
	$E_T > 8$	$2e+E_T > 8$		

*The b jet rate is for b jets in the detector that requires no electron in the trigger.

References

1. D.R.T. Jones, G.L. Kane, J.P. Leveille, Nucl. Phys. B198, 45 (1982).
2. J. Sanford et al., BNL 50718 (January 1978).
3. Frank E. Paige and S.D. Protopopescu, BNL-29777. This study was done using the latest version, ISAJET 3.24.
4. L.L. Chau et al., DPF Workshop on High Energy Physics and Future Facilities (Snowmass Co., 1982).
5. C. Fabjan et al., Nucl. Instr. Meth. 185, 119 (1981).
6. For the proceedings of a recent workshop on the subject, see "Silicon Detectors for High Energy Physics," T. Ferbel, Ed. (Fermilab, 1982).
7. B. Hyams et al., CERN Exp. NA-14 (see Ref. 2, p. 195).
8. V. Radeka and R. Boie, IEEE Trans. Nucl. Sci., NS (1979); see also Ref. 2, p. 21.
9. P. Shephard et al., Ref. 2, p. 73.
10. "A Hardware Architecture for Processing Detector Data in Real-Time," G. Benenson, et al., in Proceedings of the 1978 Summer Workshop, BNL 50885.
11. "Real-Time Processing of Detector Data," W. Sippach, et al., 1979 Nuclear Science Symposium, IEEE Trans. on Nucl. Sci. NS-27:1, Feb. 1980.
12. Appendix, FERMILAB proposal 627, B. Knapp, et al.

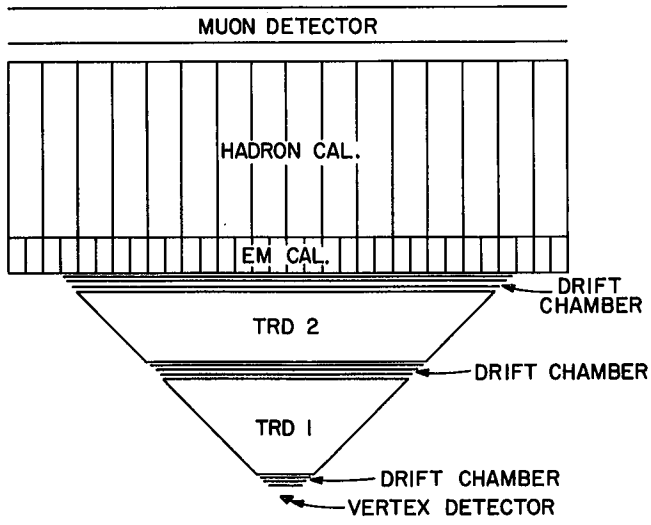

Figure 1. Single arm heavy quark detector at $\theta = 90^{\circ}$, covering ± 1 units of rapidity and 45° in azimuth.

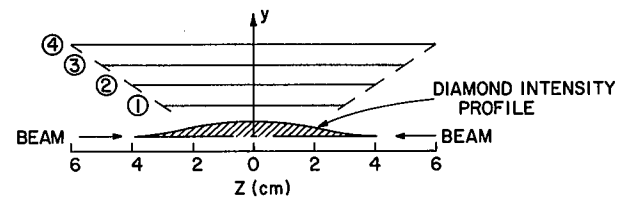

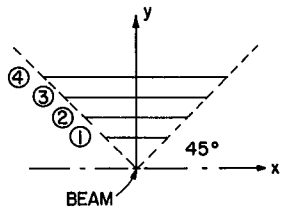

PLANE	y	x × z	OUTPUTS
①	1 cm	2×6 cm^2	170
②	1.7	3.4×8	317
③	2.3	4.6×10	462
④	3	6×12	640
			1589

Figure 2. Four plane vertex detector, shown full size.

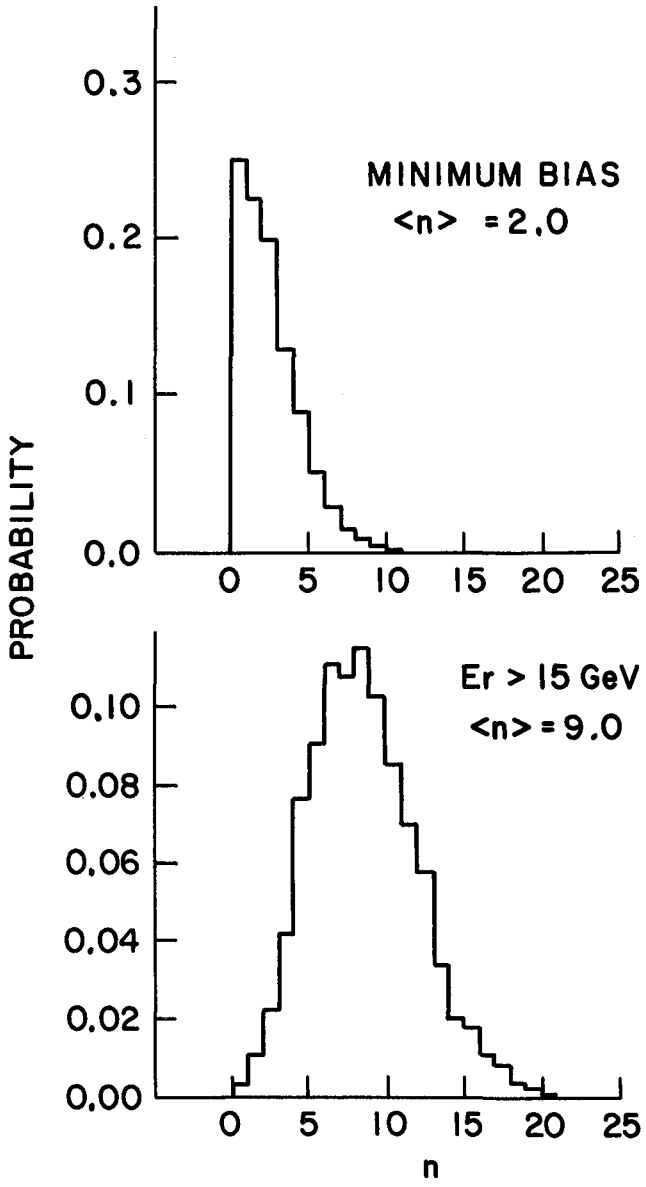

Figure 3. Multiplicity of charged tracks through the detector.

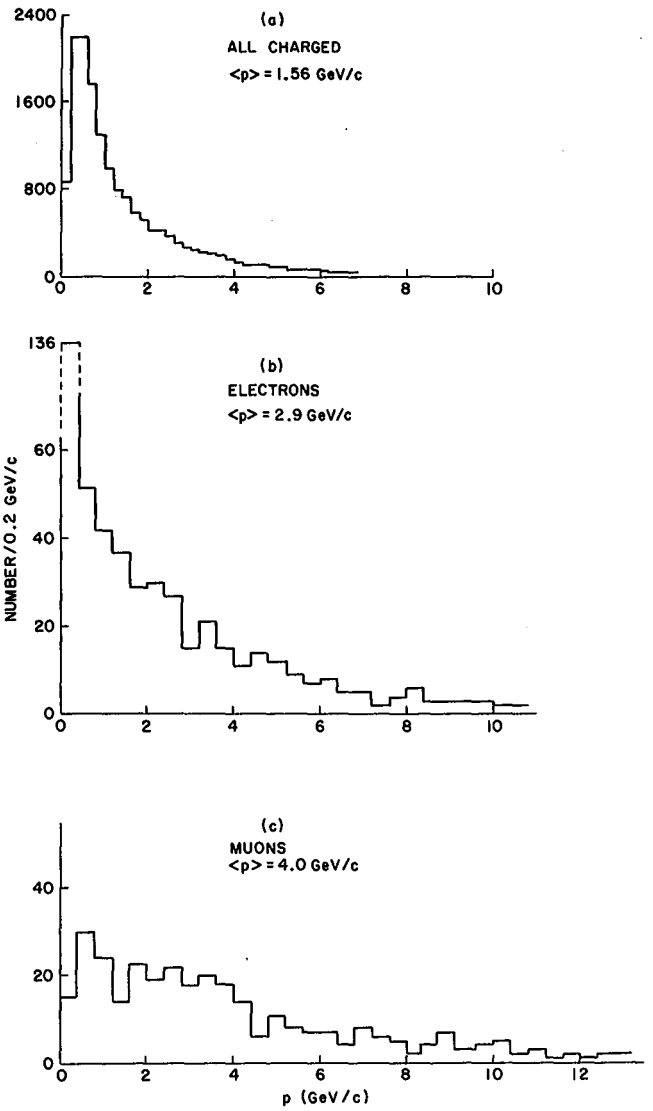

Figure 4. Momenta of charged tracks in the detector for trigger threshold E_T > 15 GeV.

(a) All charged tracks

(b) Electrons (including Dalitz decay of π^0, η)

(c) Muons

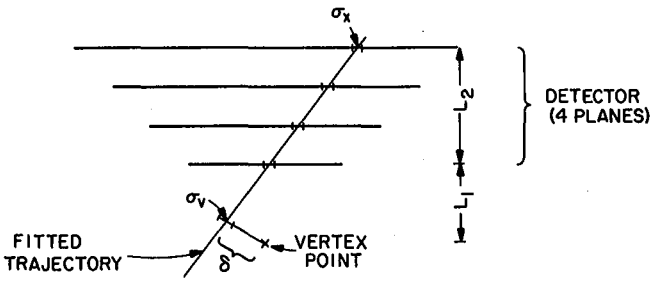

Figure 5. Resolution at the vertex for a single track (not to scale).

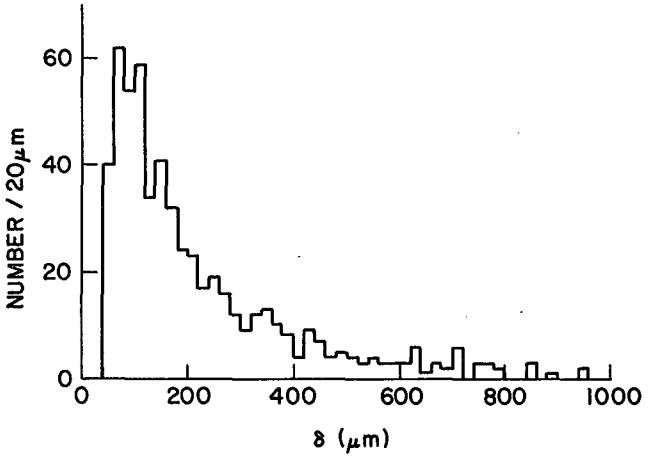

Figure 6. Projected miss distance for resolved decay tracks of $D^{\pm}$ mesons, using the criteria given in the text.

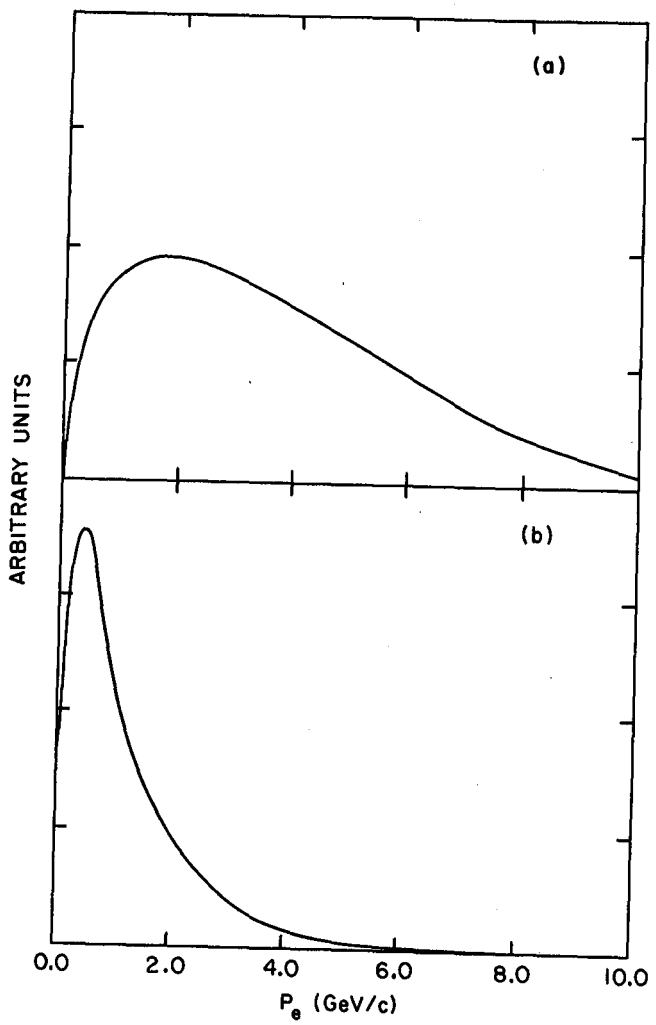

Figure 7. (a) Momentum distribution of leptons from semi-leptonic B decays.

(b) Momentum distribution of leptons from the chain decay $b \to c \to \ell$.

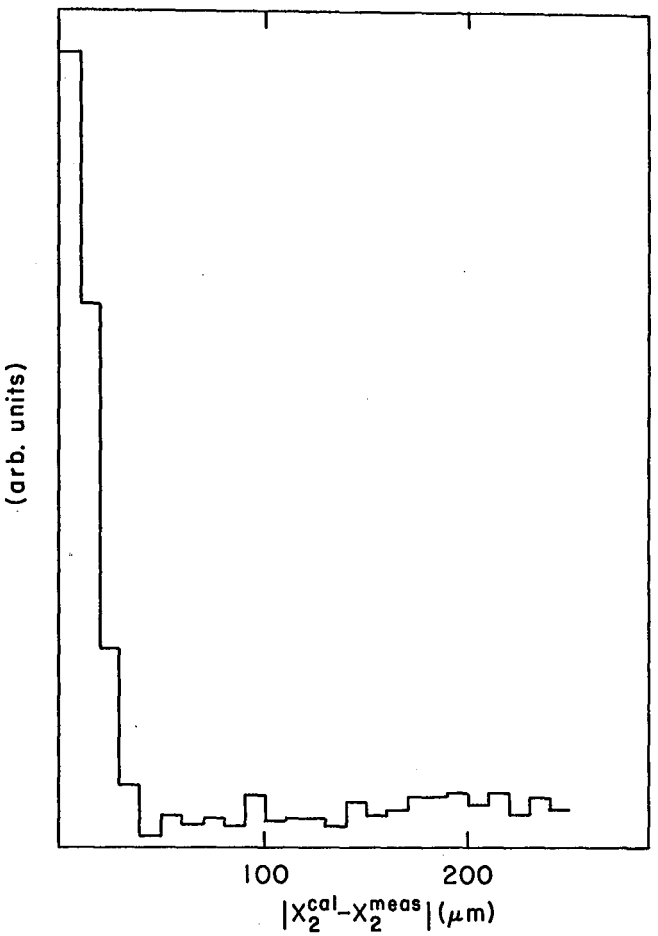

Figure 9. Difference of calculated and measured hits on plane 2 using all combinations of hits from planes 1 and 3 in the vertex detector.

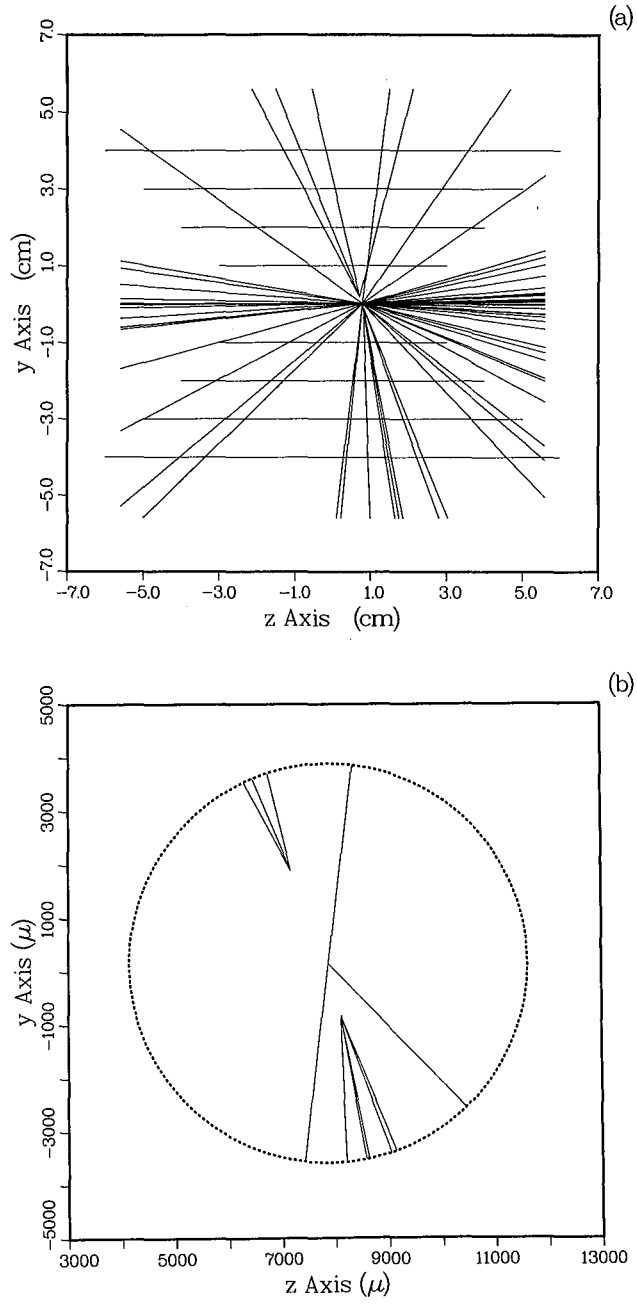

Figure 8. A $c\bar{c}$ event selected by the vertex trigger.

(a) All tracks from the event and the vertex detectors.

(b) An expanded view of the vertex with only the tracks detected in the vertex detector.

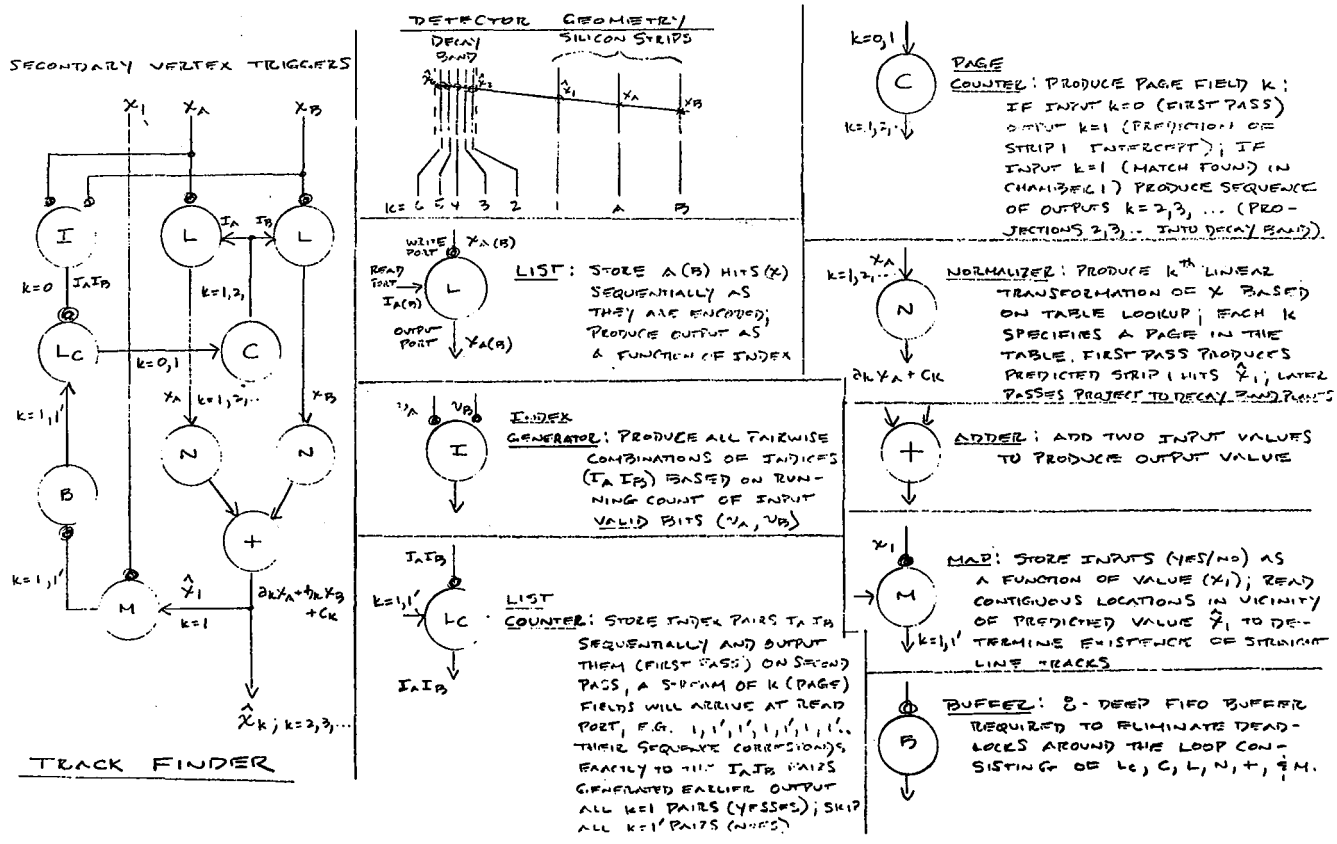

Figure 10. Hardware processor configuration for track finding.

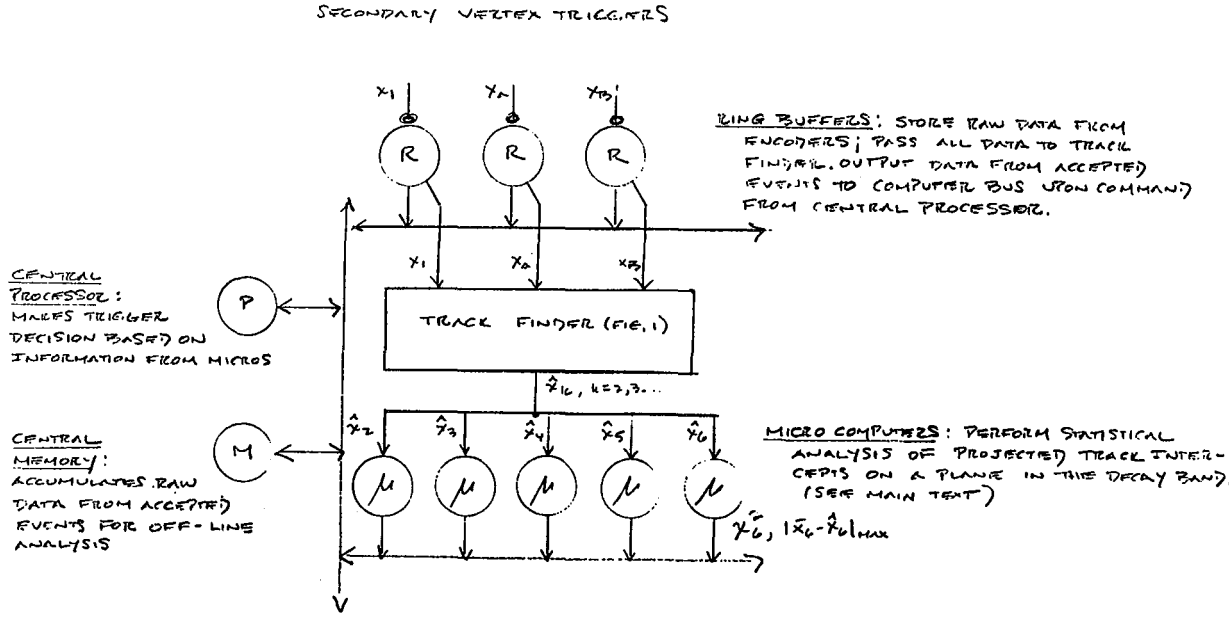

Figure 11. Array of microprocessors for vertex finding.

ANGULAR COVERAGE OF DETECTORS

R. Diebold
Argonne National Laboratory

Introduction

The total rapidity range at high energy pp and $p\bar{p}$ colliders is very large. For protons, $y_{max} = \ell n(\sqrt{s}/M_p) = 7.0$ (10.0) for $\sqrt{s} = 1$ (20) TeV. If one were to cover this entire range using pseudorapidity $\eta = -\ell n \tan \theta/2$ as a guide, the small angle limit would be 2 (0.1) mrad (corresponding to a p_T cut off of 0.94 GeV/c for elastic scattering). Heavy particles tend to give decay products at much larger angles, however, and for a given amount of money one can ask how to optimize the general purpose "4π" detector and where fine segmentation is most likely to be of use in getting out important new physics.

Parton-Parton Interactions

Here we will assume that a primary purpose of high energy colliders is to explore large subenergies in the parton-parton rest frame:

$$\hat{s} = x_1 x_2 s \quad ,$$

where x_1 and x_2 are the fractions of the beam energy carried by the two interacting partons and s is the overall center-of-mass energy squared. The large subenergy can then be used to produce massive particles, cause high p_T jets, etc. For simplicity, we will think of this as the production of a heavy system with $M = \sqrt{\hat{s}}$. Since the structure functions fall rapidly with x, the cross section for a given mass tends to be largest when $x_1 \approx x_2$, and falls rapidly in the asymmetric case, i.e., for large $|y|$.

To take a specific example,[1] we look at gluon-gluon interactions with $G(x) \propto (1-x)^5/x$. For a simple matrix element, we then have

$$\frac{d\sigma}{dy} \propto G(x_1)\, G(x_2) \propto (1 - x_1)^5 (1 - x_2)^5 / x_1 x_2 \quad ,$$

and at fixed $\sqrt{\tau} = M/\sqrt{s}$

$$\frac{d\sigma}{dy} \propto (1 - \sqrt{\tau}\, e^{y})^5 \, (1 - \sqrt{\tau}\, e^{-y})^5 \quad .$$

This function is traced out in Fig. 1 for several values of $\sqrt{\tau}$. For $\sqrt{\tau} = 0.1$ (100 GeV at $\sqrt{s} = 1$ TeV, 2 TeV at $\sqrt{s} = 20$ TeV), the distribution falls to half height at y = 1.0. For a y = 1 heavy particle decaying isotropically into relativistic particles, the median angle of the decay products will be 40° (corresponding to a pseudorapidity of 1.0) and 76% of the decay products will be within ±1 units of rapidity.

The half-height width of the distribution in Fig. 1, $y_{1/2}$, is shown in Fig. 2 as a function of $\sqrt{\tau}$. Even for a relatively light object with $M/\sqrt{s} = 0.01$ (10 GeV at $\sqrt{s} = 1$ TeV, 200 GeV at $\sqrt{s} = 20$ TeV), $y_{1/2}$ is only 2.7. Allowing an extra unit of rapidity for the decay gives the result that most of the decay products from such an object will emerge at $\theta > 3^\circ$. Heavier objects produced by parton-parton interactions will give decay products primarily at larger angles.

Diffraction Dissociation

In principle, rather heavy systems can be produced with nearly the full beam momentum (small four-momentum transfer) by single diffraction dissociation. The rapidity of the heavy object is then simply given by

$$y = \ell n\, (\sqrt{s}/M) \quad .$$

For example, a Centauro of M = 200 GeV diffractively produced at the Fermilab Collider would have y = 2.3 (median angle of 12° for relativistic decay products).

Missing p_T

Depending on the physics being investigated, an important consideration in determining the small angle cut-off of the detector may be the apparent p_T imbalance resulting from particles escaping at smaller angles. For a heavy system produced with a rapidity corresponding to the cut-off angle and decaying into two relativistic particles, one of these particles will always be observed and the other not, leading to a p_T imbalance of as much as M/2. This is a worst case since decays into more particles will tend to reduce this imbalance. Particles produced 0.5 units of rapidity away from the cut-off would have a ~ 50% chance of balancing momentum in the case of two-body decays.

As an example, we estimate from Fig. 1 that about 5% of the particles with $M/\sqrt{s} = 0.02$ would be produced with $y = 3 \pm 0.5$, and that roughly half of these would give a significant imbalance of p_T, up to $0.01\sqrt{s}$. At this level, cracks and inefficiencies in the detector are likely to give effects of a similar magnitude. This would suggest that a cut-off angle of about 5° should be adequate to hold the apparent imbalance to $p_T \lesssim 0.01\sqrt{s}$; this calculation is, of course, just a rough estimate and must be checked with a Monte Carlo program for the specific detector geometry and physics under study.

Inclusive Distributions

Even for minimum bias inclusive events at the SPS collider, the half-height of the pseudorapidity distribution is not moving out as fast as allowed by phase space. A comparison of UA5 streamer chamber data[2] taken at the ISR and SPS collider is shown in Fig. 3; the half-height point has moved out about 1.2 units of rapidity, only half the change in y_{max}.

Summary

Decay products from large p_T scatters and heavy particles will show up at "large" angles (more than a few degrees) and emphasis should be placed on this region when designing a general purpose "4π" detector. In addition to optimizing the system for a fixed cost, this means that less space is required along the beam than might be first estimated by looking at the nominal rapidity range. Smaller angles can be covered with a crude detector to tag any events with significant p_T at angles less than that covered by the high-quality detector.

References

1. R. Diebold, "Report from the CDF Workshop Group on New Particles," CDF-88 (1981).

2. K. Alpgard et al., Phys. Lett. 107B, 310 (1981).

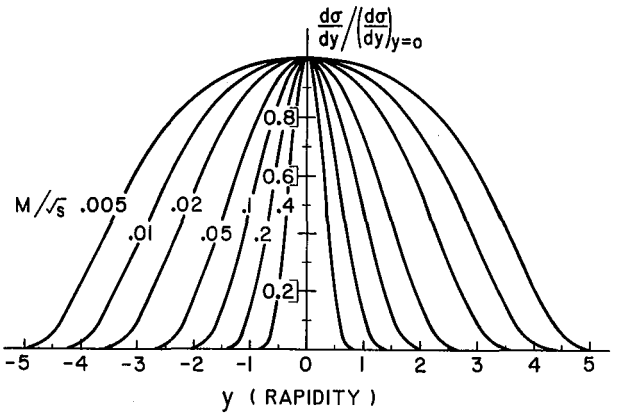

Fig. 1 Normalized rapidity distributions for heavy objects produced from gluon-gluon interactions with a simple matrix element.

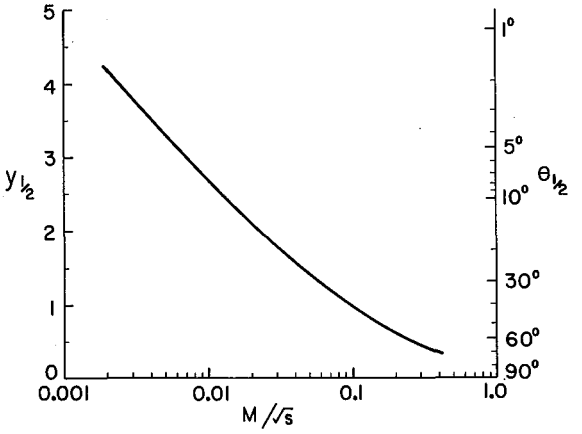

Fig. 2 Half-height widths of the distributions shown in Fig. 1; θ is the corresponding angle given by the usual formula for pseudorapidity, $\eta = -\ln \tan \theta/2$.

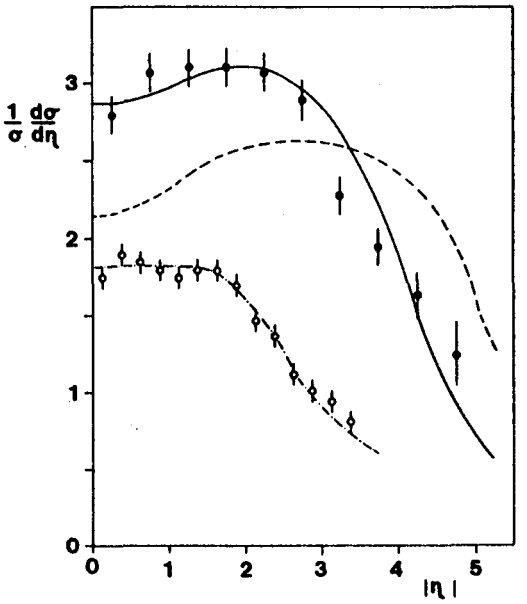

Fig. 3 Pseudorapidity distributions for inclusive particles from minimum bias events (UA5, Ref. 2). The open points are from the ISR at $\sqrt{s}$ = 53 GeV while the closed are from the SPS at $\sqrt{s}$ = 270 GeV. The broken curves are predictions for these two energies from a limited-p_T phase space model with $\langle p_T \rangle$ = 350 MeV/c; the solid curve is the same model at 540 GeV, but for $\langle p_T \rangle$ = 500 MeV/c.

A DETECTOR WITH A 3 T SOLENOID FOR A 10 TeV COLLIDER

R. Kephart and A. Tollestrup

Fermi National Accelerator Laboratory
Batavia, IL 60510

M. Mestayer

Cornell University
Ithaca, NY 14853

It has been frequently suggested that a long high field solenoid could be the basis for a high performance detector at a high luminosity machine. We explore here the properties of such a detector for a 10 TeV collider using a 3 meter diameter superconducting solenoid with a 3 T field. Such a magnet will curl up particles with $p_\perp$ less than 675 meV/c so that these particles will not penetrate the coil. Originally, we explored a very long solenoid (20 meters) with the idea that end effects could be minimized. However, it became apparent that the coil thickness (about 2 x_0 and 0.4 absorption lengths at 90°) would be intolerable at angles forward of 30°. Since it would be very hard to calorimeterize the superconducting coil, we abandoned this effort and retreated to a more "modest" coil of $\sim$ 11 m in length whose end is completely open (i.e., no end plug) yet is covered by forward calorimetry. This detector is shown in Fig. 1.

Such a detector has several interesting properties. Since the coil cuts off all momentum below 675 meV/c, we estimate that this reduces the number of charged particle tracks outside the solenoid to 29 percent of the field off value. This feature could make a tracking system outside the solenoid particularly attractive at high luminosity. On the other hand, the curling tracks presumably make tracking inside the coil more difficult and will also cause difficulties at the end regions. We will also show below that all charged tracks in the central region can have their momentum measured to quite high precision by such an "external" tracking scheme.

The arrangement of the tracking chambers proposed is shown in Fig. 1. As indicated above, tracking for the central region, $|\eta| < 1.5$ is located outside the coil but inside the E.M. calorimetry. This has three advantages:

1. The single rates on chamber wires should be lower.
2. Pattern recognition should be easier since it is done in a field free region in which the tracks will be straight lines.
3. The momentum of all charged particles can be measured with high accuracy.

To accomplish the latter, we observe the following:

1. For an invariant normalized emittance of 24 π mm/mr (95 percent) and a β^* of 2 m the transverse beam size, σ, is 28 μ.
2. The outside tracking system will measure the impact parameter which is four times as large as the more commonly measured sagitta.
3. The multiple coulomb scattering in a coil of 2 x_0 is small compared to the bend angles of particles with momenta of interest (> few GeV). For instance for a 1 TeV/c track:

   Δ = 1 mm = 1000 μ (proportional 1/p)

   $\delta\Delta$ = 21 μ due to multiple coulomb scattering (proportional 1/p)

   $\delta\Delta$ = 28 μ beam size (independent of p)

If this track is measured at R = 1.7 m and R = 2.2 m with $\sim$ 20 μ accuracy (e.g., 10 layers of 65 μ high pressure drift chambers), then the expected error in the impact parameter Δ is:

$$\delta\Delta = 44\ \mu.$$

Thus, the overall momentum resolution is:

$$\frac{\Delta p_\perp}{p_\perp} \simeq \frac{\sqrt{(21\ \mu)^2 + (28\ \mu)^2 + (44\ \mu)^2}}{1000\ \mu} \simeq 5.6 \text{ percent}$$

Measurement with "standard" atmosphere pressure chambers giving 200 μ resolution would yield:

$$\frac{\Delta p_\perp}{p_\perp} \sim 17 \text{ percent.}$$

The momentum resolution at lower momentum is better than this and approaches the 2.1 percent limit set by the multiple coulomb scattering.

In summary, we believe that very long high field solenoid is not a good candidate for a high energy, high luminosity detector, but that a somewhat shorter high field magnet with tracking chambers located outside the coil may give both good momentum resolution and easier pattern recognition than standard solenoids with tracking inside.

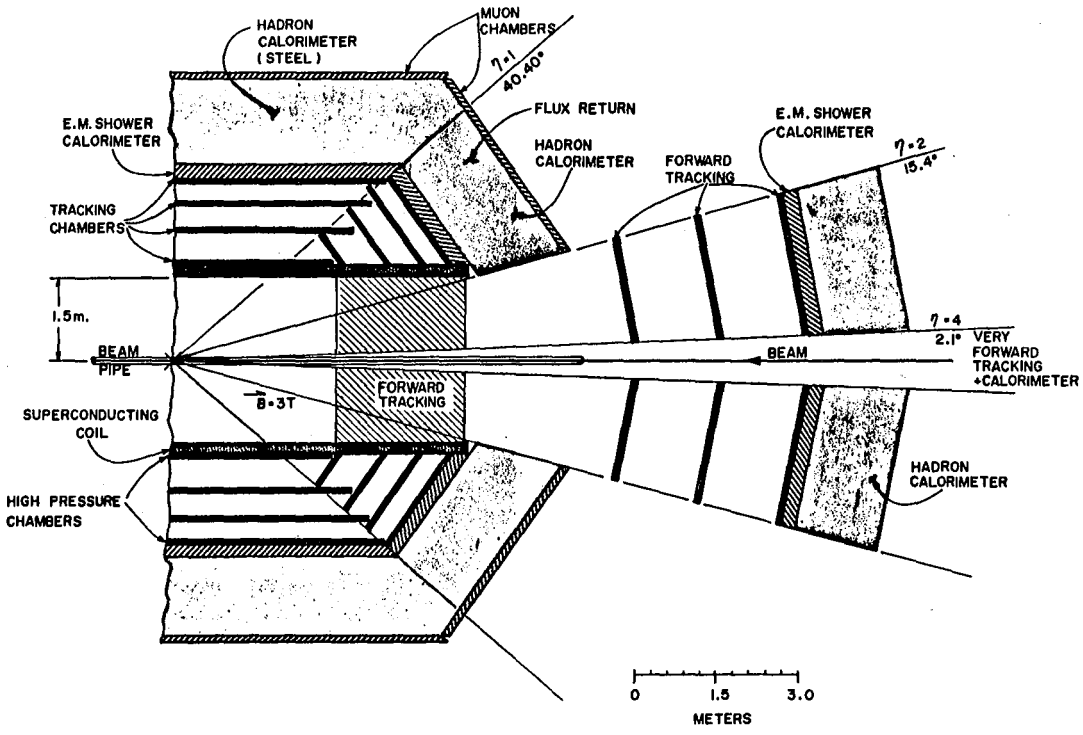

Fig. 1. Detector for a 10 TeV collider.

STATE OF THE ART

Leon M. Lederman

Fermi National Accelerator Laboratory
Batavia, Illinois

There is a large body of experience in "high luminosity" data taking in fixed target research. We try to consider a wide variety of high rate experiments which were limited by the detector (not by available beam) to a preset number of collisions per second. We then attempt to translate these state-of-the-art experiments to effective collider experiments. To this end, we extend the chosen detector to a comparison 4π collider detector operating near 1 TeV.

There are several issues: (1) effective solid angle must be translated to $\simeq 4\pi$, (2) environments may be quite different, e.g., beam dump near fixed target or beam halo muons vs. collider backgrounds, (3) the multiplicity varies over the experiments selected and (4) we have to treat open vs closed geometries. The large variety of experiments selected is designed to average over the causes for detector limitation.

Finally we chose detectors which have produced physics in order to gauge the "state of the art."

(1) Effective Solid Angle

If we use 4π in order to see "the whole event" then we must correct by the solid angle. One way to see this is via accidentals. Suppose there are n pieces of a detector, each subtending 1/n th of 4π. If the maximum sustainable rate in a piece is Rcts/sec, then the accidental rate is:

$$A = R^2\tau\ n(n-1)$$

(Dead times, pile up etc. are all forms of accidentals). If the R rate itself is arrived at by taking the maximum allowable accidental rate, then in the collider mode, each piece must be reduced by n to have acceptable accidentals. This means we must reduce the luminosity by the factor of n, i.e., the fraction of the solid angle in the fixed target run. Some fixed target experiments install a momentum or $p_\perp$ cut. If this is modest it probably conforms to the $p_\perp >$ 1-1.5 GeV/c requirement imposed in SPS collider calorimetry. However, in colliders, these events usually burden the tracking even if their influence on calorimetry is relatively benign.

(2) Environment

Fixed target environment can have beam halo, flux from nearby beam dump or poor duty cycle during the slow spill. Collider environments are also complicated by beam gas, beam wall, side splashes and the debris from forward jets striking flanges etc. C. Rubbia estimated that UA1 had 40% additional tracks per event which is event originated but not from the vertex. We'll call this a wash. The time structure of the comparison collider (and ISR) have a 100% duty cycle-- most fixed target experiments average $\geq$ 50% duty factor due to spikes or poor duty factor.

(3) Multiplicity

The FNAL experiments have mean charged particle multiplicities of 9, ISR is 13 and $\bar{p}p$ at SPS of 25. The AGS mean multiplicity is about 5. These are just the properties that burden detectors (one has to be careful to correct for thick target effects) and since we are aiming at a 1 TeV collider detector, we should make a correction to the luminosity.

(4) Closed Geometry

These are a valuable variety of experiments designed for high rates. We can treat them in two ways - as a limit of the state of the art in closed geometry experiments and, by adding back the absorbed hadrons, reduce the luminosity accordingly. A perfect absorber decreases the rates by $\geq 10^4$ i.e. direct muons to hadron ratio near y=0. More often there is either finite density absorber and some decay space. We use factors of 2×10^3 to 5×10^3 accordingly.

Conclusions

Our results are presented in Table I. One could correct all the achieved luminosities by dividing by ~ 30/multiplicity and by looking at the corresponding rapidity interval rather than solid angle. However, the lesson seems clear enough - the state of the art of published physics before 1983 seems to hit considerable resistance above 10^{31} cm^{-2} sec^{-1}. The sole exception is the I-1 experiment at the ISR. Closed geometry experiments also suffer limitations somewhere between 10^{33} and 10^{34}. This wide variety of experiments, designed by competent physicists to withstand high rates, indicates that detectors designed for much higher luminosity than 10^{31}, must break new grounds in invention, complexity and/or cost. Finally, there is the concern which, to my knowledge, is not addressed by this workshop: how can we be sure that the new, non-state-of-the-art detector can extract physics?

STATE OF THE ART

Experiment	Interaction Sec	Target/ Beam	ABS	Rapidity Ω_{cm}	Effective Luminosity**	Why?
FNAL E-						
400	10^5	Si/400 neutrons	0	1.6 π	$\sim 10^{30}$	trigger dead time
537	1×10^7	W/125 GeV π,p	60"Cu	2 π	$\lesssim 10^{30}$	Beam tagging
326*	10^9c*	Var. 225 GeV π^-	10'Fe	3 π	4×10^{30}	Drift Chambers
615	2.5×10^8	" 250 π^-	8' Be + 16' c	2 π	10^{30}	trigger dead time + PWC's
673	5×10^5	Be 200 π	0	2 π	5×10^{30}	Pb glass pileup PWC, mg.
609	10^5	H_2 400 p	0	2.9 π	2×10^{30} → 10^{31}	Halo muons Otherwise x5
623	10^5	200π,400p	0	1.8π	2×10^{30}	SC & D.C. jam.
629	10^6	c/200 p, π	0	2π @ 90°	2×10^{31}	Liq A pileup
515	4×10^5	Be/200πp	0	2.5 π	1×10^{31}	Liq A pileup C Confusion
288*	5×10^{11}*	Cu/400 p $p_\perp \gtrsim 2$ GeV/c	22'Be	.007(4π) at 90°	2×10^{31}	Scint. counter +PWC rates
ISR						
I-1 (CCOR)	1.5×10^6	30 x 30	0	2 π	$> 5 \times 10^{31}$	No problems except in E_t
I-6 (AFS)	5×10^5	30 x 30	0	$\sim \pi$	2×10^{31} 6×20^{30} EP83-01 1.4×10^{31} EP82-139 "10% pileup"	
AGS 726	2×10^6	13 GeV π	0	large	4×10^{31}	datahandling triggering beam tagging
732	5×10^6		0	1/5 of 4π	10^{31}	beam tagging

* These experiments correspond to 4×10^{33} and 1.2×10^{34} resp. in a closed geometry with no measurements before the absorber. At 1 TeV these numbers become $\sim 1 \times 10^{33}$ and 3×10^{33} respectively.

** Not yet corrected for multiplicity.

EXPERIENCE WITH HIGH LUMINOSITY RUNNING AT THE CERN ISR

James T. Linnemann

The Rockefeller University

I will discuss experience of the CCOR and COR collaborations at the ISR at the steel low β intersection region, with luminosities up to 6×10^{31} $cm^{-2}s^{-1}$. In general, this luminosity level has caused only minor inconvenience for a detector covering polar angles 45 to 135 degrees in the center of mass, except for a special unrestrictive trigger on total transverse energy.

The ISR

The ISR is a separated ring machine, with the beams intersecting at 14.77°. It is normally operated as an unbunched pp collider, the ribbon-like beams intersecting in a diamond-shaped region, at our intersection roughly 10 × 50 × 0.4 cm^3. The steel low β section gives our intersection a luminosity 2.2 times that of the standard intersection region.

Apparatus

The major elements of our detector are shown in Figure 1. I will summarize their characteristics, with emphasis on timing behavior. A 1.4 T magnetic field is provided by a superconducting solenoid[1].

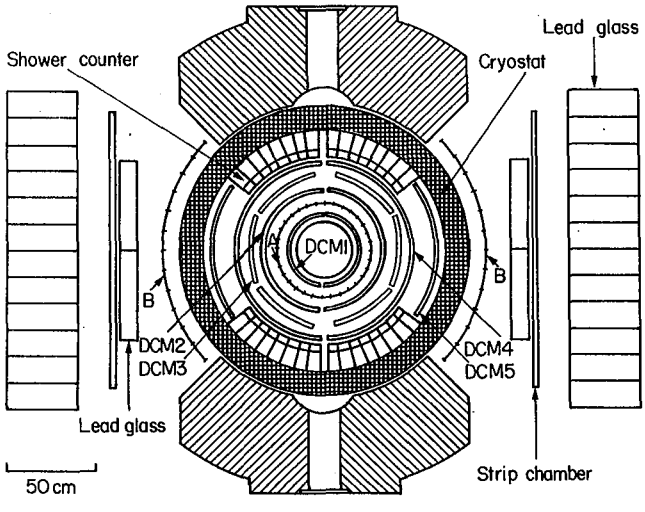

Figure 1: The apparatus viewed along the beam axis.

Lead Glass

Two arrays of lead glass are located outside the magnet coil, 1.2 m from the intersection region. They are retracted to 4 m during filling of the rings to minimize radiation damage (lead glass slivers are used as long-term dosage monitors at the ISR). This radiation damage causes a calibration drift of ≲1% per month, which is monitored by the 450 MeV single particle line in the blocks. The back arrays are each 168 blocks of 15 × 15 cm^2 × 17 X_0, and the front layers are 34 blocks of roughly 10 × 50 cm^2 × 4 X_0.

All blocks were calibrated with a CERN PS electron beam. The back blocks maintain their calibration[2] with NaI(Tl) crystals doped with the α emitter ^{241}Am, which gives a light pulse of about 1 GeV equivalent energy. The phototubes are 5" RCA 8055, inexpensive, but with a 30 ns signal halfwidth. The event gate is thus 200 ns, and the calibration gate for the slow NaI signals is 400 ns. Since this calibration system is not triggered, there is some background problem in taking calibration data with the beams circulating. This can be circumvented by running the low-threshold calibration trigger with the B counters in veto (see Figure 1). The long gate times led us to use Lecroy 2249W ADC's, AC coupled with τ = 30 μs, to achieve good linearity. The 9 mm^2 NaI sources are hit by charged particles at a rate giving an apparent cross section comparable to the π^0 cross section above p_T = 8 GeV. We remove these spurious events by making use of the slower NaI signal shape. Analogue sums of the two arrays are read in a pair of ADC's with 130 ns and 500 ns gates. Spurious events have much larger pulse heights in the long gate.

The front glass blocks use a flasher system (EGG Krytron KH22) which, in response to a trigger pulse, sends light through optical fibers to all blocks and to a well-shielded reference counter which also views a NaI crystal illuminated by a ^{137}Cs source. A 700 ns gate is required for the Krytron signal. During this gate time, 1.3 interactions are expected, but few deposit energy in any individual counter, and one could easily take flasher calibration data with the beams on.

Shower Counters

Inside the magnet were 32 lead-scintillator sandwich shower counters, each 1.5 m long (along the beam direction) and covering 6° in azimuth. They were divided longitudinally into 3.9 X_0 and 10.5 X_0 compartments. Each end of each compartment had a phototube, 128 tubes in all. These phototubes were much faster (3-6 ns halfwidth) than the lead glass tubes, allowing a 130 ns event gate. An even shorter gate could have been used had not the analogue section of the ADC's saturated at 2 V (we sent the signals to the ADC's through dispersive cables to slow them down and decrease the peak). Each tube had a TDC, Lecroy 2228A, with 0.02 ns bins and a range from -20 to +80 ns relative to the trigger time. The calibration system was a Krytron system like that used for the front lead glass. The long term drift of the calibration was <1% per month, monitored by the 175 MeV deposited by a non-interacting particle. This monitor was necessary because of the long time span between electron beam calibration of the counters. This energy implied a dynamic range of 100 : 1 in the ADC's.

Drift Chambers

Eight to ten layers of cylindrical drift chambers[3] filled the remaining magnetic volume. The coordinate along the wire was derived (σ = 1 cm) from comparing times at the ends of a delay line (velocity 0.44 cm/ns) glued near each sense wire. The TDC system designed by W. Sippach at Nevis Labs can record up to 14 hits per channel with 1.5 ns resolution. Three channels (sense and 2 delay line ends) are used for each of the 580 sense wires. The delay lines and multihit capability allow several tracks in a single drift cell, and give 3-space points as input to the pattern recognition programs, reducing the combinatoric problems. The drift wires are in paired gaps, staggered by a half cell as shown in Figure 2. This staggering assures that out-of-time tracks will have a bad χ^2 in first order. Our typical resolution of 350 μ and the drift velocity of 50 μ/ns give 3σ deviations for events 20 ns out of time.

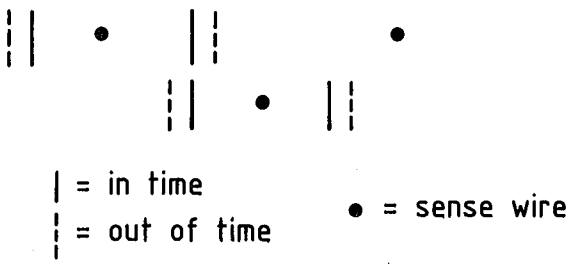

Figure 2: The effect of staggered gaps for out of time events.

Triggering

The analogue trigger electronics must slow shower counter signals in order to match the glass signals, and to provide even response along the full length of the counters (10 ns transit time). The circuitry has a fall time τ = 50 ns and a 20 ns flat-top.

Two triggers commonly used in the experiment offer a useful contrast. The ETOT trigger asks for a simple energy deposition greater than 20 GeV, summed over all shower counters and glass. It uses the entire solid angle and its purpose was to search for jet structure. It proved quite sensitive to double events. The PAIRS trigger demands a 2-cluster mass above 7.5 GeV. The calorimeter cluster was defined as a wedge in azimuth of $\Delta\phi$ = 0.22 rad × Δy = ±0.6 (glass) or ±1.1 (shower counter). The PAIRS trigger proved to be little affected by double events.

Delay Curves

To demonstrate concretely the response of the apparatus to out of time events, delay curves were measured. Drift chamber data were altered in the software by adjusting the raw time data (this discriminates slightly against late events). The results are shown in Figure 3 for ETOT and PAIRS data. The space points are rejected in software for falling outside the drift cells at a rate consistent with the drift velocity (maximum drift time for sense hits was 300-400 ns, and up to 800 ns for delay times). Track fitting, even with very loose cuts, rejects most tracks 60 ns out of time with the trigger. Notice that the ETOT data is more asymmetric in time than the PAIRS data, offering evidence that it is more contaminated by early events than PAIRS data.

Delay curves for the calorimeter data were obtained by comparing signals summed from groups of counters sent to a monitor ADC, with the software sum of the individual counter ADC's, as the timing for the individual ADC gates was moved. Events with only a single interaction in the sensitive time were selected on the basis of timing information. The selection procedure is described in more detail below. The results are shown in Figure 4. The apparent energy of signals out of time by a full gate length is less than 10-20% of the true energy.

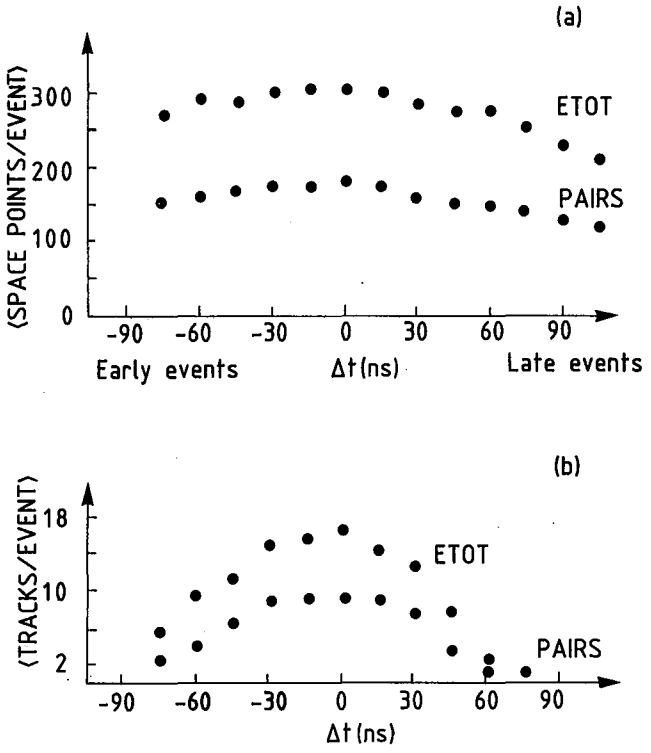

Figure 3: Delay curves for drift chamber data.
3a) <Space points / event>
3b) <tracks / event>

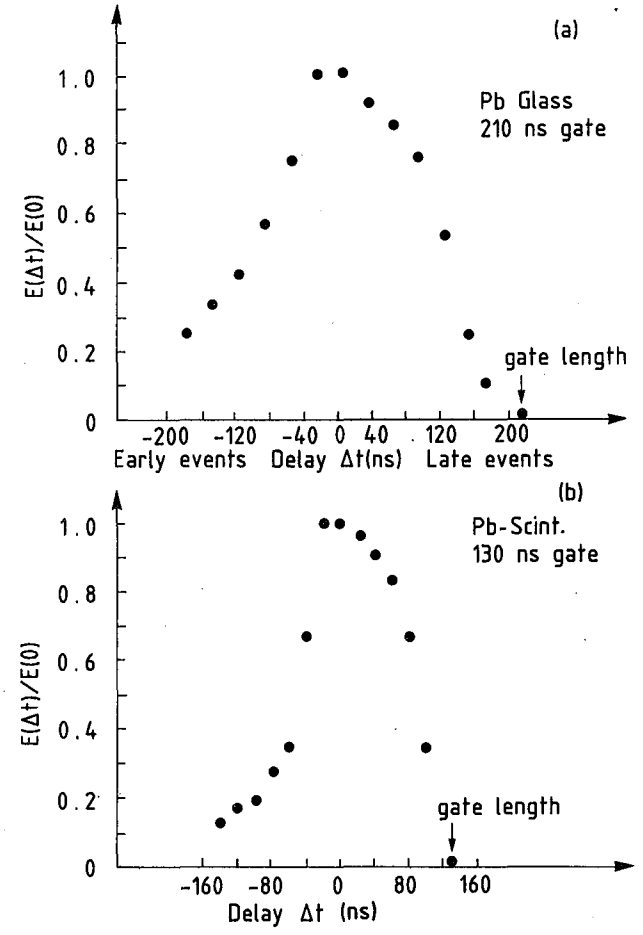

Figure 4: Delay curves for
a) Lead Glass and b) Shower counters.

Detection of Multiple Events

The timing information used to detect multiple interactions was that from the shower counters, and from a barrel scintillation hodoscope (labelled "A" in Figure 1). The A counters covered the entire solid angle seen by the drift chambers and electromagnetic shower detectors. There were 32 A counters, with a phototube at each end. Radiation damage to the light guides incurred in the 7-year stay near the ISR beam pipe has been observed. Each of the 64 A phototubes is read by a channel in the Nevis TDC system, allowing multiple hits (minimum dead time about 40 ns) and a range of ±300 ns about the trigger time. The shower counter TDC's fired with a deposit of 150 (500) MeV in the front (back) longitudinal compartments. The shower counters covered 60% of 2π in ϕ.

Multiple interactions were searched for by examining the time data for multiple clusters. The overall scheme of the time clustering is as follows. A good counter was defined as one having a coincidence between left and right end time consistent with the counter length. For each counter system (A and shower counters, separately), the average of the left and right end times of good counters was histogrammed for each individual event. A cluster was defined as a group of 2 or more times (a precaution against noise or induced radioactivity) which fell within a 12 ns interval (see Figure 5 below). This time window was slid along the histogram to find the most populated cluster. If this contained the required 2 or more counters, the counters in the cluster were removed from the histogram and the process repeated. A "double" event was defined as one with 2 or more such clusters in either the A counters or in the shower counters. Table 1 below summarizes the cuts used for the time clustering.

Table 1: Time Cluster Cuts

Counters	$t_L - t_R$	width	range	min. #
A	10 ns	12 ns	±200 ns	2
shower	12 ns	12 ns	(-20,+80) ns	2

$t_L - t_R$ is the cut on end to end time difference
width is the time window defining a cluster
range is the range in which hits are considered
min. # is the number of counters to define a hit

Figure 5 shows the distribution of good A counter times about the mean time of the cluster, for events with only one time cluster. For this plot only, the cluster width definition was widened to 15 ns. The final 12 ns width is shown on the plot. These cuts should be able to recognize multiple interactions down to a time separation even somewhat less than 12 ns.

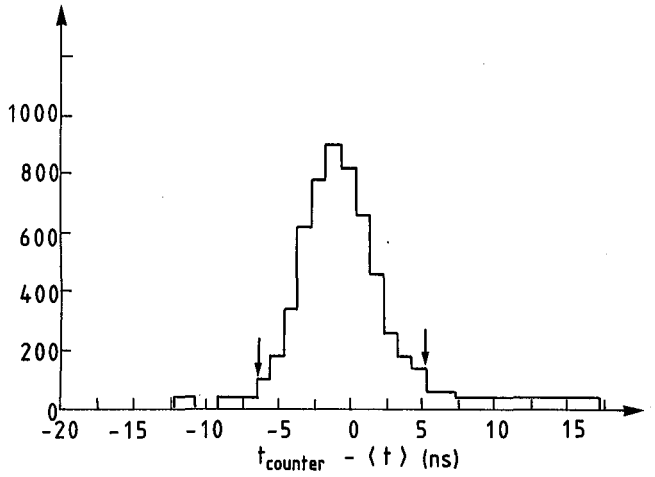

Figure 5: Deviations of A counter times from the cluster mean for events with a single time cluster.

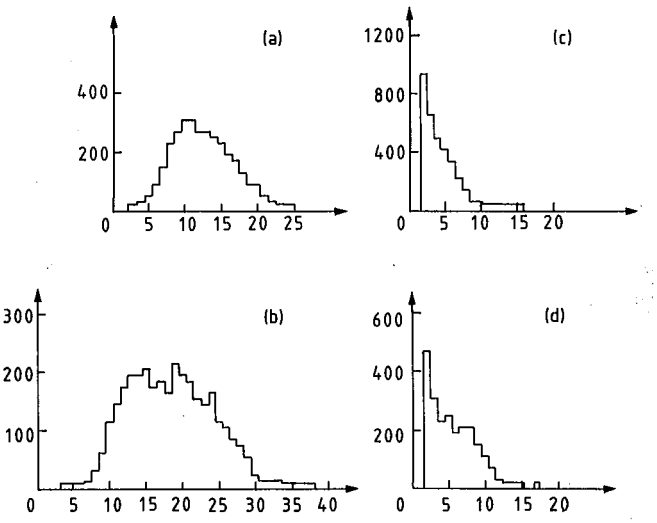

Figure 6: The number of good counters/cluster:
6a) single cluster events, A counters
6b) single cluster events, shower counters
6c) extra clusters, A counters
6d) extra clusters, shower counters

Additional characteristics of the clusters found in ETOT data are shown in Figure 6. Secondary clusters are much less populated than the primary clusters. The multiplicity distribution of primary clusters together with Figure 5 allows an estimate of the probability of falsely getting two clusters from the tails of high-multiplicity events. For example, an event with 25 A counters set (rare) should give 2 apparent clusters less than 10% of the time. One might hope to distinguish double events separated by less than the window width on the basis of the r.m.s. inside the window, but the distribution of this quantity in largest clusters is very similar in events with or without secondary clusters. In any case, one must know the time constants of the counters to about 1 ns/end to achieve stable results.

Tests of the Method

The validity of the method for separating single from multiple interactions was tested in several ways. The average times of clusters in A counters was found to correlate well with the times for shower clusters when multiple clusters were found in both systems. ETOT data were examined for "close doubles", double events with two time clusters in ±30 ns of the trigger time (in order to have good trackfinding efficiency according to the delay curve in Figure 1). The "close double" events were found to have 35% more space points and tracks than the remaining events, the "no close double" events. The average spatial resolution inferred for these close double events was 500 μ, while "no close double" events had 350 μ, the same as that observed for all PAIRS events. Of the "close double" events, 52% had multiple vertices, compared with 17% in the "no close double" class. The distribution of the number of tracks in the extra vertices is shown in Figure 7, demonstrating that the extra vertices in "close double" events have significantly more tracks than the extra vertices from the "no close double" class. One may remark that minimum bias events with 2 A counters firing have a vertex in our detector 60% of the time, and that "no close double" events may still have an extra event just outside the 30 ns cuts. Taken together, these data support the idea that the timing information is able to recognize multiple interactions.

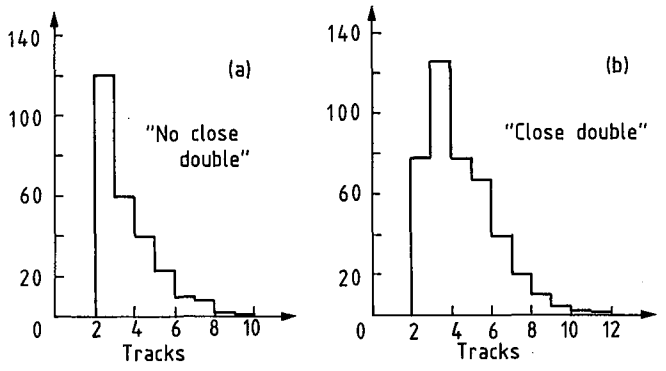

Figure 7: Tracks per event in extra vertices.
7a) events with "no close double" (defined in text)
7b) events with a "close double" (defined in text)

Effects of Timing Cuts with Varying Luminosity

The effects of the single event selection cuts were studied by varying the luminosity at our intersection with a relative vertical displacement of the beams. At each of 4 luminosities data were taken with the ETOT trigger, and the apparent cross section dN/dETOT ÷ ($\int \mathscr{L} dt$) was measured for all events and for events with the single event selection criteria (no extra time cluster in ±200 ns). The result is shown in Figure 8 for several bins of ETOT. The data without cuts show a strong luminosity dependence, while the data with the single interaction requirement are nearly independent of luminosity. The small downward slope corresponds to the effect of the random overlap rate expected from the 22 mb cross section to which the 2 A cluster definition is sensitive, perhaps diluted by an ~5% probability for double events to be misidentified as single events. The roughly linear extrapolation to zero of the single event curves agrees reasonably with the extrapolation of the unselected events, which exhibits a $\mathscr{L}$ dependence between linear and quadratic. At the highest luminosity, up to 80% of the triggers are due to multiple interactions.

Figure 9 gives further details of the luminosity dependence. Various versions of the cuts lead to extrapolations to the same cross section. Most (≈75%) of the extra apparent cross section is due to the extra events within ±40 ns of the nominal trigger time. The small time differences maximize contribution of the extra event to both the analogue trigger and in the ADC gate. The shower counters alone can detect much of the spurious cross section due to reasonable segmentation, but they are insensitive to times outside the -20 to +80 ns range. It is also seen that the A counters alone carry most of the burden.

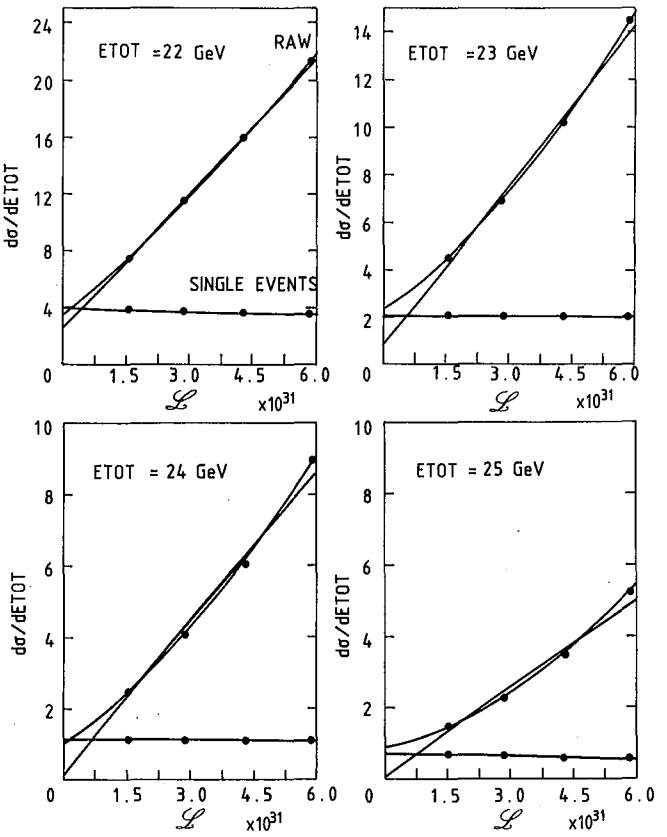

Figure 8: The cross section deduced for several ETOT bins as a function of the luminosity at which data were taken. The upper points are raw data. The lower points are events selected as single interactions (see text).

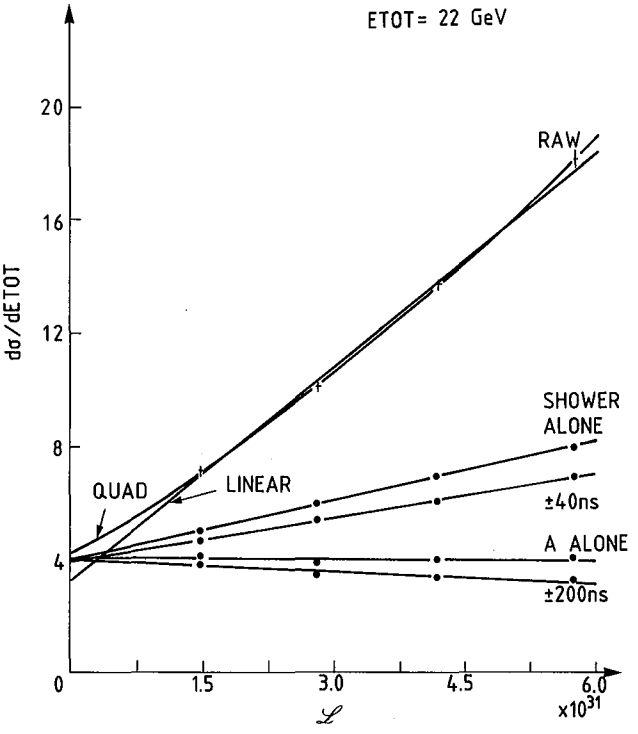

Figure 9: As for Figure 8, with other event selections added. For explanation of curves, see text.

In contrast with the ETOT data, the fraction of PAIRS events removed by a single event requirement is in close agreement with the predicted rate from fully random overlaps (contributing to neither trigger nor offline filter, but perhaps interfering with more detailed topological investigations). At most, 10% of the PAIRS triggers are due to multiple interactions at the highest luminosity.

Summary

Some general comments have been made on operating experience at $\mathcal{L} = 6\times10^{31}$ cm^{-2}s^{-1} at a $\sqrt{s}$ = 63 GeV pp collider. The problems presented by the luminosity have not been great, and pileup contributions to most triggers used have been small. An exception has been a search for jet structure with a 2π electromagnetic calorimeter[4], where the geometry readily accepts random contributions; these can be removed by use of timing information. The random contributions could also have been minimized at the trigger level by faster signal shaping, use of tower structure, or vetos on non-triggering interactions. Since this trigger was usually taken in parallel with other data, the main reduction was done offline with little penalty. Multihit readout and good segmentation were important for the success of this effort, and are expected to be more important still at higher luminosity and higher multiplicity.

References

[1] M. Morpurgo, Cryogenics 17 (1977) 89.

[2] J. S. Beale et. al. Nucl. Instrum. Methods 117 (1974) 501.

[3] L. Camilleri et. al., Nucl. Instrum. Methods 156 (1978) 275.

[4] A.L.S. Angelis et. al., submitted to Phys. Lett.

OPERATION OF THE AFS AT L = 1.4 x 10^{32} cm^{-2} sec^{-1}: A FIRST LOOK AT DATA AT HIGH LUMINOSITY FROM THE CERN ISR

The Axial Field Spectrometer Collaboration

(BNL - Cambridge - CERN - Copenhagen - LUND - Pennsylvania - Pittsburgh - Queen Mary College, London - Rutherford - Tel Aviv)

In December 1982 a run was made at the CERN ISR which utilized the superconducting low beta quadrupoles in intersection I8 at the ISR and achieved a luminosity of 1.4 x 10^{32} cm^{-2} sec^{-1} for 26 x 26 GeV pp collisions. At this luminosity the mean time between inelastic collisions is about 200 ns. A comparison run was also made at the same energy with a luminosity of 3.0 x 10^{30} cm^{-2} sec^{-1}. The luminosity under normal running conditions is typically 1.5 x 10^{31} cm^{-2} sec^{-1}. Data were collected with the Axial Field Spectrometer with a variety of calorimeter triggers. The calorimeter is a uranium-scintillator sandwich type with wavelength shifter readout[1] and covers the polar angle range $50° < \theta < 130°$. The shaping amplifiers used in the trigger have an integration time of 60 ns and the ADC gate for the photomultiplier signals has a length of 120 ns. The triggers ranged from a non-selective total transverse energy trigger (E_{TOT}) to more selective jet and single particle triggers. The jet trigger summed the transverse energy in an azimuthal range $\Delta\phi \approx 45°$.

We have compared several trigger rates at the two luminosities to see if the observed rates scale with the luminosity. This is given below for three different triggers as the ratio of the trigger rates divided by the luminosity for the two runs.

Trigger	$\frac{\text{Trigger Rate at } L_{high}/L_{high}}{\text{Trigger Rate at } L_{low}/L_{low}}$
Total Energy (E_T > 28 GeV)	4
Jet (E_T in a limited region > 9 GeV)	1.5
Two Electromagnetic Single Particle Clusters (E_{spc} > 4 GeV)	1.0

The high relative rate for the E_{TOT} trigger shows that this type of trigger is particularly sensitive to triggering on pileup events. The more selective localized energy triggers are much less sensitive to pileup and scale more closely with the luminosity.

A large fraction of the pileup events were identified with the use of the timing information from two arrays of 15 1/2 x 15 1/2 cm^2 scintillation counters surrounding each outgoing beam pipe. There are 39 separate counters in each array. After time slewing corrections the RMS time resolution for these counters is 0.7 ns. An algorithm was developed to recognize double events by first pairing counters whose time was within 3 ns for pairs within one array, or within 4 ns for a pair with one hit in one array and one in the other. Then the RMS for the mean time for the pairs was calculated from the times of all counters which were included in such pairs. A large value of this RMS indicates the presence of a double event. The fraction of triggers which were identified as double or multiple events for the E_{TOT} and jet trigger are listed below, along with the fraction found for an inelastic minimum bias trigger at normal luminosity.

Hi L E_{TOT}	66%
Lo L E_{TOT}	7%
Hi L Jet	28%
Lo L Jet	4%
Minimum Bias, Normal L	4%

These numbers suggest a lower pileup rate than would be calculated from the previously mentioned numbers since 1) not all inelastic events have hits in the counters which were used and 2) only those times within ± 17 ns of the event time were included in the analysis. Since the window for double events is approximately one half of the shaping amplifier integration time, we can estimate the expected ratio of the trigger rates by doubling the observed rate of pileup events. By this method, we obtain the values of 4.5 and 1.7 for the E_{TOT} and jet triggers, respectively. This procedure could be used to remove most of the pileup events from the high luminosity data. The timing information from elements of the barrel hodoscope and calorimeter could also be used in this manner to signify out of time events. In the case of jet and single particle triggers we expect the rate of clean events to scale roughly with the luminosity, while for the E_{TOT} trigger the fraction of events which must be rejected due to pileup may outweigh the gain due to the increased luminosity.

As an initial step we have analyzed the data from the two luminosities with a minimal number of cuts in order to see if it is possible to extract the same physics from the high luminosity data as from the low luminosity. For this we have chosen the jet trigger data where we expect a clean signature for the events. We attempted an analysis with the central drift chamber, but unfortunately the data suffered from a hardware readout problem unrelated to the higher luminosity. Therefore, after a short review of the chamber performance, we will concentrate on the analysis of the data from the 2π calorimeter.

Drift Chamber

The drift chamber was operated at reduced gain for the high luminosity run in order to maintain the chamber current at its nominal value. The wire layers at small radius, which received the highest flux, were operated at 18% of their normal gain, while the outer wire layers were operated at 80 - 100% of their full gain. We found the drift velocity remained unchanged at its normal value of 52 mm/ns. We were able to use our standard calibration programs with only a slight modification and calculate a position resolution for tracks found in the chamber. This increased to 320 μ

per point from its normal value of 220 μ. The average number of found tracks per event was 15.7 for the high luminosity data, compared with 14.4 for the low luminosity. The average track length was 30.1 cm for the high luminosity compared with 37.6 cm for the low luminosity. The most difficult problem with the drift chamber data was a malfunction in one of the discriminator crates which rendered one quarter of the chamber inoperative for both luminosity runs. Mainly because of this we decided not to follow through with a physics analysis of the drift chamber data at this time.

Calorimeter

We compared the P_T distribution of energy clusters found in the uranium calorimeter for the two luminosities for the jet triggered data. A description of the cluster finding algorithm can be found in Ref. 2. In order to set an upper limit on the effect of pileup events, we made no explicit cuts to eliminate multiple events. Fig. 1 shows the P_T distribution of the clusters appropriately normalized using the integrated luminosities of the two runs. At low P_T, there is an excess of clusters found in the high luminosity data as one would expect from the overlap of an extra inelastic event with a true jet event. However, at higher P_T ($P_T \gtrsim 5$ GeV/c) there is reasonable agreement between the two spectra. Above $P_T \approx 15$ GeV, there is a contribution from cosmic rays, particularly in the low luminosity data, as we have seen before in other low luminosity runs.[3] Rejection of cosmic ray background requires the data from the drift chamber. When the requirement that high P_T charged tracks from an event vertex point to the calorimeter jet is imposed, the cosmic ray background will be substantially reduced.

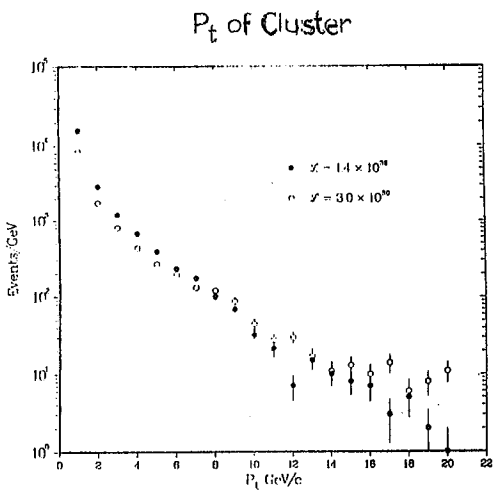

Fig. 1. P_T distribution of clusters in the AFS calorimeter at high and low luminosity.

We have also defined jets using the clusters according to a simple algorithm in order to compare the jet P_T distribution. A thrust direction was found which maximized the quantity $\sum_i \hat{T} \cdot \vec{P}_T^{\,i} / E_{TOT}$, where $\hat{T}$ is the thrust direction, $\vec{P}_T^{\,i}$ is the transverse momentum of each cluster within $\Delta y = 1/2$ and $\Delta\phi = 45°$ of $\hat{T}$ and E_{TOT} is the total energy. Once this direction was found the P_T of the clusters within $\Delta y = 1/2$ and $\Delta\phi = 45°$ of $\hat{T}$ were summed to define the P_T of the jet. Fig. 2 shows the P_T distribution of jets defined in this way for the two luminosities. Again the data have been normalized using the integrated luminosities and no cuts have been made to eliminate multiple events. One can see that above the trigger threshold ($P_T \gtrsim 10$ GeV/c), the two sets of data agree reasonably well. Below the trigger threshold there is an excess of events in the high luminosity data as one would expect from the overlap of a low P_T event with a high P_T event slightly below the threshold causing the trigger. Again, at the highest P_T there is a contribution from cosmic rays.

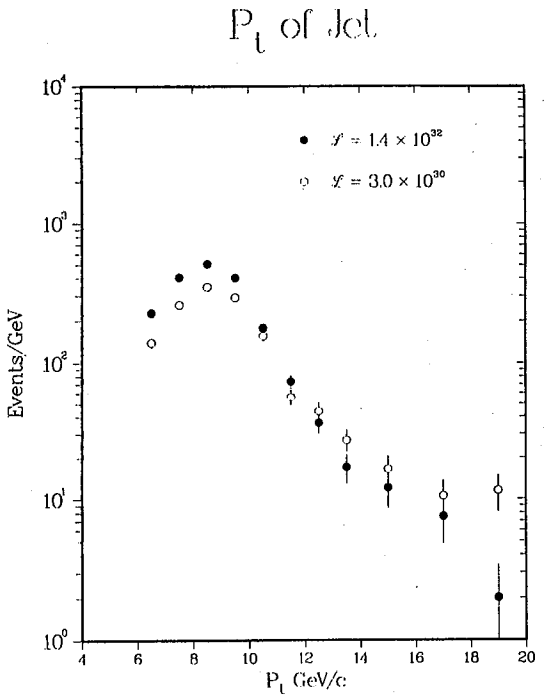

Fig. 2. P_T distribution for jets in the AFS calorimeter. See text for details.

In conclusion, we found that selective triggers such as jet or single particle triggers work well at a luminosity of 1.4×10^{32} and do not suffer severely from triggering on pileup events. In fact, the two single particle triggers will probably not be susceptible to pileup at even higher luminosity, allowing the search for high mass e^+e^- states, for example. Less selective triggers such as the total transverse energy trigger are sensitive to pileup and contain a large fraction of triggers due to the overlap of two lower E_T events. We found that our drift chamber was able to operate in a high luminosity environment and its performance was not seriously degraded. This is notable since the chamber was not designed for such high luminosity. The maximum drift time at the outer radius is 560 ns. With more closely spaced wires, the performance at high luminosity would be improved. We were able to compare the P_T spectrum of clusters and jets found in the calorimeter and found that while pileup events affected the number of events at low P_T due to our trigger definition, the spectra agreed at high P_T.

This research supported in part by the U.S. Dept. of Energy under Contract DE-AC02-76CH00016.

References

1. H. Gordon et al., Nucl. Instr. & Meth. 196, 303 (1982).
2. T. Akesson et al., Phys. Lett. 118B, 185 (1982).
3. T. Akesson et al., Phys. Lett. 121B, 439 (1983).

RATES AND TIME STRUCTURE EXPECTED FROM $\sqrt{s}$ = 40 TeV COLLIDERS

R. Diebold
Argonne National Laboratory

Summary

Luminosities and time structure for $\bar{p}p$ and pp colliders were examined at the DPF Snowmass meeting, and the results are summarized here as input for the design of detector components and systems. For bunched beams, the need to separate the beam orbits before the next bunch meeting gives a spacing between bunch collisions of about 800 nsec for $\bar{p}p$ and 100 nsec for pp. For the beam emittance assumed, as many as 25 interactions per bunch collision should be possible, giving luminosities of up to 3×10^{32} and 2.5×10^{33} cm^{-2} sec^{-1} for $\bar{p}p$ and pp, respectively. Unbunched pp beams give a better duty cycle, but require greater beam intensities for a given luminosity. Synchrotron radiation will damp the beams at these high energies and may allow one to maintain constant luminosity during a run.

Bunched Beams

For bunched beams, it is convenient to consider the luminosity per bunch collision,[1]

$$L = \langle n \rangle / \sigma_{tot} ,$$

where $\langle n \rangle$ is the average number of interactions per bunch collision; for convenience we will take σ_{tot} = 100 mb = 10^{-25} cm^2. If Δt is the time interval between bunch collisions, the luminosity is given by

$$\mathscr{L} = \langle n \rangle / \sigma_{tot} \, \Delta t .$$

In the pp case, the beams are easily split by bending magnets at each end of the interaction region. Allowing ±10 meters clear space for the detector, and taking into account the relative motion of the two beams, a bunch spacing of 30 m = 100 nsec allows adequate separation at the next bunch meeting point. This gives

$$\mathscr{L}(pp \text{ bunched}) = \langle n \rangle \times 10^{32} \text{ cm}^{-2} \text{ sec}^{-1} .$$

The optimal value for $\langle n \rangle$ depends on the detector capability, as well as the particular physics under study and its sensitivity to backgrounds from multiple events.[2]

The separation of $\bar{p}p$ beams is harder and requires electrostatic separator plates. For optimal efficiency, the separators need to be placed where the β function is large and can thus not be located too close to the interaction point. Space must also be allowed for the beam orbits to drift apart (betatron phase advance), so that the minimum distance between bunches is roughly 240 m = 800 nsec, and

$$\mathscr{L}(\bar{p}p \text{ bunched}) = 1.25 \langle n \rangle \times 10^{31} \text{ cm}^{-2} \text{ sec}^{-1} .$$

At Snowmass the "conventional" collider group[1] assumed a normalized emittance of $\varepsilon_n = 10\pi \times 10^{-6}$ meters; for 20-TeV beams, this gives

$$N = 1.4 \times 10^{10} \sqrt{\langle n \rangle} / \text{bunch}$$

as the number of antiprotons (or protons) required per bunch. For a 60-km circumference ring (8 to 10 Tesla magnets), the total number of antiprotons would be

$$N_{tot}(\bar{p}) = 3.5 \sqrt{\langle n \rangle} \times 10^{12} .$$

With an extension of the technology being developed for TeV I, it was estimated[3] that it should be possible to collect 10^{12} $\bar{p}$/hour. It is traditional in the design of hadron colliders to assume a limit for the so-called beam-beam tune shift of 0.005. Using this criteria, values of $\langle n \rangle$ up to 25 are possible with the emittance assumed; this would require 18 hours of $\bar{p}$ collection.

Even higher values of $\langle n \rangle$ are possible if the emittance is suitably increased to keep the tune shift under control, but at the expense of a linear scaling of the number of $\bar{p}$'s with $\langle n \rangle$. A low-field ring of 2.5-Tesla magnets would have three or four times the circumference and thus require as many times the number of $\bar{p}$'s. In considerations of such a machine, the "low-cost" group[4] at Snowmass assumed that a beam emittance a factor of 10 smaller could be obtained ($N \propto 1/\sqrt{\varepsilon}$ for fixed luminosity). At this smaller emittance, however, the beam-beam limit already comes into play at $\langle n \rangle$ = 2.5.

Unbunched Beams

For unbunched beams, the duty cycle for the detectors can approach 100%, but with the need for more beam particles effectively excluding the $\bar{p}p$ option. While the luminosity is inversely proportional to α, the crossing angle, this angle must be $\gtrsim$ 60 μrad if the beams are to separate cleanly[5] (each beam is diverging from its tightly focussed waist at the center of the interaction region). This leads to a "diamond" with rms length σ_ℓ = 0.28 m and

$$N_{tot}(\text{unbunched}) = 4 \times 10^{14} \sqrt{\mathscr{L}/10^{33}} / \text{beam}$$

for $\varepsilon_n = 10\pi \times 10^{-6}$ m and a 10-Tesla ring. Including the long-range contributions[5] to the beam-beam tune shift gives a nominal limit of $\mathscr{L} \lesssim 1.3 \times 10^{34}$ cm^{-2} sec^{-1}, but this would require 1.2 A in each ring, or 1.4×10^{15} protons/ring (5000 megajoules) for a 60 km circumference.

A summary of luminosity and the number of beam particles required is given in Table I for the different modes of operation. If the total number of beam particles turns out to be the limiting factor (for example, if the abort system can only handle so many gigajoules), the bunched beam would give about 20 times the luminosity of the unbunched beam.

Synchrotron Radiation

At the SPS collider there is a contribution to the duty factor from the luminosity lifetime of about 16 hours; the luminosity falls from its peak value at the beginning of the run to give a lower average value. At 20-TeV synchrotron radiation damping becomes important,[6] and if no other factors were at work, the luminosity would increase by a factor of e = 2.72 every six hours for a 10-Tesla machine (four days for 2.5 Tesla). With a high field machine, one may be able to set the luminosity to the desired value and then keep it constant for the length of the run.

References

1. R. Diebold et al., "'Conventional' 20-Tev,10-Tesla $p^{\pm}p$ Colliders", Snowmass Proceedings, p. 307.

2. R. Diebold, "Detectors and Luminosity for Hadron Colliders," Proc. Maryland DPF Meeting, Oct. 1982.

3. G. R. Lambertson and Ch. W. Leemann, "Antiproton Production and Accumulation for a 20-TeV $\bar{p}p$ Collider", Snowmass Proceedings, p. 338.

4. R. Huson et al., "20-TeV Colliding Beam Facilities: New, Low-Cost Approaches," Snowmass Proceedings, p. 315.

5. L. Smith, "Luminosity of Continuous Beams with Crossing Angle," Snowmass Proceedings, p. 351.

6. L. W. Jones, "Synchrotron Radiation in Multi-TeV Proton Synchrotrons," Snowmass Proceedings, p. 345.

Table I. Typical time structure, luminosity, and number of particles per beam for three modes of operation. For bunched beams, Δt is the time between bunch collisions; in the unbunched case, Δt is the memory time of the detector, taken to be 30 nsec as an example for this table. A circumference of 60 km was assumed to calculate N.

		$\langle n \rangle = 1$		$\langle n \rangle = 25$	
	Δt (nsec)	$\mathscr{L}$ $\left(10^{32} \text{ cm}^{-2} \text{ sec}^{-1}\right)$	N (10^{14}/beam)	$\mathscr{L}$ $\left(10^{32} \text{ cm}^{-2} \text{ sec}^{-1}\right)$	N (10^{14}/beam)
Bunched $\bar{p}p$	800	0.12	0.04	3	0.2
Bunched pp	100	1.0	0.3	25	1.4
Unbunched pp	(30)	3.3	2	80	11

ADVANTAGES OF SPATIAL AND TEMPORAL SEGMENTATION FOR DETECTORS AT HIGH LUMINOSITY CW COLLIDERS

Michael J. Tannenbaum

Brookhaven National Laboratory

The highest rate hard process at high energy colliders ($\sqrt{s} \geq 540$ GeV) is high P_T jet production. At $10^{33}cm^{-2}sec^{-1}$ luminosity, the production rate for jets with $P_T \geq 100$ GeV/c is greater than 1 per second.[1] The typical 100 GeV/c jet has a mean multiplicity of 22 charged particles in a cone of ≈15° half angle,[1] which corresponds to a mean charged particle density in the jet of 80 particles per $\Delta y\ \Delta\phi$. This is over 100 times the mean mimimum-bias charged particle density of 0.6 particles per $\Delta y\ \Delta\phi$.

A major detector problem at high energy colliders independent of the luminosity is the ability to resolve particles inside jets.[2] Only in very special cases, e.g., UA1 W± production[2] with $P_T \approx M_W/2$ will enough of the signal be clear of jets, so that events with tracks in jets can be summarily rejected. Eventually, detectors will have to cope with tracks in jets. The high track density requires good track-pair resolution and efficiency, which implies wire chambers with drift distances of 2 mm or less, independent of the luminosity.[3] The small drift distances required by the jet physics are very helpful at high luminosities[4] since the maximum drift time of 40 nsec limits the pile-up to an average of 2 events at a luminosity of $10^{33}cm^{-2}sec^{-1}$.

The segmentation of calorimeters is also set by jet physics and the desire to resolve and measure collimated jets. UA2 uses a calorimeter tower[5] with $\Delta\phi = 0.25$, $\Delta y = 0.18$; CDF[6] has $\Delta\phi = 0.25$, $\Delta y = 0.11$; and Sadoulet has discussed[7] $\Delta\phi = 0.10$, $\Delta y = 0.10$ for a 20 TeV detector. Segmentation of this order is sufficient to eliminate pile-up effects at 10^{33}. A detector considered at Snowmass[4] covered the full azimuth and the rapidity interval $-2 \leq y \leq +2$ with a 40 × 40 array of towers each covering $\Delta\phi = 0.16$ $\Delta y = 0.10$. Pile-up from an average of 10 overlapping events in a 200 nsec ADC gate could be eliminated for jets by requiring individual towers to have greater than 1 GeV/c in P_T. This simple algorithm works because jets are collimated clusters of high P_T particles while the pile-up comes from large numbers of particles with $\langle P_T \rangle \approx 0.4$ GeV/c which are uniformly distributed over the detector.

An additional feature of these highly spatially segmented detectors which can be exploited in CW colliders is to combine the spatial segmentation with time segmentation. The fast timing from the leading edge of the calorimeter signals[8] can be used to localize the time of the energy deposition in the calorimeter to ≈5 nsec. Calorimeter towers with no in-time hits to a precision of 5 nsec are simply ignored, with no loss in physics.[9] Pile-up during the ≈ 200 nsec ADC gate is only a problem if one of the ≈ 30 out of 1600 towers[4] which has an in-time hit is also struck out-of-time. This reduces the pile-up effect considerably, even for E_T triggers. The pile-up can be further reduced by using "flash" ADC's to analyze the wave-form[2] and extract the in-time energy or by speeding up the calorimeter integration times.[10]

Pile-up reduction in E_T triggers by using fast timing information was presented at this meeting by the COR R-110 experiment at the CERN ISR.[11] Before timing cuts, the E_T spectrum had a huge luminosity dependence, increasing linearly with luminosity by a factor of four over the range 1 to $6 \times 10^{31}cm^{-2}s^{-1}$. The use of precision timing (≈ 10 nsec resolution) to reject events which had additional, out-of-time, events within the 200 nsec ADC gate eliminated the pile-up. The spectrum became independent of luminosity at the expense of 35% dead time at $6 \times 10^{31}cm^{-2}s^{-1}$. It should be noted that the major part of this detector had no rapidity segmentation [$\Delta\phi = 0.11$, $\Delta y = 2.2$] and furthermore that timing information was not available on all segments. If there had been finer segmentation (in rapidity) and precision timing on all the segments in the R-110 detector, then the energy from individual out-of-time segments could have been eliminated rather than rejecting entire events. This would have eliminated both the pile-up and the dead time.

This research was supported by the U.S. Department of Energy under contract DE-AC-02-76CH00016.

References

1. F.E. Paige, "High P_T Jets," These Proceedings.
2. C. Rubbia, These Proceedings; see also CERN-EP/83-13 to be published in Physics Letters, and CERN-EP/82-170 IEEE Nuclear Science Symposium 1982.
3. D. Hartill, Tracking Summary, These Proceedings.
4. H.A. Gordon, et al., "Reasons Experiments can be performed at $L = 10^{33}cm^{-2}sec^{-1}$," DPF, Snowmass 1982.
5. M. Banner, These Proceedings.
6. CDF Design Report, August 1981, FNAL.
7. B. Barish, Systems Summary, These Proceedings.
8. M. Shochet, Trigger Summary, These Proceedings.
9. See however: C.Y. Chang, Search for Heavy Stable Particles, These Proceedings.
10. R.B. Palmer, et al., These Proceedings.
11. J. T. Linnemann, These Proceedings; see also A.L.S. Angelis et al., Observations of Jet Structure in High E_T Events, submitted to Physics Letters.

MONTE CARLO SIMULATION OF THE EFFECT OF PILEUP

H.A. Gordon, R.A. Johnson, S.A. Kahn, M.J. Murtagh and D.P. Weygand

Brookhaven National Laboratory, Upton, NY 11973

The work reported at Snowmass[1] showed that the pileup of even an average of 10 minimum bias events (Poisson distributed) would not affect the trigger of either jet events or localized electromagnetic triggers (π° or $e^\pm$). We have continued this type of study with a modification to ISAJET[2] which allows soft jets to be generated above P_T = 1 GeV such that the integral of the two jet cross section equals the total inelastic cross section of ≈ 60 mb at $\sqrt{s}$ = 800 GeV. Each event with two jets also has a so-called minimum bias event superimposed which essentially arises from the beams fragmenting. With this modification it was easy to assess the effect of the pileup of events on a jet trigger.

We considered a calorimeter covering $|y| < 2$ subdivided into 40 cells in y ($\Delta y = 0.1$) and into 40 cells in ϕ ($\Delta\phi = 9^\circ$). The trigger used the searchlight method, looking for the section of the calorimeter which had the largest transverse momentum. This section was defined as $\Delta y = 1$ and $\Delta\phi = 90^\circ$. The size of this secion was always large enough to contain the core of the jet. The curve in Figure 1 shows the cross section for triggering vs. P_T. Also shown is the cross section for an average number of 10 pileup events. The major contribution to pile-up triggers in ISAJET type events at large transverse momentum comes from one jet near the trigger threshold in conjunction with several low P_T jets, as opposed to two medium P_T jets.[3]

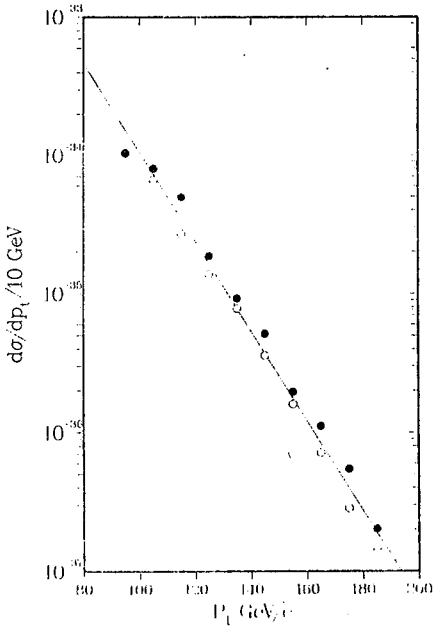

Figure 1 Cross section for triggering on jets versus P_T. Curve is for the alogorithm described in the text. Solid circles are for events with <n> = 10 events in addition to the high P_T jet. Open circles are for <n> = 10 events in addition to the high P_T jet with P_T > 1 GeV/c required for each cell.

For the cross section shown, the first jet was chosen from the full jet spectrum and then n jets with P_T < 10 GeV/c were added to the event (n was chosen from a Poisson distribution with mean n =10). This background can be reduced by demanding that each of the towers contributing to the trigger have P_T > 1 GeV. The cross section obtained after imposing this requirement is given by the lower set of points in Figure 1.

Of course the P_T plotted in Figure 1 is only that observed in the selected section of the calorimeter. To obtain the jet cross section is a much more complicated job.[4] One must make corrections for the geometric boundary, the energy leakage, the non uniformity of the electromagnetic versus hadronic response, etc. These effects are at least as important as the effect of pileup. Figure 2a shows the average value of the parton P_T obtained with a given P_T trigger threshold.

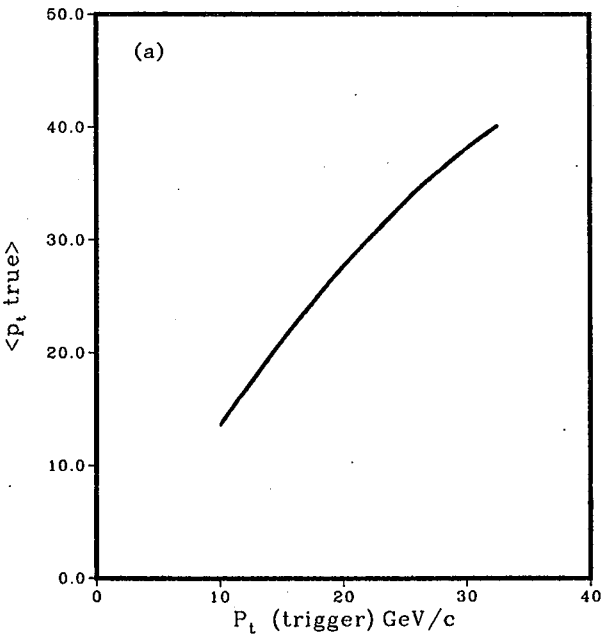

Figure 2a) Average P_T parton vs. P_T of trigger using the algorithm described in text.

Figure 2b shows the efficiency of measuring the true parton P_T with this trigger.

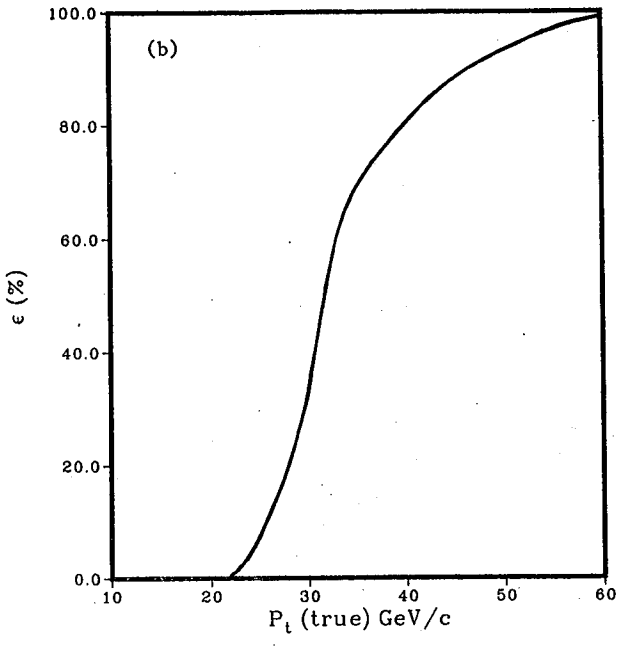

Figure 2b) Efficiency as a function of P_T of the primary parton for a trigger threshold of 25 GeV/c. Both a) and b) have $\langle n \rangle$ = 10 events in addition to the high P_T jet events.

Two other physics topics were studied at BNL to assess the effect of pileup:

A. The Effect of Pileup for $W^{\pm}$ Physics

Now that it is apparent that the $W \to e\nu$ has been discovered at CERN one may ask whether high luminosity is required for further study of the W and if so what possible effects of high rate might hamper such a high statistics study. There are at least three topics which require a large number of W's: 1) a precision determination of the Z° - W mass difference is of critical importance to determine the ρ parameter in the standard model; 2) the study of $W^{\pm}\gamma$ production would measure the magnetic moment of the W as well as testing the non-Abelian character of the gauge theory and 3) the production of $W^{+}W^{-}$ pairs would also test the non-Abelian gauge theory as well as open a new decay channel for heavy particles, for example, a heavy standard Higgs $H^{\circ} \to W^{+}W^{-}$. In the latter two cases the cross sections are rather small ($< 10^{-36} cm^2$) therefore high luminosity is required.

Kahn et al.[5] have studied the effect of extra minimum bias events on the identification of W's. In a slightly different calorimeter with cell size of $\Delta\theta = 5°$ and $\Delta\phi = 9°$ covering the central 4 units of rapidity, the trigger would be electromagnetic transverse energy deposit in one cell greater than some threshold, e.g., 20 GeV. Then a track with momentum close to that energy would be required to point to the correct cell and a particle identifier such as a transition radiation detector would signify the presence of an electron. The next selection to eliminate electrons from jets would be to require little energy in the two rings of cells adjacent to where the electron hit. The distribution of the transverse energy found in such events where only one event is analyzed at a time is shown in Fig. 3a. More than 95% of the events have $\Sigma P_T < 1$ GeV in the surrounding cells. The effect of pileup is shown in Fig. 3b where the distribution of associated energy is broader. However only ≈ 20% of the events would be lost with a $\Sigma P_T < 1$ GeV cut.

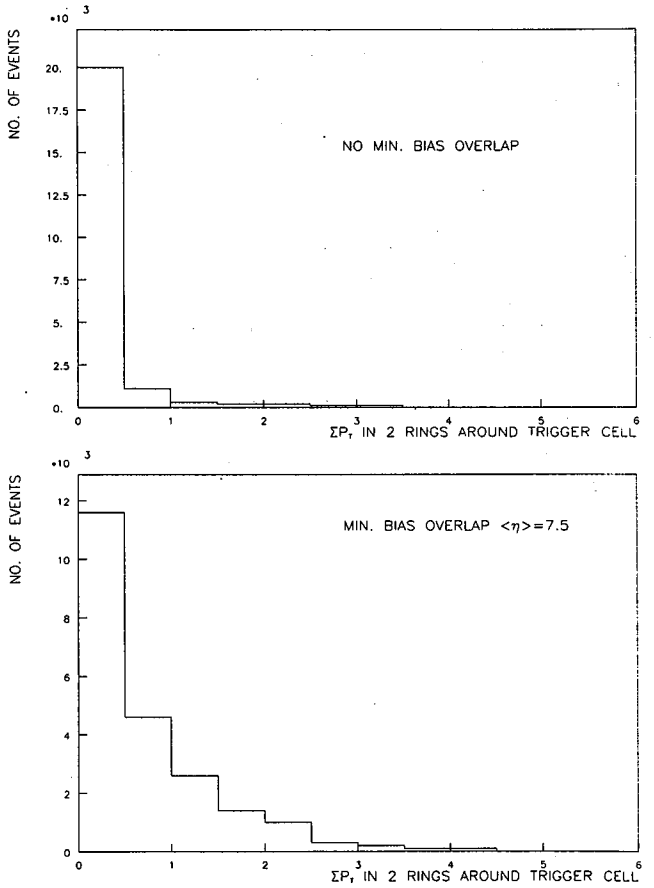

Figure 3 (a) Transverse energy in the vicinity of electrons from $W^{\pm} \to e^{\pm}\nu$.
(b) Same as a) but with $\langle n \rangle$ = 7.5 events in addition to the W.

Figure 4 shows the effect of pileup on the measurement of the P_T of the electron from the calorimeter. The P_T spectrum is broadened slightly, however an excellent determination of the Jacobian peak is still possible.

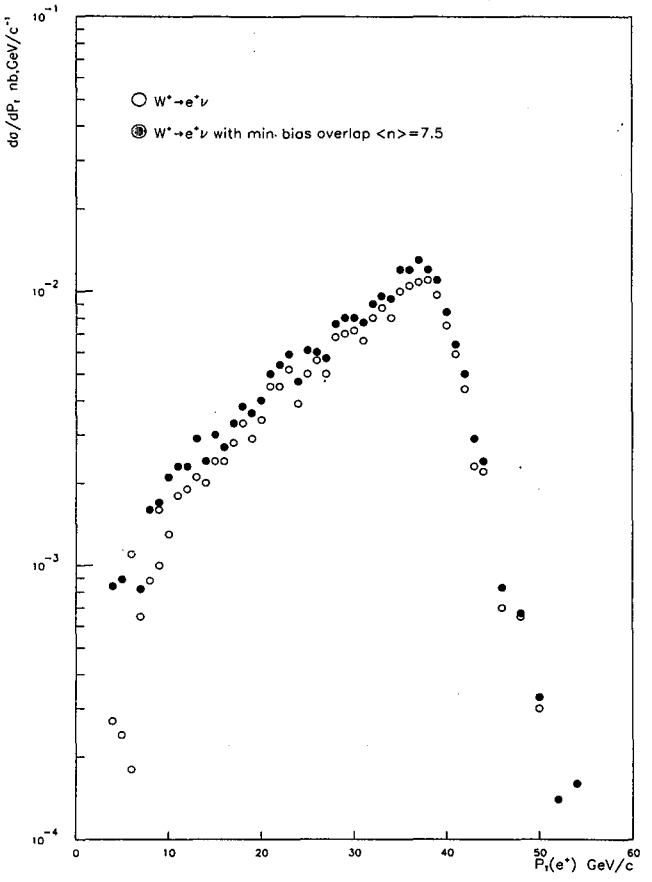

Figure 4 P_T of the electron from $W^{\pm} \to e^{+}\nu$ with and without $\langle n \rangle = 7.5$ additional events piled up.

B. The Effect of Pileup on Supersymmetric Particle Detection

Aronson et al.[6] have shown that a simple experimental signature exists for finding gluinos which are pair produced in hadron interactions. Basically each gluino decays into a photino, which is not seen in the detector, plus high P_T jets. This results in a large amount of missing P_T. The background comes from normal QCD jet events where one jet is lost geometrically or an energetic neutrino carries a large amount of P_T. To select gluino events, a sphericity analysis is used to find two hadron jets with momenta p_1 and p_2. A plane is defined by the beam and the larger momentum jet p_1. The P_T balance in the plane is measured by

$$X_E = \frac{\vec{p}_1 \cdot \vec{p}_2}{|\vec{p}_1||\vec{p}_2|} \quad ;$$

the component out of the plane is called p_{out}. Events are selected with $X_E < 0.5$, and the p_{out} distribution is plotted for both the gluino signal and the background in Fig. 5. Above $p_{out} = 25$ GeV; the gluino signal is orders of magnitude above the background. This can be understood since it is virtually impossible for a normal two jet event to have, for example, one jet at $P_T = 100$ GeV and the other at $P_T = 40$ with a relative 20 GeV of transverse momentum with respect to the first. The effect of pileup due to overlapping minimum bias events is included in the background calculation. A luminosity of $L = 2 \times 10^{32} cm^{-2} sec^{-1}$ which correponds to an average of 2 added events (Poisson distributed) is assumed. As the luminosity is increased the background increases significantly, but as shown in Figure 5, even at $L = 1 \times 10^{33} cm^{-2} sec^{-1}$, beyond P_{out} =25 GeV/c there are less than 500 background events as compared to 9000 signal, for $M_{\tilde{g}} = 100$ GeV/c^2.

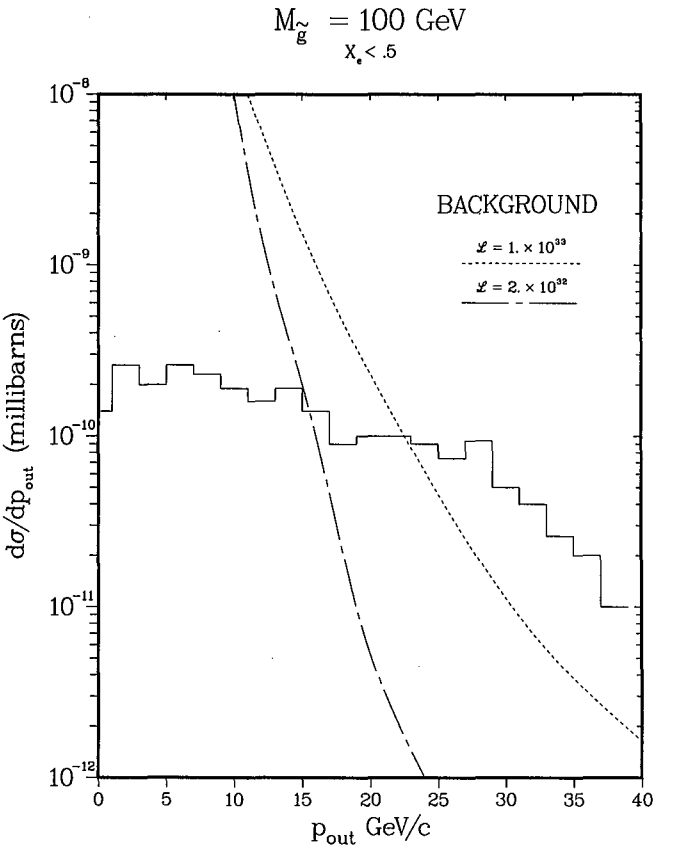

Figure 5 Gluino signal compared with backgrounds with and without pileup.

We conclude that the effect of extra events for a missing p_T trigger worsens the signal to noise--but the signal for gluinos is still clear. There has been some objection to this analysis in that there may be other more perverse backgrounds. However it appears that the effect of pileup would not be very gevere. Those unknown backgrounds would presumably obscure the signal at any luminosity.

This research was supported by the U.S. Department of Energy under contract DE-AC-02-76CH00016.

References

1. H.A. Gordon, T. Ludlam, E. Platner and M.J. Tannenbaum, Reasons Experiments can be performed at a pp machine at L = $10^{33}cm^{-2}sec^{-1}$, Proceedings of DPF Summer Workshop on Future Facilities, 1982, Snowmass, Colorado.
2. F.E. Paige and S.D. Protopopescu, ISAJET: A Monte Carlo Event Generator for pp and $\bar{p}p$ Interactions, Version 3, Proceedings of DPF Summer Workshop on Future Facilities, 1982, Snowmass, Colorado.
3. R. A. Johnson, Triggering at High Luminosity: Fake Triggers from Pileup, these Proceedings.
4. See, for example, T. Åkesson et al., Phys. Lett. 118B, 185, 1982.
5. P. Grannis, T. Killian, S. Kahn and M.J. Murtagh, BNL Report (in preparation).
6. S. Aronson et al. DPF Snowmass Proceedings ...1982. p. 505
7. L. Littenberg and D. Weygand, The Effect of Pileup on the Gluino Signal, BNL Internal Report, 1983.

CALORIMETRIC PHYSICS IN THE PRESENCE OF MULTIPLE EVENTS

John Yoh
Fermilab

Hadron colliders of the present and future generations will have to face the problem of having multiple events within the resolution time of the detector. A critical issue is the effect of multiple events on physics capabilities. This note addresses this issue. Most of the conclusions are based on Monte Carlo studies by H. Gordon, R. Johnson and J. Yoh, as well as on other considerations. H. Gordon has separately submitted his results and conclusions; the conclusions expressed in this paper are my own.

Several of the areas addressed by this note are listed below and are covered in the following pages; we give here brief conclusions of each of these areas:

1. ASSUMPTIONS AND PROCEDURE --Most of the Monte Carlo studies involve Electromagnetic (EM) and Hadron calorimetry towers covering 4π and finely segmented into bins in Phi and Eta (the pseudo-rapidity); the conclusions are based on various cluster criteria applied to events generated by various monte carlo models such as ISAJET, FOX (full QCD) and MBl (a minimum bias Monte Carlo fitted to ISR and SPS collider data) at a center of mass energy of 1 TeV.

2. SINGLE JET PHYSICS --One can trigger and measure the highest Pt narrow jet in an event using a simple window algorithm to define a cluster; clusters with Pt above 10-15 GeV are not faked by multiple minimum bias events and thus constitute a clear signature for hard scattering or production of massive particles; the effect of multiple events is to simply add some energy (typically 1.5 times the ambient background of 2.5 GeV Pt per unit rapidity per extraneous event) to the Pt of the cluster, which can readily be corrected for by Monte Carlo.

3. MULTIPLE JET PHYSICS --However, QCD invariably leads to gluon bremsstrahlung, many of which will be soft (e.g., below 7 GeV in Pt); these low energy clusters can frequently be faked by multiple events. Typically, use of a single window in each hemisphere only picks up 80-90% of the hard scattering Pt; this leads to a gradual threshold in triggering and a complicated model dependent unfolding procedure to obtain the real hard scattering cross section if one only measures the two leading clusters. This is even more serious for the signal of heavy mass decaying into many jets (e.g., Higgs, W or Z into heavy quarks). Preliminary Monte Carlo studies of the process W decay into T + Bbar shows that while th W mass can be reconstructed to an accuracy of better than 14% in the absence of multiple events, adding 2 Minimum Bias events into the W event seriously smears the resolution as well as contributes serious tails which could obscure the signature. 10 extra events totally obscure the signal.

4. MISSING ET PHYSICS --The Pt of neutrinos could be determined from the missing Et of the event and would constitute an interesting signature for leptonic decays of W, Z and gluinos. In a well designed detector, the measurement accuracy of missing Et should be dominated by energy resolution, in which case multiple events would contribute more Et and thus larger error in Et; e.g., an event with Z into 2 neutrinos could have Et totalling, say 50 GeV (with perhaps a 30 GeV gluon), while 10 extra minimum bias events would give additional total Et of 250 GeV! On the other hand, there are many other source of mismeasurement of missing Et, such as geometry, leakage, missing neutrinos from conventional sources, etc., and these could well dominate; in that case, the effect of multiple events may be less crucial.

5. ISOLATED LEPTON AND PHOTON PHYSICS --Isolated leptons from W or Z decays and isolated photons from W-γ production are some of the most interesting physics. Multiple events would increase the probability that the signal tower or adjacent ones would have particles hitting them, thus vetoing the signal. As a particular example, demanding no other particles within a 5 degree cone of the signal would throw out 2% of the signal per extraneous event; one would thus have to investigate the signature which may allow low Pt particles nearby.

6. MISCELLANEOUS COMMENTS -- We briefly comment on four other topics, advantages of continuous vs. bunched beams, effect of multiple events on tracking and on data reduction, and on recognition of multiple events.

In conclusion, while multiple events would not obscure the fact that hard scattering or heavy mass production has occurred, the measurement precision, and thus the signal to background will be seriously compromised. Most new calorimetric physics in hadron colliders are crucially dependent on signal to background; thus the effect of multiple events could be fatal; at a particular mass, the ratio of parton-parton luminosity to minimum bias events can be increased by going to higher hadronic energy, thus minimizing this problem.

(1) ASSUMPTIONS AND PROCEDURE

H. Gordon and J. Yoh independently studied the effect of multiple events on calorimetry physics; the size of window used and the event generation Monte Carlo are different, but the conclusion on single jet performance is similar.

Events are generated by various Monte Carlo programs. Minimum bias events are generated by ISAJET and MBl; ISAJET assumes exponential-like Pt dependence while MBl fits the Pt dependence to ISR and UAl observed distributions and thus includes, on the average, some contribution from soft jets. Minimum bias events from ISAJET program does not include enough medium Pt (e.g., 1-5 Gev) particles as indicated by UAl results and is thus inadequate; one would have to include some fraction of events with soft jets in order to realistically simulate the expected real minimum bias events. These minimum bias events are mixed into signal events to see the effect of multiple events.

Signal events investigated includes 2-JET events from ISAJET and FOX monte carlos, and W into T + Bbar from ISAJET. The FOX monte carlo, developed by Field, Fox, Wolfram and others, includes effects of both initial state and final state gluon bremsstrahlung; although ISAJET only include final state bremsstrahlung, the effect in the central region is probably not too significant.

The studies involve finding clusters defined by a certain size window in a tower geometry calorimeter. H. Gordon uses a wide window of 90 degrees in azimuth and 1 unit of rapidity, while J. Yoh uses a narrow window with 20 degrees in Phi and .4 in Eta.

The effect of multiple events are studied by comparing signal distribution in Pt, mass or Sum Pt with the signal events only (the +0 case), with an average of 2 extraneous minimum bias events mixed in with the signal event (the +2 case) and with 10 extraneous events (+10). The number of extraneous events are determined by poisson distribution. The case of +2 would correspond to a resolution time of 40 nsec and an instantaneous luminosity of 10^{33}.

(2) SINGLE JET PHYSICS

The simplest trigger and analysis algorithm one can imagine is to set a fixed size window in Phi and Eta and search the calorimeter for the largest Pt deposited by a event within that window at all possible locations of the window (limited by the tower boundaries). Figure 1a and 1b shows the observed Pt spectrum of

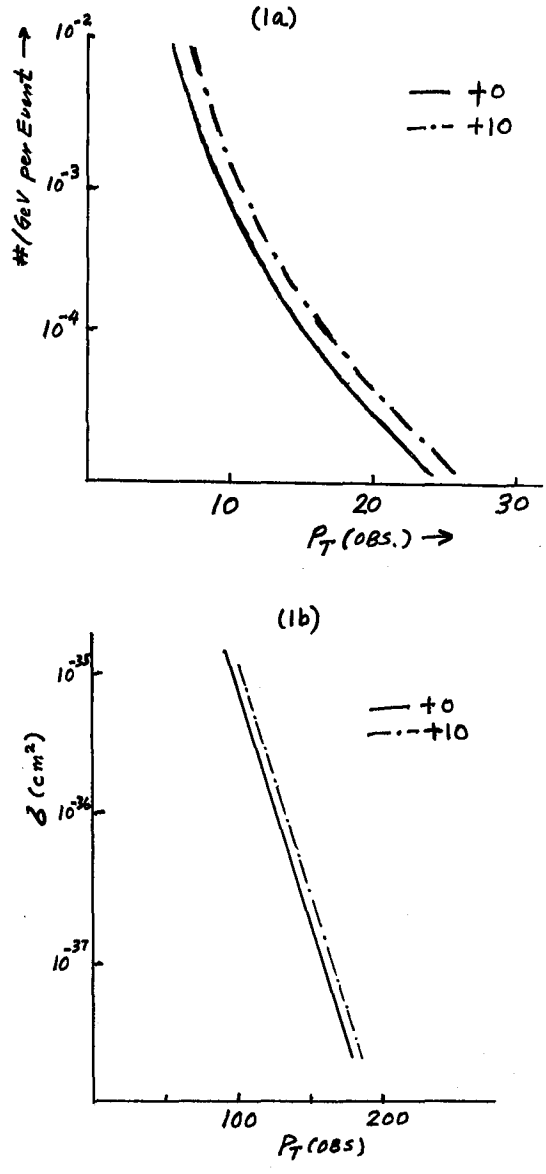

Figure 1 - Distribution of observed Pt of the highest Pt cluster observed in a event. (1a) - Minimum bias and soft jet events from MBl using Yoh's narrow window algorithm. (1b) -ISAJET 2 Jet events using Gordon's wider window algorithm.

cluster. The effect of 10 extraneous minimum bias events is merely to shift the energy scale of the spectrum by an amount roughly 1.5 times the expected ambient background from the average energy flow of 2.5 Gev transverse energy per unit rapidity per event. This corresponds to about 1 Gev in Yoh's algorithm and 8 Gev in Gordon's algorithm; the slope of the spectrum remains unchanged. While this represents a large factor in rate at fixed Et threshold due to the steep slope, a change in the threshold by the given amount would maintain the trigger rate.

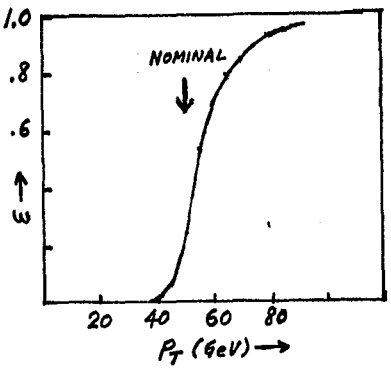

Figure 2 - Efficiency at a nominal cluster Pt threshold of 50 GeV for FOXjets vs. the Pt of the hard scattering.

While this technique of finding the window with the maximum transverse energy in the event is excellent in recognition of hard scattering or heavy mass production (and thus quite adequate for triggering purposes), the observed cluster energy only represent a fraction of the real hard scattering Pt, as is shown in figure 2. Typically, 20% of the transverse energy is outside the window due primarily to gluon bremsstrahlung and parton hadronization. Thus, the threshold, in terms of real Pt of the hard scattering, is rather gradual; one need to go to at least 1.5 the nominal threshold before efficiency becomes greater than 95%.

Hence, the leading parton physics is not seriously affected by extraneous events.

(3) MULTIPLE JET PHYSICS

The most interesting jet physics are the understanding of the QCD nature of hard scattering and the search for heavy particles in their decays to jets (and leptons). This physics requires the precision measurement, not only of the leading partons, but also of the other jets in the events. Here, extraneous events, being able to fake clusters with transverse energy up to approximately 7 GeV, leads to a serious deterioration in physics capabilities.

We have studied (i) W decays into a 35 Gev T and a 5 Gev B generated by ISAJET and (ii) 2 JET production at Pt of 50 + 50 Gev generated by FOX's full QCD Monte carlo. These two types of signals are studies under three luminosity cases -- +0, +2, and +10 extraneous events.

Figure 3 shows the number of clusters found as a function of cluster Et for the W events for three cases -- +0, +2, +10. The number of clusters per event near 5 Gev changes significantly, even for the +2 case. Figure 4a and 4b shows the preliminary attempt to reconstruct the W mass by forming the mass combining all clusters above a certain threshold, for the three intensity cases. Figure 4a uses a criteria requiring that the clusters have minimum of 2 Gev Et and 1.5 Gev in a single tower. Figure 4b raises the cluster Et threshold to 4 GeV. The percentage error (determined by FWHM divided by 2.34) is 13% for the first case and 22% for the second case. For the first case, any extraneous events apparantly will wash out the signal; the second case appears immune to the 2 extra event case, but is washed out in the case of 10 extra events. Thus, the conclusion is clear -- at minimum, extraneous events will force one to adopt a algorithm with a higher threshold so that mass resolution will be deteriorated.

We have also studied an algorithm to measure the hard scattering Pt of FOXjet events. Figure 5 shows the observed Sum of Pt of all clusters found for the three luminosity cases. Again, a deterioration is observed with multiple events. This signal is less sensitive to multiple events than for the mass signal since low Pt clusters at small polar angle contributes slightly to Sum Pt but could contribute enormously to Mass due to the cosine factor.

While these algorithms are quite simplistic, one can envisage more sophisticated algorithms, perhaps with variable size windows, which can perhaps pick up energy near the clusters. Such algorithms could result in better

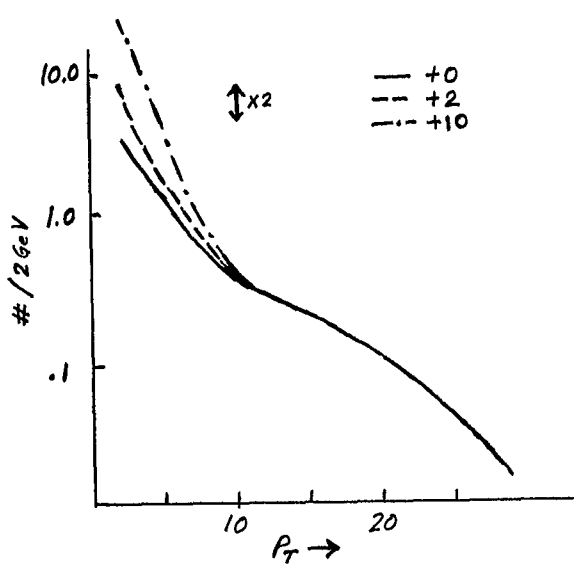

Figure 3 - Number of clusters found per W into T Bbar event vs. the observed cluster Pt. The three luminosity cases are +0, +2 and +10.

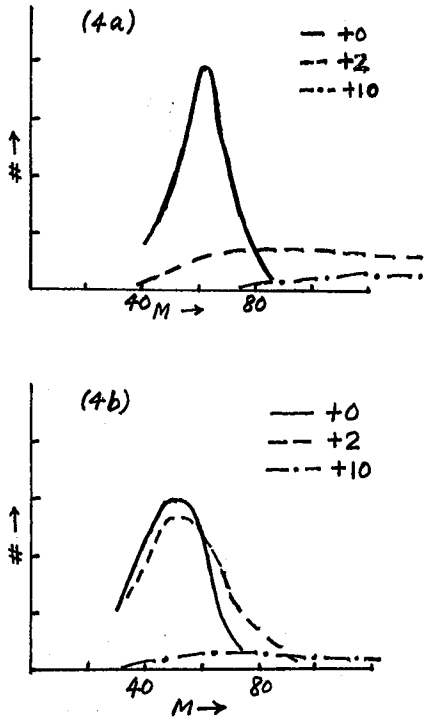

Figure 4 - Reconstructed W mass distribution for the three luminosity cases. (4a) -With cluster threshold at 2 Gev Pt. (4b)-With cluster threshold at 4 Gev Pt.

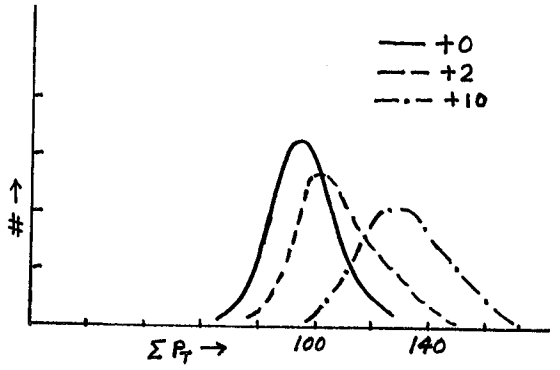

Figure 5 - Reconstructed Summed Pt in 50 + 50 Gev FOXjet events for three luminosity conditions; all observed clusters with Pt above 2 Gev is summed.

resolution, perhaps 10% for the W mass. However, it is likely that these algorithms will be even more sensitive to multiple events; we have tried a simple algorithm which attempt to sum all neighboors as long as they exceed a .4 Gev threshold; this algorithm fails abysmally in the case of +10, by having the cluster grow to a size comparable to the entire array.

(4) MISSING ET PHYSICS

One of the most exciting physics possibilities in hadronic colliders is the search for new heavy particles which decay into jets and invisible particles. Examples are Z into 2 neutrinos produced along with an energetic gluon, production of gluinos, squarks, leptoquarks, etc. These events are charaterized by one or more jets with large missing Et. Two examples are a single 30 Gev gluon with 30 Gev missing Et, and two jets 100 Gev and 50 Gev in Pt and non colinear in the azimuthal view; these are signatures of Z into 2 neutrinos and gluino pair production.

Resoution for missing Et can be smeared by many sources besides the energy resolution of the calorimeter. Other sources of smearing are leakage down the beam hole, punch through leakage, missing neutrinos from conventional sources (which may be vetoed by throwing out all events with electrons or muons, a formidable task), dead or inefficient areas, and non-uniformity due to attenuation and due to difference in EM and hadronic shower response.

Assuming that the dominant source of smearing is in fact the energy resolution, then the error in missing Et scales as square root of Sum Et. Typical minimum bias events have Sum Et of 25 Gev, while the two signals mentioned above, assuming another 20 Gev Et ambient background in the events, would be 50 Gev and 170 Gev respectively. Thus, the increase in error in missing Pt for +2 (+10) for the two cases would corresponds to factors of 1.4 (2.5) and 1.14 (1.6). This deterioration could be crucial.

Another serious consequence of multiple events is that it would make the task of lepton identification more difficult. Many proponents of missing Pt physics stress the absolute necessity of being able to identify events with charged leptons (at least above a certain Pt) and thus being able to discard these events; these charged leptons often imply heavy quark production and thus imply that the event will also likely have neutrinos. Multiple events would enable electrons, through overlap with hadrons, to simulate hadrons; in addition, photon conversion would create large numbers of electron positron pairs. This problem is likely to be critical for non-magnetic detectors.

(5) ISOLATED LEPTON AND PHOTON PHYSICS

Another important physics signature is that of an isolated energetic lepton or photon. Background rejection is usually much better for leptons which are isolated, although one could in some instances tolerate low energy particles nearby.

The effect of multiple events can easily be determined by the fact that the multiplicity is about 5 charged particles and 3 neutral particles per unit rapidity. In the case of a tower calorimeter with tower size 10 degrees and .1 in rapidity, the number of towers per unit rapidity is 360, leading to an occupancy rate of 1 in 45 towers. Thus, demanding that the signal tower have no other particle would cause a 2% loss per extraneous event; if we want to demand absence of particle in the 8 neighboring towers as well, the inefficiency increases to about 20%. Conversely, if one could tolerate particles with pt below 1 Gev, then the situation is roughly 4 times better. The problems of hadronic showers are somewhat worse since most showers would illuminate several towers.

Of greater concern is the situation with the tracking requirement for the lepton. Backgrounds to electrons such as charged-neutral overlap may be more serious. It may also be more difficult to remove photon conversion background by searching for the other electron.

(6) MISCELLANEOUS COMMENTS

We briefly comment on several other issues of relevance to multiple events. These includes thoughts on (i) Advantages of CW beams vs. bunched beam, (ii) Effects of multiple events on tracking, (iii) Effects of multiple events on data reduction and processing, and (iv) Recognition of multiple events.

(i) Advantages of continuous beam vs. bunched beams

One could reduce the resolution time down to 20-50 nsec; this would reduce the average number of events within the resolution time, in the case of continuous beam (CW); one could further use flash ADC to resolve contributions to the events from more than +-5 to 10 nsec away if one has 100-200 Mhz flash ADC's. While this is expensive, it is a serious advantage. Nevertheless, shortening the gate time and pile up is bound to degrade the energy resolution.

On the other hand, one would have to provide a t-zero for drift chambers in the continuous beam case, leading to large amounts of fast scintillators.

(ii) Effects of multiple events on tracking

The extraneous hits from multiple events will clearly have some effect on reconstruction, inefficiency, triggering, etc. The amount of reconstruction time would be increased significantly in the presence of excess hits; this is our experience when we add noise hits to our monte carlo data sample. Certain algorithms, whose time requirements goes as the square of the number of hits, must thus be discarded.

Another effect is the inefficiency induced by the extra tracks; this seems to be not a very important effect; in our studies of an isolated high Pt track in a minimum bias event, the efficiency for the high Pt track at large angles exceed 99%; thus extra events are unlikely to cause significant loss. For the case of the jet core, the density there is almost entirely due to the jet itself; extraneous events are unlikely to be too important, although it may be the straw that breaks the camel's back. A more serious problem is that extra tracks always have some probability of robbing a good hit from an important track; this can be ameliorated by increasing the number of measurements.

A third issue is the effect on a high Pt trigger; we have investigated a high Pt trigger algorithm involving using chamber cells as hodoscopes, and demanding a straight track inside a solenoid. A particular implementation would give a 10%-90% threshold of 4-7 Gev in Pt, using 11 planes; less than 1 in 500 minimum bias events would pass this criteria. However, typical occupancy in the intermediate planes within the search road is about 8%; thus, adding 10 extra events is bound to swamp this particular algorithm. Of course, a more sophisticated algorithm (presumably much more expensive) could probably provide a good rejection.

No dedicated studies on these important issues have been made. It would be important to determine how much more sophisticated the tracking system have to be, and how much more computer time one would need to reconstruct the events.

(iii) Effects on data reduction and processing

Having multiple events is definitely going to increase the load on data acquisition and reduction. Not only is the information per event significantly larger, but also the tendency to trigger preferentially on multiple events and the necessity of having larger numbers of channels will likely cause an order of magnitude increase in data rate compared with current large detectors. Thus, it is crucial to be able to process the data at a lower level.

Data processing effort is also likely to be an order of magnitude higher. As was discussed earlier, track reconstruction time will greatly increase in the presence of extraneous hits.

(iv) Recognition of multiple events

In a scenario in which the average number of events per resolution time is less than 1, one could try to bypass all of

the above problems by trying to recognize multiple events and then throwing them out. Many ideas exists; one such idea is to have a tracking system near the beam pipe whose purpose is to measure the multiple vertices; one could then hope to be able to recognize multiple interactions on line and discard them.

CONCLUSIONS

The effect of multiple events within the resolution time of a detector must be investigated much more thoroughly. Our studies show that capabilities for physics measurements are seriously compromised, especially for multiple jets. Unfortunately, due to QCD and the existence of heavy flavors, almost all interesting hadronic final state physics involved multiple jets. Whether this deterioration will wash out a particular signal will depend on signal to background for that process. In hadronic colliders, where jet physics signals are not particularly striking, the effect of multiple events could well be fatal for many physics signals. Signals involving leptons only, however, will likely not be washed out since signal to background is usually better.

VIRTUS: A MULTI-PROCESSOR EVENT SELECTOR USING FASTBUS

J. Ellett

University of California
Los Angeles, California 90024

This report describes a large, parallel array of M68000 microprocessors, designed with a throughput capacity of 10,000 events per second. FASTBUS segments interconnect the microprocessors, the experiment data readout system, and the PDP-11 data acquisition system. A single M68000 receives the complete set of data for one event and processes the event independently of other events and other processors. FASTBUS provides the medium and the protocol for the efficient transfer of data-blocks to and from processors that become available in random order. Without modification, VIRTUS is also capable of being used off-line for full event analysis.

INTRODUCTION

This report describes a programmable multi-processor system that will make the final decision in the event selection process of an experiment (VIRTUS = Very-Intelligent-Real-Time-Event-Selector). This system, designed with a throughput capability of 10,000 events per second, consists of a large, parallel array of M68000 microprocessors. FASTBUS segments interconnect the microprocessors, the experiment data readout system, and the PDP-11 data acquisition system. Events selected by the trigger logic of the experiment are distributed via FASTBUS to an available M68000. A single M68000 receives the complete set of data for one event and processes the event independently of other events and other processors. If an event is rejected, the processor becomes available for a new one. Accepted events are transferred via FASTBUS to a PDP-11. At any point in time a large number of independent events will reside in the memories of the M68000s and will be processed concurrently.

A fundamental design problem with this type of system is having efficient transfer of data-blocks to and from processors that become available in random order. FASTBUS provides the medium and the protocol for solving this problem.

The proposed processor system is designed so that a small, 16-processor version in a single FASTBUS crate can be constructed to test the concept and the hardware. The basic system can then be expanded to the desired size. A system of about 250 processors is presently envisaged, although much larger numbers are possible.

The general architectural features of the proposed system are the following:

1. Programmable
2. Simple in concept
3. Applicable either on-line or off-line
4. Processor independent
5. Host CPU independent
6. Expandable.

Some of the key features of the proposed implementation are:

1. Standardized FASTBUS system
2. Large number of powerful, low-cost microprocessors
3. Small prototype system to test concept
4. Required modules can be designed for general FASTBUS use
5. Efficient use of FASTBUS
6. Fully buffered data transfers
7. Efficient processor allocation scheme.

The initial test application of the 16-processor prototype system will be in experiment R608, which is running at the CERN-ISR. The spectrometer data are read out with a combination of standard CAMAC hard-

ware and a 16,448 channel TDC system designed and constructed at UCLA for R608. The processor system will make possible the efficient real-time selection of rare event topologies in cases where there is no other means of triggering on these events.

SYSTEM DESCRIPTION

This section describes the overall system operation in some detail. The next section describes the individual modules of the system. A block diagram of the proposed multi-processor system is shown in Figure 1; each block represents a hardware module. The initial prototype version of the system will consist of the FASTBUS crate segment, shown on the left side of the figure, along with the modules connected to it. The crate will include five modules that control the transfer of event data from the experiment to a designated processor module, 16-processor modules, and a host-computer interface module. The system may be expanded by using Simple Segment Interconnect modules to connect the original FASTBUS segment to additional FASTBUS crates filled with processor modules. Table 1 lists the modules and quantities necessary for the 16-processor basic system in the prototype application to experiment R608.

The basic concept of the proposed system is quite simple. It is composed of three primary parts, the event readout and buffering system, a large number of processors connected in a parallel array, and a connection to a host-processor. Events are received, stored, and distributed to the processors by the readout system. Each processor receives the entire data-set of an event, and processes that event independently and asynchronously from all other processors and events. Analyzed events are either discarded, if of no interest, or sent to the host-computer for recording on tape.

Control of the distribution of incoming events to the processors and outgoing events to the host is managed with the use of two queues, one in the Event Readout Control Module and the other in the Host Processor Interface Module. These queues are written to by the individual processors when they have available memory space for a new event or when a processed event is ready for transfer to the host. The processor writes a single word containing the processor address and block-mode register to use for the transfer.

TABLE 1

COMPONENT LIST OF BASIC SYSTEM

QTY	DESCRIPTION
1	FASTBUS crate with ancillary logic and power supply.
1	TDC Buffer Readout Control Module(TBRC)
4	CAMAC Crate Readout Control Module(CCRC)
5	Event Data FIFO module(EDF)
1	Event Readout Control Module(ERC)
16	M68000 Processor Element Module(M68KPE)
1	Host Processor Interface Module(HPI)
1	PDP-11 Unibus Adapter Module(PDPAM)
1	FASTBUS Monitor Module(FBM)

The block-mode register will be preset by the processor to the internal memory address. In the case of incoming events, the ERC will become bus master and execute a primary address cycle using the top element in its queue to make the connection to the processor. Then it will use a non-handshaked, block-mode write to send the event data at maximum speed to the processor.

In the case of outgoing events to the host, the host will become bus master, make the connection to the processor using the top element in its queue, and then execute a non-handshaked, block-mode read to receive the processed event data. In both cases the processor acts as a slave during the transfer. An internal processor interrupt will be generated at the completion of the block-transfer.

The advantages of this method of distributing events are the following:

1. It efficiently handles the routing of data to and from processors which become available in random order.

2. Only a single FASTBUS write cycle is required to specify the transfer of each data block, thus minimizing bus traffic.

3. The method is independent of the number of processors in the system and allows processors to be added (or removed) with little, or no, software changes.

In experiment R608, the initial application of the processor system, each event generates about 200 16-bit words of wire chamber data and 400 16-bit words of CAMAC data. With a minimum-bias trigger followed by the existing multiplicity logic, the maximum event rate available to the processor system is 10 KHz. In order to minimize the readout time, event data will be transferred to the processor system in 5 parallel channels (one channel for the wire chamber data words and one for each of four CAMAC crates). The event readout time is the time required to read the slowest of the five channels. Assuming a 0.5 μsec/word rate for the CAMAC channels and a 0.25 μsec/word rate to read from the TDC buffer memory, the time required to read the event into the Event Data FIFO modules is 50 μsec (200*0.25 or 100*0.50). If 50 μsec digitization time is allowed for the CAMAC system, the total event time is about 100 μsec. Thus, entire events can be transferred into the processor system at about a 10 KHz rate, matching the fastest rate in the experiment.

The FIFOs in the EDF modules are large enough to buffer several events, thereby allowing event data input to overlap in time with event data output, via FASTBUS, to a processor. The data will be formatted into 32-bit words for FASTBUS transfers. Assuming a non-handshaked, block-mode transfer rate of 200 nanoseconds per 32-bit word, the event transfer time from the EDFs to a processor is 60 μsec (0.20*600/2). Table 2 gives a summary of the different types of transfers that occur on the FASTBUS, the maximum anticipated rate, the length of time for each transfer, and the total bus loading in msec/sec.

TABLE 2

FASTBUS TRANSACTION SUMMARY

Type of Transfer	Rate (Hz)	Length (μsec)	Load (msec/sec)
EDF to M68KPE	10,000	60	600
Host from M68KPE	100	100	10
M68KPE to ERC queue	10,000	1	10
M68KPE to Host queue	100	1	0.1
Totals	20,200		620.1

As seen in Table 2, the projected maximum number of bus transactions is on the order of 20,000 per second, and the maximum expected bus loading is 62%.

Although the primary use for the proposed processor system is as an on-line event selector, it is clear that the system can also be used off-line to process events that have already been recorded on tape. The only functional difference would be that the host becomes the event source as well as the destination for processed events. The distribution of events to and from the processors would be handled in exactly the same manner as before, except that both queues would be maintained in the Host Processor Interface module.

The memory size of the processor modules, 512 KByte, should be large enough for relatively sophisticated compiled FORTRAN programs. Floating point hardware is optional for the processor modules, and expansion of the memory space is possible through a connector to an external memory module.

MODULE DESCRIPTIONS

This section gives a general description of each module. These descriptions are intended to give a general understanding of the function and operation of the modules and are not a final specification. The nine modules are listed below. Of these nine, eight are general purpose modules that could be used in other FASTBUS applications. The only module that is not general purpose is the UCLA TDC Buffer Readout Control Module. The Simple Segment Interconnect module is not necessary for the initial 16-processor system but is necessary when the system is expanded to a larger number of processors. The following system modules are described in this section:

1. TDC Buffer Readout Control Module (TBRC)
2. CAMAC Crate Readout Control Module (CCRC)
3. Event Data FIFO Module (EDF)
4. Event Readout Control Module (ERC)
5. M68000 Processor Element Module (M68KPE)
6. Host Processor Interface Module (HPI)
7. PDP-11 Unibus Adapter Module (PDPAM)
8. FASTBUS Monitor Module (FBM)
9. Simple Segment Interconnect (SSI)

TDC BUFFER READOUT CONTROL MODULE

This module is installed in the Memory Crate of the existing UCLA wire chamber TDC readout system. It contains the logic required to transmit the TDC data in the Memory Crate to the Event Data FIFO module upon receipt of the proper signal from the EDF. The data is transmitted in the proper format for the EDF module. When not transmitting data, this module provides access by FASTBUS to internal registers in the Memory Crate via the EDF module.

CAMAC CRATE READOUT CONTROL MODULE

This module performs the equivalent function as the previous module but for a CAMAC crate. It physically replaces the crate controller in a CAMAC crate. It should have a fast read mode that only uses the S1 CAMAC pulse. When not transmitting to the EDF, this module will allow FASTBUS to execute individual CAMAC cycles via the EDF module.

EVENT DATA FIFO MODULE

This is a FASTBUS module that is installed in a crate segment. It receives data over an external bus through a front panel connector and is controlled by the Event Readout Control Module via the auxiliary connector. This module performs two functions, which may be active simultaneously - writing a data-block to the internal FIFO (first-in, first-out) memory from an external device, and transmitting a data-block from the FIFO memory to a destination on the FASTBUS in non-handshake, block-mode. Both functions are controlled by signals from the ERC module; the signals pass through the auxiliary connector. The FIFO memory is 32-bits wide and is large enough to hold several events (1K to 2K 32-bit words). When idle, this module will allow FASTBUS access to an internal register whose contents can be used to access and control the external device over the external bus.

EVENT READOUT CONTROL

This is a FASTBUS module that controls the readout of event data from the external devices into the EDF modules and the transfer of data from the EDF modules to a destination on the FASTBUS. Both types of data transfer can occur at the same time. The ERC uses a simple Auxiliary Bus connected to the EDFs via the auxiliary connectors to control the EDFs. From the trigger logic, the ERC module receives signals that indicate when an event is available for transfer to the EDFs. When an event is available, a signal is sent to the EDFs, via the auxiliary connectors, to initiate the transfer. The completion of the transfer is indicated by the return of signals from the EDFs. As long as space remains in each EDF FIFO, a new event will be accepted by the ERC.

The ERC maintains a count of the number of complete events present in the EDFs. If this number is one or more, then the ERC will initiate a block-mode transfer from the EDFs to a destination processor. The selection of the destination processor is made using the contents of a FIFO memory on the ERC board. Each processor in the system that has available memory space for an event, will write its address to this FIFO. The ERC then uses the top value in the FIFO as the destination address. To execute the transfer of the event data, the ERC arbitrates for, and gains control of, the FASTBUS. It then executes a primary address cycle to set up the transfer. Via the Auxiliary Bus, the ERC then enables each of the EDF modules in turn to transmit its data in non-handshaked, block-mode. When the final EDF has completed its transmission, the ERC interrupts the destination processor and drops control of the bus. This process is repeated as long as at least one event is present in the EDF modules.

M68000 PROCESSOR ELEMENT MODULE

This module contains the M68000 microprocessor along with its memory, peripherals, and an interface to the FASTBUS. The M68000 bus is used internally as a private bus to interconnect all the devices on the processor module, thereby allowing the M68000 to execute instructions independently of any transactions on the FASTBUS. This module can be either a slave or master FASTBUS device. In the slave mode, the FASTBUS interface becomes master of the internal M68000 bus, thereby allowing FASTBUS access to addresses on that bus. Two sets of incrementing address registers are available for use in block-mode transfers.

In the FASTBUS master mode, two methods of access are provided. In the first method, M68000 addresses within a certain range will be mapped into FASTBUS address space and will automatically cause FASTBUS cycles. The second method gives the M68000 direct control over FASTBUS cycles through a set of special purpose registers. These registers can be used to generate single cycles or block-mode transfers from M68000 address space to FASTBUS address space.

The M68KPE will contain two types of RAM memory.

Space for up to 512 KByte of program memory will be available, as well as a smaller amount of faster RAM, to facilitate high-speed block transfers of data. The internal bus can be extended through a front panel connector to allow additional memory or peripheral devices to be added.

HOST PROCESSOR INTERFACE MODULE

This module provides the connection between the host-processor and the FASTBUS system. It is intended to be a general purpose interface, which can connect to any minicomputer through special purpose adapter modules. It is essentially the same module as the M68KPE without the M68000 and has the same FASTBUS master and slave capabilities. The internal bus is connected to the host-processor through the special purpose adapter module for that host, thereby allowing the host to, in effect, take the place of the M68000.

PDP-11 UNIBUS ADAPTER MODULE

This module, installed on the PDP-11 UNIBUS, allows the PDP-11 to access the internal bus of the Host Processor Interface Module. Various modes of access to the internal bus are provided to the PDP-11. These include registers to gain master control of the internal bus and address mapping logic, which allows direct access to internal bus addresses from Unibus addresses. Interrupts generated by devices on the internal bus will cause PDP-11 interrupts.

FASTBUS MONITOR MODULE

This is a diagnostic module that monitors signals on a FASTBUS segment, thereby facilitating tests of hardware and software. The module contains a large memory that continuously stores the states of the FASTBUS signal lines. The sampling time can be provided externally or derived internally from cycles on the FASTBUS.

Writing to the memory can be stopped N sample periods after a certain pattern of signals is detected, where both N and the pattern can be set. The contents of the memory can be read via the FASTBUS or through an auxiliary connector.

SIMPLE SEGMENT INTERCONNECT MODULE

This is a FASTBUS module that implements a subset of the standard Segment Interconnect Module. It is designed to connect two, and only two, FASTBUS crate segments together using a simple cable, which is not a FASTBUS segment. In addition, it only provides the minimum logic necessary to effect segment to segment FASTBUS cycles.

SOFTWARE

The software components required for the processor system fall into the catagories listed below:

1. Cross software,
2. M68000 resident operating system,
3. Processor interface driver,
4. Host utility programs,
5. On-line application programs,
6. Off-line application programs,
7. System diagnostics.

CROSS SOFTWARE

Several software packages for the host computer are required to allow it to be used for development of the programs that will be run by the M68000 processors. These packages will allow assembly language and FORTRAN programs to be compiled and linked together into programs that are executable by the M68000. The following software will be required:

1. M68000 assembly language cross assembler,
2. M68000 FORTRAN cross compiler,
3. Object module linker,
4. Downline loader.

M68000 RESIDENT OPERATING SYSTEM

An operating system is required that will permanently reside in each M68000 module and will contain

those routines that are necessary for operation of the processor system at the most fundamental level. This operating system will consist of a ROM portion and a down-line loadable RAM portion. The ROM resident part will be a program which contains the initialization code that is entered whenever a power-up occurs or a reset command is received. This code will include diagnostic routines that test for proper operation of the M68KPE module and routines that allow down-line loading of other programs from the host.

The RAM resident portion will provide routines that can be called from application programs to execute system level functions, such as peripheral data I/O, data I/O to the host or another processor in the system, memory allocation, floating point functions, etc.

The operating system software will also contain the routines which receive commands, from the host-processor, to control the loading and execution of the M68000 programs.

PROCESSOR INTERFACE DRIVER

The processor interface driver is an assembly language program that runs (on the host machine) as a driver under the host's operating system and provides the routines that allow control of, and communications with, the processor system via the Host Processor Interface module. All programs running on the host will call this driver to do data I/O to the processor system.

HOST UTILITY PROGRAMS

The utility programs are complete programs that run on the host and allow the operator to perform specific functions involving the processor system. One such program might allow an operator to down-load specified diagnostics to one or more M68000 processors and receive and display diagnostic messages returned from these processors.

ON-LINE APPLICATION PROGRAMS

The on-line application program is the program that runs on the M68000 and implements the event selection algorithm. This program will input an event data-set from the readout system, analyze the data using the appropriate algorithm, and transfer the event to the Host Processor Interface, if the event satisfies the selection criteria. This program will run under the M68000 resident operating system. It will probably be written in M68000 assembly language to optimize execution speed.

Associated with the on-line application program are the changes that will be required in the existing experiment data acquisition software, which runs on the host during on-line data taking. These changes, which incorporate calls to the processor interface driver, allow the processor system to be used as the event source.

OFF-LINE APPLICATION PROGRAM

The off-line application program is a program that runs on the M68000 processor and does full event momentum analysis. It receives unprocessed events from the host computer via the Host Processor Interface and returns analyzed events to the host computer. This program will probably be written in FORTRAN and compiled on the host computer using the FORTRAN cross compiler. It will run under the M68000 resident operating system just as the on-line application program does.

SYSTEM DIAGNOSTICS

To verify proper system operation and to aid in locating faulty system components, a complete set of system diagnostic programs will be required. The following programs must be provided as a minimum set of diagnostics.

1. UCLA Readout System Diagnostic - Modifications to allow the existing diagnostics for the UCLA TDC Readout System to run properly with the processor system.

2. Processor System Exerciser - An overall system exerciser, which is comprehensive enough to exercise each system component. Successful completion of this program should indicate a properly functioning system. Error messages generated should indicate the general location of the faulty component.

3. Module Diagnostics - Individual diagnostic programs for each system component. These programs would exhaustively exercise specific parts of the system.

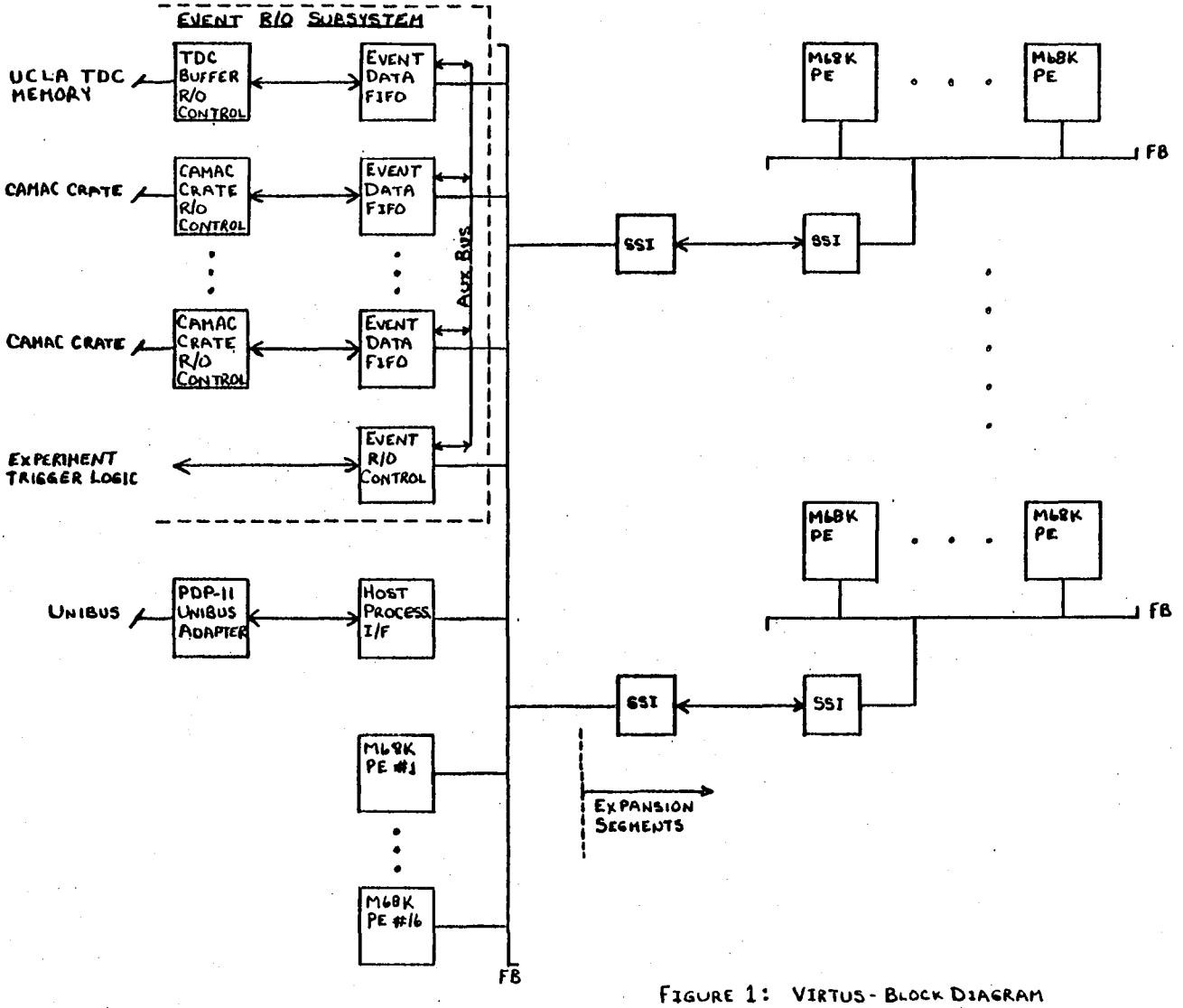

FIGURE 1: VIRTUS - BLOCK DIAGRAM

TECHNICAL INFORMATION DEPARTMENT
LAWRENCE BERKELEY LABORATORY
UNIVERSITY OF CALIFORNIA
BERKELEY, CALIFORNIA 94720